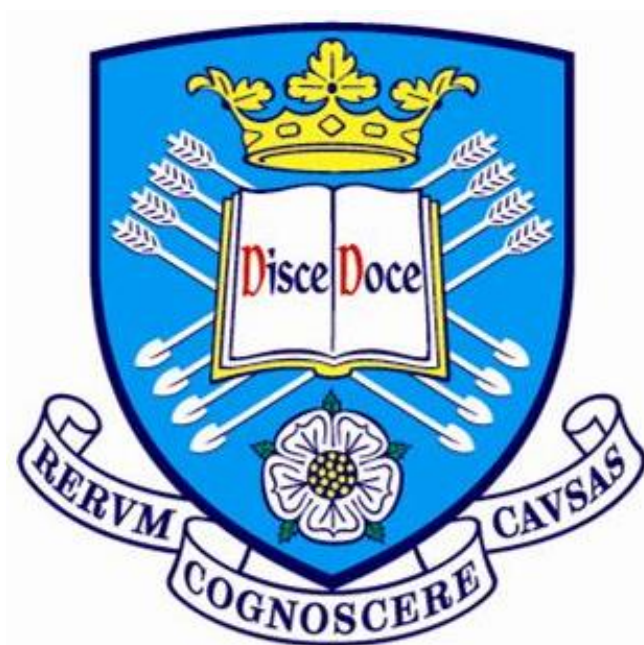


# **Pickering Emulsifiers Based on Block Copolymer Nanoparticles Prepared by Polymerisation-Induced Self-Assembly**



**Saul John Hunter**

**Department of Chemistry  
University of Sheffield**

Submitted to the University of Sheffield in partial fulfilment of the requirements for the degree of Doctor of Philosophy

**September 2021**

## Declaration

---

### Declaration

The work described in this Thesis was carried out at the University of Sheffield under the supervision of Professor Steven P. Armes and Doctor Oleksandr O. Mykhaylyk between October 2017 and September 2021 and has not been submitted, either wholly or in part, for this or any other degree. All the work is the original work of the author, except where acknowledged by references.

Signature:  \_\_\_\_\_

Saul John Hunter

September 2021

**Abstract**

This Thesis evaluates the use of a range of block copolymer nanoparticles prepared by polymerisation-induced self-assembly (PISA) as putative Pickering emulsifiers. Firstly, reversible addition-fragmentation chain transfer (RAFT) solution polymerisation was used to prepare well-defined poly(glycerol monomethacrylate) (PGMA) chains bearing either carboxylic acid, tertiary amine or neutral end-groups. Each of these PGMA precursors was then chain-extended in turn *via* RAFT aqueous emulsion polymerisation of 2,2,2-trifluoroethyl methacrylate (TFEMA) to form spherical nanoparticles. High-shear homogenisation of *n*-dodecane in the presence of such sterically-stabilised nanoparticles led to the formation of oil-in-water Pickering macroemulsions. High-pressure microfluidisation was then used to prepare the three corresponding Pickering nanoemulsions. The nanoparticle adsorption efficiency at the oil/water interface was assessed for each type of nanoparticle at both pH 3 and pH 7 by gel permeation chromatography (GPC) using a UV detector. Nanoparticles with charged end-groups exhibited relatively low adsorption efficiency, whereas up to 90% of the neutral nanoparticles were adsorbed onto the oil droplets. This was confirmed using small-angle X-ray scattering (SAXS) experiments, which indicated that the packing efficiency of neutral nanoparticles around oil droplets was higher than that of nanoparticles bearing charged end-groups. Moreover, Pickering nanoemulsions stabilised with nanoparticles bearing charged end-groups proved to be significantly less stable than those prepared using neutral end-groups.

Sterically-stabilised diblock copolymer nanoparticles were prepared in *n*-dodecane using RAFT dispersion polymerisation. In the absence of any salt dissolved in the aqueous phase, high-pressure microfluidisation of precursor water-in-oil macroemulsions led to the formation of relatively large aqueous droplets, with dynamic light scattering (DLS) measurements indicating a mean diameter of more 600 nm. However, systemically increasing the salt concentration prior to microfluidisation produced finer aqueous droplets, until a limiting diameter of around 250 nm was obtained at 0.11 M NaCl. SAXS studies conducted on a nanoemulsion confirmed that the water droplets are coated with a loosely-packed monolayer of adsorbed nanoparticles. The effect of varying the amount of NaCl dissolved in the aqueous droplets on their initial rate of Ostwald ripening was investigated using DLS. Finally, the long-term stability of these water-in-oil Pickering nanoemulsions was examined using analytical centrifugation. The rate of droplet ripening can be substantially reduced by using 0.11 M NaCl instead of pure water. However, increasing the salt concentration up to 0.43 M provided no discernible improvement in long-term stability.

RAFT aqueous emulsion polymerisation of hydroxybutyl methacrylate (HBMA) has been conducted using a relatively short PGMA<sub>41</sub> precursor as a steric stabiliser block. <sup>1</sup>H NMR studies indicated that conversions of more than 99% were achieved within 2 h at 50 °C using a low-temperature VA-044 initiator. GPC analysis confirmed that high blocking efficiencies and relatively low dispersities ( $M_w/M_n < 1.37$ ) could be achieved. A pseudo-phase diagram was constructed by systematically increasing the PHBMA target degree of polymerisation from 10 to 120 while varying the copolymer concentration between 5 and 20% w/w. The evolution in copolymer morphology when targeting PGMA<sub>41</sub>-PHBMA<sub>120</sub> vesicles was monitored using TEM. This technique revealed intermediate morphologies that are similar to those reported during the preparation of PGMA<sub>47</sub>-PHPMA<sub>200</sub> vesicles *via* RAFT aqueous dispersion polymerisation. Linear PGMA<sub>41</sub>-PHBMA<sub>110</sub> vesicles survive high-shear homogenisation to act as genuine Pickering emulsifiers for *n*-dodecane droplets.

Finally, the first example of thermoresponsive diblock copolymer nano-objects prepared *via* RAFT aqueous emulsion polymerisation of HBA is reported. More specifically, a poly(ethylene glycol) (PEG) precursor is chain extended with HBMA. The resulting PEG<sub>45</sub>-PHBMA<sub>20</sub> diblock copolymer exhibited three thermoreversible transitions in aqueous solution, as confirmed by DLS, SAXS, and rheology studies. Variable temperature <sup>1</sup>H NMR studies suggest that these transitions are initially driven by dehydration of the PEG<sub>45</sub> stabiliser block and subsequently facilitated by uniform hydration of the hydrophobic PHBMA block at higher temperatures.

### Publications

M. J Rymaruk.; **S. J. Hunter**; C. T. O'Brien; S. L. Brown; C. N. Williams; S. P. Armes, 'RAFT Dispersion Polymerization in Silicone Oil' *Macromolecules* **2019**, *52*, 2822-2832.

**S. J Hunter**; K. L. Thompson; J. R. Lovett; F. L. Hatton; M. J. Derry; C. Lindsay; P. Taylor; S. P. Armes, 'Synthesis, Characterization, and Pickering Emulsifier Performance of Anisotropic Cross-Linked Block Copolymer Worms: Effect of Aspect Ratio on Emulsion Stability in the Presence of Surfactant' *Langmuir* **2019**, *35*, 254-265.

**S. J. Hunter**; N. J. W. Penfold; D. H. Chan; O. O. Mykhaylyk; S. P. Armes, 'How Do Charged End-Groups on the Steric Stabilizer Block Influence the Formation and Long-Term Stability of Pickering Nanoemulsions Prepared Using Sterically Stabilized Diblock Copolymer Nanoparticles?' *Langmuir* **2020**, *36*, 769-780.

C. György; **S. J. Hunter**; C. Girou; M. J. Derry; S. P. Armes, 'Synthesis of Poly(stearyl methacrylate)-poly(2-hydroxypropyl methacrylate) Diblock Copolymer Nanoparticles *via* RAFT Dispersion Polymerization of 2-Hydroxypropyl Methacrylate in Mineral oil' *Polym. Chem.* **2020**, *11*, 4579-4590.

**S. J. Hunter**; S. P. Armes, 'Pickering Emulsifiers Based on Block Copolymer Nanoparticles Prepared by Polymerization-Induced Self-Assembly' *Langmuir* **2020**, *36*, 15463-15484.

**S. J. Hunter**; E. J. Cornel; O. O. Mykhaylyk; S. P. Armes, 'Effect of Salt on the Formation and Stability of Water-in-Oil Pickering Nanoemulsions Stabilized by Diblock Copolymer Nanoparticles' *Langmuir* **2020**, *36*, 15523-155

## Publications

---

**S. J. Hunter**; J. R. Lovett; O. O. Mykhaylyk; E. R. Jones; S. P. Armes, ‘Synthesis of Diblock Copolymer Spheres, Worms and Vesicles *via* RAFT Aqueous Emulsion Polymerization of Hydroxybutyl Methacrylate’ *Polym. Chem.* **2021**, *12*, 3629-3639.

**S. J. Hunter**; N. J. W. Penfold; O. O. Mykhaylyk; E. R. Jones; S. P. Armes, ‘Synthesis of Thermoreponsive Diblock Copolymer Nano-Objects by RAFT Aqueous Emulsion Polymerization of Hydroxybutyl Methacrylate’ manuscript in preparation.

### Conferences

- March 2018**      *Oral Presentation* at the 255th National Meeting & Exposition of the American Chemical Society, New Orleans, USA
- July 2018**      *Poster Presentation* at the Young Researchers Meeting, Dublin, UK
- April 2019**      *Oral Presentation* at the 13th International Conference on Advanced Polymers via Macromolecular Engineering, Stellenbosch, SA
- August 2019**      *Oral Presentation* at the 258th National Meeting & Exposition of the American Chemical Society, San Diego, USA
- April 2021**      *Oral Presentation* at the American Chemical Society Spring Virtual Online Meeting 2021

### Acknowledgements

I am immensely appreciative of all the guidance and support I have received from so many people over the past four years. Foremost, I am indebted to both of my supervisors: Prof. Steve Armes and Dr. Oleksandr (Sasha) Mykhaylyk. Firstly, I would like to thank Steve for providing me with an opportunity to conduct research in his lab during my undergraduate years and carry out my PhD studies in his group. Your wealth of scientific knowledge, meticulous proof reading and abundance of ideas have been greatly appreciated. I must also thank you for providing me with the opportunity to travel to international conferences. Thank you to Sasha for all the help and guidance you have provided. Your door was always open when I had any questions or problems and I really appreciate that. Also, my thanks to Prof. Tony Ryan for providing me with an opportunity to learn how to ski (well not quite).

I would like to thank the ESPRC and DSM for funding my PhD. In particular, I would like to thank my industrial contacts Dr. Lizzy Jones and Dr. Paul Wyman for the interesting discussions and ideas. Thank you to all the local contacts at the various beamlines we have been lucky enough to make use of: Dr. Andy Smith at Diamond, Dr. Thomas Zinn at the ESRF and Dr. Adam Washington at ISIS.

I would like to express my gratitude to the many extremely helpful University of Sheffield staff members that have helped me over the years. Chris and Svet for all their help and preparation at TEM. Sandra and Khalid for running my NMR experiments and for their useful discussions. I would also like to thank all of the staff in the Accounts office and Stores for their help throughout my project. Thanks to the CDT managers, Dr. Joe Gaunt and Dr. Jennifer Dick.

Thanks to all those in the D42 office (RoR). A massive cheers, J to Adam Czajka. We have had such a laugh these past three years and I truly appreciate all your generosity and all you have done for the Dovahkiin. Thanks to the Badminton crew – Sarah, Pash, Shan, Debs and Courtney!

A huge thank you to every member of the Armes group past and present. Thanks to Matt Rymurk for teaching me the RAFT ropes. Thanks to Joe and Kate for their support during my MChem project. Thanks to Matt Derry for all the SAXS and flute help and to Penfold for all the help and laughs in lab. Massive thanks to Tom Neal for helping me with SAXS and rheology throughout my PhD. Thanks to Craig, Erik, Yin, Amy, Olly, Reb, Drewdog and all the ex-Armes Group members that have helped me. Thank you to Derek, Izzy, Csilla, Emma, Rory and all the current Armes group members.

I am very lucky to have such a large and supportive family. Thanks to my Mum and Dad for the encouragement and always making sure I have enough fish. A big thanks to Hunter's gym. To all my nieces and nephews who always put a smile on my face. Thank you to the Foster crew for their kindness and generosity. In particular, a special thanks to Marrow and Sausage. Thank you to the boys, Mr. Choo and Ronkle for the well needed walks whilst writing this Thesis.

Finally, thank you to Claudia for you everything you do and for always supporting me.

### Abbreviations

$\eta^*$	Complex viscosity
$\chi$	Flory-Huggins parameter
$\omega$	Rate of Ostwald Ripening
$a_0$	Surface area occupied by the hydrophilic head-group
$A_{\text{eff}}$	Adsorption efficiency
AA	Acrylic acid
ACVA	4,4'-Azobis(4-cyanopentanoic acid)
ATRP	Atom transfer radical polymerisation
BzMA	Benzyl methacrylate
CDB	Cumyl dithiobenzoate
CGT	Critical gelation temperature
CMC	Critical micelle concentration
CPDB	2-Cyano-2-propyl dithiobenzoate
CTA	Chain transfer agent
$D_z$	Hydrodynamic $z$ -average diameter
DAAM	Diacetone acrylamide
DDMAT	2-(Dodecylthiocarbonothioylthio)-2-methylpropionic acid
DLS	Dynamic light scattering
DMAC	<i>N,N</i> -dimethyl acrylamide
DP	Mean degree of polymerisation
EGA	(Ethylene glycol) methyl ether acrylate
EGDMA	Ethylene glycol dimethacrylate
EHA	2-Ethylhexyl acrylate
FRP	Free radical polymerisation
$G'$	Storage modulus
$G''$	Loss modulus
GMA	Glycerol monomethacrylate
GlyMA	Glycidyl methacrylate
GPC	Gel permeation chromatography
HBA	4-Hydroxybutyl acrylate
HBMA	Hydroxybutyl methacrylate
HEMA	2-Hydroxyethyl methacrylate
HLB	Hydrophilic-lipophile balance

## Abbreviations

---

HPMA	2-Hydroxypropyl methacrylate
HPMAC	<i>N</i> -(2-hydroxypropyl) methacrylamide
$l_c$	Effective length of the hydrophobic chain
LAM	Less activated monomer
LAP	Living anionic polymerisation
LCST	Lower critical solution temperature
LMA	Lauryl methacrylate
$M_n$	Number-average molecular weight
$M_p$	Peak molecular weight
$M_w$	Weight-average molecular weight
MA	Methyl acrylate
MAA	Methacrylic acid
MAM	More activated monomer
MEA	2-Methoxyethyl acrylate
MOEMA	2-Methoxyethyl methacrylate
MPETTC	Morpholine-PETTC
$N$	Number of nanoparticles per droplet
$N_s$	Number of copolymer chains per sphere
NAEP	<i>N</i> -(2-acryloyloxy)ethyl pyrrolidone
<i>n</i> BA	<i>n</i> -Butyl acrylate
NIPAM	<i>N</i> -isopropylacrylamide
NMP	Nitroxide-mediated polymerisation
NMR	Nuclear magnetic resonance
$P$	Packing parameter
$P_{\text{eff}}$	Packing efficiency
PDI	Polydispersity index
PEG	Poly(ethylene glycol)
PETTC	4-Cyano-4-(2-phenylethanesulfanylthiocarbonyl)sulfanyl pentanoic acid
PISA	Polymerisation-induced self-assembly
$pK_a$	Acid dissociation constant
PMMA	Poly(methyl methacrylate)
PNVP	Poly( <i>N</i> -vinylpyrrolidone)
PPG-TDI	poly(propylene glycol), tolylene-2,4-diisocyanate terminated

## Abbreviations

---

PS	Polystyrene
$q$	Scattering vector
$R_g$	Radius of gyration
$R_n$	Number-average radius
$R_s$	Spherical core radius
RAFT	Reversible addition-fragmentation chain transfer
RDRP	Reversible deactivation radical polymerisation
SAXS	Small angle X-ray scattering
SDS	Sodium dodecyl sulfate
SIPLI	Shear-induced polarised light imaging
SMA	Stearyl methacrylate
T21s	<i>Tert</i> -butyl peroxy-2-ethylhexanoate
$T_m$	Vesicle membrane thickness
$T_g$	Glass transition temperature
$T_s$	Adsorbed shell thickness
$T_w$	Worm thickness
TEM	Transmission electron microscopy
THF	Tetrahydrofuran
TFEMA	2,2,2-Trifluoroethyl methacrylate
UCST	Upper critical solution temperature
UV-Vis	Ultraviolet-Visible
$V$	Volume occupied by the hydrophobic chain
VA-044	2,2'-Azobis(2-(2-imidazolin-2-yl)propane)dihydrochloride
$x_{sol}$	Volume fraction of solvent within the core domain

## Table of Contents

<b>Chapter 1</b>	<b>Introduction</b>	<b>1</b>
<b>1.1</b>	<b>General Concepts in Polymer Science</b>	<b>2</b>
<b>1.2</b>	<b>Free Radical Polymerisation</b>	<b>3</b>
<b>1.3</b>	<b>Living Anionic Polymerisation</b>	<b>7</b>
<b>1.4</b>	<b>Reversible Deactivation Radical Polymerisation</b>	<b>9</b>
<b>1.5</b>	<b>Reversible Addition-Fragmentation Chain Transfer Polymerisation</b>	<b>10</b>
<b>1.6</b>	<b>Polymerisation Methods</b>	<b>13</b>
1.6.1	Solution Polymerisation	13
1.6.2	Emulsion Polymerisation	14
1.6.3	Dispersion Polymerisation	16
<b>1.7</b>	<b>Self-Assembly</b>	<b>17</b>
<b>1.8</b>	<b>Polymerisation-Induced Self-Assembly</b>	<b>21</b>
1.8.1	PISA by RAFT Aqueous Emulsion Polymerisation	22
1.8.2	PISA by RAFT Aqueous Dispersion Polymerisation	30
1.8.2	PISA by RAFT Dispersion Polymerisation in Non-Polar Solvents	34
<b>1.9</b>	<b>Emulsions</b>	<b>36</b>
1.9.1	General Concepts in Emulsion Science	36
1.9.2	Emulsion Characterisation Techniques	41
1.9.3	Pickering Emulsions	46
1.9.4	Pickering Emulsions Stabilised by Block Copolymer Nanoparticles	49
1.9.5	Pickering Nanoemulsions	54
<b>1.10</b>	<b>Thesis Outline</b>	<b>57</b>
<b>1.11</b>	<b>References</b>	<b>59</b>
<b>Chapter 2</b>	<b>How do Charged End-Groups on the Steric Stabiliser Block Influence the Formation and Long-Term Stability of Pickering Nanoemulsions Prepared Using Sterically-Stabilised Diblock Copolymer Nanoparticles?</b>	<b>71</b>
<b>2.1</b>	<b>Introduction</b>	<b>72</b>

## Abbreviations

---

<b>2.2</b>	<b>Experimental</b>	<b>75</b>
2.2.1	Materials	75
2.2.2	Synthesis of PGMA <sub>48</sub> Precursor <i>via</i> RAFT Solution Polymerisation in Ethanol	75
2.2.3	Synthesis of PGMA <sub>48</sub> -PTFEMA <sub>50</sub> Diblock Copolymer Nanoparticles <i>via</i> RAFT Aqueous Emulsion Polymerisation of TFEMA	76
2.2.4	Preparation of PGMA <sub>48</sub> -PTFEMA <sub>50</sub> -Stabilised Pickering Macroemulsions Using High-Shear Homogenisation	77
2.2.5	Preparation of PGMA <sub>48</sub> -PTFEMA <sub>50</sub> -Stabilised Pickering Nanoemulsions Using High-Pressure Microfluidisation	77
2.2.6	Characterisation	77
<b>2.3</b>	<b>Results and Discussion</b>	<b>81</b>
2.3.1	Synthesis and Characterisation of PGMA <sub>48</sub> -PTFEMA <sub>50</sub> Diblock Copolymer Nanoparticles	81
2.3.2	Effect of End-Group Charge on the Formation of Pickering Nanoemulsion	88
2.3.3	Effect of End-Group Charge on the Stability of Pickering Nanoemulsion	100
<b>2.4</b>	<b>Conclusions</b>	<b>103</b>
<b>2.5</b>	<b>References</b>	<b>104</b>
<b>Chapter 3</b>	<b>Effect of Salt on the Formation and Stability of Water-in-Oil Pickering Nanoemulsions Stabilised by Diblock Copolymer Nanoparticles</b>	<b>108</b>
<b>3.1</b>	<b>Introduction</b>	<b>109</b>
<b>3.2</b>	<b>Experimental</b>	<b>114</b>
3.2.1	Materials	114
3.2.2	Synthesis of a PSMA <sub>32</sub> precursor <i>via</i> RAFT Solution Polymerisation in Toluene	115
3.2.3	Synthesis of PSMA <sub>32</sub> -PTFEMA <sub>53</sub> Diblock Copolymer Nanoparticles <i>via</i> RAFT Dispersion Polymerisation of TFEMA	115
3.2.4	Preparation of PSMA <sub>32</sub> -PTFEMA <sub>53</sub> -Stabilised Pickering Macroemulsions Using High-Shear Homogenisation	115
3.2.5	Preparation of PSMA <sub>32</sub> -PTFEMA <sub>53</sub> -Stabilised Pickering Nanoemulsions Using High-Pressure Microfluidisation	116

## Abbreviations

---

3.2.6	Characterisation	116
<b>3.3</b>	<b>Results and Discussion</b>	<b>120</b>
3.3.1	Synthesis and Characterisation of PSMA <sub>32</sub> -PTFEMA <sub>53</sub> Diblock Copolymer Nanoparticles	120
3.3.2	Effect of Salt on the Formation of w/o Pickering Nanoemulsions	123
3.3.3	Characterisation of w/o Pickering Nanoemulsions	132
3.3.4	Effect of Salt on the Stability of w/o Pickering Nanoemulsions	136
<b>3.4</b>	<b>Conclusions</b>	<b>142</b>
<b>3.5</b>	<b>References</b>	<b>143</b>
<b>Chapter 4</b>	<b>Synthesis of Diblock Copolymer Spheres, Worms and Vesicles via RAFT Aqueous Emulsion Polymerisation of Hydroxybutyl Methacrylate</b>	<b>147</b>
<b>4.1</b>	<b>Introduction</b>	<b>148</b>
<b>4.2</b>	<b>Experimental</b>	<b>152</b>
4.2.1	Materials	152
4.2.2	Synthesis of a PGMA <sub>41</sub> precursor <i>via</i> RAFT Solution Polymerisation in Ethanol	152
4.2.3	Synthesis of PGMA <sub>41</sub> -PHBMA <sub>x</sub> Diblock Copolymer Nano-Objects by RAFT Aqueous Emulsion Polymerisation of HBMA	153
4.2.4	Preparation of Pickering Emulsions Stabilised by PGMA <sub>41</sub> -PHBMA <sub>110</sub> Diblock Copolymer Vesicles	153
4.3.5	Preparation of Colloidosomes Stabilised by PGMA <sub>41</sub> -PHBMA <sub>110</sub> Diblock Copolymer Vesicles	153
4.2.6	Characterisation	154
<b>4.3</b>	<b>Results and Discussion</b>	<b>156</b>
4.3.1	Synthesis of PGMA <sub>41</sub> -PHBMA <sub>x</sub> Diblock Copolymer Nano-Objects <i>via</i> RAFT Aqueous Emulsion Polymerisation of HBMA	156
4.3.2	Preparation of Pickering Emulsions Stabilised by Diblock Copolymer Vesicles	167
<b>4.4</b>	<b>Conclusions</b>	<b>173</b>
<b>4.5</b>	<b>References</b>	<b>174</b>
<b>Chapter 5</b>	<b>Synthesis of Thermoresponsive Diblock Copolymer Nano-Objects via RAFT Aqueous Emulsion Polymerisation of Hydroxybutyl Methacrylate</b>	<b>177</b>

## Abbreviations

---

<b>5.1</b>	<b>Introduction</b>	<b>178</b>
<b>5.2</b>	<b>Experimental</b>	<b>180</b>
5.2.1	Materials	180
5.2.2	Synthesis of PEG <sub>45</sub> -PHBMA <sub>20</sub> Diblock Copolymer Nano-Objects <i>via</i> RAFT Aqueous Emulsion Polymerisation of HBMA	180
5.2.3	Characterisation	181
<b>5.3</b>	<b>Results and Discussion</b>	<b>184</b>
5.3.1	RAFT Aqueous Emulsion Polymerisation of HBMA using a PEG <sub>45</sub> -TTC Precursor	184
5.3.2	Characterisation of Thermoresponsive PEG <sub>41</sub> -PHBMA <sub>20</sub> Diblock Copolymer Nano-Objects	186
<b>5.4</b>	<b>Conclusions</b>	<b>200</b>
<b>5.5</b>	<b>References</b>	<b>202</b>
<b>Chapter 6</b>	<b>Conclusions and Outlook</b>	<b>207</b>
<b>6.1</b>	<b>Conclusions and Outlook</b>	<b>208</b>
<b>6.2</b>	<b>References</b>	<b>214</b>
<b>Chapter 7</b>	<b>Appendix</b>	<b>217</b>
<b>7.1</b>	<b>Structural Models for Small-Angle X-ray Scattering Analysis</b>	<b>218</b>
7.1.1	Core-Shell Particle Model	218
7.1.2	Homogenous Spherical Particle Model	219
7.1.3	Spherical Micelle Model	220
7.1.4	Worm-Like Micelle Model	223
7.1.5	Vesicle Model	224
<b>7.2</b>	<b>UV GPC Calibration Plots</b>	<b>226</b>
<b>7.3</b>	<b>References</b>	<b>227</b>

# Chapter 1:

# Introduction

Reproduced in part with permission from:

[S. J. Hunter and S. P. Armes, *Langmuir* **2020**, *51*, 15463-15484]

## 1.1 General Concepts in Polymer Science

Polymers are long-chain molecules composed of smaller molecules. Such building blocks are known as monomers and are combined during a polymerisation reaction. A homopolymer is synthesised by the polymerisation of a single monomer. In contrast, copolymers consist of two or more chemically different monomer units. Examples of linear architectures include statistical, alternating and block copolymers. For example, the latter comprise blocks of different types of homopolymer that are joined together by one or more covalent bonds. A copolymer consisting of two chemically different blocks comprising monomers A and B is known as an AB diblock copolymer.

Staudinger was among the first to recognise the polydispersity associated with the molecular weight of a synthetic polymer, which does not exhibit a unique molecular weight.<sup>1</sup> Instead, such polymers comprise a range of chain lengths, resulting in a molecular weight distribution. The two most important mathematical moments of this distribution are the number-average molecular weight  $M_n$  and the weight-average molecular weight  $M_w$ . The  $M_n$  is defined according to Equation 1.1:

$$M_n = \frac{\sum n_i M_i}{\sum n_i} \quad 1.1$$

where  $n_i$  is the number of chains containing  $i$  repeat units, and  $M_i$  is the molecular weight of such chains.  $M_n$  represents the statistical average molecular weight of all the chains in a sample. Experimental methods for determining  $M_n$  measure the colligative properties of solutions, such as cryoscopy and ebulliometry.<sup>2</sup> The  $M_w$  is defined according to Equation 1.2:

$$M_w = \frac{\sum w_i M_i}{\sum w_i} = \frac{\sum n_i M_i^2}{\sum n_i M_i} \quad 1.2$$

where  $w_i$  is the weight fraction of chains with  $i$  repeat units.  $M_w$  accounts for the molecular weight of each chain when determining their contribution to the average molecular weight.<sup>2</sup>  $M_w$  can be obtained from light scattering measurements on polymer solutions, hence it is biased towards polymers with higher molecular weights. If the average number of monomer units for each

polymer chain (known as the mean degree of polymerisation or DP) was identical, then  $M_w/M_n$  is equal to unity. Certain biopolymers, for example proteins, can be considered to be perfectly monodisperse. The molecular weight distribution of a polymer is relatively narrow if the  $M_w/M_n$  is less than 1.20, and relatively broad if it is greater than 1.5 - 2.0.<sup>3</sup>

Flory was the first to recognise that synthetic polymers can be classified as either step or chain polymers, depending on their polymerisation mechanism.<sup>4</sup> Step polymerisations proceed by stepwise reactions between the functional groups of the respective comonomers. Therefore, the polymer chains grow slowly from monomer to oligomers, with high molecular weight polymers only being formed towards the end of the reaction. In contrast, chain polymerisations involve propagation of multiple monomer units *via* a reactive centre (e.g. a radical, an ion or a polymer-catalyst bond). In this case, high molecular weight polymers can be formed almost immediately after initiation. The most common form of chain polymerisation is free radical polymerisation (FRP).

## 1.2 Free Radical Polymerisation

FRP provides a convenient method for the efficient polymerisation of many functional vinyl monomers using a wide range of physical conditions such as solution, suspension, emulsion or dispersion polymerisation (see later). FRP is an example of chain polymerisation in which the reactive centre is a radical. The growth of the polymer chain involves a kinetic chain of reactions: decomposition, initiation, propagation and termination, as shown overleaf in Figure 1.1.<sup>2, 5</sup> Molecularly dissolved oxygen must be removed from the reaction mixture prior to initiation because oxygen can react with the growing polymer radical to form a relatively unreactive peroxy-capped polymer chain. Therefore, FRP is typically carried out in inert atmosphere to prevent retardation.

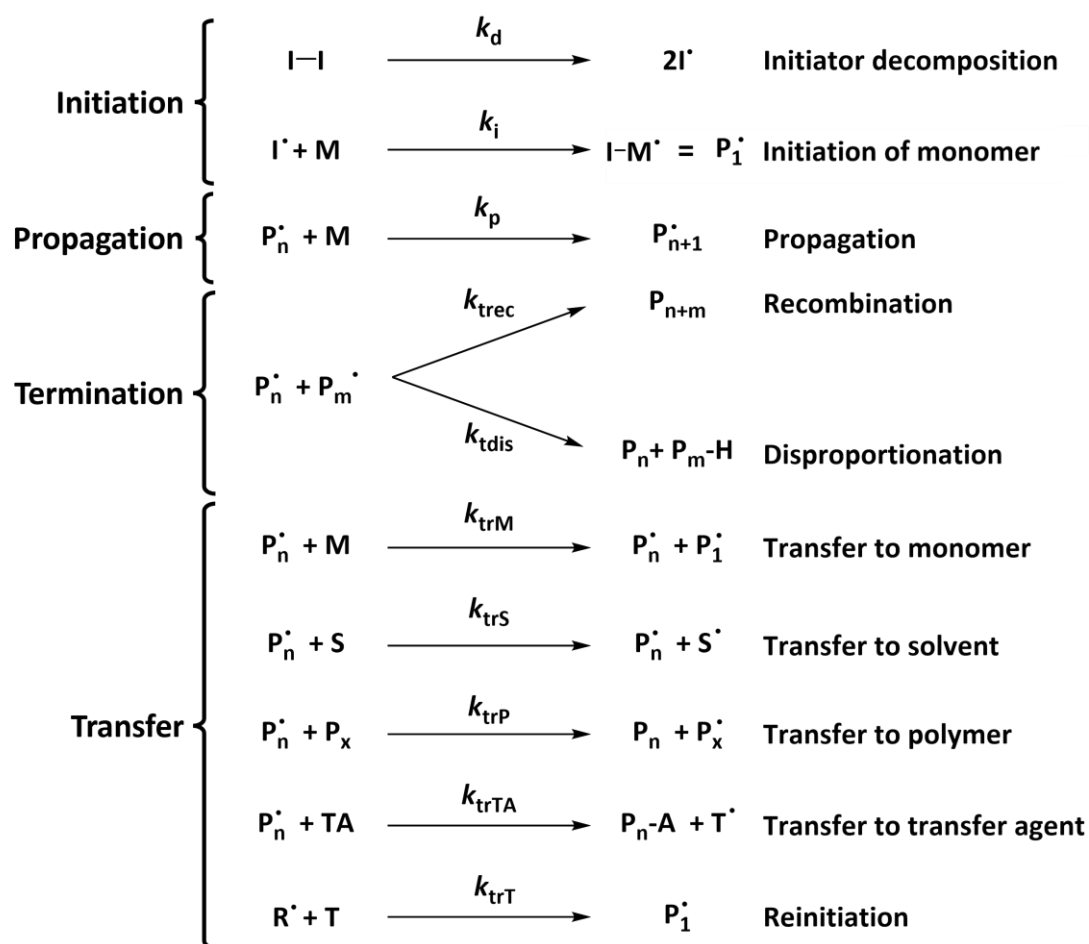


**Figure 1.1.** Reaction mechanism and associated rate constants for free radical polymerisation comprising decomposition, initiation, propagation, and termination.<sup>2</sup>

Initiation consists of two steps. The first step involves the homolytic dissociation of an initiator, typically by thermal degradation. This produces two primary radicals  $I^{\bullet}$  with first order kinetics and a rate constant for initiator decomposition,  $k_d$ . The half-life  $t_{1/2}$  is related to  $k_d$  by Equation 1.3:

$$k_d = \frac{\ln 2}{t_{1/2}} \quad 1.3$$

The rate of initiator decomposition is usually the rate-determining step for the polymerisation, with rate constant  $k_d$  typically being of the order of  $10^{-5} \text{ s}^{-1}$ .<sup>2</sup> The second step involves virtually instantaneous addition of initiator radicals to monomer, producing a monomer-radical adduct. The rate constant for initiation,  $k_i$ , is of the order of  $10^4 \text{ M}^{-1} \text{ s}^{-1}$ .<sup>2</sup> Since the rate of reaction of the primary radicals with monomer is much faster than the rate of initiator decomposition, the overall rate of initiation  $R_i$  can be expressed by Equation 1.4:

$$R_i = \frac{d[P_1^*]}{dt} = 2k_d f [I] \quad 1.4$$

where  $f$  is the initiator efficiency, which is the fractional probability that the generated radicals react with monomer, as opposed to undergoing recombination or side reactions. Following initiation, monomer-radical adducts undergo successive monomer addition during propagation to produce polymer radicals  $P_n^*$  (with propagation rate constant  $k_p \sim 10^2 - 10^4 \text{ M}^{-1} \text{ s}^{-1}$ ). Assuming that the rate of propagation  $R_p$  is independent of the chain length,<sup>6</sup> successive addition of multiple monomer units occurs at essentially the same rate, as indicated by Equation 1.5:

$$R_p = -\frac{d[M]}{dt} = k_p [P_n^*][M] \quad 1.5$$

At some point during the polymerisation, the propagating polymer chains  $P_n^*$  and  $P_m^*$  terminate by either recombination or disproportionation. Recombination occurs when two polymer radicals combine to form an inactive polymer chain with a DP equal to the sum of the two initial reactive species. Alternatively, disproportionation occurs when a polymer radical abstracts a hydrogen atom from another radical. This results in one polymer chain with an unsaturated terminus and a second polymer chain with a saturated terminus. This latter mechanism is favoured by methacrylic monomers. The rate of termination  $R_t$  can be expressed by Equation 1.6:

$$R_t = 2k_t [P^*]^2 \quad 1.6$$

The rate of termination is significantly faster than the rate of propagation ( $R_t \gg R_p$ ) with the rate constant for termination ( $k_t \sim 10^8 \text{ M}^{-1} \text{ s}^{-1}$ ) approaching the diffusion-controlled limit.<sup>2</sup> Thus when growing long polymer chains *via* FRP it is essential that  $R_t$  is relatively slow compared to  $R_p$ . This can be achieved by using relatively low radical concentrations because  $R_t$  is second-order with respect to the radical concentration (see Equation 1.6) whereas  $R_p$  is first-order (see Equation 1.5). Since the instantaneous concentration of free radicals is very low, it can be assumed to be constant within very short time scales. Therefore, the steady-state approximation (or  $R_i \approx R_t$ ) can be applied, which yields Equation 1.7.

$$2k_d f[I] = 2k_t [P_n^*]^2 \quad 1.7$$

Rearranging Equation 1.7 for the polymer radical concentration  $[P_n^*]$ , gives Equation 1.8.

$$[P_n^*] = \sqrt{\frac{fk_d[I]}{k_t}} \quad 1.8$$

The overall rate of polymerisation  $R_{\text{polym}}$  is given by Equation 1.9:

$$R_{\text{poly}} = -\frac{d[M]}{dt} = R_i + R_p \quad 1.9$$

Since  $R_p$  is significantly faster than  $R_i$ , the number of monomers consumed during initiation is negligible compared to the number of monomers consumed during propagation, hence  $R_i + R_p \approx R_p$ . Substituting Equation 1.8 into Equation 1.5 gives Equation 1.10:

$$R_{\text{poly}} = k_p [M] \sqrt{\frac{fk_d[I]}{k_t}} \quad 1.10$$

When the initiator efficiency  $f$  is high (close to unity), Equation 1.10 indicates that  $R_{\text{polym}}$  is proportional to  $[M]$  and  $[I]^{1/2}$ . As previously discussed, relatively low initiator concentrations are required to produce high molecular weight polymers. Thus it is difficult to produce high molecular weight polymers by FRP under homogeneous conditions. In FRP, polymer radicals are susceptible to chain transfer reactions with monomer, solvent, dormant polymer chains or added transfer agents (see Figure 1.1). Since such side reactions are fast and radicals are conserved, they should have no effect on the overall polymerisation kinetics. However, this can affect the polydispersity and molecular weight of the resulting polymers owing to branching.

Despite its widespread use on an industrial scale, there are several shortcomings to conventional FRP. Upon initiation, high molecular weight polymers are rapidly generated, and therefore little control can be obtained over the molecular weight distribution (see Figure 1.2). Furthermore, the very short lifetime of such propagating polymer radicals prevents the synthesis of block copolymers by sequential monomer addition.<sup>7</sup> Moreover, since initiation occurs throughout the polymerisation, relatively low molecular weight polymer chains are formed under

monomer-starved conditions towards the end of the polymerisation. The combination of intrinsic termination and chain transfer side reactions, plus the slow rate of initiation relative to that of propagation, ensures that the dispersity of the resulting polymers prepared by FRP is relatively high ( $M_w/M_n > 1.50$ , typically 2 - 5). In principle, suppressing termination, faster initiation and extending the mean lifetime of the polymer radicals should provide much better control over the polymerisation.

### 1.3 Living Anionic Polymerisation

A truly living polymerisation technique involves no intrinsic termination step.<sup>2</sup> The first example of a living anionic polymerisation (LAP) was the synthesis of polystyrene in dry THF, as reported by Szwarc and co-workers in the 1950s.<sup>8</sup> LAP is an example of a chain polymerisation where the reactive centre is an anion.<sup>9</sup> The living character of anionic polymerisations arises because, unlike radicals, the propagating carbanions cannot react together. Therefore, intrinsic termination is eliminated in LAP. Suitable vinyl monomers ( $H_2C=CHX$ ) must contain electron-withdrawing groups ( $X = \text{phenyl, ester or cyano functionality}$ ), in order to stabilise the active carbanion chain-end.

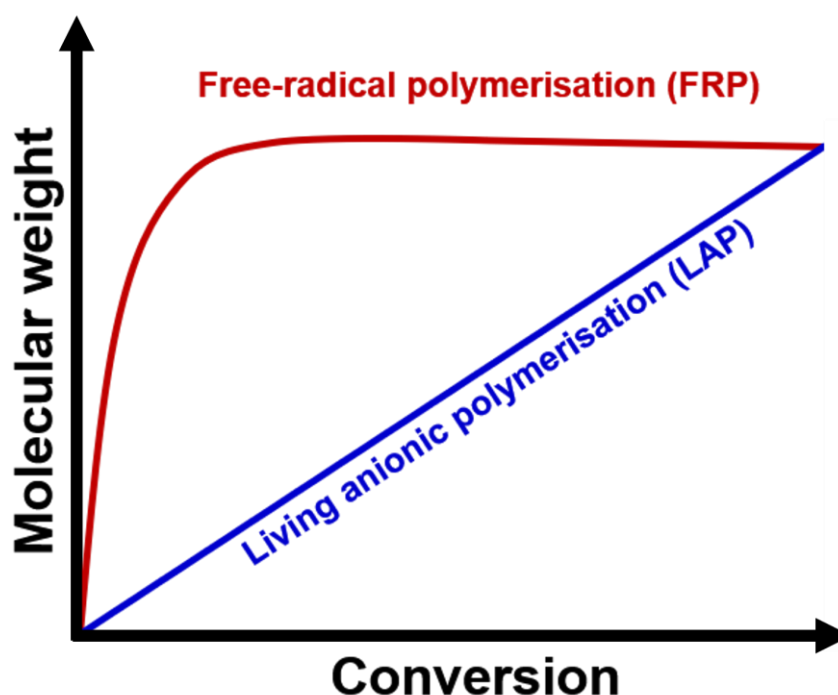


**Figure 1.2.** Evolution of molecular weight with monomer conversion for living anionic polymerisation (LAP) and free radical polymerisation (FRP).

In LAP, the rate of initiation is significantly faster than the rate of propagation ( $R_i \gg R_p$ ). This is because the initiation is complete before any propagation, allowing uniform growth of polymer chains. Thus the polymer molecular weight increases linearly with conversion (see Figure 1.2). Since the number of propagating species remains constant throughout the polymerisation, the resulting polymers typically possess narrow molecular weight distributions ( $M_w/M_n < 1.20$ ). Moreover, LAP can be used to prepare polymers with very narrow molecular weight distributions ( $M_w/M_n \sim 1.06$ ).<sup>10</sup> The polymer chains stop growing once all the monomer has reacted, but the carbanion chain-ends remain active. This enables the preparation of well-defined block copolymers *via* sequential monomer addition.<sup>11</sup> Szwarc *et al.* demonstrated that polyisoprene-polystyrene-polyisoprene (PI-PS-PI) triblock copolymers could be formed by the addition of isoprene to living PS chains that had been initiated with a sodium-naphthalene complex (see Figure 1.3).<sup>9</sup>

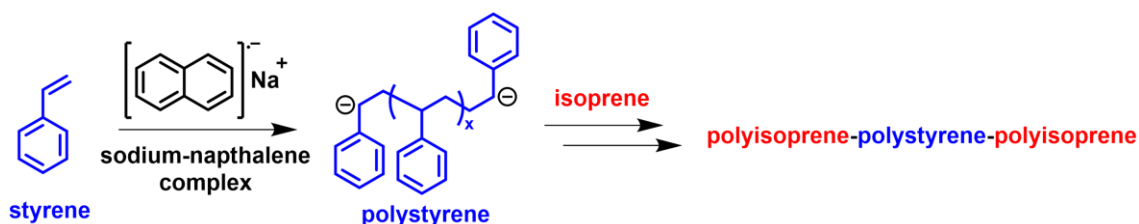


**Figure 1.3.** Schematic representation of the synthesis of polyisoprene-polystyrene-polyisoprene triblock copolymer using living anionic polymerisation. Polystyrene is initially prepared using a sodium-naphthalene complex, which is then chain-extended by the addition of isoprene monomer.

Alternatively, AB diblock copolymers can also be prepared by LAP when using *n*-butyllithium as a monofunctional initiator.<sup>12</sup> If each initiator gives rise to one propagating polymer chain, the DP of the polymer can be conveniently adjusted by varying the initial monomer/initiator molar feed ratio, as shown in Equation 1.11:

$$DP = \frac{[M]_0}{[I]_0} \quad \mathbf{1.11}$$

where  $[M]_0$  and  $[I]_0$  are the respective initial concentrations of the monomer and initiator, and the monomer conversion is assumed to be 100%. In addition, the molecular weight of the final polymer can also be calculated by multiplying the DP of the polymer by the molecular weight of the monomer repeat unit. Despite the synthetic advantages offered by LAP, its intolerance towards

protic impurities and restricted monomer palette have somewhat restricted its industrial applications.<sup>7</sup>

### 1.4 Reversible Deactivation Radical Polymerisation

Reversible deactivation radical polymerisation (RDRP), also known as controlled radical polymerisation, is a class of chain polymerisations that is characterised by a low rate of termination relative to propagation. RDRPs are pseudo-living polymerisations because termination is only suppressed, rather than eliminated. Nevertheless, RDRP enables the routine synthesis of polymers with predictable molecular weights and narrow molecular weight distributions ( $M_w/M_n < 1.20$ ). Importantly, RDRP requires much less synthetically demanding conditions than anionic polymerisation. Like conventional FRP, these techniques are compatible with a wide range of functional vinyl monomers and various solvents (including protic solvents). Similar to LAP, sequential monomer addition provides access to well-defined block copolymer architectures.<sup>13</sup> Thus RDRP techniques combine the advantages of conventional FRP and LAP, without their respective shortcomings. The pseudo-living character is achieved by extending the lifetime of the propagating polymer radicals. This is accomplished by establishing a rapid dynamic equilibrium between a relatively low concentration of polymer radicals and a relatively high concentration of dormant polymer chains.<sup>14</sup> This minimises the probability of premature termination, because the rate of termination is suppressed relative to the rate of propagation.

The most commonly used forms of RDRP are nitroxide-mediated polymerisation (NMP),<sup>15-17</sup> atom transfer radical polymerisation (ATRP),<sup>18-21</sup> and reversible addition-fragmentation chain transfer (RAFT) polymerisation.<sup>7, 22-25</sup> RAFT polymerisation has been used for the synthetic polymer chemistry conducted in this Thesis and hence shall be discussed in detail.

## 1.5 Reversible Addition-Fragmentation Chain Transfer

### Polymerisation

RAFT polymerisation was first reported by Rizzardo and co-workers<sup>22</sup> in 1998. Various reviews have highlighted the substantial growth of academic interest in this RDRP technique since its inception.<sup>24-27</sup> As with conventional FRP, the RAFT polymerisation mechanism includes initiation, propagation and termination steps. However, RAFT polymerisations also involve an organosulfur chain transfer agent (CTA). This CTA mediates the polymerisation by establishing a dynamic equilibrium between growing polymer radicals and dormant chains *via* a degenerative transfer mechanism. The R and Z groups within a RAFT CTA each play vital roles in controlling the polymerisation.<sup>28</sup>

The general RAFT mechanism is shown overleaf in Figure 1.4.<sup>23,29</sup> Like FRP, initiation involves the thermal decomposition of a free radical initiator to generate radicals  $I\cdot$ . Subsequent reactions with multiple monomer units generate a propagating polymer radical  $P_n\cdot$ . This polymer radical can either undergo further propagation with monomer M or undergo reversible capping with the RAFT CTA (1) to form a dormant radical species (2). Fragmentation of this intermediate generates a dormant CTA-capped polymer (3) and a new radical leaving group  $R\cdot$ . The latter species can reinitiate polymerisation to form a new propagating polymer radical  $P_m\cdot$ . A rapid reversible equilibrium between the active and dormant (capped) states of  $P_n\cdot$  and  $P_m\cdot$  is set up with the formation of an intermediate RAFT adduct (4). Finally, termination of the propagating polymer chains involves reactions between two radicals, as in FRP.



termination relative to propagation. For the synthesis of well-defined block copolymers, it is essential that the CTA end-groups are retained to preserve pseudo-living character.

The generic chemical structures for the dithioester and trithiocarbonate CTAs used in this Thesis are shown in Figure 1.5.<sup>28, 30</sup> The key to achieving a well-controlled polymerisation is careful selection of an appropriate CTA for a given monomer. In particular, it is critical to match the reactivity of the CTA with that of the monomer. The Z group dictates the rate of addition of a propagating radical to the CTA while the R group must be a better leaving group than the propagating species for efficient polymerisation.

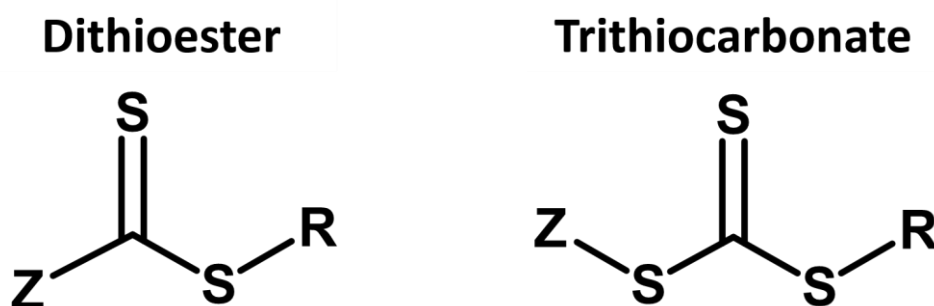


**Figure 1.5.** Generic chemical structures of (left) dithioester and (right) trithiocarbonate RAFT CTAs, where C=S is a reactive bond, Z denotes a radical stabilising group and R is a good radical leaving group.<sup>28</sup>

A set of guidelines for selection of the correct CTA for a given monomer class have been provided by Moad and co-workers.<sup>25</sup> There are two classes of monomers: more-activated monomers (MAMs) and less-activated monomers (LAMs). MAMs are those whose double bond is conjugated to an adjacent functional group for example, a carbonyl, (such as methacrylates, acrylates, acrylamides or methacrylamides), a nitrile (such as acrylonitrile), or an aromatic ring (e.g. styrene).<sup>28, 31</sup> To achieve narrow molecular weight distributions for MAM-based polymers, the C=S double bond should be sufficiently reactive towards the polymer radical. Therefore, polymerisation control can be achieved by using more active RAFT agents, such as dithioesters (Z = aryl or alkyl) or trithiocarbonates (Z = alkylthio).<sup>25, 28</sup> In the case of LAMs, the double bond is adjacent to an unsaturated carbon or a heteroatom lone pair, such as vinyl acetate (VAc), *N*-vinylpyrrolidone (NVP) or *N*-vinylcarbazole (NVC). For LAMs, control is conferred by using less reactive RAFT agents such as dithiocarbamates or xanthates.<sup>25, 28</sup>

RAFT polymerisation offers several advantages for the syntheses conducted in this Thesis. Conservation of the RAFT agent end-group means that sequential monomer addition can be used to prepare well-defined functional diblock copolymers.<sup>32</sup> Moreover, RAFT polymerisation can provide good control over the final molecular weight of (co)polymers, with narrow molecular weight distributions ( $M_w/M_n < 1.30$ ) being routinely attained.<sup>32</sup> Furthermore, the functional chain-ends of the resulting copolymer chains can be selected by designing an appropriate RAFT CTA for the polymerisation.<sup>22, 33</sup> Finally, the desired DP can be targeted simply by adjusting the monomer/CTA molar ratio, as shown in Equation 1.12:

$$DP = \frac{[M]}{[CTA]} \quad 1.12$$

However, the organosulfur-based CTA is malodorous and confers intrinsic colour; it must be removed for many potential applications.<sup>34</sup> Many methods have been developed to remove such CTA end-groups, including thermolysis, reaction with amines and use of oxidants such as hydrogen peroxide or ozone.<sup>33, 35</sup> This Thesis focuses on the preparation of methacrylate-based diblock copolymers using RAFT polymerisation. Thus dithioester and trithiocarbonate RAFT agents are employed to obtain well-controlled solution, dispersion and emulsion polymerisations.

## 1.6 Polymerisation Methods

### 1.6.1 Solution Polymerisation

Solution polymerisation is the preparation of soluble polymer chains by polymerising a miscible monomer in a suitable solvent using an appropriate initiator (or catalyst). All components in the formulation are soluble, leading to a homogeneous reaction solution. Conducting the polymerisation in a solvent produces lower-viscosity reaction mixtures than bulk polymerisations performed in the absence of any solvent, enabling more efficient heat dissipation and easier stirring.

### 1.6.2 Emulsion Polymerisation

Conventional emulsion polymerisation provides a convenient route to colloiddally stable latexes by forming a water-insoluble polymer in the presence of a stabiliser. A typical formulation consists of a water-immiscible monomer (e.g. styrene or methyl methacrylate), a water-soluble initiator (e.g.  $K_2S_2O_8$ ), surfactant (e.g. sodium dodecyl sulfate (SDS)) and water.<sup>36</sup> Using water as the reaction medium offers important advantages: it is a cheap, non-flammable and environmentally-friendly solvent and its high specific heat capacity enables efficient heat dissipation. Typically, emulsion polymerisation produces particles with mean diameters of the order of 100 - 500 nm.<sup>37</sup> The size of the final latex particles depends on the concentration of surfactant added to the formulation. In the presence of surfactant, coagulation of nuclei is limited giving rise to a large number of relatively small particles. In contrast, surfactant-free emulsion polymerisations produce fewer nuclei and hence yields a significantly larger final particle size. The molecular weight distribution obtained by conventional emulsion polymerisation is typically broad because FRP is used. A relatively high molecular weight is usually obtained owing to the effect of microcompartmentalisation.<sup>38</sup>

Conventional emulsion polymerisation proceeds *via* three stages, known as Interval I, II and III.<sup>36, 38-40</sup> Homogenisation of the heterogeneous initial reaction mixture produces micron-sized surfactant-stabilised monomer droplets and surfactant micelles (see Figure 1.6a). The monomer has a relatively low aqueous solubility, but a small amount is nevertheless present within the aqueous phase. Oligomer radicals remain water-soluble until a critical DP is attained, above which there can be either homogeneous or heterogeneous nucleation. The former involves amphiphilic oligomer radicals aggregating with free surfactant to generate mixed micelles.<sup>41</sup> This is the dominant mechanism when the surfactant concentration is below the critical micelle concentration (CMC). If the surfactant concentration is above the CMC, heterogeneous nucleation occurs. This mechanism involves the oligomer radicals entering preformed surfactant micelles. Owing to the high local monomer concentration within the micelles, the rate of polymerisation is rapid during Interval I (see Figure 1.6b). When all of the surfactant micelles have become

monomer-swollen nascent latex particles, the rate of polymerisation becomes constant; this corresponds to Interval II. At this stage, both surfactant-stabilised monomer droplets and monomer-swollen growing particles are present and the monomer concentration within the aqueous solution remains relatively constant. This is because the micron-sized surfactant-stabilised droplets act as reservoirs to replace the dissolved monomer in the aqueous phase as it enters the swollen nascent particles and is polymerised. This results in a constant rate of polymerisation rate. When there are no more surfactant-stabilised droplets yet, the polymerisation enters Interval III. This final stage is characterised by a slower rate of polymerisation owing to the gradual reduction in the monomer concentration within the monomer-swollen growing particles. The polymerisation is complete when all of the monomer has been consumed and only colloiddally stable latex particles remain.

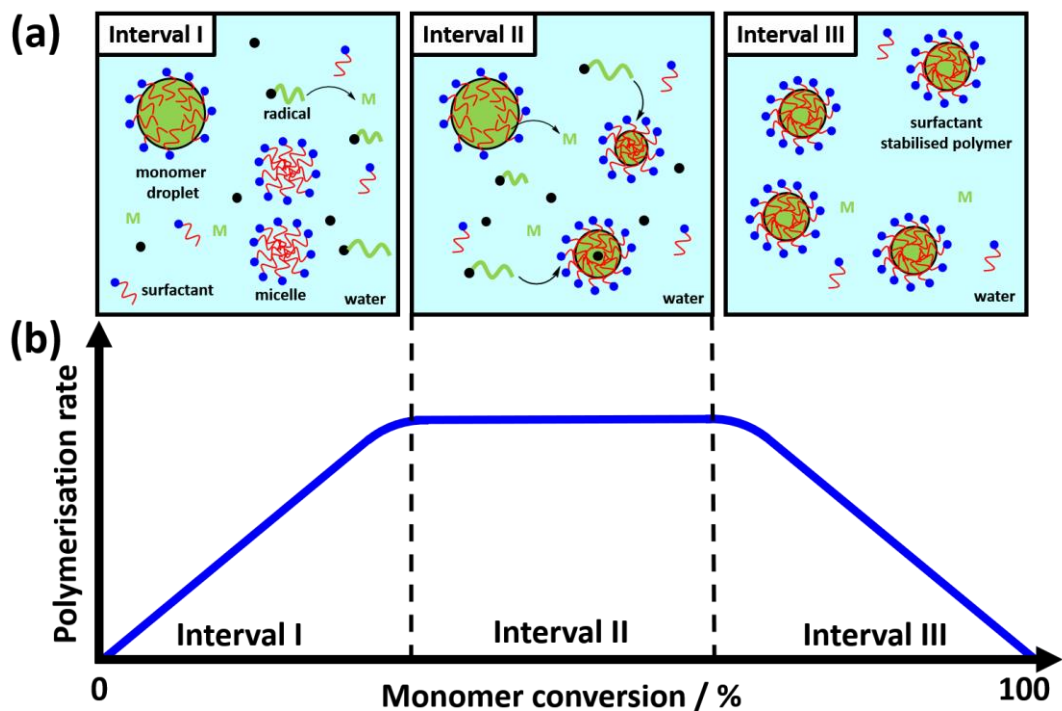


**Figure 1.6.** (a) Schematic representation of the three main Intervals (I, II, III) and (b) the rate of polymerisation vs monomer conversion in a conventional emulsion polymerisation.<sup>36, 39</sup>

The stabilisation mechanism can be either electrostatic or steric in nature.<sup>38</sup> Electrostatic stabilisation is achieved by using ionic surfactants<sup>42</sup> and/or ionic initiators.<sup>43</sup> In this case, a repulsive force arises from the unfavourable overlap of electrical double layers surrounding the

polymer latex particles. In contrast, steric stabilisation is conferred by a layer of either strongly adsorbed or chemically bound hydrophilic polymer chains.<sup>44</sup> When two particles approach one another, interpenetration of the adsorbed stabiliser chains is unfavourable on both enthalpic and entropic grounds, which leads to a strong steric repulsion force.

### 1.6.3 Dispersion Polymerisation

Dispersion polymerisation can be conducted in many different solvents, including water.<sup>45-</sup><sup>48</sup> The generally accepted mechanism for a dispersion polymerisation is as follows.<sup>45</sup> Initially, all components are soluble in the reaction solution. The initiator-derived radicals react with the monomer to form soluble polymer radicals. At some critical DP, these radicals become insoluble and form colloiddally unstable aggregates. In the absence of a suitable polymeric stabiliser, this leads to macroscopic precipitation. However, if a polymeric stabiliser is present, it can adsorb onto these nascent particles and confer steric stabilisation, which ultimately leads to the formation of colloiddally stable latex particles.<sup>46, 49</sup>

An aqueous dispersion polymerisation formulation consists of water, a water-miscible monomer, a water-soluble initiator, and a suitable polymeric stabiliser. For a successful dispersion polymerisation formulation, the water-miscible monomer must form an insoluble polymer when polymerised.<sup>45</sup> There are relatively few literature reports of vinyl monomers that fulfil this criterion. One noteworthy example is 2-hydroxypropyl methacrylate (HPMA), as reported by Ali and co-workers.<sup>46</sup> More specifically, 100 – 1000 nm diameter PHPMA latexes were prepared by free radical aqueous dispersion polymerisation of HPMA in the presence of poly(*N*-vinylpyrrolidone) (PNVP) steric stabiliser or SDS surfactant (see Figure 1.7). Varying the initiator or stabiliser concentration provided control over the final latex diameter.

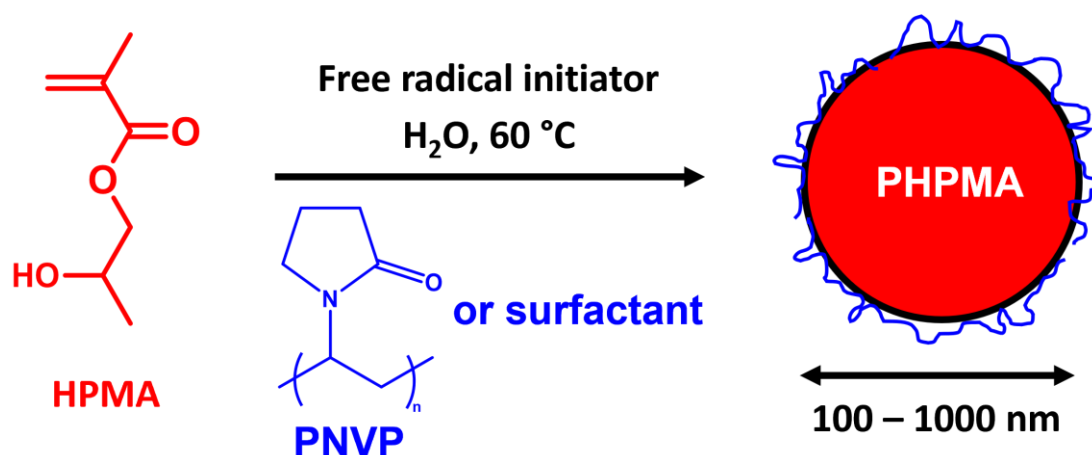


**Figure 1.7.** Schematic representation of the preparation of a 2-hydroxypropyl methacrylate (PHPMA) latex by aqueous dispersion polymerisation of HPMA in the presence of a poly(*N*-vinylpyrrolidone) (PNVP) polymeric stabiliser or surfactant.<sup>46</sup>

## 1.7 Self-Assembly

Amphiphilic molecules such as surfactants consist of hydrophilic and hydrophobic components. Amphiphiles spontaneously self-assemble in aqueous solution to form various structures known as micelles.<sup>50</sup> The most common morphologies are spherical micelles, cylindrical micelles and vesicles. From a thermodynamic perspective, self-assembly occurs when the energy for a small molecule to exist in its free state is greater than the entropic penalty for the formation of colloidal aggregates.<sup>51</sup> In aqueous solution, water molecules can form hydrogen bonds with polar surfactant head-groups but not hydrophobic species (e.g. surfactant alkyl chains). This drives spontaneous self-organisation of such amphiphiles to form micelles in aqueous solution. This self-assembly process is governed by the subtle interplay of weak interactions (e.g. hydrogen bonding, van der Waal forces, hydrophobic interactions and electrostatic interactions), which results in soft, dynamic structures.

Israelachvili and co-workers<sup>50</sup> were the first to describe how the surfactant morphology can be predicted using the dimensionless packing parameter  $P$ . This parameter depends on the volume occupied by the hydrophobic chain  $V$ , the surface area occupied by the hydrophilic head-group  $a_0$ , and the effective length of the hydrophobic chain  $l_c$ , as illustrated overleaf in Figure 1.8. Spherical micelles are obtained if  $P \leq 0.33$ , worm-like (or cylindrical) micelles are formed if  $P$

lies between 0.33 and 0.50 and  $0.50 \leq P \leq 1.0$  corresponds to vesicles. The packing parameter is a purely geometric concept: it does not account for kinetic or thermodynamic aspects.

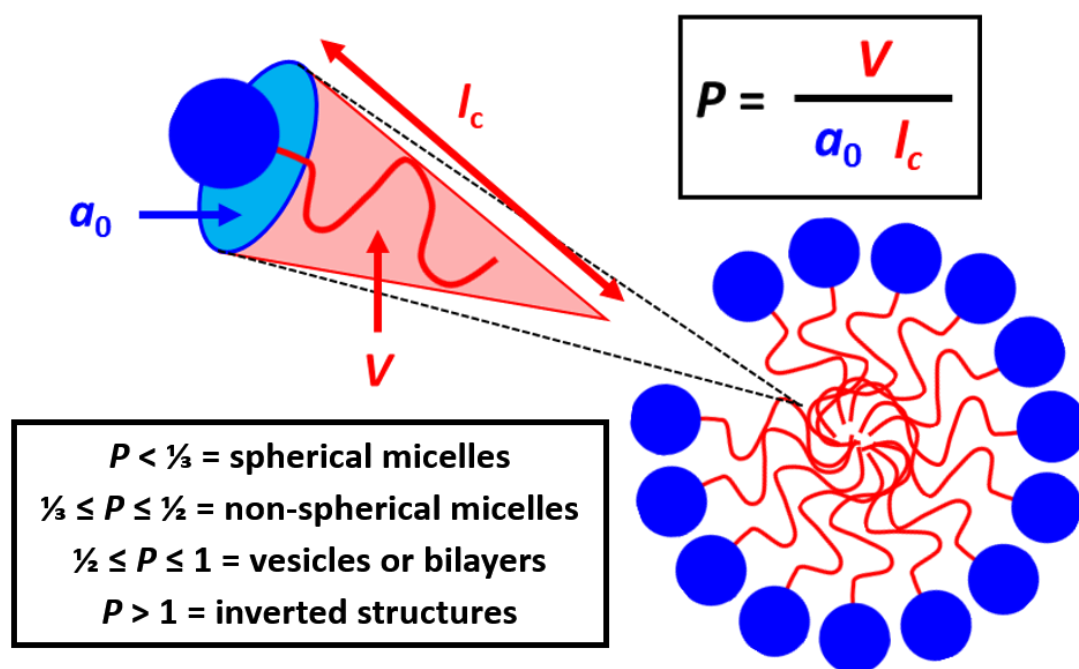


**Figure 1.8.** Schematic representation of the three parameters that influence the packing of a surfactant molecule within a micelle. The equation for the packing parameter  $P$ , and typical ranges for  $P$  for various surfactant morphologies are also given. [ $V$  = volume occupied by the hydrophobic alkyl chains,  $a_0$  = surface area occupied by the hydrophilic head-group and  $l_c$  = effective length of the hydrophobic alkyl chains].<sup>51</sup>

As previously discussed, anionic polymerisation has enabled the preparation of well-defined block copolymers. Important examples include amphiphilic diblock copolymers such as poly(acrylic acid)-polystyrene and poly(ethylene oxide)-polystyrene.<sup>52-57</sup> Like surfactants, such amphiphilic diblock copolymers undergo self-assembly either in the solid state or in a solvent that is selective for one block (e.g. water). Furthermore, block copolymer self-assembly affords micellar aggregates that are much more stable than surfactant micelles: the former systems exhibit much lower critical micelle concentrations and the rate of exchange between the micelles and individual copolymer chains is much slower than that between micelles and small molecule surfactants. Hence block copolymer micelles have received considerable attention for a wide range of applications over the past five decades.<sup>58</sup>

AB block copolymers undergo microphase separation in the solid state because the A and B blocks are mutually immiscible yet are connected by a covalent bond.<sup>59</sup> Self-assembly is driven by an unfavourable enthalpy of mixing  $\Delta H_{\text{mix}}$ , and a relatively small entropy of mixing  $\Delta S_{\text{mix}}$ :

$$\Delta G_{\text{mix}} = \Delta H_{\text{mix}} - T\Delta S_{\text{mix}} \quad \mathbf{1.13}$$

In 1942, Flory<sup>60</sup> and Huggins<sup>61</sup> independently developed a lattice model for determining the Gibbs energy of mixing  $\Delta G_{\text{mix}}$ , for polymer blends, see Equation 1.14:

$$\left(\frac{\Delta G_{\text{mix}}}{k_{\text{B}}T}\right) = \left(\frac{f_{\text{A}} \ln f_{\text{A}}}{N_{\text{A}}}\right) + \left(\frac{f_{\text{B}} \ln f_{\text{B}}}{N_{\text{B}}}\right) + f_{\text{A}}f_{\text{B}}\chi_{\text{AB}} \quad \mathbf{1.14}$$

where  $f_{\text{A}}$  and  $f_{\text{B}}$  are the relative volume fractions of the A and B blocks,  $N_{\text{A}}$  and  $N_{\text{B}}$  are their respective DPs and  $\chi_{\text{AB}}$  is the so-called Flory-Huggins parameter. The Flory-Huggins parameter describes the degree of enthalpic incompatibility between the two blocks:

$$\chi_{\text{AB}} = \left(\frac{z}{k_{\text{B}}T}\right) \left[ \varepsilon_{\text{AB}} - \frac{1}{2}(\varepsilon_{\text{AA}} + \varepsilon_{\text{BB}}) \right] \quad \mathbf{1.15}$$

where  $z$  is the number of nearest neighbours per molecule,  $k_{\text{B}}T$  is the thermal energy and  $\varepsilon_{\text{AB}}$ ,  $\varepsilon_{\text{AA}}$  and  $\varepsilon_{\text{BB}}$  are the respective interaction energies between the A and B repeat units. In order for microphase separation to occur spontaneously, the Flory-Huggins parameter must be negative, or more explicitly, the A-B interactions results in a lower overall energy. Furthermore, Equation 1.15 indicates that  $\chi_{\text{AB}}$  is inversely proportional to temperature. Combining  $\chi_{\text{AB}}$  with the DP gives  $\chi N$ , which is a measure of the degree of immiscibility between the two blocks.<sup>62</sup> If  $\chi N$  exceeds the strong segregation limit, then microphase separation occurs. Self-consistent mean field theory has been used to predict the phase behaviour of AB diblock copolymers in the bulk. As shown in Figure 1.9, the copolymer morphology depends on the relative volume fraction of each block: it evolves from close-packed spheres to spheres to hexagonally-packed cylinders to bicontinuous gyroids and finally lamellae as  $f_{\text{A}}$  is increased from 0.00 to 0.50, at a fixed  $\chi N$ .<sup>63</sup> When  $f_{\text{A}}$  exceeds 0.50, inverse structures are obtained. Such phases have been observed experimentally for polyisoprene-polystyrene block copolymers (Figure 1.9c).

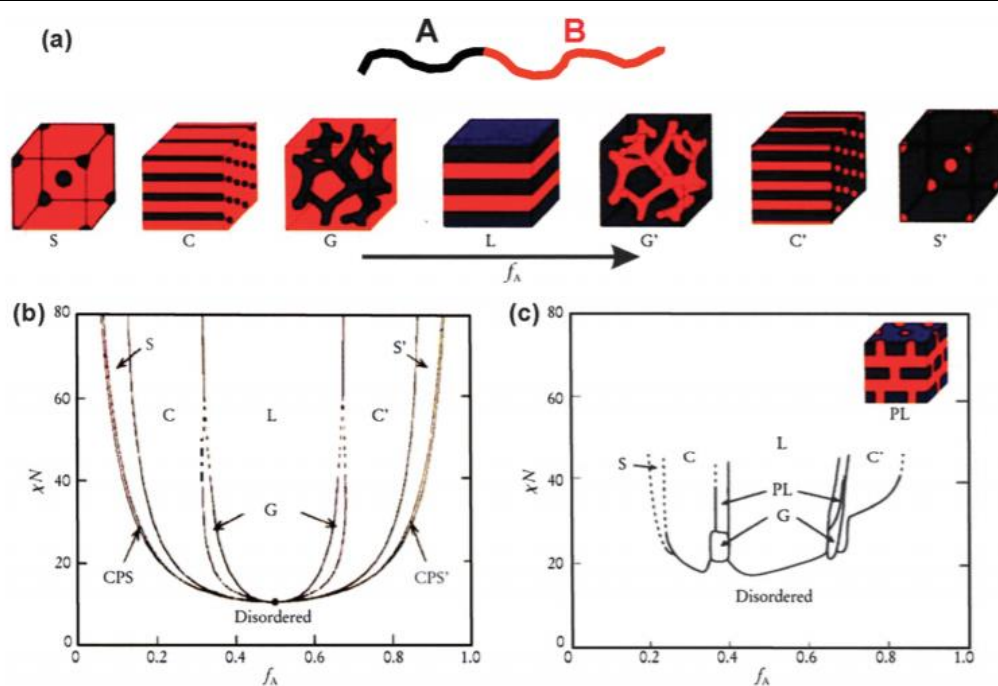


**Figure 1.9.** (a) Schematic representation of various solid-state morphologies adopted by a series of AB diblock copolymers with an increasing volume fraction of component A ( $f_A$ ). Here S and S' are body-centred-cubic spheres, C and C' are hexagonally-packed cylinders, G and G' are gyroid phases and L represents lamellae. (b) Theoretical phase diagram predicted by self-consistent mean-field theory for the same series of AB diblock copolymers as a function of  $f_A$  and the segregation product  $\chi_N$ . (c) Experimental phase diagram constructed for a series of a polyisoprene-polystyrene (PI-PS) diblock copolymers where PI is the A block and PL denotes a perforated lamella phase.<sup>62, 63</sup>

Like surfactant amphiphiles, block copolymers can spontaneously self-assemble in solution to form various morphologies.<sup>64</sup> Block copolymer assembly occurs in a solvent that is selective for only one of the two blocks. Therefore, block copolymer self-assembly in solution has been traditionally achieved *via* post-polymerisation processing by initial molecular dissolution of the copolymer chains in a non-selective solvent, followed by slow solvent exchange (e.g. *via* dialysis) using a selective solvent.<sup>52, 53, 65</sup> Alternative strategies to achieve self-assembly include direct addition of a selective solvent,<sup>66, 67</sup> a pH<sup>68, 69</sup> or temperature switch<sup>70</sup> or thin film rehydration.<sup>71, 72</sup> However, the final copolymer concentration is invariably low (< 1.0% w/w solids), which severely limits potential commercial applications. In contrast, the recent development of polymerisation-induced self-assembly (PISA) enables the direct preparation of many types of copolymer morphologies in concentrated solution.<sup>73</sup>

## 1.8 Polymerisation-Induced Self-Assembly

The development of controlled radical polymerisation techniques<sup>15, 18, 23</sup> such as RAFT polymerisation<sup>22, 24-26</sup> has enabled the efficient synthesis of block copolymer nano-objects *via* PISA.<sup>73-82</sup> As previously discussed, RAFT polymerisation is exceptionally tolerant of monomer functionality, which enables the rational design of nano-objects bearing hydroxyl, amine or carboxylic acid groups.<sup>83-85</sup> Moreover, such PISA syntheses can be conducted at relatively high copolymer concentration (up to 50% w/w).<sup>86, 87</sup> In a typical protocol, a soluble homopolymer is chain-extended using a second monomer in a suitable solvent such that the growing second block gradually becomes insoluble, which drives *in situ* self-assembly to form diblock copolymer nanoparticles, as depicted in Figure 1.10. Depending on the solubility of the second monomer in the continuous phase, the synthesis of the insoluble second block involves either dispersion or emulsion polymerisation.<sup>76, 88-104</sup> Systematic variation of the relative volume fractions of the two blocks can provide excellent control over the copolymer morphology.<sup>86, 105, 106</sup>

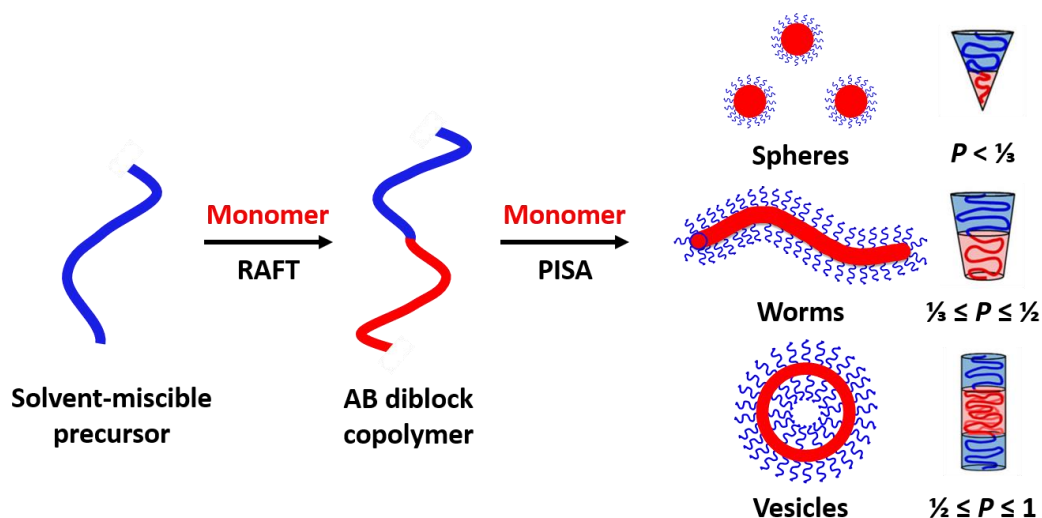


**Figure 1.10.** Schematic representation of the self-assembly of an AB diblock copolymer prepared *via* PISA into three different copolymer morphologies (spheres, worms or vesicles) depending on the packing parameter  $P$ .<sup>107</sup>

Over the past decade or so, the generic nature of PISA has been demonstrated for a wide range of vinyl monomers in various solvents including water,<sup>83, 102, 107-112</sup> polar solvents (e.g. ethanol or methanol),<sup>113-126</sup> non-polar solvents (e.g. *n*-alkanes),<sup>78, 127-132</sup> ionic liquids,<sup>133</sup> silicone oil<sup>134, 135</sup> and supercritical CO<sub>2</sub>.<sup>136-139</sup> Typically, pseudo-phase diagrams are constructed to enable

the reproducible targeting of morphologies for a given PISA formulation.<sup>83</sup> The basic design rules for the preparation of spheres,<sup>83, 127</sup> worms,<sup>140-144</sup> vesicles,<sup>145-148</sup> framboidal vesicles,<sup>108, 149-151</sup> and lamellae<sup>152-154</sup> are now well-established. In many cases, the final copolymer morphology is dictated primarily by the relative volume fractions of the two blocks, as indicated by the geometric packing parameter  $P$ .<sup>50</sup> For example, spheres are produced when using a relatively long soluble stabiliser block and/or working at relatively low copolymer concentrations,<sup>83, 127</sup> while vesicles can be obtained when targeting highly asymmetric diblock compositions (i.e. relatively long insoluble blocks) at higher copolymer concentrations.<sup>108, 114</sup> It is also well-established that worm-like particles typically occupy a relatively narrow phase space between that of spheres and vesicles,<sup>131, 140, 141</sup> while framboidal vesicles can be produced from ABC triblock copolymers in which the B and C blocks are both insoluble and enthalpically incompatible<sup>149, 155</sup> and targeting stiff, inflexible insoluble blocks favours lamellae formation.<sup>153, 154</sup>

### 1.8.1 PISA *via* RAFT Aqueous Emulsion Polymerisation

RAFT aqueous emulsion polymerisation is an important aspect of this Thesis. One key difference between such formulations and conventional emulsion polymerisation is the use of a homopolymer CTA as a reactive water-soluble precursor, rather than a surfactant.<sup>156</sup> This technique offers a potentially efficient surfactant-free route for the efficient synthesis of block copolymer nanoparticles. In a typical formulation, a water-soluble homopolymer precursor is chain-extended with a water-immiscible monomer *via* RAFT polymerisation. However, initial studies involved the addition of a RAFT CTA directly to a conventional emulsion polymerisation formulation.<sup>156</sup> This was briefly reported for the polymerisation of *n*-butyl acrylate (*n*BA) in the first RAFT publication by Rizzardo and co-workers.<sup>22</sup> However, this synthesis was conducted in the presence of a surfactant (SDS). Despite this initial success, subsequent attempts suffered from poor molecular weight control, colloidal instability and substantially incomplete monomer conversions.<sup>88, 157-159</sup> Such technical problems were attributed to the relatively high solubility of the CTA within the micron-sized monomer droplets.<sup>158, 160</sup> Alternatively, if the CTA is too water-

soluble it can diffuse out of the growing polymer particles and remain in the aqueous phase, thus leading to uncontrolled FRP.<sup>152, 154</sup>

Subsequently, seeded RAFT aqueous emulsion polymerisation was explored.<sup>152, 154</sup> In such polymerisations, a polymer is grown in the presence of a CTA using a preformed polymer latex, initially prepared by FRP. Monteiro *et al.* used this method to prepare poly(styrene)-poly(methyl methacrylate) (PS-PMMA) particles by conducting the RAFT polymerisation of styrene in the presence of a PMMA seed plus surfactant.<sup>158</sup> Unfortunately, such polymerisations were retarded relative to FRP and broad molecular weight distributions were observed for the final copolymer. These problems were attributed to the CTA exiting the seed particles after fragmentation. As a result, polymerisation occurred within the monomer droplets, rather than the seed particles. Furthermore, the final dispersion contained coagulum, indicating poor colloidal stability.

Prescott and co-workers improved this formulation by using a water-miscible co-solvent to facilitate the transport of the CTA into PS latex seed particles.<sup>160</sup> More specifically, acetone was added to the seeded emulsion polymerisation of styrene. This approach provided reasonable control over the molecular weight distribution ( $M_w/M_n < 1.40$ ) with little to no coagulum produced during the polymerisation. The living nature of the polymerisation was confirmed by the linear evolution of molecular weight with conversion. The acetone co-solvent facilitated the transport of the RAFT CTA into the seed particles and reduced the extent of polymerisation within the monomer droplets.

Seeded emulsion polymerisation provided some useful insights into the mechanism of RAFT emulsion polymerisation. However, many significant issues were not resolved, including incomplete monomer conversion, contamination of the final product by the seed particles and the use of surfactant. These disadvantages were overcome by the development of *ab initio* RAFT aqueous polymerisation using a water-soluble homopolymer precursor (see Figure 1.11). In this approach, the precursor block confers steric stabilisation on the growing nanoparticles, so a surfactant is not required.<sup>161</sup> Self-assembly to form nascent micelles occurs early in the

polymerisation owing to the hydrophobic character of the growing second block. Such micelles act as the locus for the polymerisation so no pre-formed seed is required.

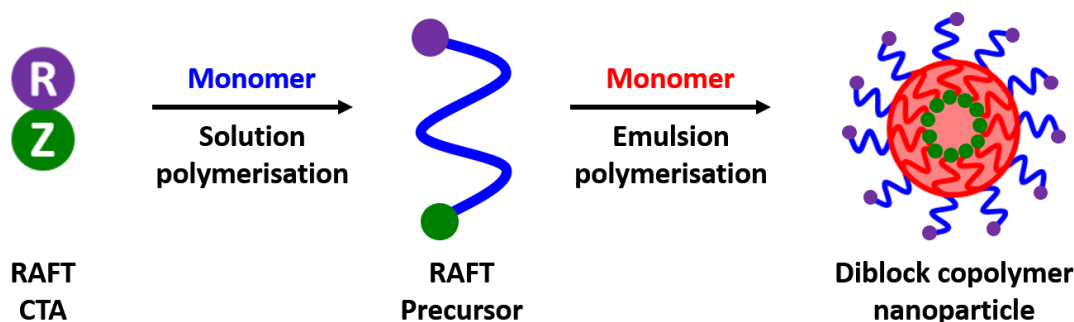


**Figure 1.11.** Schematic representation of the synthesis of sterically-stabilised diblock copolymer nanoparticles *via* RAFT aqueous emulsion polymerisation.

The first successful RAFT-mediated emulsion polymerisations using a water-soluble precursor block were conducted by Ferguson *et al.*<sup>76, 90, 92</sup> In the first study, a poly(acrylic acid) (PAA) precursor was chain-extended with *n*BA to form PAA-*Pn*BA diblock copolymer nanoparticles of approximately 60 nm diameter. The RAFT polymerisation was well-controlled as demonstrated by a linear increase in molecular weight with conversion, although the molecular weight distribution was not particularly narrow ( $M_w/M_n < 1.50$ ). Subsequently, the same team chain-extended such PAA-*Pn*BA diblock copolymer nanoparticles using styrene to form well-defined PAA-*Pn*BA-PS triblock copolymer nanoparticles.<sup>90</sup> In both cases, only a kinetically-trapped spherical morphology was obtained.

More recently, Charleux and co-workers have developed several robust *ab initio* RAFT aqueous emulsion polymerisation protocols for the synthesis of block copolymer nanoparticles employing a range of hydrophilic stabilisers (acrylic,<sup>162</sup> methacrylic<sup>163</sup> and acrylamide<sup>98</sup>), various hydrophobic core-forming blocks (MMA,<sup>99</sup> benzyl methacrylate (BzMA),<sup>164</sup> and styrene)<sup>163</sup> and a number of RAFT agents (both trithiocarbonates<sup>162</sup> and dithiobenzoates<sup>163</sup>). The reaction conditions (pH, salt concentration and stirring rate) of such formulations were optimised to produce high monomer conversions, narrow molecular weight distributions and well-defined copolymer morphologies.

There have been relatively few reports of non-ionic steric stabiliser blocks used in RAFT aqueous emulsion polymerisation.<sup>97, 98</sup> For example, Charleux and co-workers utilised a water-soluble trithiocarbonate-capped poly(ethylene glycol) (PEG) precursor for the RAFT aqueous emulsion polymerisation of either styrene or *n*BA.<sup>97</sup> This precursor acted as both a macromolecular RAFT agent for the emulsion polymerisation and served as an effective steric stabiliser for the formation of diblock copolymer nanoparticles. Furthermore, systematically changing the PEG/monomer molar ratio enabled the final particle size to be tuned.

Cunningham *et al.*<sup>87</sup> developed a similar protocol using poly(glycerol monomethacrylate) PGMA as a non-ionic steric stabiliser, as summarised in Figure 1.12. More specifically, this polymeric precursor was chain-extended *via* RAFT aqueous emulsion polymerisation of BzMA to form a series of spherical nanoparticles of increasing particle diameter at up to 50% w/w copolymer concentration.

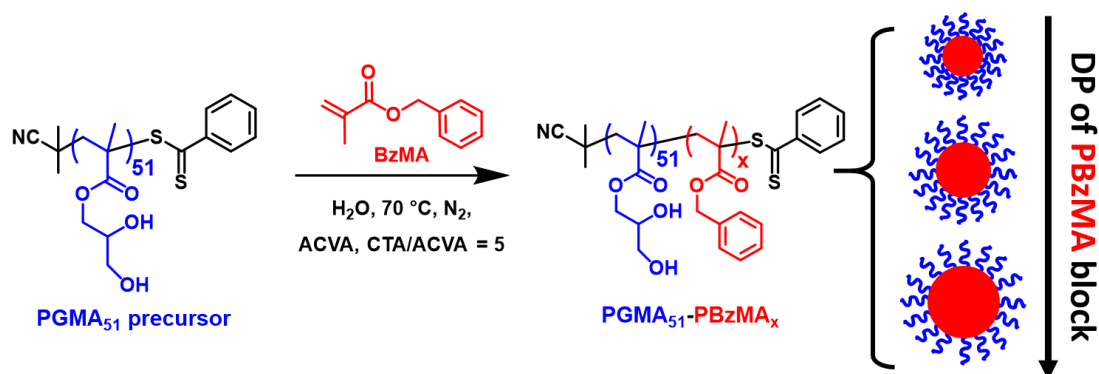


**Figure 1.12.** Synthesis of PGMA<sub>51</sub>–PBzMA<sub>x</sub> diblock copolymer spheres *via* RAFT aqueous emulsion polymerisation of benzyl methacrylate (BzMA). Systematically increasing the target DP of the PBzMA core-forming block leads to a monotonic increase in the mean particle diameter.

Since this initial study, other water-immiscible monomers such as hydroxybutyl methacrylate (HBMA),<sup>165</sup> 2,2,2-trifluoroethyl methacrylate (TFEMA),<sup>166</sup> glycidyl methacrylate (GlyMA),<sup>167, 168</sup> and isopropylidene glycerol methacrylate (IPGMA) have been used instead of BzMA.<sup>169</sup> Furthermore, other non-ionic hydrophilic precursors have also been used for RAFT emulsion polymerisations, such as poly(*N,N*-dimethylacrylamide) (PDMAC)<sup>85, 98</sup> and poly(2-(*N*-acryloyloxy)ethyl pyrrolidone) (PNAEP).<sup>170</sup>

Many RAFT aqueous emulsion polymerisation formulations are restricted to kinetically-trapped spheres, even when targeting highly asymmetric diblock copolymers.<sup>87, 90, 91, 95, 97-99, 166-171</sup> This unexpected morphological restriction is not well-understood, despite attempts to rationalise the various studies in the literature.<sup>100, 103</sup> In contrast, there are relatively few reports of access to worms and vesicles *via* RAFT aqueous emulsion polymerisation.<sup>100, 101, 103, 104, 162, 172-180</sup> Empirically, it is well-established that using a statistical copolymer precursor comprising a 1:1 mixture of a non-ionic and an anionic comonomer can provide access to worms and vesicles.<sup>162</sup> For example, Charleux and co-workers reported the first PISA synthesis of block copolymer worms (a.k.a. nano-fibers) *via* RAFT aqueous emulsion polymerisation in 2010.<sup>162</sup> In this case, a water-soluble statistical copolymer precursor comprising poly((ethylene glycol) methyl ether acrylate) (PEGA) and acrylic acid (AA) was chain-extended with styrene.<sup>100, 162</sup> Using the analogous all-methacrylic statistical copolymer as the stabiliser block also produced well-defined worms.<sup>101, 103</sup> The final copolymer morphology was influenced by various synthesis parameters, such as the concentration of added salt and the solution pH. More specifically, worms were observed by transmission electron microscopy (TEM) at either low pH or high salt concentrations, as shown in Figure 1.13.

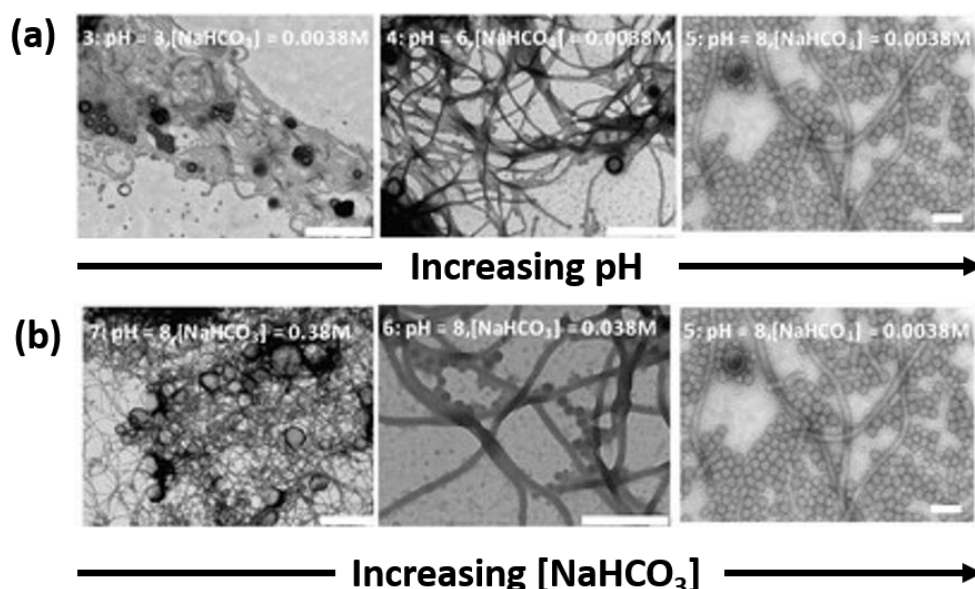


**Figure 1.13.** Representative TEM images of the different morphologies that can be obtained when performing the RAFT aqueous emulsion polymerisation of styrene with a trithiocarbonate-capped P(AA-co-PEGA) (AA/PEGA = 50/50) precursor at different (a) pH and (b) salt concentrations.

Currently, we have only a very limited understanding of why only a small sub-set of such PISA formulations can produce non-spherical morphologies. The effect of various synthesis parameters on the final copolymer morphology have been investigated, including the topology of the stabiliser block,<sup>172</sup> the post-polymerisation addition of monomer<sup>181</sup> and the nature of the RAFT end-groups and initiator concentration.<sup>182</sup> However, generic design rules have yet to be established. In this context, Armes and co-workers recently proposed that the aqueous solubility of the water-immiscible monomer is a key parameter for preparing block copolymer worms or vesicles *via* RAFT aqueous emulsion polymerisation.<sup>173, 177, 178, 182, 183</sup> More specifically, three monomers (HBMA, GlyMA and 2-methoxyethyl methacrylate (MOEMA), see Figure 1.14) with aqueous solubilities of  $\sim 20 \text{ g dm}^{-3}$  were examined in turn and, in each case, spheres, worms or vesicles could be obtained by adjusting the synthesis conditions. These aqueous solubilities are somewhat higher than those for traditional vinyl monomers such as styrene or *n*BA.<sup>184</sup>

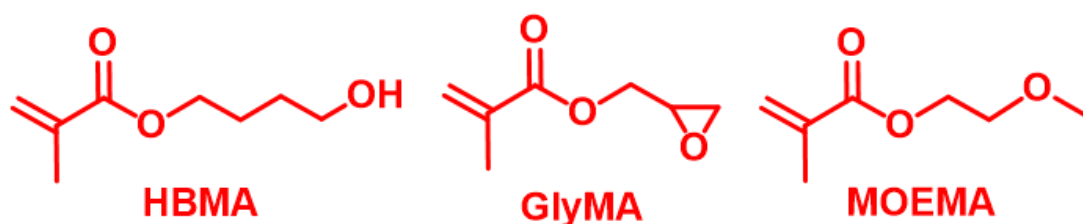


**Figure 1.14.** Chemical structures of hydroxybutyl methacrylate (HBMA), glycidyl methacrylate (GlyMA) and 2-methoxyethyl methacrylate (MOEMA). All three of these monomers are water-immiscible with an aqueous solubility of  $\sim 20 \text{ g dm}^{-3}$ , at their respective polymerisation temperatures, and non-spherical block copolymer nanoparticles (e.g. worms or ‘monkey nuts’ or vesicles) have been reported in each case.<sup>173, 177, 178, 183</sup>

Initially, Cockram *et al.*<sup>177</sup> investigated the RAFT aqueous emulsion polymerisation of HBMA. Conducting such syntheses using a partially ionised poly(methacrylic acid) (PMAA) stabiliser block produced a novel non-spherical ‘monkey nut’ morphology at pH 5.<sup>177</sup> Subsequently, Foster and co-workers obtained a mixed phase of worms and vesicles by chain-extending a non-ionic PEG<sub>113</sub> precursor with HBMA.<sup>179</sup>

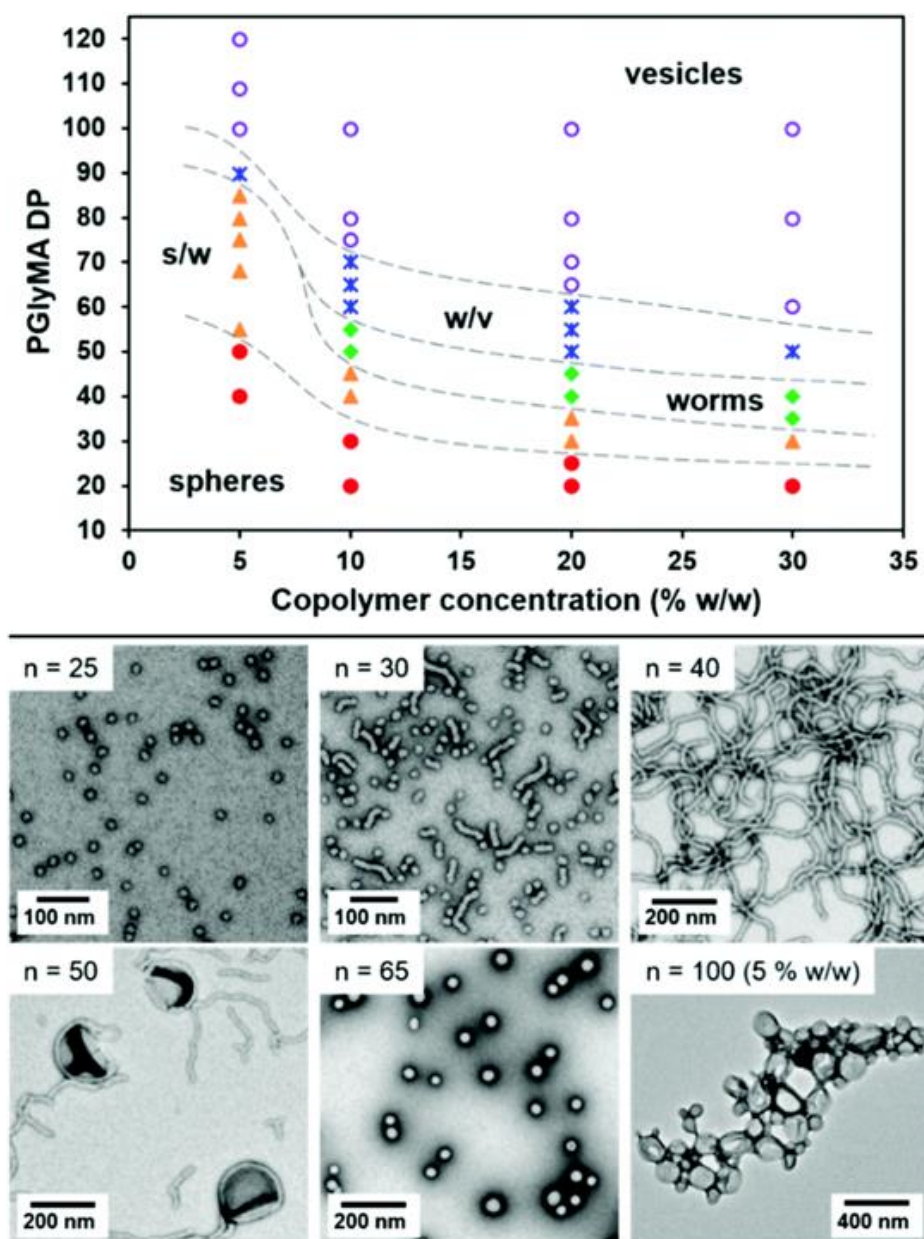


**Figure 1.15.** Pseudo-phase diagram constructed for a series of PGMA<sub>28</sub>-PGlyMA<sub>n</sub> diblock copolymer nano-objects synthesised by chain extending a PGMA<sub>28</sub> homopolymer precursor with GlyMA *via* RAFT aqueous emulsion polymerisation at of 10 – 30% w/w (s/w = mixed phase of spheres and worms; w/v = mixed phase of worms and vesicles). Representative TEM images are shown for selected nano-objects prepared at 20% w/w (where n indicates the mean PGlyMA DP).<sup>183</sup>

Similarly, Hatton *et al.* explored the RAFT aqueous emulsion polymerisation of GlyMA using a non-ionic PGMA precursor as a steric stabiliser block.<sup>167, 173, 183</sup> According to Ratcliffe and co-workers, this monomer has an aqueous solubility of 18 - 20 g dm<sup>-3</sup> at 50 °C.<sup>185</sup> Well-defined diblock copolymer worms and vesicles could be obtained if the PGMA stabiliser block was sufficiently short, which is known to aid access to higher order morphologies.<sup>83, 173, 178, 183</sup>

Figure 1.15 shows the pseudo-phase diagram that was constructed by systematically varying the PGlyMA DP and the copolymer concentration. This enabled the efficient, facile and reproducible synthesis of spheres, worms and vesicles. Presumably, its relatively high monomer solubility enables faster diffusion of GlyMA through the aqueous phase into the cores of the nascent nanoparticles. This leads to greater solvation and hence enhanced mobility for the growing PGlyMA chains. This in turn facilitates sphere-sphere fusion, which is a prerequisite for the formation of diblock copolymer worms (see Figure 1.16 below). In contrast, monomers with lower aqueous solubilities (e.g. BzMA) diffuse more slowly through the aqueous phase, hence providing less solvation for the growing hydrophobic chains within the nanoparticle cores during the initial stages of the polymerisation. This explains why only kinetically-trapped spheres can be obtained *via* RAFT aqueous emulsion polymerisation of BzMA when using a PGMA precursor.<sup>87</sup>

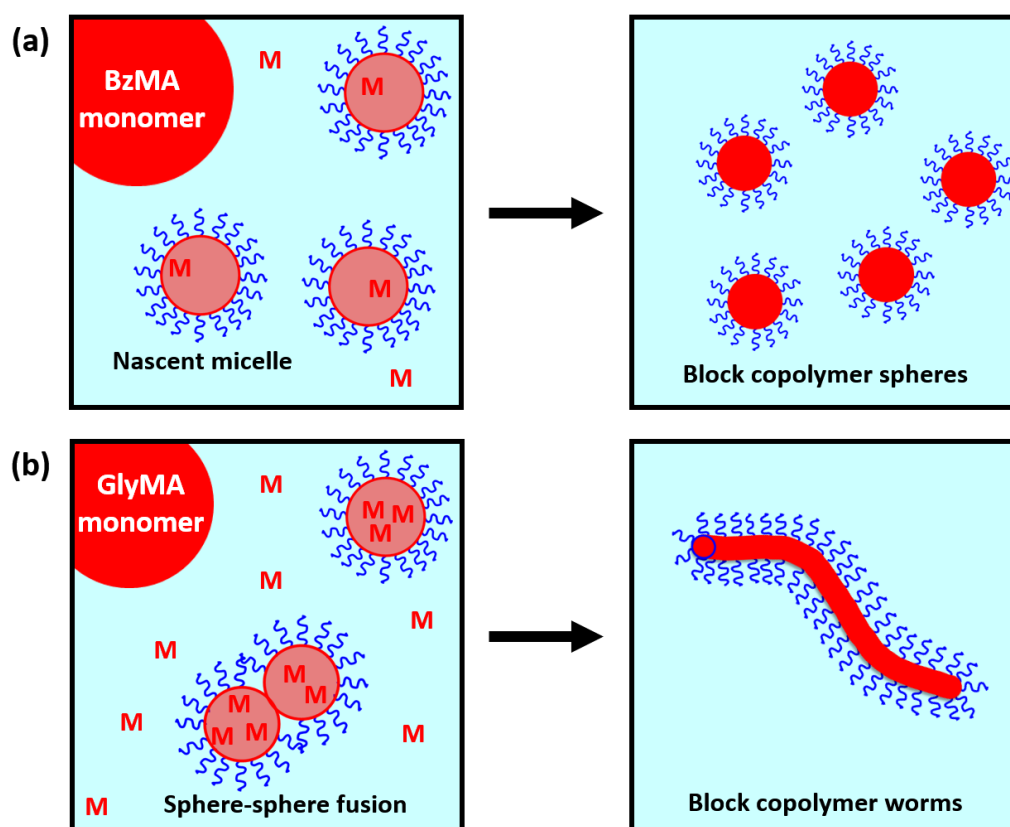


**Figure 1.16.** Schematic cartoon of the RAFT aqueous emulsion polymerisation of (a) BzMA, resulting in the formation of kinetically-trapped spheres, and (b) GlyMA, which leads to the formation of non-spherical morphologies (e.g. worms). The latter monomer has an aqueous solubility of 18-20 g dm<sup>-3</sup> at 50 °C, enabling efficient monomer mass transport through the aqueous phase and hence solvation of the nascent micelle cores *within the time scale of the polymerisation*. The improved mobility of the PGlyMA chains is believed to promote sphere-sphere fusion, which is the essential first step for the formation of block copolymer worms.<sup>173, 183</sup>

More recently, Brotherton and co-workers reported the RAFT aqueous emulsion polymerisation of MOEMA.<sup>178</sup> This was the third example of a methacrylic monomer with moderate aqueous solubility (19.6 g dm<sup>-3</sup> at 70 °C) that enabled higher order copolymer morphologies to be produced *via* RAFT aqueous emulsion polymerisation.<sup>178</sup> Small-angle x-ray scattering (SAXS) was used to monitor the *in situ* evolution in copolymer morphology from spheres to worms to vesicles during the RAFT aqueous emulsion polymerisation of MOEMA.<sup>178</sup>

### 1.8.2 PISA *via* RAFT Aqueous Dispersion Polymerisation

Initially, RAFT aqueous dispersion polymerisation formulations comprise homogeneous solutions containing the monomer, initiator and water-soluble steric stabiliser. As the monomer is polymerised, it forms an increasingly hydrophobic block from one end of the precursor. At some critical DP, this growing block becomes insoluble and the amphiphilic diblock copolymer undergoes *in situ* self-assembly to form sterically-stabilised nanoparticles.<sup>73</sup>

In 2007, Hawker *et al.* reported the first example of PISA *via* RAFT aqueous dispersion polymerisation.<sup>186</sup> In this seminal study, a PDMAC precursor was chain-extended with *N*-isopropylacrylamide (NIPAM) to produce spherical nanoparticles at 70 °C. However, such nanoparticles dissolved upon cooling to ambient temperature owing to the lower critical solution temperature (LCST) of 32 °C of the PNIPAM cores. Thus these nanoparticles were cross-linked using bisacrylamide to afford colloiddally stable nanogels at room temperature.

In 2009, Rieger *et al.* chain-extended a hydrophilic PEG block with DMAC to produce a range of water-soluble PEG-PDMAC precursors of varying chain lengths.<sup>187</sup> Subsequently, these diblock copolymer precursors were chain-extended with *N,N*-diethylacrylamide to produce thermoresponsive spherical nanoparticles. The addition of a bisacrylamide cross-linker was required to ensure that the nanoparticles remained colloiddally stable at room temperature, as the poly(*N,N*-diethylacrylamide) core-forming block exhibits an LCST of approximately 32 °C.

In 2010, Li and Armes reported that diblock copolymer spheres could be prepared *via* RAFT aqueous dispersion polymerisation of HPMA using a PGMA<sub>65</sub> precursor.<sup>188</sup> According to

dynamic light scattering (DLS) studies, the diameter of the spherical nanoparticles increased systematically when targeting longer PHPMA core-forming blocks and final monomer conversions exceeded 99%. Furthermore, chain-extending this PGMA<sub>65</sub> precursor when targeting a PHPMA DP of 300 produced relatively large polydisperse vesicles at 20% w/w solids, as judged by TEM and DLS studies.

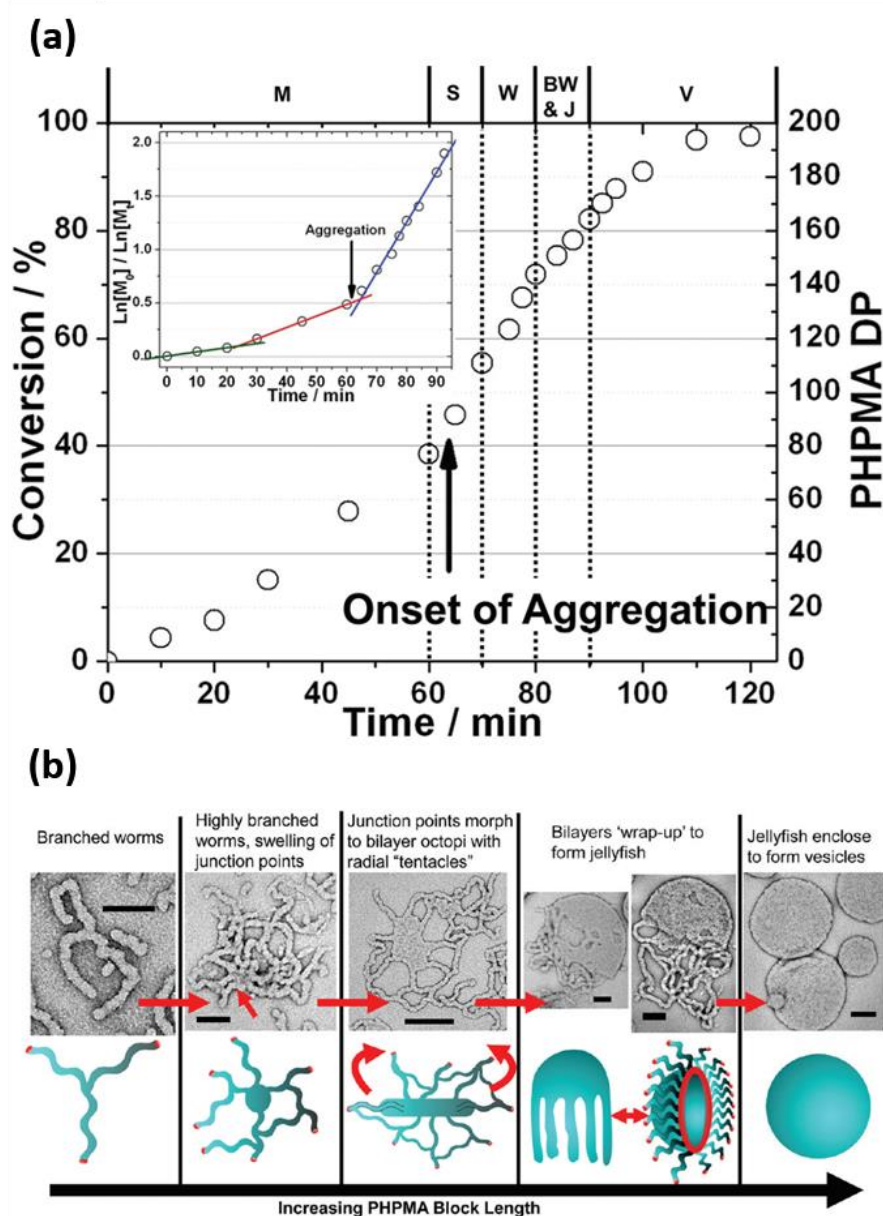


**Figure 1.17.** (a) Monomer conversion (and the corresponding effective PHPMA DP) as a function of time for the synthesis of PGMA<sub>47</sub>-PHPMA<sub>200</sub> vesicles *via* RAFT aqueous dispersion polymerisation of HEMA at 10% w/w solids and 70 °C. The corresponding semi-logarithmic vs time plot is shown as an inset. Five morphology regimes were observed by TEM studies. (b) Proposed mechanism for the *in situ* worm-to-vesicle morphological transition *via* a jellyfish intermediate [abbreviations: M = molecularly dissolved copolymer chains, S = spheres, W = worms, BW = branched worms, J = jellyfish, V = vesicles].<sup>109</sup>

Since this study, the Armes group has conducted many studies involving the prototypical PGMA-PHPMA PISA formulation.<sup>67, 83, 107, 109, 149, 150, 189-198</sup> Blanazs *et al.* provided fascinating mechanistic insights into the self-assembly process that occurs during the RAFT aqueous dispersion polymerisation of HPMA when using a PGMA<sub>47</sub> precursor to target vesicles.<sup>109</sup> <sup>1</sup>H NMR spectroscopy and TEM studies confirmed that a significant rate enhancement occurs after micellar nucleation, as shown in Figure 1.17. The formation of monomer-swollen nascent particles increases the local monomer concentration, thereby enhancing the rate of polymerisation. TEM analysis of aliquots extracted during the HPMA polymerisation enabled various intermediate morphologies to be identified. More specifically, the copolymer morphology evolved from spheres to worms to branched worms to ‘jellyfish’ and finally to vesicles, as the DP of the structure-directing PHPMA block increased from 92 to 200.<sup>109</sup> These observations can be rationalised in terms of a gradual increase in the packing parameter during the polymerisation.

Aqueous dispersions of PGMA<sub>54</sub>-PHPMA<sub>140</sub> diblock copolymer worms have been reported to exhibit thermoresponsive behaviour.<sup>110, 190</sup> More specifically, a reversible worm-to-sphere transition can be initiated by simply *cooling* an aqueous worm dispersion to 5-10 °C. According to Blanazs *et al.*, this morphological transformation involves surface hydration of the weakly hydrophobic PHPMA chains within the worm cores.<sup>128</sup> Overall, this results in a smaller core volume and an associated reduction in the packing parameter, as depicted in Figure 1.18. Accompanying this morphological transition is macroscopic degelation owing to the loss of multiple inter-worm contacts, thus resulting in a free-flowing dispersion of non-interacting isotropic spheres.<sup>199</sup> This transformation is fully reversible if the copolymer concentration is not too low (< 1% w/w solids), otherwise sphere-sphere fusion to form dimers (and ultimately worms) becomes improbable.

Recently, various research groups have explored the RAFT dispersion polymerisation of PHPMA using a PEG-based precursor instead of a PGMA stabiliser.<sup>108, 141, 145, 179, 200</sup> Such PEG<sub>x</sub>-PHPMA<sub>y</sub> worms exhibit thermoresponsive behaviour similar to that of PGMA-PHPMA worms. Warren and co-workers showed that if the PEG stabiliser is relatively long (i.e. DP = 113), then

PEG-PHPMA worms are thermoresponsive but not *thermoreversible*.<sup>108</sup> More specifically, cooling such worms from 25 °C to 4 °C leads to a worm-to-sphere morphological transition. However, worms do not reform (at least, not within normal experimental timescales) on returning to 25 °C. Presumably, the PEG<sub>113</sub> block confers sufficient steric stabilisation to inhibit the sphere-sphere fusion that is essential for worm reconstitution. In a later study, Penfold and co-workers used a binary mixture of PEG<sub>113</sub> and PEG<sub>45</sub> precursors to identify a PEG-PHPMA formulation that exhibited thermoreversible behaviour.<sup>141</sup> This was possible because the presence of the shorter PEG<sub>45</sub> chains reduced the steric stabilisation efficiency compared to that conferred by solely PEG<sub>113</sub> chains.

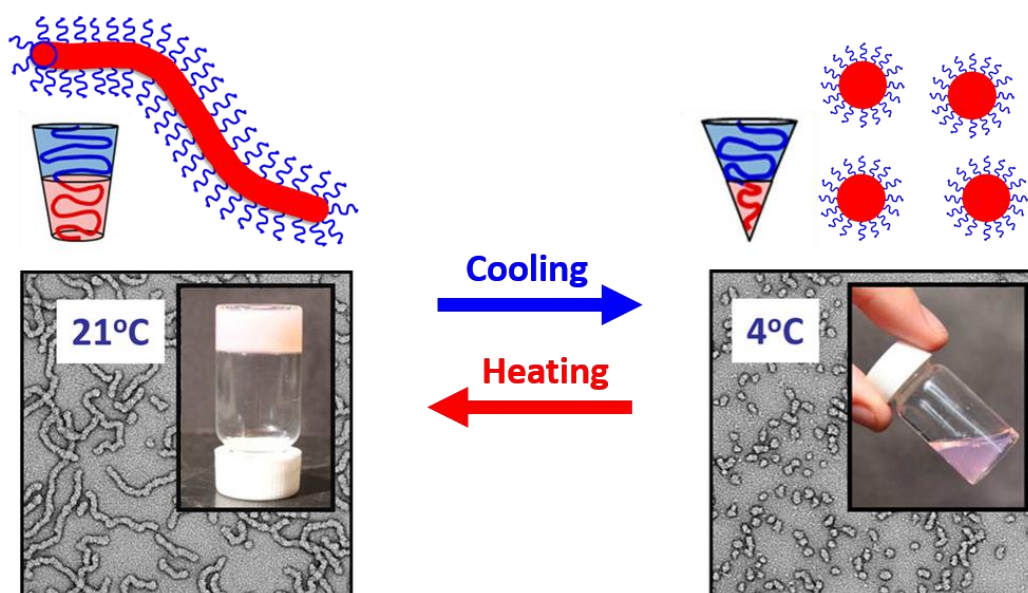


**Figure 1.18.** Schematic representation, digital photographs (see insets), and TEM images of the reversible worm-to-sphere transition that occurs on cooling a PGMA<sub>54</sub>-PHPMA<sub>140</sub> diblock copolymer from 20 °C to 4 °C.<sup>190</sup>

In 2019, Ratcliffe *et al.* reported the first example of a single thermoresponsive amphiphilic diblock copolymer that can form spheres, worms or vesicles in aqueous solution simply by varying the temperature.<sup>201</sup> More specifically, poly(2-hydroxypropyl methacrylamide)-poly(2-hydroxypropyl methacrylate) (PHPMAC-PPHMA) diblock copolymer formed spheres at 4 °C, worms at 22 °C and vesicles at 50 °C.<sup>201</sup> More recently, we have reported three distinct examples of 4-hydroxybutyl acrylate (HBA)-based diblock copolymers that undergo the same sphere/worm and worm/vesicle morphological transitions.<sup>142, 202, 203</sup> However, these transitions are much more

thermoreversible than those observed for the methacrylic PHPMA block.<sup>201</sup> This was attributed to the greater chain mobility of the structure-directing PHBA block, which exhibits a significantly low glass transition temperature  $T_g$  than PHPMA.<sup>142</sup>

### 1.8.3 PISA *via* RAFT Dispersion Polymerisation in Non-Polar Solvents

Over the past seven years or so, there has been significant interest in conducting PISA in non-polar media.<sup>78</sup> Initially, Houillot *et al.* explored RAFT dispersion polymerisation in non-polar media using an all-acrylic formulation.<sup>129</sup> More specifically, poly(2-ethylhexyl acrylate)-poly(methyl acrylate) (PEHA-PMA) diblock copolymer nanoparticles were prepared in *iso*-decane at 80 °C. Using a dithiobenzoate-based CTA for the chain extension of a PEHA precursor using MA led to significant rate retardation and extremely poor RAFT control ( $M_w/M_n > 6.00$ ) at  $\geq 85\%$  conversion compared to that achieved when using a trithiocarbonate-based precursor. In the latter case, DLS studies suggested that a spherical morphology was obtained but no TEM studies were undertaken (presumably owing to the relatively low  $T_g$  of the PMA block).

Fielding and co-workers developed the first well-controlled all-methacrylic RAFT dispersion polymerisation formulation in non-polar media.<sup>127</sup> More specifically, a cumyl dithiobenzoate (CDB) was used to prepare a poly(lauryl methacrylate) (PLMA) precursor in toluene. This precursor was then chain-extended with BzMA to afford PLMA-PBzMA diblock copolymer nanoparticles in *n*-heptane. Using a relatively short PLMA<sub>17</sub> precursor provides access to spheres, worms or vesicles. In contrast, using a longer PLMA<sub>37</sub> stabiliser block restricted the copolymer morphology to kinetically-trapped spheres. As expected, the diameter of such spheres could be tuned by varying the target DP of the PBzMA core-forming block.

In a later study, this PBzMA formulation was extended from *n*-heptane to *n*-dodecane, with the higher boiling point of the latter solvent allowing high temperature studies to be undertaken.<sup>128</sup> This proved to be interesting because PLMA-PBzMA diblock copolymer nanoparticles can undergo morphological transformations on heating.<sup>128</sup> For example, Fielding and co-workers used rheology to characterise the thermoresponsive behaviour of a PLMA<sub>16</sub>-PBzMA<sub>37</sub> worm gel,

which undergoes degelation above 50 °C as a result of a worm-to-sphere transition.<sup>128</sup> Variable temperature <sup>1</sup>H NMR studies conducted in *d*<sub>26</sub>-dodecane indicated partial solvation of the core-forming PBzMA chains. Similar observations were described by Lowe and co-workers for thermoresponsive worms prepared in ethanol.<sup>116</sup> The worm-to-sphere transition was rationalised in terms of *surface plasticisation* of the core-forming block. This leads to an increase in the effective volume fraction of the stabiliser block, which in turn reduces the packing parameter. More recently, Derry *et al.* reported that poly(stearyl methacrylate)-poly(benzyl methacrylate) (PSMA<sub>13</sub>-PBzMA<sub>96</sub>) vesicles prepared in mineral oil undergo a vesicle-to-worm transition on heating up to 150 °C, which offers a potential new high-temperature thickening mechanism for automotive engine oils.<sup>204</sup>

Recently, TFEMA has been utilised as a core-forming block for non-aqueous RAFT dispersion formulations. For example, Cornel *et al.* reported the synthesis of sterically-stabilised PSMA-PTFEMA spherical nanoparticles in various *n*-alkanes.<sup>205</sup> Such nanoparticles were almost perfectly isorefractive with *n*-tetradecane at 70 °C, enabling the kinetics of the RAFT dispersion polymerisation of PTFEMA to be monitored in this solvent using visible absorption spectroscopy. Importantly for this Thesis, the same study confirmed that relatively small spherical nanoparticles can be prepared using this PISA formulation. More specifically, PSMA<sub>12</sub>-PTFEMA<sub>98</sub> spheres with a mean DLS diameter of 33 nm were prepared *via* RAFT dispersion polymerisation of TFEMA in *n*-tetradecane at 70 °C (see Figure 1.19). Later, György and co-workers extended this formulation to prepare highly transparent PSMA-PTFEMA diblock copolymer vesicles.<sup>206</sup>

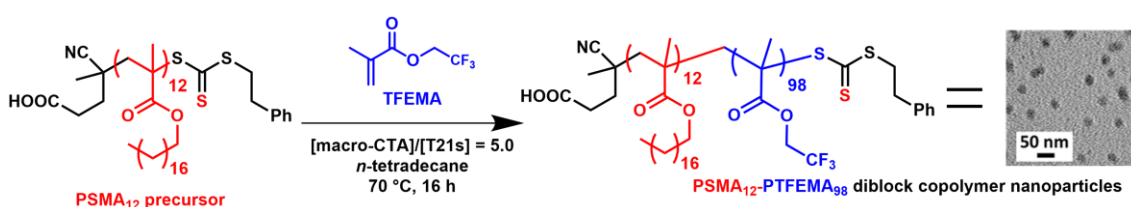


**Figure 1.19.** Chain extension of a PSMA<sub>12</sub> homopolymer precursor *via* RAFT dispersion polymerisation of TFEMA in *n*-tetradecane at 70 °C to form spherical diblock copolymer nanoparticle (see TEM image) with a mean *z*-average diameter of 33 nm as judged by DLS.<sup>205</sup>

## 1.9 Emulsions

### 1.9.1 General Concepts in Emulsion Science

Emulsions are mixtures of two immiscible liquids, such as oil and water, stabilised by an emulsifier. Emulsions are ubiquitous in everyday life; they are found in food, pharmaceuticals, cosmetics, printing, and the petroleum industry.<sup>207</sup> There are three different classes of emulsions depending on the size of the droplets (see Figure 1.20).<sup>208</sup> *Macroemulsions* are composed of large, polydisperse droplets of 1 - 100  $\mu\text{m}$  diameter. *Nanoemulsions* possess a mean droplet diameter below approximately 200 nm, and typically have a relatively low polydispersity. *Microemulsions* comprise very small (< 50 nm diameter) near-monodisperse droplets. The latter are formed by either diblock copolymers or suitable surfactant/co-surfactant mixtures and are thermodynamically stable; they shall not be discussed further in this Thesis. In contrast, macroemulsions and nanoemulsions are only kinetically stable and can be prepared using various emulsifiers, including surfactants, amphiphilic copolymers and colloidal particles with appropriate wettability.

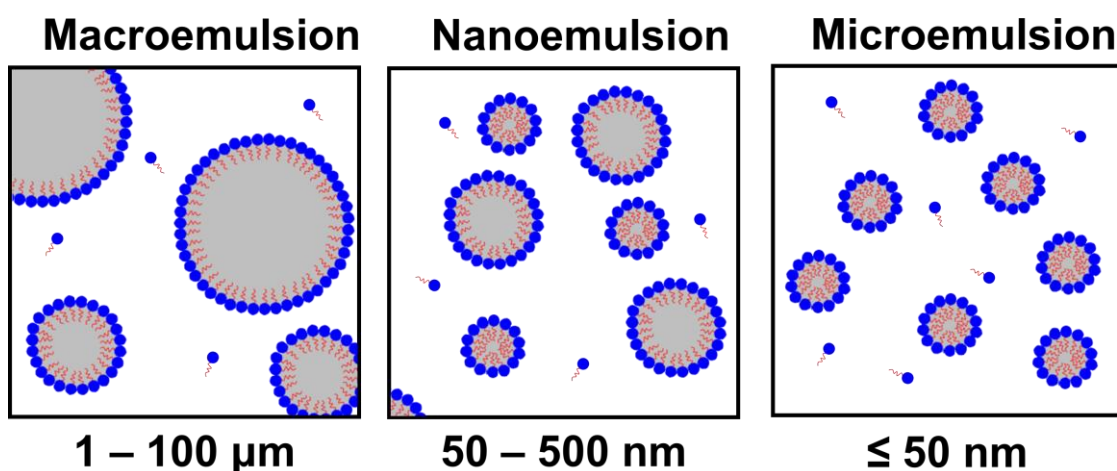


**Figure 1.20.** Schematic cartoon of the three different types of emulsions: macroemulsions, nanoemulsions and microemulsions.<sup>208</sup>

Simple emulsions can be classified as either oil-in-water (o/w) or water-in-oil (w/o). The type of emulsion that is formed depends on the nature of the emulsifier. In 1913, Bancroft proposed a useful rule of thumb for predicting emulsion type based on the solubility of the

emulsifier.<sup>209</sup> In essence, the continuous phase of an emulsion tends to be the phase in which the emulsifier is preferentially soluble. In 1949, Griffin introduced the concept of hydrophilic-lipophile balance (HLB) as a method for predicting the emulsion type based on the composition of surfactant emulsifiers.<sup>210</sup> This is a quantitative measure of the balance between the hydrophilic and hydrophobic components within a given surfactant molecule. Surfactants with lower HLB numbers (e.g. non-ionic surfactants) are predicted to stabilise w/o emulsions. In contrast, surfactants with higher HLB numbers (e.g. anionic or cationic surfactants) normally form o/w emulsions. However, such HLB numbers are calculated for free surfactant molecules, rather than for surfactant adsorbed at an oil/water interface. Moreover, other conditions such as temperature, electrolyte concentration, and oil type are not considered. Furthermore, the packing parameter of the surfactant at an oil/water interface has been shown to dictate the tendency of the monolayer to curve towards the oil or water.<sup>211</sup>

The thermodynamics of emulsions are dictated by their interfacial properties. For two immiscible liquids, a flat interface can be defined between the two bulk phases. According to the Gibbs model,<sup>212</sup> the interfacial region is assumed to be ideally thin and its thermodynamic properties differ compared to that for the two bulk phases (see Figure 1.21a). These properties reflect the unfavourable change in interaction energy that occurs on moving a molecule from the bulk to the surface, which leads to a reduction in the number of nearest neighbours. This gives rise to an interfacial tension  $\gamma$ . The interfacial free energy  $dG$  can be expressed by an entropic term  $-SdT$ , an interfacial area term  $\gamma dA$  (where  $\gamma$  is the surface tension and  $dA$  is the change in the interfacial area), and a composition term  $\sum n_i d\mu_i$  (where  $n_i$  is the number of moles of component  $i$  with chemical potential  $\mu_i$ ). The Gibbs-Duhem equation is given by:

$$dG = -SdT + \gamma dA + \sum \mu_i dn_i \quad \mathbf{1.16}$$

At constant temperature and composition, Equation 1.16 can be expressed as:

$$dG = \gamma dA$$

$$\gamma = \left( \frac{\partial G}{\partial A} \right)_{T, n_i} \quad 1.17$$

According to Equation 1.17, interfacial tension can be regarded as the increase in Gibbs free energy per unit area. Unlike a flat interface, the interfacial tension at a curved interface must be balanced by an equal and opposite force. Spherical droplets tend to shrink to reduce their interfacial area until there is an excess pressure inside the droplet compared to that outside (see Figure 1.21b). The smaller the droplet, the larger the excess pressure  $p$ . This is expressed by the Young-Laplace equation:

$$\Delta p = \gamma \left( \frac{1}{r_1} + \frac{1}{r_2} \right) \quad 1.18$$

where  $r_1$  and  $r_2$  are the principal radii of curvature. For a perfectly spherical droplet,  $r_1 = r_2 = r$  and Equation 1.18 becomes:

$$\Delta p = \frac{2\gamma}{r} \quad 1.19$$

Equation 1.19 has important implications for the destabilisation of nanoemulsions *via* Ostwald ripening, which is discussed later in this Thesis.

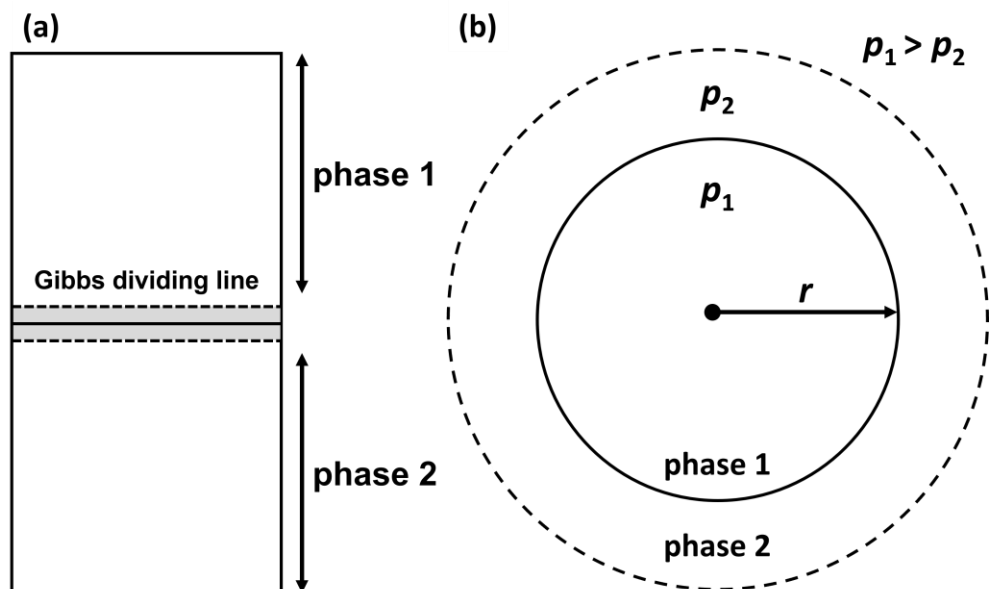


**Figure 1.21.** (a) The Gibbs model of an ideally thin interface between two immiscible phases.<sup>212</sup> (b) Cross-section of a droplet (phase 1) suspended in a different phase (phase 2). The internal pressure within the droplet ( $p_1$ ) is greater than the external pressure ( $p_2$ ). This difference in pressure across the interface is related to the curvature of the droplet by its radius  $r$ .

The process of preparing an emulsion, known as emulsification, requires energy to generate new interfacial area  $A$ . Here,  $\Delta A$  is the difference in interfacial area between the initial state comprising two immiscible bulk liquids and the final droplets. The total free energy change of emulsification ( $\Delta G_{\text{emul}}$ ) is given by:

$$\Delta G_{\text{emul}} = \gamma \Delta A - T \Delta S \quad \mathbf{1.20}$$

Given that  $\gamma \Delta A$  is large and positive, while  $T \Delta S$  is small and positive,  $\Delta G$  must also be positive. Therefore, emulsion formation costs energy. The energy required to generate an emulsion is dependent on the final droplet diameter, since smaller droplets possess a higher interfacial area. Therefore, macroemulsions are relatively easy to prepare by well-known methods such as high-shear homogenisation. On the other hand, nanoemulsions typically require high-energy emulsification techniques, such as high-pressure microfluidisation or ultrasonication.<sup>213</sup> Relatively high surfactant concentrations are often used to lower the interfacial tension between the two immiscible phases.

Both macroemulsions and nanoemulsions are thermodynamically unstable. In the absence of any stabilisation mechanism, demulsification occurs *via* creaming, coalescence, flocculation, Ostwald ripening, or some combination of such processes. These destabilisation mechanisms are summarised overleaf in Figure 1.22. However, in the presence of a suitable emulsifier (i.e. surfactant, polymer or surface-active particles), an energy barrier is created between the droplets, providing kinetic stability. Nevertheless, given sufficient time, the emulsion will eventually revert to its two constituent bulk phases. The more stable an emulsion, the longer phase separation takes to occur. The predominant mechanism of destabilisation depends on the size of the emulsion droplets. For macroemulsions, creaming is usually a dominant mechanism, whereas nanoemulsions show negligible gravitational creaming (or sedimentation) due to their relatively small mean droplet diameter. However, nanoemulsions can undergo Ostwald ripening within relatively short time scales.

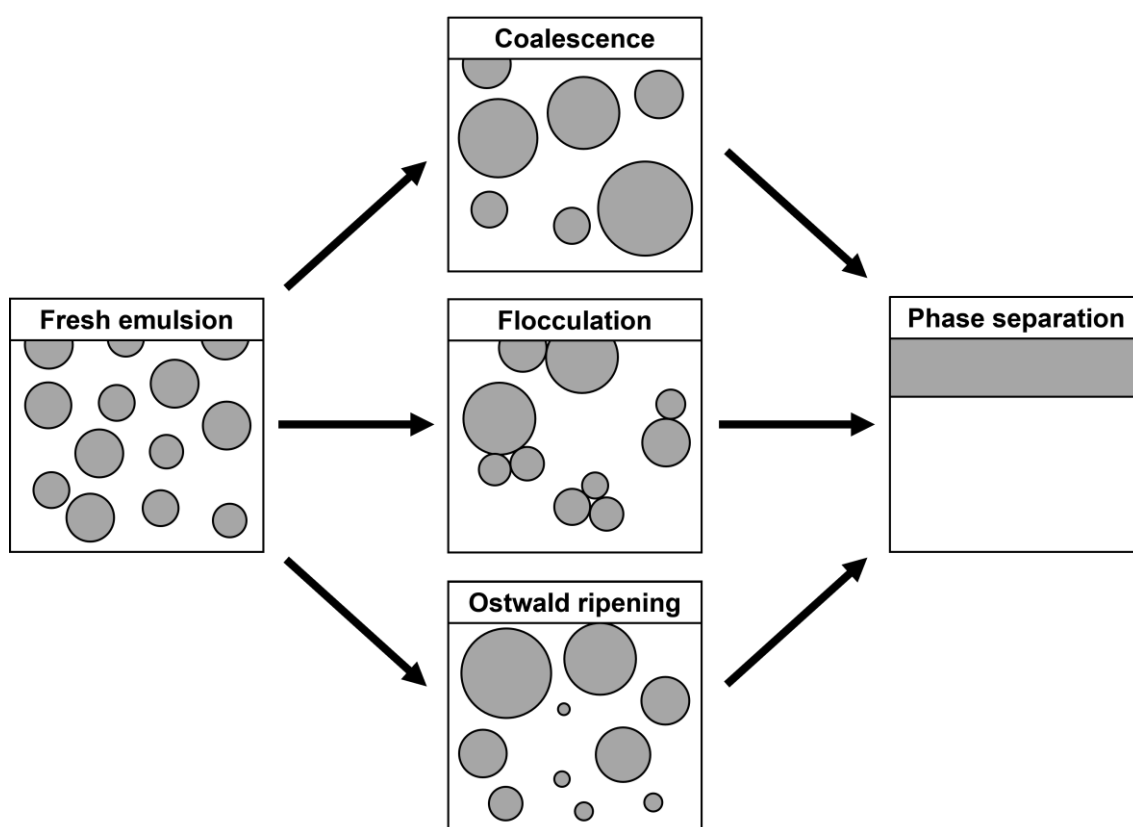


**Figure 1.22.** Schematic cartoon of three emulsion destabilisation mechanisms: coalescence, flocculation, and Ostwald ripening. A fourth mechanism (not shown) is gravitational creaming or sedimentation, but this normally only applies to macroemulsions.

Ostwald ripening is the growth of larger droplets at the expense of smaller ones over time.<sup>214, 215</sup> It is the consequence of subtle solubility differences between droplets of differing diameters. Smaller droplets have a higher Laplace pressure, and therefore higher solubility, than larger droplets. The Kelvin equation describes the relationship between spherical droplets of mean radius  $r$  and their solubility within the continuous phase:

$$C(r) = C(\infty) \exp\left(\frac{2\gamma V_m}{rRT}\right) \quad 1.21$$

where  $C(r)$  is the solubility of the spherical droplets dispersed within the continuous phase,  $C(\infty)$  is the bulk phase solubility (i.e. the solubility of an infinitely large droplet), and  $V_m$  is the molar volume of the dispersed phase. The higher solubility of smaller droplets means that its constituent molecules dissolve faster in the continuous phase, recondensing onto larger droplets. Over time, this mass transport leads to an overall increase in droplet size and a corresponding reduction in the interfacial area. Theoretically, this phenomenon should terminate when all of the smaller

droplets have recondensed into a single droplet. In reality, the rate of Ostwald ripening decreases as the mean droplet size increases so this upper limit is seldom attained.

Lifshitz and Slyozov (LS)<sup>216</sup> and Wagner (W)<sup>217</sup> independently developed a quantitative theory for Ostwald ripening. The LSW theory assumes that the dispersed phase droplets are spherical and are separated from one another by distances that are significantly larger than the droplet diameters. Moreover, mass transport is assumed to be limited by molecular diffusion through the continuous phase. Given these assumptions, the rate of Ostwald ripening,  $\omega$ , is given by Equation 1.22:

$$\omega = \frac{R_n^3}{dt} = \frac{8}{9} \left[ \frac{C(\infty)\gamma V_m D}{\rho RT} \right] \quad 1.22$$

where  $D$  is the diffusion coefficient of the dissolved species in the continuous phase,  $\rho$  is the density of the dispersed phase, and  $R_n$  is the number-average droplet radius. Therefore, if the predominant mechanism of destabilisation is Ostwald ripening, the  $R_n$  cubed term should increase linearly over time. Several strategies have been employed to suppress the rate of Ostwald ripening, particularly for nanoemulsions. For example, using an oil with a relatively low aqueous solubility improves the long-term stability of o/w nanoemulsions.<sup>218</sup> Alternatively, a suitable species can be added to the droplet phase that is highly insoluble in the continuous phase. For example, adding a long hydrocarbon such as squalane to the oil droplets of an o/w nanoemulsion enhances its stability towards Ostwald ripening.<sup>219</sup> Similarly, addition of salt to the aqueous phase of an w/o emulsion is known to inhibit mass transfer between aqueous droplets.<sup>220</sup>

### 1.9.2 Emulsion Characterisation Techniques

There are many techniques that can be used to measure the size of particles and emulsion droplets. Each sizing technique reports a specific moment of the particle size distribution and possess various advantages and disadvantages, such as instrument-biased resolution, upper and low size limits, and cost. In practice, there is no single method that is universally used to size emulsions. Some characterisation techniques provide information regarding the structure, as well as the emulsion droplet size distribution.

Optical microscopy reports the number-average droplet diameter  $D_n$  of an emulsion, which is defined by Equation 1.23:

$$D_n = \frac{\sum N_i D_i}{\sum N_i} \quad 1.23$$

where  $N_i$  is the number of droplets with diameter  $D_i$ . Optical microscopy is a widely available technique and requires minimal sample preparation. However, since optical microscopy uses visible light, its resolution is limited to emulsions with mean droplet diameters greater than 1  $\mu\text{m}$ . Furthermore, optical microscopy is not statistically robust since droplet size distributions are assessed by counting a relatively small number (typically hundreds) of droplets.

The interaction of light with matter produces four types of scattering: diffraction, refraction, reflection and absorption. Laser diffraction (or low-angle laser light scattering (LALLS)) is commonly used to size emulsion droplets ranging from 0.1 to 3000  $\mu\text{m}$ .<sup>221</sup> A laser diffraction instrument consists of a laser, detector, and some means of passing the sample through the laser beam. Typically, a He-Ne gas laser is employed as an intense source of coherent light with a fixed wavelength ( $\lambda = 633 \text{ nm}$ ). The laser passes light through the emulsion, which is scattered onto a detector. This technique uses the Fraunhofer approximation for light scattering (or diffraction).<sup>222</sup> This assumes that (i) the particle is much larger than the wavelength of light, (ii) light is scattered only at narrow angles, (iii) the particles are opaque discs and scattering occurs only from the particle surface, and (iv) particles of all sizes scatter light with the same efficiency. In many cases, these assumptions are invalid, particularly as both absorption and refraction of light are ignored. For sufficiently small particles ( $< 25 \mu\text{m}$  diameter), such interactions become important, and the more rigorous Mie theory of scattering must be applied.<sup>223</sup> Mie theory predicts the relative intensity of scattered light as a function of particle size, provided that the particle is spherical, optically homogeneous and has a known refractive index.<sup>224</sup> This theory can predict the effect of refraction, reflection and absorption, as well as diffraction. To determine the volume-average distribution using laser diffraction, the refractive indices of both the material and solvent must be known, as well as the absorption component of the refractive index.

Dynamic light scattering (DLS) reports the intensity-average (or  $z$ -average) diameter, which is biased towards larger particles.<sup>225</sup> This is because the intensity of scattered light from a spherical particle is proportional to the sixth power of its diameter.<sup>225</sup> Hence larger particles scatter much more light than smaller ones and therefore dominate the scattered light intensity. DLS is widely used as a sizing technique owing to its convenience, but it is sensitive to the presence of dust particles and it can often oversize a sample with a multimodal particle size distribution. DLS is suitable for sizing emulsions with a mean droplet diameter below approximately 5  $\mu\text{m}$ , which corresponds to its upper size limit. DLS reports the sphere-equivalent hydrodynamic diameter  $D_h$ , which is calculated from the translational diffusion coefficient  $D$ , using the Stokes-Einstein equation:

$$D_h = \frac{k_B T}{3\pi\eta D} \quad 1.24$$

where  $k_B$  is the Boltzmann constant and  $\eta$  is the solution viscosity. The translational diffusion coefficient of the particles (or droplets) is measured by monitoring the decay of the correlation function over time. As the particles undergo Brownian motion, the scattering intensity fluctuates. Since smaller particles diffuse faster than larger particles, they exhibit a larger diffusion coefficient in a given solvent. Since an isotropic diffusion coefficient is used for the particle size calculation (Equation 1.24), this technique is not suitable for anisotropic (non-spherical) particles.

Small-angle X-ray scattering (SAXS) is a powerful characterisation technique for the structural analysis of nanoparticles and emulsions.<sup>226</sup> Measurements can provide information on the size, shape and interactions between nanoparticles or droplets. Furthermore, SAXS can be used to characterise anisotropic nanoparticles and it is a non-destructive, statistically robust technique because the observed patterns are a result of scattering from many millions of particles. During a SAXS measurement, the sample is irradiated with collimated monochromatic X-rays of a known wavelength  $\lambda$ . The interaction of incident X-rays with electrons composing the sample results in X-ray elastic scattering. The scattered signal is described in reciprocal space using a scattering vector as a measure of the reciprocal length magnitude and direction of the X-ray

scattering. This scattering vector  $q$  is a momentum transfer defined as a difference between wave vectors of the incoming and scattered waves (Figure 1.23) and its length is given by:<sup>226</sup>

$$q = \frac{4\pi}{\lambda} \sin\theta \quad 1.25$$

where  $2\theta$  is the scattering angle.

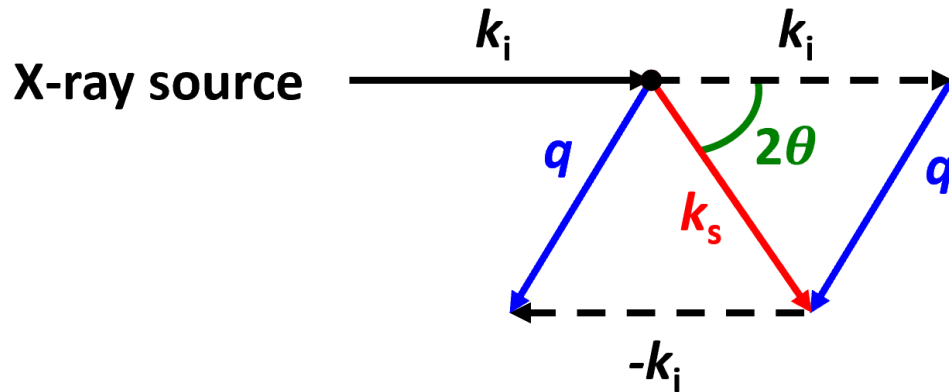


**Figure 1.23.** Schematic representation of the scattering vector  $q$ , based on the incoming and scattered wave vectors,  $k_i$  and  $k_s$ , and the scattering angle  $2\theta$ .

SAXS measures the scattered intensity  $I(q)$  as a function of  $q$ . The normalised scattered intensity of a monomodal dispersion of particles at any given  $q$  is indicated by Equation 1.26:

$$I(q) = NV^2\Delta\rho^2P(q)S(q) \quad 1.26$$

where  $N$  is the particle (scatterer) number density,  $V$  is the volume of the scattering particles,  $\Delta\rho$  is the contrast in scattering length density between the scattering particles and the continuous phase,  $P(q)$  is the form factor and  $S(q)$  is the structure factor.<sup>226</sup>  $P(q)$  describes the shape of the particles, whereas  $S(q)$  represents the spatial arrangement of the scattering objects (particles). For dilute dispersions (typically  $\leq 1\%$  v/v), where no interparticle interactions are expected,  $S(q)$  is usually equal to unity, which simplifies the SAXS analysis. However, a structure factor may still be present if there are repulsive (e.g. charge repulsion) or attractive (e.g. van der Waals ) forces between neighbouring particles. The scattered X-rays form a 2D scattering pattern. An isotropic scattering pattern can be reduced to a 1D profile. The background scattering arising from the continuous phase and sample holder can be subtracted to produce a 1D scattering profile that is

solely characteristic of the X-ray scattering from the particles. Such scattering curves can be analysed using an appropriate scattering model, which usually contain various fitting parameters.

Another sizing technique that can be used to characterise emulsion droplets is analytical centrifugation.<sup>227</sup> The LUMiSizer is an example of a commercial analytical centrifuge, see Figure 1.24. This instrument employs space- and time-resolved extinction profiles (STEP) technology to measure the intensity of transmitted near-infrared light simultaneously as a function of time and position over the entire length of the sample cell.<sup>228</sup> The gradual progression of these transmission profiles contains information on the rate of sedimentation or creaming and, in principle, enables assessment of the particle size distribution. The sedimentation of a particle or droplet due to gravity is characterised by its sedimentation coefficient  $s$ , as defined by Equation 1.27:

$$s = \frac{u}{\omega^2 r} \quad 1.27$$

where  $u$  is the sedimentation velocity,  $\omega$  is the angular velocity and  $r$  is the distance from the axis of rotation. The diameter of a particle  $r_p$  can be directly linked to its hydrodynamic properties using Stokes' law:

$$r_p = \sqrt{\frac{18\eta s}{\rho_p - \rho_s}} \quad 1.28$$

where  $\eta$  is the solvent viscosity and  $\rho_p$  and  $\rho_s$  are the densities of the particle and solvent, respectively. Equation 1.28 enables the particle size distribution to be calculated from the sedimentation velocity, which is obtained directly from the instrument. Therefore, an accurate particle density is an essential input parameter for such analytical centrifugation studies. This can be problematic for particles where the effective density is unknown or ill-defined. For example, emulsion droplets stabilised by surfactant, polymer or particles may have an effective density that differs from that of the pure dispersed phase. In contrast to light scattering techniques, the emulsion droplets are fractionated *via* centrifugation prior to detection. This is because different sized droplets become differentially accelerated in a gravitational field. Such fractionation leads to relatively high resolution and also enables the assessment of emulsions with broad droplet size distributions.

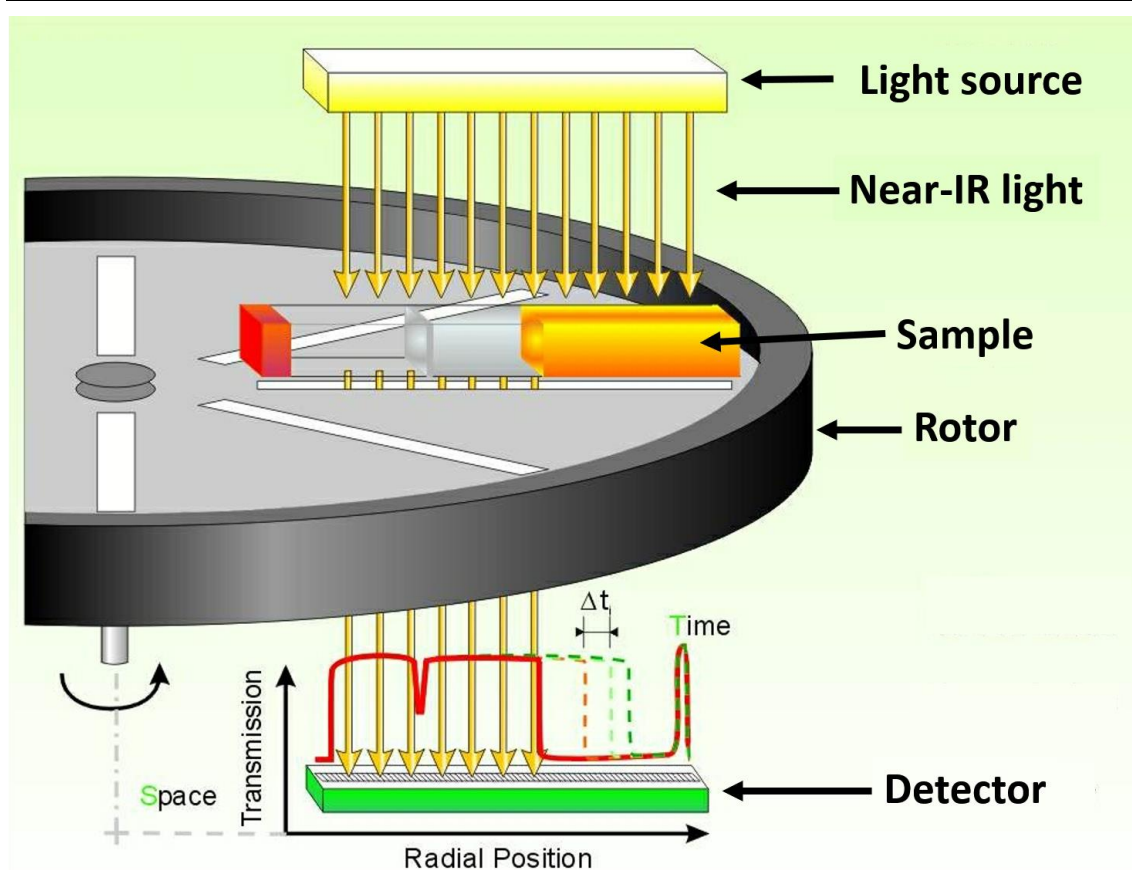


**Figure 1.24.** Schematic representation of a measurement using a LUMiSizer analytical centrifuge. The light source emits a parallel near-IR light beam, which passes through each of the transparent sample cells lying horizontally on the rotor. The distribution of local transmission is recorded over the entire sample length by the detector.<sup>229</sup>

### 1.9.3 Pickering Emulsions

Around the turn of the last century, Ramsden<sup>230</sup> and Pickering<sup>231</sup> independently discovered that various types of particles can stabilise emulsions. Over the past two decades, seminal studies by Binks and co-workers have led to a resurgence of interest in such Pickering emulsions.<sup>232-237</sup> This is because particulate emulsifiers offer numerous advantages over conventional surfactant or polymeric emulsifiers, including superior long-term emulsion stability and reduced foaming during high-shear homogenisation.<sup>235</sup> Consequently, Pickering emulsions have been evaluated for various applications in food manufacture,<sup>238-240</sup> agrochemicals,<sup>241</sup> cosmetics<sup>242, 243</sup> and pharmaceuticals.<sup>242, 244</sup>

It is well-known that surfactants typically adsorb and desorb from interfaces on short timescales.<sup>245</sup> Unlike surfactants, colloidal particles adsorbed at oil/water or air/water interfaces are not necessarily amphiphilic.<sup>232, 234-236, 246, 247</sup> Nevertheless, such particles are often irreversibly adsorbed at an interface if they are of sufficient size and have appropriate surface wettability.<sup>248-250</sup> The driving force for particle adsorption is minimisation of the interfacial area, which lowers the free energy of the system.<sup>235, 245</sup> The amount of energy  $\Delta E$  required to remove a spherical particle of radius  $r$  from the oil/water interface is given by Equation 1.29.<sup>251</sup>

$$\Delta E = \pi r^2 \gamma_{ow} (1 \pm \cos \theta_w)^2 \quad \mathbf{1.29}$$

where  $\gamma_{ow}$  is the oil/water interfacial tension and  $\theta_w$  is the three-phase contact angle. Figure 1.25 shows how the three-phase contact angle affects the detachment energy for a 20 nm particle adsorbed at the toluene/water interface.<sup>234</sup> The calculated energy of detachment is greatest for  $\theta_w = 90^\circ$  and falls rapidly either side of this value. The contact angle is directly related to the particle wettability, which dictates the emulsion type.<sup>235</sup> More specifically, *hydrophilic* particles are preferentially wetted by the aqueous phase ( $\theta_w < 90^\circ$ ) and hence form oil-in-water (o/w) emulsions. In this case, a higher proportion of the particle resides in the aqueous phase. Hence the adsorbed particle monolayer becomes curved such that most of the particle surface remains on the outside of the droplet. In contrast, *hydrophobic* particles ( $\theta_w > 90^\circ$ ) give rise to water-in-oil (w/o) emulsions.<sup>234</sup> In principle, using a judicious combination of hydrophilic and hydrophobic particles should enable the preparation of either water-in-oil-in-water (w/o/w) or oil-in-water-in-oil (o/w/o) Pickering double emulsions.<sup>252, 253</sup>

Many types of inorganic particles have been utilised as Pickering emulsifiers, including silica,<sup>232, 254</sup> titania,<sup>255, 256</sup> magnetite,<sup>257</sup> and clay.<sup>232, 233, 254, 255, 257-261</sup> Similarly, various organic particles such as cellulose nanorods,<sup>262-265</sup> carbon black,<sup>266, 267</sup> carbon nanotubes,<sup>268</sup> graphene oxide sheets<sup>269, 270</sup> and aqueous polymer particles (e.g. latexes,<sup>246, 271-278</sup> microgels<sup>279, 280</sup> and block copolymer nanoparticles<sup>281</sup>) have been evaluated in this context. Within the latter category, it is typically found that charge-stabilised latexes produce w/o emulsions whereas sterically-stabilised latexes usually form o/w emulsions, as depicted in Figure 1.26.<sup>246, 273</sup>

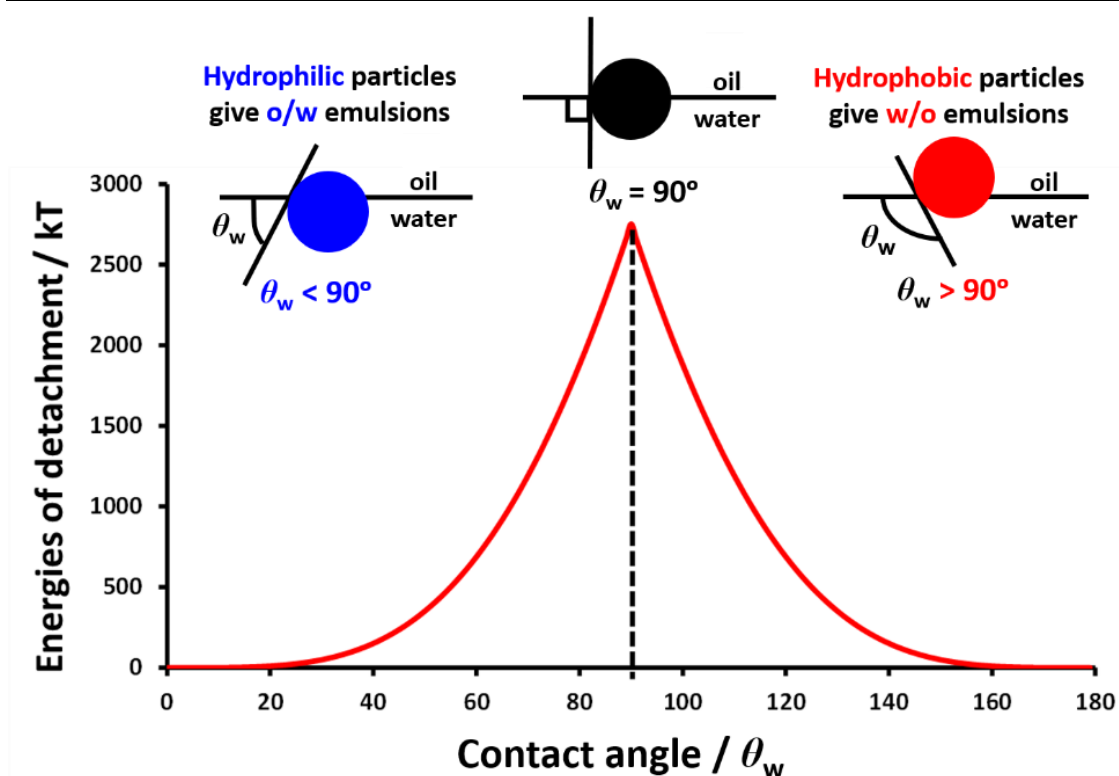


**Figure 1.25.** Spatial location of a spherical particle adsorbed at a planar oil/water interface for a contact angle  $\theta_w$  measured through the aqueous phase such that  $\theta_w$  is less than  $90^\circ$  (blue), equal to  $90^\circ$  (black) or greater than  $90^\circ$  (red). In general, hydrophilic particles ( $\theta_w < 90^\circ$ ) form oil-in-water (w/o) Pickering emulsions, whereas hydrophobic particles ( $\theta_w > 90^\circ$ ) give rise to water-in-oil (w/o) Pickering emulsions. The energy of detachment versus contact angle is shown for the specific case of a spherical nanoparticle of 10 nm radius adsorbed at a planar toluene-water interface for which  $\gamma_{ow} = 0.036 \text{ N m}^{-1}$ .<sup>234, 235</sup>

Based on seminal studies by Binks and others, the use of *inorganic* particles to form Pickering emulsions is now well-understood.<sup>235, 245, 250, 259, 282-289</sup> In the prototypical case of silica, particle wettability can be tuned by partial alkylation of the silanol surface groups<sup>234</sup> or by adding either a cationic surfactant<sup>285, 290</sup> or electrolyte.<sup>232, 258</sup> However, such approaches tend to produce incipient flocculation in solution, which in turn leads to the formation of relatively thick multilayers of adsorbed particles. In principle, polymer-based particles offer several advantages as Pickering emulsifiers. If they are designed to have appropriate surface wettability, no surface modification is required and adsorption at the oil/water interface leads to the formation of well-defined monolayers.<sup>149, 232, 237, 246, 275, 281, 291-297</sup> Moreover, surface wettability can be readily tuned by selecting an appropriate steric stabiliser block.<sup>296</sup>

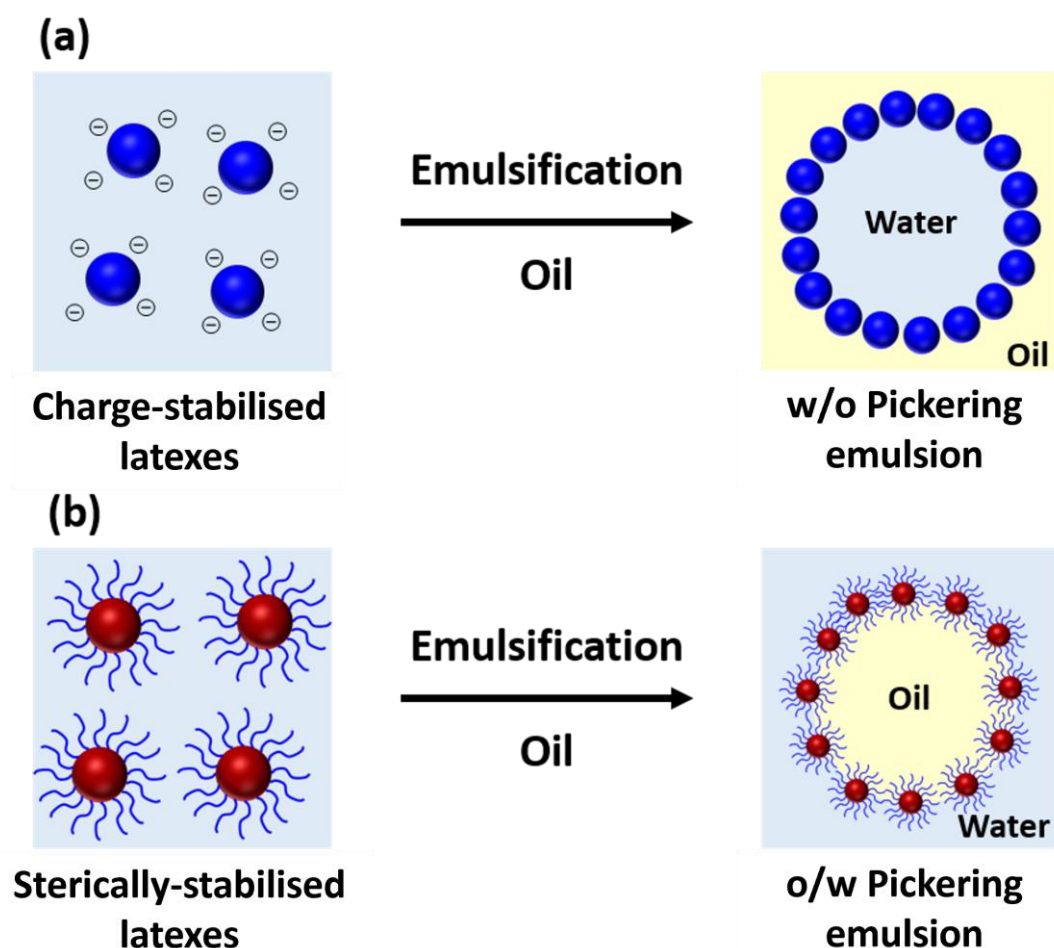


**Figure 1.26.** Schematic representation of the formation of (a) water-in-oil (w/o) Pickering emulsions using charge-stabilised latex particles or (b) oil-in-water (o/w) Pickering emulsions using sterically-stabilised latex particles *via* high-shear homogenisation of an aqueous dispersion of latex particles with oil.<sup>246, 273</sup>

#### 1.9.4 Pickering Emulsions Stabilised by Block Copolymer Nanoparticles

Over the past ten years or so, the Armes group have exploited PISA to design new block copolymer nano-objects for use as bespoke Pickering emulsifiers.<sup>87, 149, 295-306</sup> More specifically, PISA enables the copolymer morphology and surface chemistry to be tuned by judicious selection of the soluble stabiliser and insoluble structure-directing blocks, as shown overleaf in Figure 1.27. Such syntheses can be conducted in either water or in *n*-alkanes to afford either *hydrophilic* or *hydrophobic* sterically-stabilised nanoparticles, respectively. Such nanoparticles can be used to prepare oil-in-water,<sup>87, 298, 299</sup> water-in-oil<sup>295, 300</sup> and multiple emulsions.<sup>296, 302</sup>

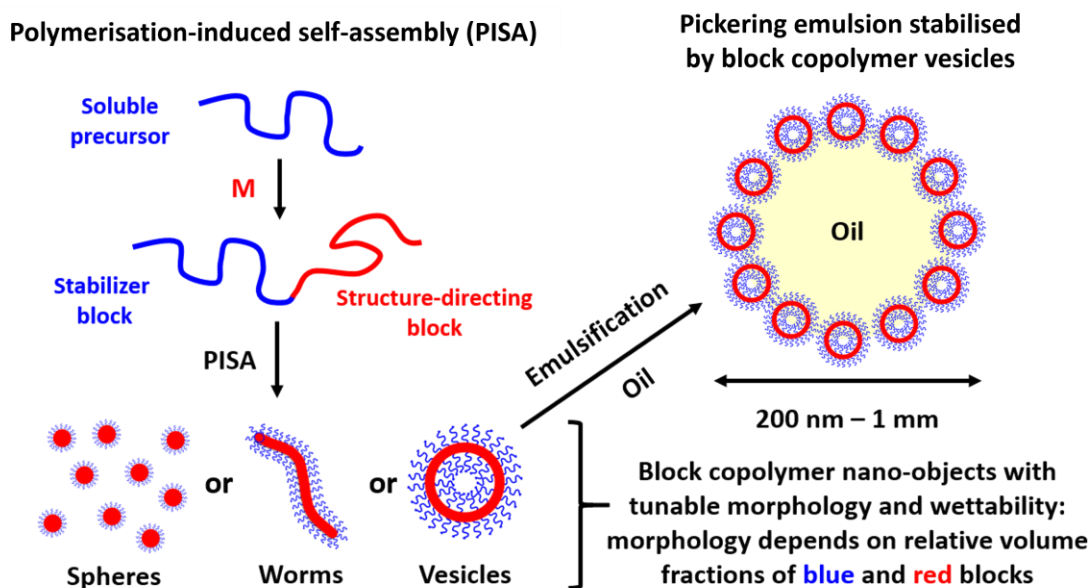


**Figure 1.27.** Schematic representation of polymerisation-induced self-assembly (PISA), whereby a soluble blue precursor block is chain-extended using a suitable vinyl monomer to produce a red insoluble structure-directing block. Depending on the relative volume fractions of the blue and red blocks, *in situ* self-assembly produces spheres, worms or vesicles. PISA can be conducted in either water or various oils. In the case of aqueous PISA, addition of a suitable oil followed by emulsification *via* high-shear homogenisation leads to the formation of Pickering emulsions, as illustrated above for the case of vesicles.<sup>298</sup>

Thompson *et al.* reported the first example of polymer-based Pickering emulsifiers prepared *via* PISA.<sup>298</sup> Linear PGMA<sub>45</sub>-PHPMA<sub>200</sub> diblock copolymer vesicles were prepared at 10% w/w solids using a RAFT aqueous dispersion polymerisation formulation. Such linear vesicles did not survive the high-shear homogenisation conditions required for emulsification with *n*-dodecane. Instead, *in situ* dissociation occurred and the resulting oil droplets became stabilised by individual amphiphilic PGMA<sub>45</sub>-PHPMA<sub>200</sub> chains. This problem was confirmed using two characterisation techniques. Firstly, the volume-average oil droplet diameter determined by laser diffraction proved to be essentially independent of the copolymer concentration, whereas a strong concentration dependence is invariably observed for Pickering emulsions (compare red and blue data sets shown in Figure 1.28a).<sup>282, 307</sup> Secondly, TEM studies of the dried oil droplets indicated a smooth, featureless morphology with no evidence for the original vesicles, see Figure 1.28b.

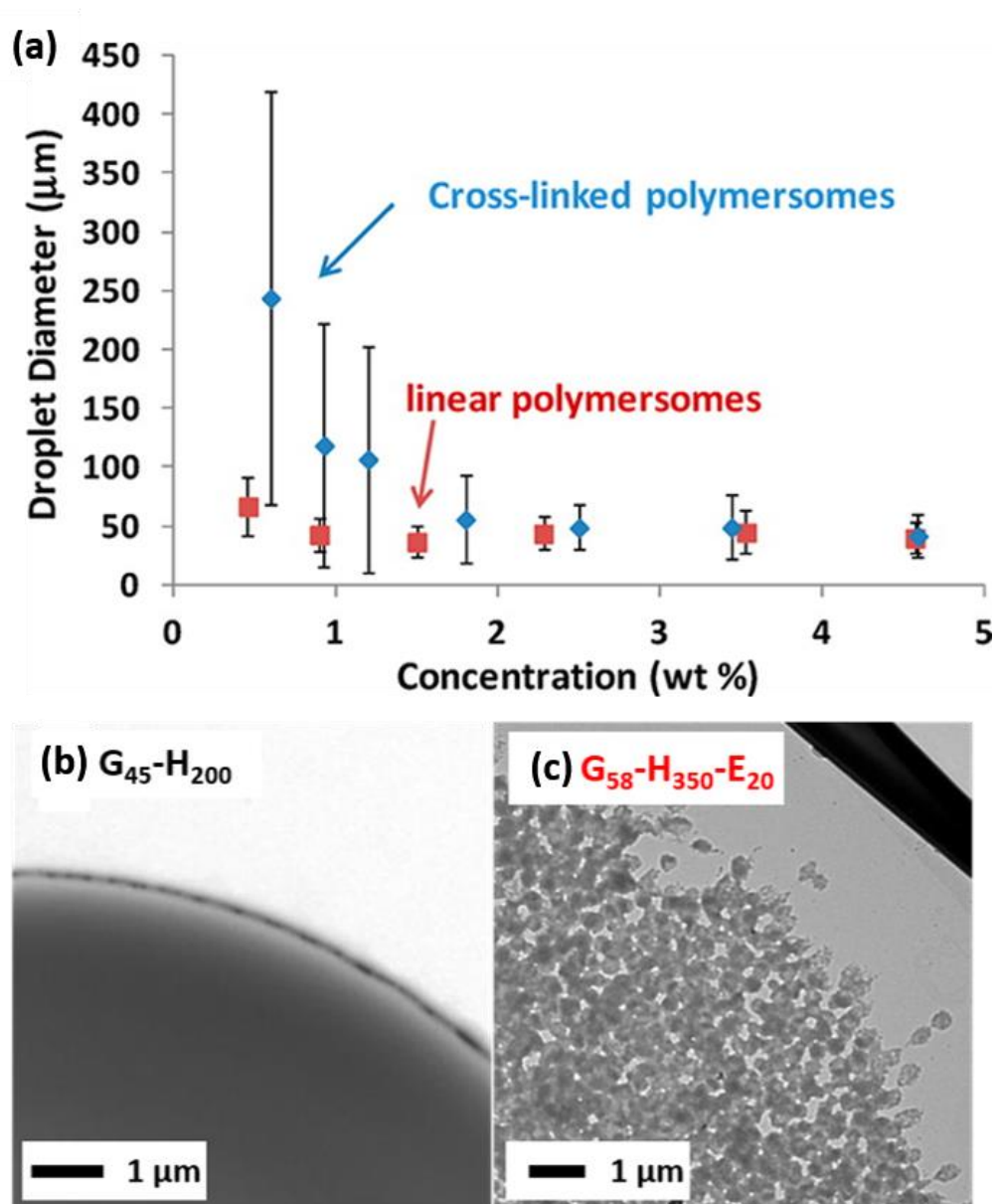


**Figure 1.28.** (a) Volume-average droplet diameter (obtained by laser diffraction) vs. copolymer concentration for both linear PGMA<sub>45</sub>-PHPMA<sub>200</sub> (G<sub>45</sub>-H<sub>200</sub>) and cross-linked PGMA<sub>58</sub>-PHPMA<sub>350</sub>-PEGDMA<sub>20</sub> (G<sub>58</sub>-H<sub>350</sub>-E<sub>20</sub>) vesicles. TEM images recorded for an individual dried cross-linked colloidosome prepared using (b) linear PGMA<sub>45</sub>-PHPMA<sub>200</sub> vesicles and (c) cross-linked PGMA<sub>58</sub>-PHPMA<sub>350</sub>-PEGDMA<sub>20</sub> vesicles.<sup>298</sup>

This study highlighted the importance of verifying the formation of genuine Pickering emulsions when using block copolymer nanoparticles. *In situ* vesicle dissociation was attributed to the weakly hydrophobic nature of the membrane-forming PHPMA block.<sup>308, 309</sup> In view of this problem, ethylene glycol dimethacrylate (EGDMA) was added as a third comonomer to form cross-linked triblock copolymer vesicles, which proved to be stable when subjected to high-shear homogenisation.<sup>298</sup> In this case, the expected upturn in oil droplet diameter was observed as the

vesicle concentration was lowered (see Figure 1.28a). Furthermore, TEM studies revealed the presence of intact vesicles at the oil/water interface (see Figure 1.28c). Such vesicle-stabilised Pickering emulsions were covalently-stabilised by dissolving a tolylene-2,4-diisocyanate-terminated poly(propylene glycol) diisocyanate cross-linker (PPG-TDI) in the oil phase prior to homogenisation, leading to the formation of so-called colloidosomes.<sup>272, 298, 310</sup> Turbidimetry experiments indicated that most of the vesicles were not adsorbed at the oil/water interface and instead remained within the continuous aqueous phase. As the copolymer concentration used to prepare such Pickering emulsions was reduced from 2.5% to 0.6% w/w, the vesicle adsorption efficiency increased from 57 to 78% w/w. The relatively weak affinity of the vesicles for the oil/water interface is presumably related to their aqueous cores, which necessarily lowers the Hamaker constant and hence reduces the enthalpy of adsorption.

Subsequently, Thompson and co-workers reported that linear PGMA-PHPMA spheres and worms also underwent *in situ* dissociation to form soluble copolymer chains during high shear homogenisation.<sup>299</sup> However, laser diffraction studies confirmed that this problem could be circumvented by either covalent stabilisation using EGDMA cross-linker or by addition of a sufficiently hydrophobic third block such as PBzMA. Using the former strategy, PGMA<sub>100</sub>-PHPMA<sub>200</sub>-PEGDMA<sub>20</sub> spheres and PGMA<sub>45</sub>-PHPMA<sub>100</sub>-PEGDMA<sub>10</sub> worms were prepared *via* PISA and their performance as putative Pickering emulsifiers for the stabilisation of *n*-dodecane-in-water emulsions was compared.<sup>299</sup> It is well-established that worms are formed during PISA *via* 1D stochastic fusion of multiple spheres.<sup>83, 109, 311</sup> This is important, because it means that the mean worm thickness is directly related to the dimensions of the initial spheres. Moreover, given that both types of nanoparticles utilised a hydroxyl-functional PGMA block as a steric stabiliser, essentially identical surface wettabilities can be assumed. Thompson and co-workers<sup>299</sup> argued that, for sufficiently anisotropic worms, their specific surface area  $A_w$  can be estimated using the relation  $A_w \sim 2/\rho R$ , where  $\rho$  is the particle density and  $R$  is the mean worm cross-sectional radius. In contrast, prior to their 1D fusion to form worms, the spheres have a specific surface area  $A_s$  given by  $A_s = 3/\rho r$ , where  $r$  is the mean sphere radius and, to a reasonable

approximation,  $r \sim R$ . Therefore, the reduction in specific surface area ( $A_w/A_s$ ) that occurs during the 1D fusion of multiple spheres to form a single worm is only around 33%, whereas the energy of attachment of a sufficiently anisotropic worm ( $L/2R > 20$ ) composed of  $x$  spheres is estimated to be at least  $x$  times higher than that of the individual spherical nanoparticles. In summary, highly anisotropic diblock copolymer worms are expected to adsorb at an oil/water interface much more strongly than the corresponding precursor diblock copolymer spheres, while retaining a relatively high specific surface area.

Thompson *et al.* also directly compared the Pickering emulsifier performance of linear hydrophobic PLMA–PBzMA worms and spheres prepared in *n*-dodecane.<sup>300</sup> For this PISA formulation, the worms are thermoresponsive and can be transformed into spheres when heated to 150 °C owing to surface plasticisation of the core-forming PBzMA chains.<sup>128</sup> Moreover, this morphological transition is effectively irreversible if it is conducted at sufficiently low copolymer concentration (e.g.  $\leq 1.0\%$  w/w).<sup>128</sup> SAXS studies conducted on a worm-stabilised Pickering emulsion indicated that the mean thickness of the worm layer surrounding the water droplets is comparable to the worm cross-sectional diameter. This indicates monolayer coverage rather than multilayer formation. Finally, the thermoresponsive behaviour of PLMA<sub>16</sub>–PBzMA<sub>37</sub> worms was exploited to induce demulsification. Heating the w/o Pickering emulsion up to 95 °C induced a worm-to-sphere transition, with concomitant droplet coalescence being observed owing to copolymer desorption from the oil/water interface.

Chambon and co-workers reported that chain extension of PGMA-PHPMA precursor vesicles using a water-immiscible monomer, such as BzMA, resulted in the formation of framboidal (raspberry-like) triblock copolymer vesicles *via* seeded RAFT aqueous emulsion polymerisation.<sup>155</sup> Subsequently, a series of PGMA<sub>63</sub>-PHPMA<sub>350</sub>-PBzMA<sub>*z*</sub> framboidal vesicles were evaluated by Mable *et al.* as putative Pickering emulsifiers (see Figure 1.29a and b).<sup>149</sup> As expected, the PGMA<sub>63</sub>-PHPMA<sub>350</sub> precursor vesicles did not survive the high shear conditions required to generate Pickering emulsions. In contrast, PGMA<sub>63</sub>-PHPMA<sub>350</sub>-PBzMA<sub>*z*</sub> vesicles led to the formation of genuine Pickering emulsions, as confirmed by laser diffraction and TEM

studies.<sup>149</sup> Moreover, the strongly hydrophobic nature of the third PBzMA block proved to be sufficient to prevent vesicle dissociation. Turbidimetric analysis of the lower aqueous phase after emulsion creaming was again used to assess the Pickering emulsifier performance of these framboidal vesicles. Systematic variation of the DP (or  $z$ ) of the PBzMA block enabled their surface roughness to be tuned, which enabled the adsorption efficiency to be determined as a function of surface roughness (see Figure 1.29c). Increasing the PBzMA DP from 25 to 125 at a constant copolymer concentration led to an increase in adsorption efficiency from 36% to 94%. Furthermore, framboidal vesicles with optimal surface roughness exhibited significantly higher adsorption efficiency than that observed for non-framboidal  $\text{PGMA}_{63}\text{-PHPMA}_{350}\text{-PEGDMA}_{20}$  cross-linked vesicles (67%).<sup>298</sup>

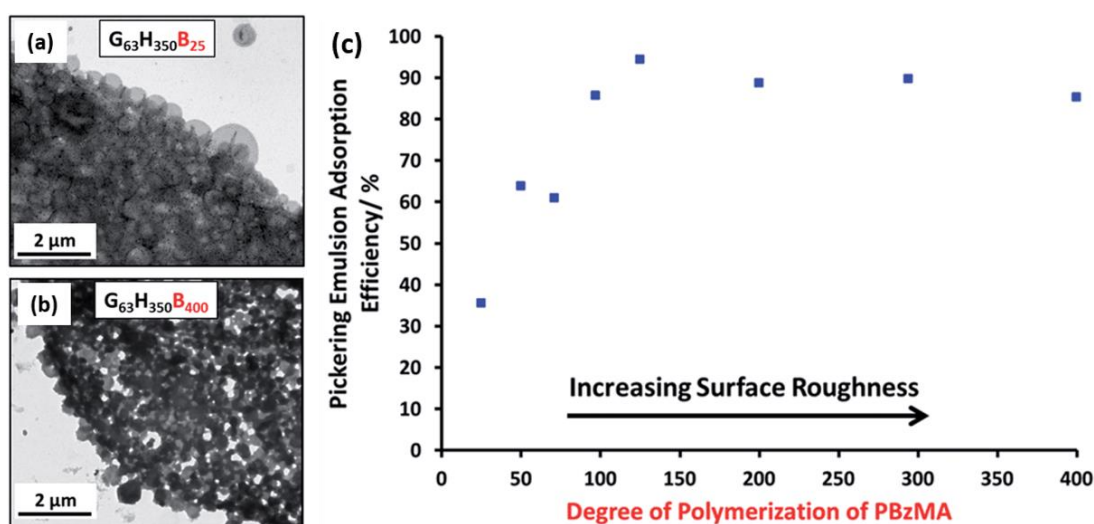


**Figure 1.29.** TEM images obtained for Pickering emulsions of *n*-dodecane stabilised using aqueous dispersions of (a)  $\text{PGMA}_{63}\text{-PHPMA}_{350}\text{-PBzMA}_{25}$  ( $\text{G}_{63}\text{-H}_{350}\text{-B}_{25}$ ) and (b)  $\text{PGMA}_{63}\text{-PHPMA}_{350}\text{-PBzMA}_{400}$  ( $\text{G}_{63}\text{-H}_{350}\text{-B}_{400}$ ) vesicles. (c) Variation of Pickering emulsion adsorption efficiency against PBzMA DP ( $z$ ) for a series of  $\text{PGMA}_{63}\text{-PHPMA}_{350}\text{-PBzMA}_z$  vesicles of increasing surface roughness.

### 1.9.5 Pickering Nanoemulsions

Nanoemulsions comprise stable oil or water droplets for which the mean droplet diameter is below approximately 200 nm.<sup>208, 312</sup> There are various reports of copolymer- or surfactant-stabilised nanoemulsions in the literature.<sup>213</sup> In contrast, there have been remarkably few examples of Pickering nanoemulsions, in which the droplets are solely stabilised by solid particles.<sup>303, 304, 313-315</sup> No doubt one reason for the paucity of such studies is the rule of thumb

requirement that the Pickering emulsifier should be at least 5 - 10 times smaller than the mean droplet diameter. However, the recent development of PISA has enabled the highly convenient synthesis of sterically-stabilised diblock copolymer spheres of 20 - 25 nm diameter directly in the form of concentrated aqueous dispersions.<sup>87, 166</sup> In principle, such nanoparticles should constitute model Pickering emulsifiers for oil-in-water nanoemulsions.

For example, Thompson and co-workers chain-extended a water-soluble PGMA<sub>48</sub> precursor *via* RAFT aqueous emulsion polymerisation of TFEMA to form PGMA<sub>48</sub>-PTFEMA<sub>50</sub> spheres of approximately 25 nm diameter,<sup>303</sup> as previously reported by Akpınar and co-workers.<sup>166</sup> As discussed above, the hydrophobic character of the core-forming block is of critical importance when preparing Pickering emulsions using block copolymer nanoparticles. Selecting a weakly hydrophobic block such as PHPMA usually means that the nanoparticles do not survive the high shear homogenisation conditions required for droplet formation. On the other hand, nanoparticles comprising highly hydrophobic core-forming blocks such as PTFEMA typically remain intact and therefore can act as genuine Pickering emulsifiers. Indeed, this criterion is particularly important for Pickering nanoemulsions because even more energy-intensive conditions are required for their formation.

Initially, a Pickering macroemulsion of approximately 40 µm diameter was prepared *via* high-shear homogenisation of a 7.0% w/w aqueous dispersion of PGMA<sub>48</sub>-PTFEMA<sub>50</sub> spheres with *n*-dodecane at 15 500 rpm. A relatively high copolymer concentration was deliberately employed during this stage because a large excess of non-adsorbed nanoparticles was required to stabilise the nanoemulsion generated in the second stage. Such precursor emulsions were then subjected to high-pressure microfluidisation to generate much finer droplets (see Figure 1.30a). TEM studies confirmed that the nanoparticles adsorbed onto the oil droplets to form Pickering nanoemulsions (see Figure 1.30b). The final size of the oil droplets depended on both the applied pressure and also the number of passes through the microfluidiser, as shown overleaf in Figure 1.30c and d. At least eight passes were required to reach the minimum mean droplet diameter of 220 nm at an applied pressure of 20 000 psi.

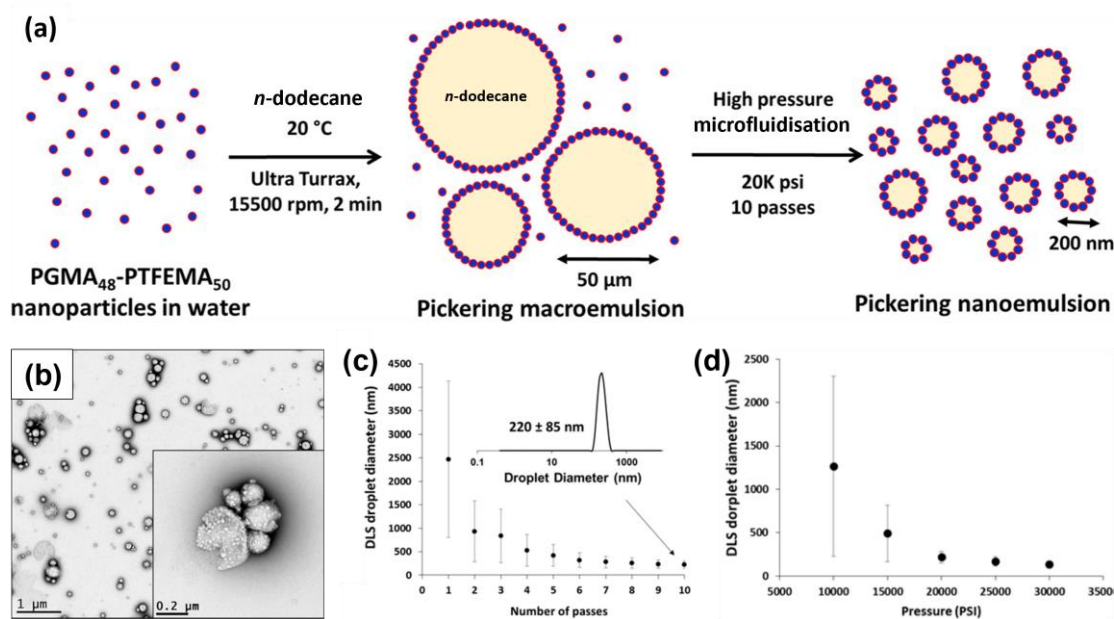


**Figure 1.30.** (a) Schematic representation of the two-step preparation of Pickering nanoemulsions. First, a 7.0% w/w aqueous dispersion of PGMA<sub>48</sub>-PTFEMA<sub>50</sub> nanoparticles are homogenised with *n*-dodecane to form an *n*-dodecane-in-water Pickering macroemulsion of around 50 μm diameter using conventional high-shear homogenisation at 15,500 rpm for 2 min at 20 °C. This relatively coarse precursor emulsion is then refined *via* ten passes through a commercial LV1 microfluidiser to obtain the final Pickering nanoemulsions of approximately 200 nm diameter that are used in this study. (b) TEM image of the PGMA<sub>48</sub>-PTFEMA<sub>50</sub> nanoparticles. (c) Reduction of the DLS droplet diameter with increasing number of passes. (d) Reduction of the DLS droplet diameter with increasing applied pressure.

Subtracting the thickness of the adsorbed monolayer of 25 nm PGMA<sub>48</sub>-PTFEMA<sub>50</sub> spheres indicates a mean oil droplet diameter of less than 200 nm, which lies within the range required for a genuine nanoemulsion.<sup>208</sup> Moreover, such nanoparticles enabled the formation of high internal phase nanoemulsions at oil volume fractions of up to 0.80. However, TEM analysis of dried nanoemulsion droplets prepared at 30 000 psi revealed no evidence of the original nanoparticles. At this higher applied pressure, nanoparticle dissociation occurred and the molecularly-dissolved PGMA<sub>48</sub>-PTFEMA<sub>50</sub> copolymer chains simply acted as an amphiphilic polymeric surfactant. This problem could be circumvented by incorporating EGDMA as a third block: the resulting covalently-stabilised PGMA<sub>48</sub>-PTFEMA<sub>45</sub>-PEGDMA<sub>5</sub> nanoparticles remained intact even at an applied pressure of 30 000 psi, thus ensuring the formation of genuine Pickering emulsions under such conditions.

In a follow-up study, Thompson *et al.* examined the effect of varying the oil type on the long-term stability of Pickering nanoemulsions prepared using the same PGMA<sub>48</sub>-PTFEMA<sub>50</sub> nanoparticles.<sup>304</sup> Thus a series of nanoemulsions prepared using four *n*-alkanes were prepared using an LV1 microfluidiser and their relative long-term stabilities were assessed using analytical centrifugation.<sup>31</sup> More specifically, a LUMiSizer instrument was employed to size the ageing droplets over a six-week period, see Figure 1.31. Significant broadening of the droplet size distribution was observed in each case, although the change in the mean droplet diameter was minimal. For the more stable nanoemulsions prepared using *n*-tetradecane or *n*-dodecane, over 90% of the droplets remained below 1  $\mu\text{m}$  diameter after six weeks. Conversely, nanoemulsions prepared using *n*-octane proved to be relatively unstable, which correlates with the higher aqueous solubility of this oil.

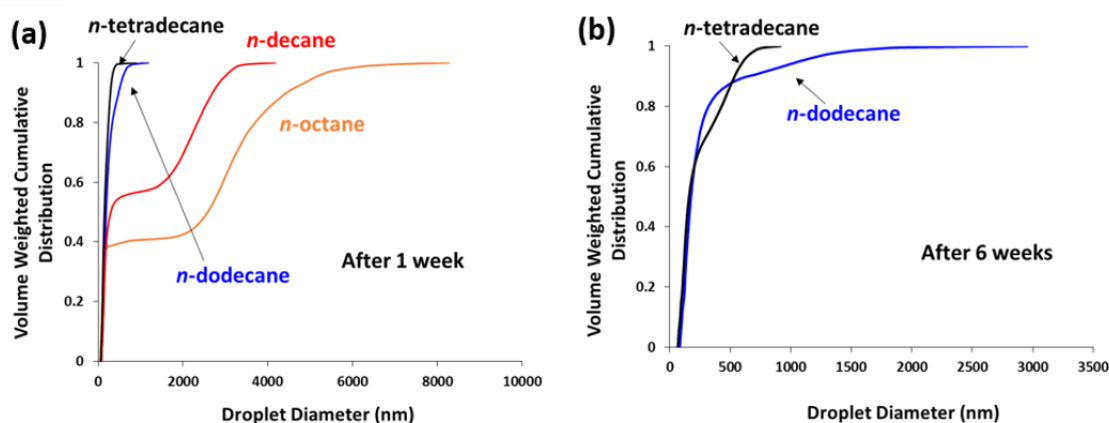


**Figure 1.31.** Volume-weighted cumulative particle size distributions determined by analytical centrifugation (LUMiSizer instrument) for a series of four *n*-alkane-in-water Pickering nanoemulsions: (a) after ageing for one week at 20 °C and (b) after ageing for six weeks at 20 °C. Significant evaporation of the more volatile *n*-octane and *n*-decane oils occurred within one week so no further analysis was possible for these two nanoemulsions.

## 1.10 Thesis Outlook

The primary aim of this Thesis is to expand our understanding of the formation, structure and long-term stability of Pickering emulsions stabilised by various types of block copolymer nanoparticles. The first two Chapters build on the prior work by Thompson *et al.*<sup>303, 304</sup> by using relatively small block copolymer nanoparticles to stabilise either o/w or w/o Pickering

nanoemulsions. The following two Chapters explore the synthesis and Pickering performance of block copolymer nanoparticles with PHBMA as the core-forming block.

The main aim in Chapter 2 is to examine how the presence of charged end-groups on the steric stabiliser chains of diblock copolymer nanoparticles affects the formation and long-term stability of o/w Pickering nanoemulsions. RAFT aqueous emulsion polymerisation of TFEMA is used to prepare PGMA<sub>48</sub>-PTFEMA<sub>50</sub> spheres of approximately 25 nm diameter bearing carboxylic acid, tertiary amine or neutral end-groups. The adsorption efficiency of nanoparticles at the oil/water interface is assessed by UV GPC. The long-term stability of the Pickering nanoemulsions stabilised by nanoparticles bearing either charged or end-groups is evaluated using analytical centrifugation.

The main aim of Chapter 3 is to prepare the first example of a w/o Pickering nanoemulsion stabilised by diblock copolymer nanoparticles. RAFT dispersion polymerisation of TFEMA in *n*-dodecane is used to prepare relatively small hydrophobic PSMA-PTFEMA spheres, as reported by Cornel *et al.*<sup>205</sup> Addition of salt to the aqueous phase prior to emulsification is demonstrated to be important for the formation of Pickering nanoemulsions. Finally, the effect of added salt on the long-term stability of the nanoemulsions is assessed using analytical centrifugation.

Chapter 4 explores the RAFT aqueous emulsion polymerisation of HBMA using a relatively short non-ionic PGMA<sub>41</sub> precursor as a steric stabiliser. This formulation is only the third example of a water-immiscible monomer with a relatively high aqueous solubility that can provide convenient access to worms and vesicles, as well as spheres. A pseudo-phase diagram is constructed by systematically varying the target PHBMA DP and the copolymer concentration. TEM studies conducted on aliquots extracted during the synthesis of PGMA-PHBMA vesicles reveal intermediate morphologies that are similar to those reported during the preparation of PGMA-PHPMA vesicles *via* RAFT aqueous dispersion polymerisation. Linear PGMA-PHBMA

vesicles are evaluated as putative Pickering emulsifiers for the stabilisation of *n*-dodecane-in-water emulsions.

In Chapter 5, the thermoresponsive behaviour of PEG<sub>45</sub>-PHBMA<sub>20</sub> diblock copolymer nano-objects in aqueous solution is investigated using TEM and variable temperature <sup>1</sup>H NMR spectroscopy, DLS, SAXS and rheology.

### 1.11 References

1. H. Staudinger, *Ber Dtsch Chem Ges*, 1928, **61**, 2427-2431.
2. G. Odian, *Principles of Polymerization*, John Wiley & Sons, Ltd., New Jersey, 2004.
3. P. C. Hiemenz and T. P. Lodge, *Polymer Chemistry*, CRC Press, New York, 2nd edn., 2007.
4. P. J. Flory, *Principles of Polymer Chemistry*, Cornell University Press, Ithaca, 1953.
5. G. Moad and D. H. Solomon, *The Chemistry of Free Radical Polymerization*, Elsevier Science Ltd, Oxford, Second edn., 2005.
6. A. A. Gridnev and S. D. Ittel, *Macromolecules*, 1996, **29**, 5864-5874.
7. W. A. Braunecker and K. Matyjaszewski, *Prog. Polym. Sci.*, 2007, **32**, 93-146.
8. M. Szwarc, *Nature*, 1956, **178**, 1168-1169.
9. M. Szwarc, M. Levy and R. Milkovich, *J. Am. Chem. Soc.*, 1956, **78**, 2656-2657.
10. R. Waack, A. Rembaum, J. D. Coombes and M. Szwarc, *J. Am. Chem. Soc.*, 1957, **79**, 2026-2027.
11. N. Hadjichristidis, M. Pitsikalis, S. Pispas and H. Iatrou, *Chem. Rev.*, 2001, **101**, 3747-3792.
12. J. G. Zilliox, J. E. L. Roovers and S. Bywater, *Macromolecules*, 1975, **8**, 573-578.
13. N. Hadjichristidis, H. Iatrou, M. Pitsikalis and J. Mays, *Prog. Polym. Sci.*, 2006, **31**, 1068-1132.
14. K. Matyjaszewski and J. Spanswick, *Mater. Today*, 2005, **8**, 26-33.
15. C. J. Hawker, A. W. Bosman and E. Harth, *Chem. Rev.*, 2001, **101**, 3661-3688.
16. G. Moad, E. Rizzardo and S. H. Thang, *Acc. Chem. Res.*, 2008, **41**, 1133-1142.
17. J. Nicolas, Y. Guillaneuf, C. Lefay, D. Bertin, D. Gigmes and B. Charleux, *Prog. Polym. Sci.*, 2013, **38**, 63-235.
18. T. E. Patten and K. Matyjaszewski, *Adv. Mater.*, 1998, **10**, 901-915.
19. K. Matyjaszewski and J. H. Xia, *Chem. Rev.*, 2001, **101**, 2921-2990.
20. J. S. Wang and K. Matyjaszewski, *J. Am. Chem. Soc.*, 1995, **117**, 5614-5615.
21. K. Matyjaszewski, *Macromolecules*, 2012, **45**, 4015-4039.
22. J. Chiefari, Y. K. Chong, F. Ercole, J. Krstina, J. Jeffery, T. P. T. Le, R. T. A. Mayadunne, G. F. Meijs, C. L. Moad, G. Moad, E. Rizzardo and S. H. Thang, *Macromolecules*, 1998, **31**, 5559-5562.

23. G. Moad, E. Rizzardo and S. H. Thang, *Aust. J. Chem.*, 2005, **58**, 379-410.
24. G. Moad, E. Rizzardo and S. H. Thang, *Aust. J. Chem.*, 2009, **62**, 1402-1472.
25. G. Moad, E. Rizzardo and S. H. Thang, *Aust. J. Chem.*, 2012, **65**, 985-1076.
26. G. Moad, E. Rizzardo and S. H. Thang, *Aust. J. Chem.*, 2006, **59**, 669-692.
27. S. Perrier, *Macromolecules*, 2017, **50**, 7433-7447.
28. D. J. Keddie, G. Moad, E. Rizzardo and S. H. Thang, *Macromolecules*, 2012, **45**, 5321-5342.
29. G. Moad, J. Chiefari, Y. K. Chong, J. Krstina, R. T. A. Mayadunne, A. Postma, E. Rizzardo and S. H. Thang, *Polym. Int.*, 2000, **49**, 993-1001.
30. S. H. Thang, Y. K. Chong, R. T. A. Mayadunne, G. Moad and E. Rizzardo, *Tetrahedron Lett.*, 1999, **40**, 2435-2438.
31. A. Goto, K. Sato, Y. Tsujii, T. Fukuda, G. Moad, E. Rizzardo and S. H. Thang, *Macromolecules*, 2001, **34**, 402-408.
32. Y. K. Chong, T. P. T. Le, G. Moad, E. Rizzardo and S. H. Thang, *Macromolecules*, 1999, **32**, 2071-2074.
33. Y. K. Chong, G. Moad, E. Rizzardo and S. H. Thang, *Macromolecules*, 2007, **40**, 4446-4455.
34. S. Perrier, P. Takolpuckdee and C. A. Mars, *Macromolecules*, 2005, **38**, 2033-2036.
35. H. Willcock and R. K. O'Reilly, *Polym. Chem.*, 2010, **1**, 149-157.
36. P. A. Lovell, *Emulsion Polymerization and Emulsion Polymers*, Wiley, Chichester, 1997.
37. W. Qun, F. Shoukuan and Y. Tongyin, *Prog. Polym. Sci.*, 1994, **19**, 703-753.
38. P. A. Lovell and F. J. Schork, *Biomacromolecules*, 2020, **21**, 4396-4441.
39. C. S. Chern, *Prog. Polym. Sci.*, 2006, **31**, 443-486.
40. W. D. Harkins, *J. Chem. Phys.*, 1945, **13**, 381-382.
41. R. G. Gilbert, *Emulsion polymerization: a mechanistic approach*, Academic Press, London, 1995.
42. A. Czajka and S. P. Armes, *J. Am. Chem. Soc.*, 2021, **143**, 1474-1484.
43. M. J. Ballard, D. H. Napper and R. G. Gilbert, *Journal of Polymer Science: Polymer Chemistry Edition*, 1984, **22**, 3225-3253.
44. F. Stoffelbach, B. Belardi, J. M. R. C. A. Santos, L. Tessier, K. Matyjaszewski and B. Charleux, *Macromolecules*, 2007, **40**, 8813-8816.
45. S. Kawaguchi and K. Ito, in *Polymer Particles*, ed. M. Okubo, Springer, Berlin, 2005, pp. 299-328.
46. A. M. I. Ali, P. Pareek, L. Sewell, A. Schmid, S. Fujii, S. P. Armes and I. M. Shirley, *Soft Matter*, 2007, **3**, 1003-1013.
47. R. J. R. Cairns, R. H. Ottewill, D. W. J. Osmond and I. Wagstaff, *J. Colloid Interface Sci.*, 1976, **54**, 45-51.
48. F. M. Winnik and A. J. Paine, *Langmuir*, 1989, **5**, 903-910.
49. S. Kawaguchi and K. Ito, *Dispersion Polymerization*, Springer, Berlin, 2005.
50. J. N. Israelachvili, D. J. Mitchell and B. W. Ninham, *J. Chem. Soc., Trans.*, 1976, **72**, 1525-1568.

51. J. N. Israelachvili, *Intermolecular and Surface Forces*, Academic Press, San Diego, Third edn., 2011.
52. L. Zhang and A. Eisenberg, *Science*, 1995, **268**, 1728-1731.
53. L. Zhang and A. Eisenberg, *J. Am. Chem. Soc.*, 1996, **118**, 3168-3181.
54. L. Zhang, K. Yu and A. Eisenberg, *Science*, 1996, **272**, 1777-1779.
55. L. Zhang and A. Eisenberg, *Polym. Adv. Technol.*, 1998, **9**, 677-699.
56. K. Yu and A. Eisenberg, *Macromolecules*, 1996, **29**, 6359-6361.
57. K. Yu and A. Eisenberg, *Macromolecules*, 1998, **31**, 3509-3518.
58. Y. Mai and A. Eisenberg, *Chem. Soc. Rev.*, 2012, **41**, 5969-5985.
59. F. S. Bates and G. H. Fredrickson, *Physics Today*, 1999, **52**, 32-38.
60. P. J. Flory, *J. Chem. Phys.*, 1942, **10**, 51-61.
61. M. L. Huggins, *J. Am. Chem. Soc.*, 1942, **64**, 1712-1719.
62. M. W. Matsen and F. S. Bates, *Macromolecules*, 1996, **29**, 1091-1098.
63. A. K. Khandpur, S. Foerster, F. S. Bates, I. W. Hamley, A. J. Ryan, W. Bras, K. Almdal and K. Mortensen, *Macromolecules*, 1995, **28**, 8796-8806.
64. M. Antonietti and S. Förster, *Adv. Mater.*, 2003, **15**, 1323-1333.
65. K.-V. Peinemann, V. Abetz and P. F. W. Simon, *Nat. Mater.*, 2007, **6**, 992-996.
66. B. M. Discher, Y.-Y. Won, D. S. Ege, J. C.-M. Lee, F. S. Bates, D. E. Discher and D. A. Hammer, *Science*, 1999, **284**, 1143-1146.
67. M. K. Kocik, O. O. Mykhaylyk and S. P. Armes, *Soft Matter*, 2014, **10**, 3984-3992.
68. J. Rodríguez-Hernández and S. Lecommandoux, *J. Am. Chem. Soc.*, 2005, **127**, 2026-2027.
69. V. Bütün, S. P. Armes and N. C. Billingham, *Polymer*, 2001, **42**, 5993-6008.
70. M. Arotçaréna, B. Heise, S. Ishaya and A. Laschewsky, *J. Am. Chem. Soc.*, 2002, **124**, 3787-3793.
71. P. P. Ghoroghchian, P. R. Frail, K. Susumu, D. Blessington, A. K. Brannan, F. S. Bates, B. Chance, D. A. Hammer and M. J. Therien, *Proc. Natl. Acad. Sci. U.S.A.*, 2005, **102**, 2922.
72. D. R. Arifin and A. F. Palmer, *Biomacromolecules*, 2005, **6**, 2172-2181.
73. S. L. Canning, G. N. Smith and S. P. Armes, *Macromolecules*, 2016, **49**, 1985-2001.
74. A. Mühlebach, S. G. Gaynor and K. Matyjaszewski, *Macromolecules*, 1998, **31**, 6046-6052.
75. G. Delaittre, J. Nicolas, C. Lefay, M. Save and B. Charleux, *Chem. Commun.*, 2005, 614-616.
76. C. J. Ferguson, R. J. Hughes, B. T. T. Pham, B. S. Hawkett, R. G. Gilbert, A. K. Serelis and C. H. Such, *Macromolecules*, 2002, **35**, 9243-9245.
77. N. J. Warren and S. P. Armes, *J. Am. Chem. Soc.*, 2014, **136**, 10174-10185.
78. M. J. Derry, L. A. Fielding and S. P. Armes, *Prog. Polym. Sci.*, 2016, **52**, 1-18.
79. N. J. W. Penfold, J. Yeow, C. Boyer and S. P. Armes, *ACS Macro Lett.*, 2019, **8**, 1029-1054.
80. F. D'Agosto, J. Rieger and M. Lansalot, *Angew. Chem. Int. Ed.*, 2020, **59**, 8368-8392.

81. J. Rieger, *Macromol. Rapid Commun.*, 2015, **36**, 1458-1471.
82. B. Charleux, G. Delaittre, J. Rieger and F. D'Agosto, *Macromolecules*, 2012, **45**, 6753-6765.
83. A. Blanz, A. J. Ryan and S. P. Armes, *Macromolecules*, 2012, **45**, 5099-5107.
84. D. Li, M. Huo, L. Liu, M. Zeng, X. Chen, X. S. Wang and J. Y. Yuan, *Macromol. Rapid Commun.*, 2019, **40**, 5.
85. S. L. Canning, V. J. Cunningham, L. P. D. Ratcliffe and S. P. Armes, *Polym. Chem.*, 2017, **8**, 4811-4821.
86. M. J. Derry, L. A. Fielding and S. P. Armes, *Polym. Chem.*, 2015, **6**, 3054-3062.
87. V. J. Cunningham, A. M. Alswieleh, K. L. Thompson, M. Williams, G. J. Leggett, S. P. Armes and O. M. Musa, *Macromolecules*, 2014, **47**, 5613-5623.
88. S. W. Prescott, M. J. Ballard, E. Rizzardo and R. G. Gilbert, *Aust. J. Chem.*, 2002, **55**, 415-424.
89. S. W. Prescott, M. J. Ballard, E. Rizzardo and R. G. Gilbert, *Macromol. Theory Simul.*, 2006, **15**, 70-86.
90. C. J. Ferguson, R. J. Hughes, D. Nguyen, B. T. T. Pham, R. G. Gilbert, A. K. Serelis, C. H. Such and B. S. Hawkett, *Macromolecules*, 2005, **38**, 2191-2204.
91. N. P. Truong, M. V. Dussert, M. R. Whittaker, J. F. Quinn and T. P. Davis, *Polym. Chem.*, 2015, **6**, 3865-3874.
92. D. E. Ganeva, E. Sprong, H. de Bruyn, G. G. Warr, C. H. Such and B. S. Hawkett, *Macromolecules*, 2007, **40**, 6181-6189.
93. I. Chaduc, A. Crepet, O. Boyron, B. Charleux, F. D'Agosto and M. Lansalot, *Macromolecules*, 2013, **46**, 6013-6023.
94. I. Chaduc, W. Zhang, J. Rieger, M. Lansalot, F. D'Agosto and B. Charleux, *Macromol. Rapid Commun.*, 2011, **32**, 1270-1276.
95. I. Chaduc, M. Girod, R. Antoine, B. Charleux, F. D'Agosto and M. Lansalot, *Macromolecules*, 2012, **45**, 5881-5893.
96. C. K. Poon, O. Tang, X.-M. Chen, B. T. T. Pham, G. Gody, C. A. Pollock, B. S. Hawkett and S. Perrier, *Biomacromolecules*, 2016, **17**, 965-973.
97. J. Rieger, F. Stoffelbach, C. Bui, D. Alaimo, C. Jérôme and B. Charleux, *Macromolecules*, 2008, **41**, 4065-4068.
98. J. Rieger, W. Zhang, F. Stoffelbach and B. Charleux, *Macromolecules*, 2010, **43**, 6302-6310.
99. J. Rieger, G. Osterwinter, C. Bui, F. Stoffelbach and B. Charleux, *Macromolecules*, 2009, **42**, 5518-5525.
100. S. Boissé, J. Rieger, G. Pembouong, P. Beaunier and B. Charleux, *J. Polym. Sci., Part A: Polym. Chem.*, 2011, **49**, 3346-3354.
101. W. Zhang, F. D'Agosto, O. Boyron, J. Rieger and B. Charleux, *Macromolecules*, 2011, **44**, 7584-7593.
102. C. Gazon, J. Rieger, N. Sanson and B. Charleux, *Soft Matter*, 2011, **7**, 3482-3490.
103. W. Zhang, F. D'Agosto, O. Boyron, J. Rieger and B. Charleux, *Macromolecules*, 2012, **45**, 4075-4084.
104. W. Zhang, F. D'Agosto, P.-Y. Dugas, J. Rieger and B. Charleux, *Polymer*, 2013, **54**, 2011-2019.

105. I. Canton, N. J. Warren, A. Chahal, K. Amps, A. Wood, R. Weightman, E. Wang, H. Moore and S. P. Armes, *ACS Cent. Sci.*, 2016, **2**, 65-74.
106. N. J. W. Penfold, Y. Ning, P. Verstraete, J. Smets and S. P. Armes, *Chem. Sci.*, 2016, **7**, 6894-6904.
107. A. Blanazs, S. P. Armes and A. J. Ryan, *Macromol. Rapid Commun.*, 2009, **30**, 267-277.
108. N. J. Warren, O. O. Mykhaylyk, D. Mahmood, A. J. Ryan and S. P. Armes, *J. Am. Chem. Soc.*, 2014, **136**, 1023-1033.
109. A. Blanazs, J. Madsen, G. Battaglia, A. J. Ryan and S. P. Armes, *J. Am. Chem. Soc.*, 2011, **133**, 16581-16587.
110. R. Verber, A. Blanazs and S. P. Armes, *Soft Matter*, 2012, **8**, 9915-9922.
111. Y. Jiang, N. Xu, J. Han, Q. Yu, L. Guo, P. Gao, X. Lu and Y. Cai, *Polym. Chem.*, 2015, **6**, 4955-4965.
112. W. Shen, Y. Chang, G. Liu, H. Wang, A. Cao and Z. An, *Macromolecules*, 2011, **44**, 2524-2530.
113. M. Semsarilar, E. R. Jones, A. Blanazs and S. P. Armes, *Adv. Mater.*, 2012, **24**, 3378-3382.
114. C. Gonzato, M. Semsarilar, E. R. Jones, F. Li, G. J. P. Krooshof, P. Wyman, O. O. Mykhaylyk, R. Tuinier and S. P. Armes, *J. Am. Chem. Soc.*, 2014, **136**, 11100-11106.
115. E. R. Jones, M. Semsarilar, A. Blanazs and S. P. Armes, *Macromolecules*, 2012, **45**, 5091-5098.
116. Y. Pei, N. C. Dharsana, J. A. van Hensbergen, R. P. Burford, P. J. Roth and A. B. Lowe, *Soft Matter*, 2014, **10**, 5787-5796.
117. E. R. Jones, M. Semsarilar, P. Wyman, M. Boerakker and S. P. Armes, *Polym. Chem.*, 2016, **7**, 851-859.
118. R. R. Gibson, E. J. Cornel, O. M. Musa, A. Fernyhough and S. P. Armes, *Polym. Chem.*, 2020, **11**, 1785-1796.
119. Z. Ding, C. Gao, S. Wang, H. Liu and W. Zhang, *Polym. Chem.*, 2015, **6**, 8003-8011.
120. D. Zehm, L. P. D. Ratcliffe and S. P. Armes, *Macromolecules*, 2013, **46**, 128-139.
121. A. B. Lowe, *Polymer*, 2016, **106**, 161-181.
122. W.-M. Wan, X.-L. Sun and C.-Y. Pan, *Macromol. Rapid Commun.*, 2010, **31**, 399-404.
123. C.-Q. Huang and C.-Y. Pan, *Polymer*, 2010, **51**, 5115-5121.
124. C.-Q. Huang, Y. Wang, C.-Y. Hong and C.-Y. Pan, *Macromol. Rapid Commun.*, 2011, **32**, 1174-1179.
125. W.-D. He, X.-L. Sun, W.-M. Wan and C.-Y. Pan, *Macromolecules*, 2011, **44**, 3358-3365.
126. B. Karagoz, C. Boyer and T. P. Davis, *Macromol. Rapid Commun.*, 2014, **35**, 417-421.
127. L. A. Fielding, M. J. Derry, V. Ladmiral, J. Rosselgong, A. M. Rodrigues, L. P. D. Ratcliffe, S. Sugihara and S. P. Armes, *Chem. Sci.*, 2013, **4**, 2081-2087.
128. L. A. Fielding, J. A. Lane, M. J. Derry, O. O. Mykhaylyk and S. P. Armes, *J. Am. Chem. Soc.*, 2014, **136**, 5790-5798.
129. L. Houillot, C. Bui, M. Save, B. Charleux, C. Farcet, C. Moire, J.-A. Raust and I. Rodriguez, *Macromolecules*, 2007, **40**, 6500-6509.

130. Y. Pei, L. Thurairajah, O. R. Sugita and A. B. Lowe, *Macromolecules*, 2015, **48**, 236-244.
131. A. P. Lopez-Oliva, N. J. Warren, A. Rajkumar, O. O. Mykhaylyk, M. J. Derry, K. E. B. Doncom, M. J. Rymaruk and S. P. Armes, *Macromolecules*, 2015, **48**, 3547-3555.
132. G. N. Smith, S. L. Canning, M. J. Derry, E. R. Jones, T. J. Neal and A. J. Smith, *Macromolecules*, 2020, **53**, 3148-3156.
133. Q. Zhang and S. Zhu, *ACS Macro Lett.*, 2015, **4**, 755-758.
134. M. J. Rymaruk, S. J. Hunter, C. T. O'Brien, S. L. Brown, C. N. Williams and S. P. Armes, *Macromolecules*, 2019, **52**, 2822-2832.
135. M. J. Rymaruk, C. T. O'Brien, S. L. Brown, C. N. Williams and S. P. Armes, *Macromolecules*, 2020, **53**, 1785-1794.
136. T. Hasell, K. J. Thurecht, R. D. W. Jones, P. D. Brown and S. M. Howdle, *Chem. Commun.*, 2007, 3933-3935.
137. M. Zong, K. J. Thurecht and S. M. Howdle, *Chem. Commun.*, 2008, 5942-5944.
138. S. Dong, W. Zhao, F. P. Lucien, S. Perrier and P. B. Zetterlund, *Polym. Chem.*, 2015, **6**, 2249-2254.
139. A. Xu, Q. Lu, Z. Huo, J. Ma, B. Geng, U. Azhar, L. Zhang and S. Zhang, *RSC Advances*, 2017, **7**, 51612-51620.
140. S. J. Byard, M. Williams, B. E. McKenzie, A. Blanazs and S. P. Armes, *Macromolecules*, 2017, **50**, 1482-1493.
141. N. J. W. Penfold, J. R. Whatley and S. P. Armes, *Macromolecules*, 2019, **52**, 1653-1662.
142. S. J. Byard, C. T. O'Brien, M. J. Derry, M. Williams, O. O. Mykhaylyk, A. Blanazs and S. P. Armes, *Chem. Sci.*, 2020, **11**, 396-402.
143. B. Zhang, X. Lv, A. Zhu, J. Zheng, Y. Yang and Z. An, *Macromolecules*, 2018, **51**, 2776-2784.
144. B. Zhang, X. Lv and Z. An, *ACS Macro Lett.*, 2017, **6**, 224-228.
145. L. D. Blackman, K. E. B. Doncom, M. I. Gibson and R. K. O'Reilly, *Polym. Chem.*, 2017, **8**, 2860-2871.
146. L. Qiu, H. Zhang, B. Wang, Y. Zhan, C. Xing and C.-Y. Pan, *ACS Appl. Mater. Interfaces*, 2020, **12**, 1348-1358.
147. S. Varlas, J. C. Foster, P. G. Georgiou, R. Keogh, J. T. Husband, D. S. Williams and R. K. O'Reilly, *Nanoscale*, 2019, **11**, 12643-12654.
148. H. Yao, Y. Ning, C. P. Jesson, J. He, R. Deng, W. Tian and S. P. Armes, *ACS Macro Lett.*, 2017, **6**, 1379-1385.
149. C. J. Mable, N. J. Warren, K. L. Thompson, O. O. Mykhaylyk and S. P. Armes, *Chem. Sci.*, 2015, **6**, 6179-6188.
150. C. J. Mable, L. A. Fielding, M. J. Derry, O. O. Mykhaylyk, P. Chambon and S. P. Armes, *Chem. Sci.*, 2018, **9**, 1454-1463.
151. Q. Xu, Y. Zhang, X. Li, J. He, J. Tan and L. Zhang, *Polym. Chem.*, 2018, **9**, 4908-4916.
152. X. Wang, J. Zhou, X. Lv, B. Zhang and Z. An, *Macromolecules*, 2017, **50**, 7222-7232.
153. P. Yang, L. P. D. Ratcliffe and S. P. Armes, *Macromolecules*, 2013, **46**, 8545-8556.
154. P. Yang, O. O. Mykhaylyk, E. R. Jones and S. P. Armes, *Macromolecules*, 2016, **49**, 6731-6742.

155. P. Chambon, A. Blanazs, G. Battaglia and S. P. Armes, *Macromolecules*, 2012, **45**, 5081-5090.
156. M. F. Cunningham, *Prog. Polym. Sci.*, 2008, **33**, 365-398.
157. I. Uzulina, S. Kanagasabapathy and J. Claverie, *Macromol. Symp.*, 2000, **150**, 33-38.
158. M. J. Monteiro, M. Hodgson and H. De Brouwer, *J. Polym. Sci., Part A: Polym. Chem.*, 2000, **38**, 3864-3874.
159. D. Charmot, P. Corpart, H. Adam, S. Z. Zard, T. Biadatti and G. Bouhadir, *Macromol. Symp.*, 2000, **150**, 23-32.
160. S. W. Prescott, M. J. Ballard, E. Rizzardo and R. G. Gilbert, *Macromolecules*, 2002, **35**, 5417-5425.
161. J. Zhou, H. Yao and J. Ma, *Polym. Chem.*, 2018, **9**, 2532-2561.
162. S. Boissé, J. Rieger, K. Belal, A. Di-Cicco, P. Beaunier, M.-H. Li and B. Charleux, *Chem. Commun.*, 2010, **46**, 1950-1952.
163. M. Maggy, S. Maud and C. Bernadette, *Macromol. Rapid Commun.*, 2006, **27**, 399-404.
164. X. Zhang, J. Rieger and B. Charleux, *Polym. Chem.*, 2012, **3**, 1502-1509.
165. L. P. D. Ratcliffe, A. Blanazs, C. N. Williams, S. L. Brown and S. P. Armes, *Polym. Chem.*, 2014, **5**, 3643-3655.
166. B. Akpinar, L. A. Fielding, V. J. Cunningham, Y. Ning, O. O. Mykhaylyk, P. W. Fowler and S. P. Armes, *Macromolecules*, 2016, **49**, 5160-5171.
167. F. L. Hatton, J. R. Lovett and S. P. Armes, *Polym. Chem.*, 2017, **8**, 4856-4868.
168. C. György, J. R. Lovett, N. J. W. Penfold and S. P. Armes, *Macromol. Rapid Commun.*, 2019, **40**, 1800289.
169. C. P. Jesson, V. J. Cunningham, M. J. Smallridge and S. P. Armes, *Macromolecules*, 2018, **51**, 3221-3232.
170. O. J. Deane, O. M. Musa, A. Fernyhough and S. P. Armes, *Macromolecules*, 2020, **53**, 1422-1434.
171. A. A. Cockram, R. D. Bradley, S. A. Lynch, P. C. D. Fleming, N. S. J. Williams, M. W. Murray, S. N. Emmett and S. P. Armes, *React. Chem. Eng.*, 2018, **3**, 645-657.
172. J. Lesage de la Haye, X. Zhang, I. Chaduc, F. Brunel, M. Lansalot and F. D'Agosto, *Angew. Chem. Int. Ed.*, 2016, **55**, 3739-3743.
173. F. L. Hatton, A. M. Park, Y. Zhang, G. D. Fuchs, C. K. Ober and S. P. Armes, *Polym. Chem.*, 2019, **10**, 194-200.
174. B. T. T. Pham, D. Nguyen, V. T. Huynh, E. H. Pan, B. Shirodkar-Robinson, M. Carey, A. K. Serelis, G. G. Warr, T. Davey, C. H. Such and B. S. Hawkett, *Langmuir*, 2018, **34**, 4255-4263.
175. D. Nguyen, V. Huynh, N. Pham, B. Pham, A. Serelis, T. Davey, C. Such and B. Hawkett, *Macromol. Rapid Commun.*, 2019, **40**, 1800402.
176. J. Tan, X. Dai, Y. Zhang, L. Yu, H. Sun and L. Zhang, *ACS Macro Lett.*, 2019, **8**, 205-212.
177. A. A. Cockram, T. J. Neal, M. J. Derry, O. O. Mykhaylyk, N. S. J. Williams, M. W. Murray, S. N. Emmett and S. P. Armes, *Macromolecules*, 2017, **50**, 796-802.
178. E. E. Brotherton, F. L. Hatton, A. A. Cockram, M. J. Derry, A. Czajka, E. J. Cornel, P. D. Topham, O. O. Mykhaylyk and S. P. Armes, *J. Am. Chem. Soc.*, 2019, **141**, 13664-13675.

179. J. C. Foster, S. Varlas, B. Couturaud, J. R. Jones, R. Keogh, R. T. Mathers and R. K. O'Reilly, *Angew. Chem. Int. Ed.*, 2018, **57**, 15733-15737.
180. X. Dai, L. Yu, Y. Zhang, L. Zhang and J. Tan, *Macromolecules*, 2019, **52**, 7468-7476.
181. N. P. Truong, J. F. Quinn, A. Anastasaki, D. M. Haddleton, M. R. Whittaker and T. P. Davis, *Chem. Commun.*, 2016, **52**, 4497-4500.
182. S. Y. Khor, N. P. Truong, J. F. Quinn, M. R. Whittaker and T. P. Davis, *ACS Macro Lett.*, 2017, **6**, 1013-1019.
183. F. L. Hatton, M. J. Derry and S. P. Armes, *Polym. Chem.*, 2020, **11**, 6343-6355.
184. W. H. Lane, *Ind. Eng. Chem., Anal. Ed.*, 1946, **18**, 295-296.
185. L. P. D. Ratcliffe, A. J. Ryan and S. P. Armes, *Macromolecules*, 2013, **46**, 769-777.
186. Z. An, Q. Shi, W. Tang, C.-K. Tsung, C. J. Hawker and G. D. Stucky, *J. Am. Chem. Soc.*, 2007, **129**, 14493-14499.
187. J. Rieger, C. Grazon, B. Charleux, D. Alaimo and C. Jérôme, *J. Polym. Sci., Part A: Polym. Chem.*, 2009, **47**, 2373-2390.
188. Y. Li and S. P. Armes, *Angew. Chem. Int. Ed.*, 2010, **49**, 4042-4046.
189. S. Sugihara, S. P. Armes, A. Blanazs and A. L. Lewis, *Soft Matter*, 2011, **7**, 10787-10793.
190. A. Blanazs, R. Verber, O. O. Mykhaylyk, A. J. Ryan, J. Z. Heath, C. W. I. Douglas and S. P. Armes, *J. Am. Chem. Soc.*, 2012, **134**, 9741-9748.
191. P. Chambon, A. Blanazs, G. Battaglia and S. P. Armes, *Langmuir*, 2012, **28**, 1196-1205.
192. C. J. Mable, R. R. Gibson, S. Prevost, B. E. McKenzie, O. O. Mykhaylyk and S. P. Armes, *J. Am. Chem. Soc.*, 2015, **137**, 16098-16108.
193. J. R. Lovett, L. P. D. Ratcliffe, N. J. Warren, S. P. Armes, M. J. Smallridge, R. B. Cracknell and B. R. Saunders, *Macromolecules*, 2016, **49**, 2928-2941.
194. N. J. W. Penfold, J. R. Lovett, N. J. Warren, P. Verstraete, J. Smets and S. P. Armes, *Polym. Chem.*, 2016, **7**, 79-88.
195. N. J. W. Penfold, J. R. Lovett, P. Verstraete, J. Smets and S. P. Armes, *Polym. Chem.*, 2017, **8**, 272-282.
196. C. G. Clarkson, J. R. Lovett, J. Madsen, S. P. Armes and M. Geoghegan, *Macromol. Rapid Commun.*, 2015, **36**, 1572-1577.
197. J. R. Lovett, N. J. Warren, L. P. D. Ratcliffe, M. K. Kocik and S. P. Armes, *Angew. Chem. Int. Ed.*, 2015, **54**, 1279-1283.
198. J. R. Lovett, N. J. Warren, S. P. Armes, M. J. Smallridge and R. B. Cracknell, *Macromolecules*, 2016, **49**, 1016-1025.
199. J. R. Lovett, M. J. Derry, P. Yang, F. L. Hatton, N. J. Warren, Patrick W. Fowler and S. P. Armes, *Chem. Sci.*, 2018, **9**, 7138-7144.
200. D. L. Beattie, O. O. Mykhaylyk and S. P. Armes, *Chem. Sci.*, 2020, **11**, 10821-10834.
201. L. P. D. Ratcliffe, M. J. Derry, A. Ianiro, R. Tuinier and S. P. Armes, *Angew. Chem. Int. Ed.*, 2019, **58**, 18964-18970.
202. O. J. Deane, J. Jennings, O. M. Musa, A. Fernyhough and S. P. Armes, *Chem. Mater.*, 2021, in the press.
203. O. J. Deane, J. Jennings and S. P. Armes, *Chem. Sci.*, 2021, submitted.
204. M. J. Derry, O. O. Mykhaylyk and S. P. Armes, *Angew. Chem.*, 2017, **129**, 1772-1776.

205. E. J. Cornel, S. van Meurs, T. Smith, P. S. O'Hora and S. P. Armes, *J. Am. Chem. Soc.*, 2018, **140**, 12980-12988.
206. C. György, M. J. Derry, E. J. Cornel and S. P. Armes, *Macromolecules*, 2021, **54**, 1159-1169.
207. T. F. Tadros, *Adv. Colloid Interface Sci.*, 1993, **46**, 1-47.
208. D. J. McClements, *Soft Matter*, 2012, **8**, 1719-1729.
209. W. D. Bancroft, *J. Phys. Chem.*, 1913, **17**, 501-519.
210. W. C. Griffin, *J. Soc. Cosmet. Chem.*, 1949, **1**, 311-326.
211. R. Aveyard, B. P. Binks and J. Mead, *J. Chem. Soc., Faraday Trans. 1*, 1987, **83**, 2347-2357.
212. J. W. Gibbs, *The Collected Works of J. Willard Gibbs, vol. 1*, Yale University Press, New Haven, 1928.
213. A. Gupta, H. B. Eral, T. A. Hatton and P. S. Doyle, *Soft Matter*, 2016, **12**, 2826-2841.
214. P. Taylor, *Adv. Colloid Interface Sci.*, 1998, **75**, 107-163.
215. A. Kabalnov, *J. Dispers. Sci. Technol.*, 2001, **22**, 1-12.
216. I. M. Lifshitz and V. V. Slyozov, *J. Phys. Chem. Solids*, 1961, **19**, 35-50.
217. C. Wagner, *Zeitschrift für Elektrochemie, Berichte der Bunsengesellschaft für physikalische Chemie*, 1961, **65**, 581-591.
218. J. Weiss, C. Cancelliere and D. J. McClements, *Langmuir*, 2000, **16**, 6833-6838.
219. T. J. Wooster, M. Golding and P. Sanguansri, *Langmuir*, 2008, **24**, 12758-12765.
220. M. Y. Koroleva and E. V. Yurtov, *Colloid Journal*, 2003, **65**, 40-43.
221. A. Bürkholz and R. Polke, *Part. Part. Syst. Charact.*, 1984, **1**, 153-160.
222. M. Born and E. Wolf, *Principles of Optics: Electromagnetic Theory of Propagation, Interference and Diffraction of Light*, Cambridge University Press, Cambridge, 7th edn., 1999.
223. G. Mie, *Annalen der Physik*, 1908, **330**, 377-445.
224. G. B. J. de Boer, C. de Weerd, D. Thoenes and H. W. J. Goossens, *Part. Part. Syst. Charact.*, 1987, **4**, 14-19.
225. J. Buffle and H. P. van Leeuwen, *Environmental Particles*, Lewis Publishers, New York, 1993.
226. O. Glatter and O. Kratky, *Small-angle X-ray Scattering*, Academic Press, London, 1982.
227. K. L. Planken and H. Cölfen, *Nanoscale*, 2010, **2**, 1849-1869.
228. J. Walter, T. Thajudeen, S. Süß, D. Segets and W. Peukert, *Nanoscale*, 2015, **7**, 6574-6587.
229. T. Detloff and D. Lerche, *Acta Mech.*, 2008, **201**, 83-94.
230. W. Ramsden, *Proc. R. Soc. London*, 1903, **72**, 156-164.
231. S. U. Pickering, *J. Chem. Soc.*, 1907, **91**, 2001-2021.
232. B. P. Binks and S. O. Lumsdon, *Phys. Chem. Chem. Phys.*, 1999, **1**, 3007-3016.
233. N. P. Ashby and B. P. Binks, *Phys. Chem. Chem. Phys.*, 2000, **2**, 5640-5646.
234. B. P. Binks and S. O. Lumsdon, *Langmuir*, 2000, **16**, 8622-8631.
235. B. P. Binks, *Curr. Opin. Colloid Interface Sci.*, 2002, **7**, 21-41.

236. R. Aveyard, B. P. Binks and J. H. Clint, *Adv. Colloid Interface Sci.*, 2003, **100**, 503-546.
237. B. P. Binks, *Langmuir*, 2017, **33**, 6947-6963.
238. J. Wu, M. Shi, W. Li, L. Zhao, Z. Wang, X. Yan, W. Norde and Y. Li, *Colloids Surf, B*, 2015, **127**, 96-104.
239. J. Xiao, Y. Li and Q. Huang, *Trends in Food Science & Technology*, 2016, **55**, 48-60.
240. F. Liu and C.-H. Tang, *J. Agr. Food Chem.*, 2013, **61**, 8888-8898.
241. C. Tang, Y. Li, J. Pun, A. S. Mohamed Osman and K. C. Tam, *Colloids Surf., A*, 2019, **570**, 403-413.
242. J. Marto, A. Ascenso, S. Simoes, A. J. Almeida and H. M. Ribeiro, *Expert Opin. Drug Deliv.*, 2016, **13**, 1093-1107.
243. D. Marku, M. Wahlgren, M. Rayner, M. Sjöö and A. Timgren, *Int. J. Pharm.*, 2012, **428**, 1-7.
244. J. Frelichowska, M.-A. Bolzinger, J. Pelletier, J.-P. Valour and Y. Chevalier, *Int. J. Pharm.*, 2009, **371**, 56-63.
245. P. Finkle, H. D. Draper and J. H. Hildebrand, *J. Am. Chem. Soc.*, 1923, **45**, 2780-2788.
246. B. P. Binks and S. O. Lumsdon, *Langmuir*, 2001, **17**, 4540-4547.
247. T. G. Anjali and M. G. Basavaraj, *Langmuir*, 2019, **35**, 3-20.
248. P. J. Wilde, *Curr. Opin. Colloid Interface Sci.*, 2000, **5**, 176-181.
249. A. Kabalnov, *Curr. Opin. Colloid Interface Sci.*, 1998, **3**, 270-275.
250. S. Levine, B. D. Bowen and S. J. Partridge, *Colloids Surf.*, 1989, **38**, 325-343.
251. J. H. Clint and S. E. Taylor, *Colloids Surf.*, 1992, **65**, 61-67.
252. N. Garti, *Colloids Surf., A*, 1997, **123-124**, 233-246.
253. A. G. Cunha, J.-B. Mougel, B. Cathala, L. A. Berglund and I. Capron, *Langmuir*, 2014, **30**, 9327-9335.
254. B. P. Binks and S. O. Lumsdon, *Langmuir*, 2000, **16**, 2539-2547.
255. A. Menner, V. Ikem, M. Salgueiro, M. S. P. Shaffer and A. Bismarck, *Chem. Commun.*, 2007, 4274-4276.
256. V. O. Ikem, A. Menner and A. Bismarck, *Langmuir*, 2010, **26**, 8836-8841.
257. J. Zhou, X. Qiao, B. P. Binks, K. Sun, M. Bai, Y. Li and Y. Liu, *Langmuir*, 2011, **27**, 3308-3316.
258. B. P. Binks and C. P. Whitby, *Colloids Surf., A*, 2005, **253**, 105-115.
259. J. Frelichowska, M.-A. Bolzinger and Y. Chevalier, *Colloids Surf., A*, 2009, **343**, 70-74.
260. S. Tcholakova, N. D. Denkov and A. Lips, *Phys. Chem. Chem. Phys.*, 2008, **10**, 1608-1627.
261. F. Yang, S. Liu, J. Xu, Q. Lan, F. Wei and D. Sun, *J. Colloid Interface Sci.*, 2006, **302**, 159-169.
262. I. Kalashnikova, H. Bizot, B. Cathala and I. Capron, *Langmuir*, 2011, **27**, 7471-7479.
263. I. Kalashnikova, H. Bizot, P. Bertoncini, B. Cathala and I. Capron, *Soft Matter*, 2013, **9**, 952-959.
264. C. Jiménez Saelices and I. Capron, *Biomacromolecules*, 2018, **19**, 460-469.

265. I. Capron, O. J. Rojas and R. Bordes, *Curr. Opin. Colloid Interface Sci.*, 2017, **29**, 83-95.
266. A. Saha, A. Nikova, P. Venkataraman, V. T. John and A. Bose, *ACS Appl. Mater. Interfaces*, 2013, **5**, 3094-3100.
267. H. Katepalli, V. T. John and A. Bose, *Langmuir*, 2013, **29**, 6790-6797.
268. N. M. Briggs, J. S. Weston, B. Li, D. Venkataramani, C. P. Aichele, J. H. Harwell and S. P. Crossley, *Langmuir*, 2015, **31**, 13077-13084.
269. Y. Q. He, F. Wu, X. Y. Sun, R. Q. Li, Y. Q. Guo, C. B. Li, L. Zhang, F. B. Xing, W. Wang and J. P. Gao, *ACS Appl. Mater. Interfaces*, 2013, **5**, 4843-4855.
270. J. Kim, L. J. Cote, F. Kim, W. Yuan, K. R. Shull and J. X. Huang, *J. Am. Chem. Soc.*, 2010, **132**, 8180-8186.
271. O. D. Velev, K. Furusawa and K. Nagayama, *Langmuir*, 1996, **12**, 2374-2384.
272. A. D. Dinsmore, M. F. Hsu, M. G. Nikolaides, M. Marquez, A. R. Bausch and D. A. Weitz, *Science*, 2002, **298**, 1006-1009.
273. J. I. Amalvy, S. P. Armes, B. P. Binks, J. A. Rodrigues and G. F. Unali, *Chem. Commun.*, 2003, 1826-1827.
274. J. I. Amalvy, G. F. Unali, Y. Li, S. Granger-Bevan, S. P. Armes, B. P. Binks, J. A. Rodrigues and C. P. Whitby, *Langmuir*, 2004, **20**, 4345-4354.
275. B. P. Binks, R. Murakami, S. P. Armes and S. Fujii, *Angew. Chem.*, 2005, **117**, 4873-4876.
276. B. P. Binks, R. Murakami, S. P. Armes, S. Fujii and A. Schmid, *Langmuir*, 2007, **23**, 8691-8694.
277. S. Fujii, Y. Cai, J. V. M. Weaver and S. P. Armes, *J. Am. Chem. Soc.*, 2005, **127**, 7304-7305.
278. S. Coertjens, R. De Dier, P. Moldenaers, L. Isa and J. Vermant, *Langmuir*, 2017, **33**, 2689-2697.
279. T. Ngai, S. H. Behrens and H. Auweter, *Chem. Commun.*, 2005, 331-333.
280. B. Brugger, B. A. Rosen and W. Richtering, *Langmuir*, 2008, **24**, 12202-12208.
281. F. Wang, J. Tang, H. Liu, G. Yu and Y. Zou, *Mater. Chem. Front.*, 2019, **3**, 356-364.
282. B. P. Binks and C. P. Whitby, *Langmuir*, 2004, **20**, 1130-1137.
283. T. S. Horozov and B. P. Binks, *Angew. Chem. Int. Ed.*, 2006, **45**, 773-776.
284. L. A. Fielding and S. P. Armes, *Journal of Materials Chemistry*, 2012, **22**, 11235-11244.
285. B. P. Binks, J. A. Rodrigues and W. J. Frith, *Langmuir*, 2007, **23**, 3626-3636.
286. B. P. Binks, L. Isa and A. T. Tyowua, *Langmuir*, 2013, **29**, 4923-4927.
287. S. Fouilloux, F. Malloggi, J. Daillant and A. Thill, *Soft Matter*, 2016, **12**, 900-904.
288. K. Liu, J. Jiang, Z. Cui and B. P. Binks, *Langmuir*, 2017, **33**, 2296-2305.
289. P. Pieranski, *Phys Rev Lett*, 1980, **45**, 569-572.
290. B. P. Binks and J. A. Rodrigues, *Langmuir*, 2007, **23**, 7436-7439.
291. S. Arditty, C. P. Whitby, B. P. Binks, V. Schmitt and F. Leal-Calderon, *Eur. Phys. J. E*, 2003, **11**, 273-281.
292. D. Dupin, S. P. Armes, C. Connan, P. Reeve and S. M. Baxter, *Langmuir*, 2007, **23**, 6903-6910.

293. H. Guo, D. Yang, M. Yang, Y. Gao, Y. Liu and H. Li, *Soft Matter*, 2016, **12**, 9683-9691.
294. A. Walsh, K. L. Thompson, S. P. Armes and D. W. York, *Langmuir*, 2010, **26**, 18039-18048.
295. K. L. Thompson, J. A. Lane, M. J. Derry and S. P. Armes, *Langmuir*, 2015, **31**, 4373-4376.
296. K. L. Thompson, C. J. Mable, J. A. Lane, M. J. Derry, L. A. Fielding and S. P. Armes, *Langmuir*, 2015, **31**, 4137-4144.
297. S. L. Rizzelli, E. R. Jones, K. L. Thompson and S. P. Armes, *Colloid. Polym. Sci.*, 2016, **294**, 1-12.
298. K. L. Thompson, P. Chambon, R. Verber and S. P. Armes, *J. Am. Chem. Soc.*, 2012, **134**, 12450-12453.
299. K. L. Thompson, C. J. Mable, A. Cockram, N. J. Warren, V. J. Cunningham, E. R. Jones, R. Verber and S. P. Armes, *Soft Matter*, 2014, **10**, 8615-8626.
300. K. L. Thompson, L. A. Fielding, O. O. Mykhaylyk, J. A. Lane, M. J. Derry and S. P. Armes, *Chem. Sci.*, 2015, **6**, 4207-4214.
301. C. J. Mable, K. L. Thompson, M. J. Derry, O. O. Mykhaylyk, B. P. Binks and S. P. Armes, *Macromolecules*, 2016, **49**, 7897-7907.
302. M. J. Rymaruk, K. L. Thompson, M. J. Derry, N. J. Warren, L. P. D. Ratcliffe, C. N. Williams, S. L. Brown and S. P. Armes, *Nanoscale*, 2016, **8**, 14497-14506.
303. K. L. Thompson, N. Cinotti, E. R. Jones, C. J. Mable, P. W. Fowler and S. P. Armes, *Langmuir*, 2017, **33**, 12616-12623.
304. K. L. Thompson, M. J. Derry, F. L. Hatton and S. P. Armes, *Langmuir*, 2018, **34**, 9289-9297.
305. S. J. Hunter, K. L. Thompson, J. R. Lovett, F. L. Hatton, M. J. Derry, C. Lindsay, P. Taylor and S. P. Armes, *Langmuir*, 2019, **35**, 254-265.
306. V. J. Cunningham, E. C. Giakoumatos, P. M. Ireland, C. J. Mable, S. P. Armes and E. J. Wanless, *Langmuir*, 2017, **33**, 7669-7679.
307. R. Aveyard, B. P. Binks and J. H. Clint, *Adv. Colloid Interface Sci.*, 2003, **100-102**, 503-546.
308. J. Madsen, S. P. Armes and A. L. Lewis, *Macromolecules*, 2006, **39**, 7455-7457.
309. J. Madsen, S. P. Armes, K. Bertal, S. MacNeil and A. L. Lewis, *Biomacromolecules*, 2009, **10**, 1875-1887.
310. K. L. Thompson, M. Williams and S. P. Armes, *J. Colloid Interface Sci.*, 2015, **447**, 217-228.
311. M. J. Derry, L. A. Fielding, N. J. Warren, C. J. Mable, A. J. Smith, O. O. Mykhaylyk and S. P. Armes, *Chem. Sci.*, 2016, **7**, 5078-5090.
312. C. Solans, P. Izquierdo, J. Nolla, N. Azemar and M. J. Garcia-Celma, *Curr. Opin. Colloid Interface Sci.*, 2005, **10**, 102-110.
313. K. H. Persson, I. A. Blute, I. C. Mira and J. Gustafsson, *Colloids Surf., A*, 2014, **459**, 48-57.
314. S. Sihler, A. Schrade, Z. Cao and U. Ziener, *Langmuir*, 2015, **31**, 10392-10401.
315. A. Schrade, K. Landfester and U. Ziener, *Chem. Soc. Rev.*, 2013, **42**, 6823-6839.

## **Chapter 2:**

# **How do Charged End-Groups on the Steric Stabiliser Block Influence the Formation and Long-Term Stability of Pickering Nanoemulsions Prepared Using Sterically-Stabilised Diblock Copolymer Nanoparticles?**

Reproduced in part with permission from:

[S. J. Hunter, N. J. W. Penfold, D. H. Chan, O. O. Mykhaylyk, and S. P. Armes, *Langmuir* **2020**, *36*, 769-780]

## 2.1 Introduction

Surface-active particles of sufficient size and appropriate wettability adsorb irreversibly at fluid interfaces.<sup>1, 2</sup> The thermodynamic driving force for such adsorption is the reduction in the effective interfacial area, which lowers the overall energy of the system (see Figure 1.25). However, when a particle approaches a fluid interface it usually has to overcome an energy barrier for adsorption to occur.<sup>3</sup> This adsorption barrier derives from particle-fluid interactions, which are dependent on the particle surface chemistry and the nature of the fluid.<sup>4</sup> More specifically, the barrier is the sum of the van der Waals forces, electrostatic forces and image charge effects.<sup>4, 5</sup> Generally, adsorption occurs during emulsification whereby additional energy is provided to generate greater interfacial area between two immiscible liquids (see Equation 1.20). However, if the energy of mixing is less than the energy barrier for adsorption, then the particles will simply remain suspended in the fluid in which they are most wetted.<sup>3</sup>

The van der Waals force between a particle and fluid interface can be either repulsive or attractive depending on the dielectric properties of the three components (see Figure 2.1a).<sup>6</sup> Moreover, the oil/water interface is known to possess anionic character,<sup>7, 8</sup> which is likely to hinder the adsorption of nanoparticles possessing the same surface charge (see Figure 2.1b).<sup>9, 10</sup> If this was the only electrostatic interaction between fluid interfaces and particles then highly cationic particles should encounter no difficulty in forming stable Pickering emulsions using an appropriate oil. However, Wang *et al.* reported that highly cationic PS latexes are unable to stabilise hexadecane-in-water emulsions.<sup>4</sup> These workers suggested that the interfacial adsorption of cationic and anionic particles is suppressed by image charge effects (see Figure 2.1c).<sup>4</sup> More specifically, it was postulated that interfacial adsorption of charged particles was hindered by repulsion from their electrostatic “image” on the non-polar side of the liquid interface.

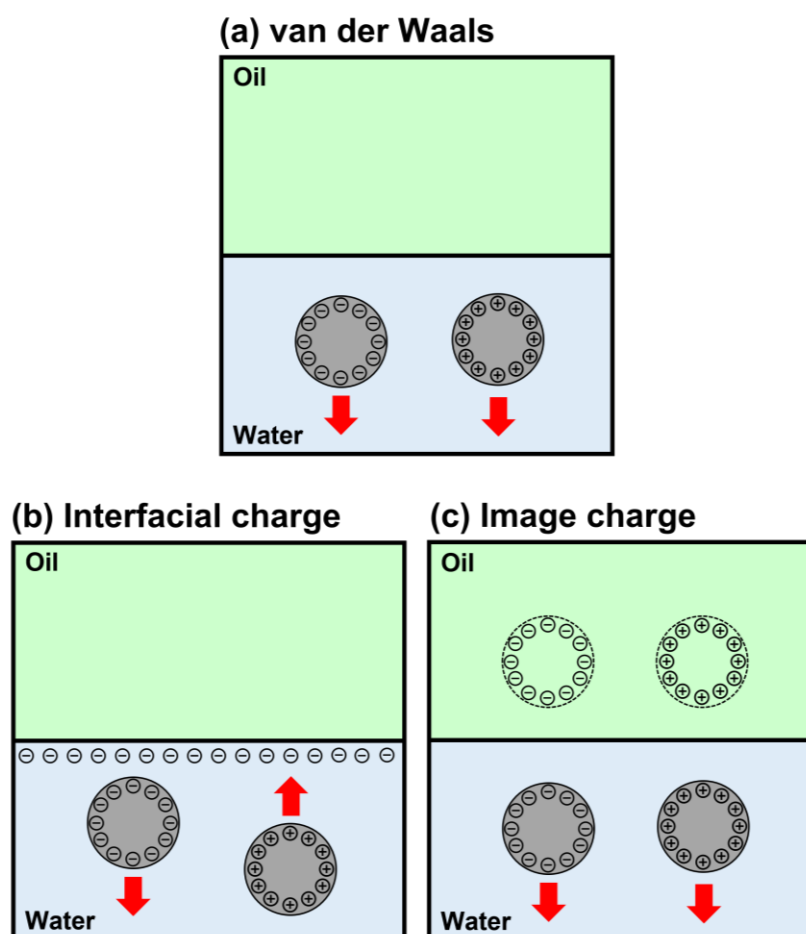


**Figure 2.1.** Interactions of particles possessing either cationic or anionic surface charge close to an oil/water interface: (a) van der Waals repulsive interactions, (b) interactions between particles possessing surface charge and an anionic oil/water interface, (c) interactions between particles possessing surface charge and their image charge formed within the oil phase.<sup>4,7</sup>

Many studies have reported that preparing stable Pickering emulsions using charged nanoparticles can be rather problematic.<sup>4, 11-16</sup> When at an interface, the strong repulsive electrostatic interactions between particles can offset the particle attachment energy (see Equation 1.29) to such an extent that the overall energy of adsorption is comparable to the thermal energy of the nanoparticles. Furthermore, even if a sufficient number of nanoparticles can be forced to occupy the interface, such adsorption is invariably weak owing to their poor wettability by the oil.<sup>15</sup> Several strategies have been employed to prepare stable Pickering emulsions using charged particles.<sup>5</sup> One approach is to simply increase the mixing force employed during emulsification.<sup>4</sup> If sufficient force is applied, then the particles should

## **Chapter 2: How do Charged End-Groups on the Steric Stabiliser Block Influence the Formation and Long-Term Stability of Pickering Nanoemulsions Prepared Using Sterically-Stabilised Diblock Copolymer Nanoparticles?**

---

overcome the repulsive forces and adsorb at the oil/water interface. However, this approach may not be suitable for more delicate particles since the extra energy may cause a loss of particle integrity or morphology.<sup>17</sup> More subtle strategies include adjusting the particle surface charge and/or wettability.<sup>5</sup> This could involve adjusting the pH<sup>4, 18, 19</sup> or ionic strength<sup>20, 21</sup> of the aqueous dispersion of particles or simply using an oil with an appropriate dielectric constant.<sup>4, 16</sup> This approach inevitably leads to aggregation<sup>22</sup> unless there is a secondary stabilisation mechanism (i.e., the presence of a suitable steric stabiliser on the surface of the particles).<sup>23</sup> Additives that are able to complex with the particulate emulsifier (e.g. charged surfactants,<sup>5, 9-11, 24</sup> polymers<sup>25, 26</sup> or particles)<sup>27, 28</sup> can also be used to adjust the particle surface charge, as highlighted in a recent review article.<sup>5</sup>

The recent development of PISA has enabled the convenient synthesis of well-defined diblock copolymer nanoparticles.<sup>29-33</sup> This powerful and versatile technique allows the convenient synthesis of 20-25 nm spherical nanoparticles in the form of a concentrated dispersions by, for example, RAFT aqueous emulsion polymerisation.<sup>30, 33-42</sup> The resulting sterically-stabilised nanoparticles can be used to prepare either Pickering macroemulsions<sup>30, 43</sup> or Pickering nanoemulsions.<sup>44, 45</sup> RAFT polymerisation also provides convenient access to a wide range of functional end-groups, which can be readily controlled by using a specific CTA, as depicted in Figure 1.11.<sup>46-48</sup> In PISA formulations, such end-groups are located at the terminus of the steric stabiliser chains of the block copolymer nanoparticles. Thus they can directly influence the nanoparticle surface charge and in some cases can also be used to induce changes in copolymer morphology or colloidal stability.<sup>49-53</sup>

The aim of this Chapter is to examine the effect of systematically varying the surface charge of model sterically-stabilised diblock copolymer nanoparticles (see Figure 2.2) on their emulsifier performance during the production of Pickering nanoemulsions *via* high-pressure microfluidisation. In addition, the effect of surface charge on the long-term stability of such Pickering nanoemulsions is assessed using analytical centrifugation.

## **2.2 Experimental**

### **2.2.1 Materials**

All reagents were used as received unless otherwise stated. Glycerol monomethacrylate (GMA) (99.8% purity) was obtained from GEO Specialty Chemicals (Hythe, UK). 2-Cyano-2-propyl benzodithioate, 2,2,2-trifluoroethyl methacrylate (TFEMA), 4,4'-azobis(4-cyanopentanoic acid) (ACVA), *n*-dodecane, and deuterium oxide were purchased from Aldrich (UK). 2,2'-Azobis[2-(2-imidazolin-2-yl)propane]dihydrochloride (VA-044;  $\geq 97\%$ ) was purchased from Wako Chemicals GmbH. 2-Cyano-2-propyl dithiobenzoate (CPDB) was purchased from STREM Chemicals Ltd. (Cambridge, UK). The 4-cyano-4-(2-phenylethanesulfanylthiocarbonyl)sulfanylpentanoic acid (PETTC) RAFT agent was synthesised as previously reported.<sup>31</sup> The morpholine-PETTC (MPETTC) RAFT agent was also synthesised as previously reported.<sup>51</sup>  $d_6$ -Acetone and  $d_4$ -methanol were purchased from Goss Scientific Instruments Ltd. (Cheshire, UK). All other solvents were purchased from Fisher Scientific (Loughborough, UK). Deionised water was used for all experiment.

### **2.2.2 Synthesis of PGMA<sub>48</sub> Precursor *via* RAFT Solution Polymerisation in Ethanol**

Three PGMA<sub>48</sub> precursors were synthesised *via* RAFT polymerisation of glycerol monomethacrylate (GMA) in ethanol at 70 °C, using either neutral CPDB, carboxylic acid-functional PETTC or morpholine-functional MPETTC as the RAFT agent to produce (0) PGMA<sub>48</sub>, (-) PGMA<sub>48</sub> or (+) PGMA<sub>48</sub> (see Figure 2.2), as described previously.<sup>30, 49, 51</sup> <sup>1</sup>H NMR studies in  $d_4$ -methanol indicated a mean DP of 48 *via* end-group analysis in each case (integrated aromatic RAFT end-group signals at 7.1–7.4 ppm were compared to those of the two oxymethylene protons at 3.5–4.4 ppm).

### **2.2.3 Synthesis of PGMA<sub>48</sub>-PTFEMA<sub>50</sub> Diblock Copolymer Nanoparticles *via* RAFT Aqueous Emulsion Polymerisation of TFEMA**

A typical protocol for the synthesis of neutral (0) PGMA<sub>48</sub>-PTFEMA<sub>50</sub> diblock copolymer nanoparticles was conducted as follows. (0) PGMA<sub>48</sub> (0.398 g, 0.050 mmol), and ACVA (2.79 mg, 0.010 mmol; PGMA<sub>48</sub> precursor/ACVA molar ratio = 5.0) and deionised water (7.37 g, 10% w/w) were weighed into a 14 mL sample vial, sealed with a rubber septum, and degassed with nitrogen for 30 min. TFEMA monomer (0.420 g, 2.5 mmol), which had been deoxygenated separately with nitrogen for 30 min, was then added to the solution under nitrogen and immersed in an oil bath set at 70 °C. After 6 h, the TFEMA polymerisation was quenched by exposing the reaction mixture to air and cooling to ambient temperature.

A typical protocol for the synthesis of anionic (-) PGMA<sub>48</sub>-PTFEMA<sub>50</sub> diblock copolymer nanoparticles was conducted as follows. (-) PGMA<sub>48</sub> (0.401 g, 0.050 mmol), and ACVA (2.80 mg, 0.01 mmol; PGMA<sub>48</sub> precursor / ACVA molar ratio = 5.0) and deionised water (7.41 g, 10% w/w) were weighed into a 14 mL sample vial, sealed with a rubber septum, and degassed with nitrogen for 30 min. The pH was adjusted to pH 3 using 1 M HCl. TFEMA monomer (0.415 g, 2.5 mmol), which had been deoxygenated separately with nitrogen for 30 min, was then added to the solution under nitrogen and immersed in an oil bath set at 70 °C. After 6 h, the TFEMA polymerisation was quenched by exposing the reaction mixture to air and cooling to ambient temperature.

A typical protocol for the synthesis of cationic (+) PGMA<sub>48</sub>-PTFEMA<sub>50</sub> diblock copolymer was conducted as follows. (+) PGMA<sub>48</sub> (0.402 g, 0.05 mmol), and VA-044 (3.19 mg, 0.01 mmol; PGMA<sub>48</sub> precursor/VA-044 molar ratio = 5.0) and deionised water (7.38 g, 10% w/w) were weighed into a 14 mL sample vial, sealed with a rubber septum, and degassed with nitrogen for 30 min. The pH was adjusted to pH 7 using 1 M NaOH. TFEMA monomer (0.415 g, 2.5 mmol), which had been deoxygenated separately with nitrogen for 30 min, was then added to the solution

## **Chapter 2: How do Charged End-Groups on the Steric Stabiliser Block Influence the Formation and Long-Term Stability of Pickering Nanoemulsions Prepared Using Sterically-Stabilised Diblock Copolymer Nanoparticles?**

---

under nitrogen and immersed in an oil bath set at 70 °C. After 6 h, the TFEMA polymerisation was quenched by exposing the reaction mixture to air and cooling to ambient temperature.

### **2.2.4 Preparation of PGMA<sub>48</sub>-PTFEMA<sub>50</sub>-Stabilised Pickering Macroemulsions Using High-Shear Homogenisation**

An aqueous dispersion of PGMA<sub>48</sub>-PTFEMA<sub>50</sub> nanoparticles (4.0 mL, 7.0% w/w) was added to a 14 mL glass vial. The pH was adjusted to either pH 7 or pH 3 using 1 M NaOH or HCl respectively and then homogenised with *n*-dodecane (1.0 mL, 20% v/v) for 2.0 min at 20 °C using an IKA Ultra-Turrax T-18 homogeniser equipped with a 10 mm dispersing tool and operating at 13 500 rpm.

### **2.2.5 Preparation of PGMA<sub>48</sub>-PTFEMA<sub>50</sub>-Stabilised Pickering Nanoemulsions Using High-Pressure Microfluidisation**

A Pickering macroemulsion (5.0 mL, initial nanoparticle concentration in the aqueous phase = 7.0% w/w) was further processed using an LV1 low-volume microfluidiser processor (Microfluidics, USA). The pressure was fixed at 20 000 psi and each emulsion was passed ten times through the LV1 unit to achieve well-defined Pickering nanoemulsions.

### **2.2.6 Characterisation**

#### **<sup>1</sup>H NMR Spectroscopy**

All <sup>1</sup>H NMR spectra were recorded at 400 MHz in either *d*<sub>6</sub>-acetone or *d*<sub>4</sub>-methanol using a Bruker Avance-400 spectrometer with 64 scans being averaged per spectrum.

#### **Gel Permeation Chromatography (GPC)**

0.50% w/w copolymer solutions were prepared in HPLC-grade DMF containing 10 mM LiBr and DMSO (1.0 % v/v) was used as a flow-rate marker. GPC studies were conducted at

## **Chapter 2: How do Charged End-Groups on the Steric Stabiliser Block Influence the Formation and Long-Term Stability of Pickering Nanoemulsions Prepared Using Sterically-Stabilised Diblock Copolymer Nanoparticles?**

---

60 °C using a constant flow rate of 1.0 mL min<sup>-1</sup>. The GPC set-up comprised an Agilent 1260 Infinity series degasser and pump, an Agilent PL-gel guard column, two Agilent PL-gel 5 µm Mixed-C columns and a refractive index detector. Sixteen near-monodisperse PMMA standards with peak molecular weights ( $M_p$ ) ranging from 645 to 2 480 000 g mol<sup>-1</sup> were used for calibration.

### Dynamic Light Scattering (DLS)

Hydrodynamic *z*-average diameters were obtained by DLS using a Malvern Zetasizer NanoZS instrument at a fixed scattering angle of 173°. Aqueous dispersions of 0.10% w/w nanoparticles and 0.50% v/v nanoemulsions were analysed using disposable cuvettes, and the results were averaged over three consecutive runs, each comprising ten analyses. The deionised water used to dilute each sample was ultrafiltered through a 0.20 µm membrane to remove extraneous dust. Aqueous electrophoresis studies were performed on 0.10% w/w aqueous copolymer dispersions containing 1 mM KCl as background electrolyte using a Malvern Zetasizer NanoZS instrument at 25 °C. The pH of the copolymer dispersion was initially weakly basic and adjusted as required with either 0.1 M or 1M HCl. Zeta potentials were calculated using the Henry equation by applying the Smoluchowski approximation. All data were averaged over three consecutive runs.

### Transmission Electron Microscopy (TEM)

Nanoemulsion samples were diluted to 0.50% v/v and PGMA<sub>48</sub>-PTFEMA<sub>50</sub> nanoparticle dispersions were diluted to 0.10% w/w using deionised water at either pH 3 or 7 at 20 °C for TEM studies. Copper/palladium TEM grids (Agar Scientific, UK) were surface-coated in-house to produce a thin film of amorphous carbon. The grids were then plasma glow-discharged for 30 s to create a hydrophilic surface. Individual samples (0.50% v/v or 0.10% w/w, 10 µL) were adsorbed onto the freshly-treated grids for 1 min and then blotted with filter paper to remove

## Chapter 2: How do Charged End-Groups on the Steric Stabiliser Block Influence the Formation and Long-Term Stability of Pickering Nanoemulsions Prepared Using Sterically-Stabilised Diblock Copolymer Nanoparticles?

---

excess solution. To stain the nanoemulsions and nanoparticles, uranyl formate solution (0.75% w/w, 9  $\mu$ L) was soaked on the sample-loaded grid for 20 s and then carefully blotted to remove excess stain. Each grid was then dried using a vacuum hose. Imaging was performed using a FEI Tecnai Spirit microscope fitted with a Gatan 1kMS600CW CCD camera operating at 80 kV.

### Analytical Centrifugation (LUMiSizer)

Droplet size distributions were assessed using a LUMiSizer analytical photocentrifuge (LUM GmbH, Berlin, Germany) at 20 °C. Measurements were conducted on diluted Pickering nanoemulsions (1.0% v/v *n*-dodecane) in 2 mm path length polyamide cells at 400 rpm for 200 profiles (allowing 10 s between profiles) and then the rate of centrifugation was increased up to 4000 rpm for a further 800 profiles. The slow initial rate of centrifugation enabled detection of any larger oil droplets that might be present within the nanoemulsion. The LUMiSizer instrument employs space- and time-resolved extinction profiles (STEP) technology to measure the intensity of transmitted near-infrared light as a function of time and position over the entire cell length simultaneously. The gradual progression of these transmission profiles contains information on the rate of creaming of the oil droplets and hence enables assessment of the droplet size distribution.

### Small-Angle X-Ray Scattering (SAXS)

SAXS data were recorded using a laboratory SAXS beamline (Xeuss 2.0, Xenocs, France) equipped with a liquid gallium MetalJet X-ray source (Excillum, Sweden) (wavelength  $\lambda = 0.134$  nm), two sets of motorised scatterless slits for beam collimation and a Pilatus 1M two-dimensional pixel SAXS detector (Dectris, Switzerland) (sample-to-detector distance = 1.889 m). A flow-through glass capillary (2 mm diameter) was connected to an injecting syringe and a waste container *via* plastic tubing and mounted horizontally on the beamline stage; this set-up was used as a sample holder. SAXS patterns were recorded using an exposure time of 600 seconds over a  $q$  range of  $0.02 \text{ nm}^{-1}$  to  $1.4 \text{ nm}^{-1}$ , where  $q = (4\pi\sin\theta)/\lambda$  is the length of the scattering vector and  $\theta$

## Chapter 2: How do Charged End-Groups on the Steric Stabiliser Block Influence the Formation and Long-Term Stability of Pickering Nanoemulsions Prepared Using Sterically-Stabilised Diblock Copolymer Nanoparticles?

---

is one-half of the scattering angle. Data were reduced, calibrated and integrated using the Foxtrot software package supplied with the instrument and further analysed (background subtraction and data modelling) using Irena SAS macros<sup>54</sup> for Igor Pro.

Packing Efficiency Calculation:

The nanoparticle packing efficiency was estimated by first calculating the mean number of nanoparticles,  $N$ , adsorbed onto an individual  $n$ -dodecane droplet using Equation 2.1:<sup>45</sup>

$$N = \frac{\text{total number of nanoparticles}}{\text{total number of droplets}} = \frac{m_p N_A / (N_s M_n)}{V_{\text{oil}} / (\frac{4}{3} \pi R_{\text{oil}})^3} \quad 2.1$$

where,  $m_{\text{particles}}$  is the mass of PGMA<sub>48</sub>-PTFEMA<sub>50</sub> nanoparticles used to prepare the nanoemulsion,  $N_A$  is Avogadro's constant,  $M_n$  is the number-average molecular weight of the PGMA<sub>48</sub>-PTFEMA<sub>50</sub> chains,  $V_{\text{oil}}$  is the total volume of oil used to prepare each nanoemulsion and  $R_{\text{oil}}$  is the mean radius of the bare  $n$ -dodecane droplets. Finally,  $N_s$  is the number of PGMA<sub>48</sub>-PTFEMA<sub>50</sub> chains per nanoparticle as determined using  $N_s = \frac{\frac{4}{3} \pi R_s^3}{V_{\text{PTFEMA}}}$ , where  $R_s$  is the mean radius of the PTFEMA cores determined by SAXS and  $V_{\text{PTFEMA}}$  is the volume of the core-forming block of a single copolymer chain. We calculate  $R_{\text{oil}}$  to be equal to the  $z$ -average radius  $R_{\text{DLS}}$  of the overall nanoemulsion droplets minus the diameter of the adsorbed nanoparticles (or  $R_{\text{oil}} = R_{\text{DLS}} - 2R_{\text{particle}}$ ).

Assuming that an area of a large spherical particle (e.g. the droplet) covered by small spheres (e.g. the nanoparticles) can be represented by the total area of projection of the small spheres on the surface of the large particle,<sup>55</sup> the packing efficiency  $P_{\text{eff}}$ , of the small spheres within the shell surrounding the large central particle is given by Equation 2.2:

$$P_{\text{eff}} \cong \frac{N(R_{\text{particle}})^2}{4(R_{\text{oil}} + R_{\text{particle}})^2} \quad 2.2$$

The following two assumptions are made in such nanoparticle packing efficiency calculations. First, the  $z$ -average droplet diameter reported by DLS includes both the oil droplet and the

## Chapter 2: How do Charged End-Groups on the Steric Stabiliser Block Influence the Formation and Long-Term Stability of Pickering Nanoemulsions Prepared Using Sterically-Stabilised Diblock Copolymer Nanoparticles?

adsorbed nanoparticle shell. Secondly, the nanoparticles adsorb at the oil/water interface with an effective contact angle of  $0^\circ$  with respect to the nanoparticle cores. Clearly, this is not the true nanoparticle contact angle, hence the droplet diameter will be slightly overestimated.

### 2.3 Results and Discussion

#### 2.3.1 Synthesis and Characterisation of PGMA<sub>48</sub>-PTFEMA<sub>50</sub> Diblock Copolymer Nanoparticles

The PGMA<sub>48</sub>-PTFEMA<sub>50</sub> nanoparticles used in this study were prepared by RAFT aqueous emulsion polymerisation of TFEMA at 10% w/w solids using three different PGMA<sub>48</sub> precursors in turn (see Figure 2.2a).

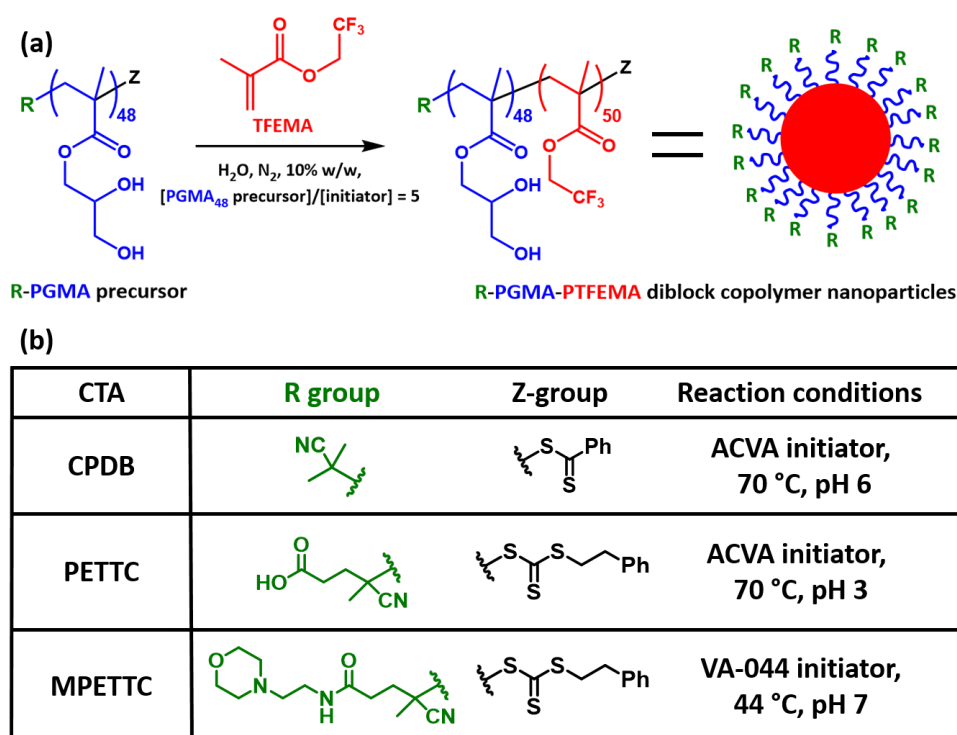


**Figure 2.2** (a) Synthesis of PGMA<sub>48</sub>-PTFEMA<sub>50</sub> diblock copolymer nanoparticles *via* RAFT aqueous emulsion polymerisation of TFEMA, using CPDB, PETTC, or MPETTC RAFT agents, which confer either neutral (0), anionic (-) or cationic (+) end-groups on the PGMA<sub>48</sub> steric stabiliser chains at a solution pH of 6, 7 or 3, respectively. (b) Summary of the chemical structures for the diblock copolymers synthesised using either CPDB, PETTC or MPETTC and the specific reaction conditions used in each case.

These precursors were prepared using either neutral CPDB, carboxylic acid-functional PETTC or morpholine-functional MPETTC as the RAFT agent to confer either neutral, anionic or cationic

## Chapter 2: How do Charged End-Groups on the Steric Stabiliser Block Influence the Formation and Long-Term Stability of Pickering Nanoemulsions Prepared Using Sterically-Stabilised Diblock Copolymer Nanoparticles?

end-groups. In each case, the aqueous solution pH was adjusted prior to polymerisation to ensure that each RAFT end-group remained in its neutral form. An amidine-based azo initiator (VA-044) was used for the synthesis of the (+) PGMA<sub>48</sub> precursor, whereas a carboxylic acid-based azo initiator (ACVA) was employed for the synthesis of the (-) PGMA<sub>48</sub> precursor (see Figure 2.2b).

All three TFEMA polymerisations proceeded to high conversion within 6 h as judged by both <sup>1</sup>H and <sup>19</sup>F NMR spectroscopy (see Figure 2.3). The latter technique is particularly convenient because <sup>19</sup>F has 100% abundance and <sup>19</sup>F NMR studies do not require deuterated solvents. Moreover, unlike <sup>1</sup>H NMR spectra, <sup>19</sup>F NMR spectra typically do not suffer from overlapping signals.

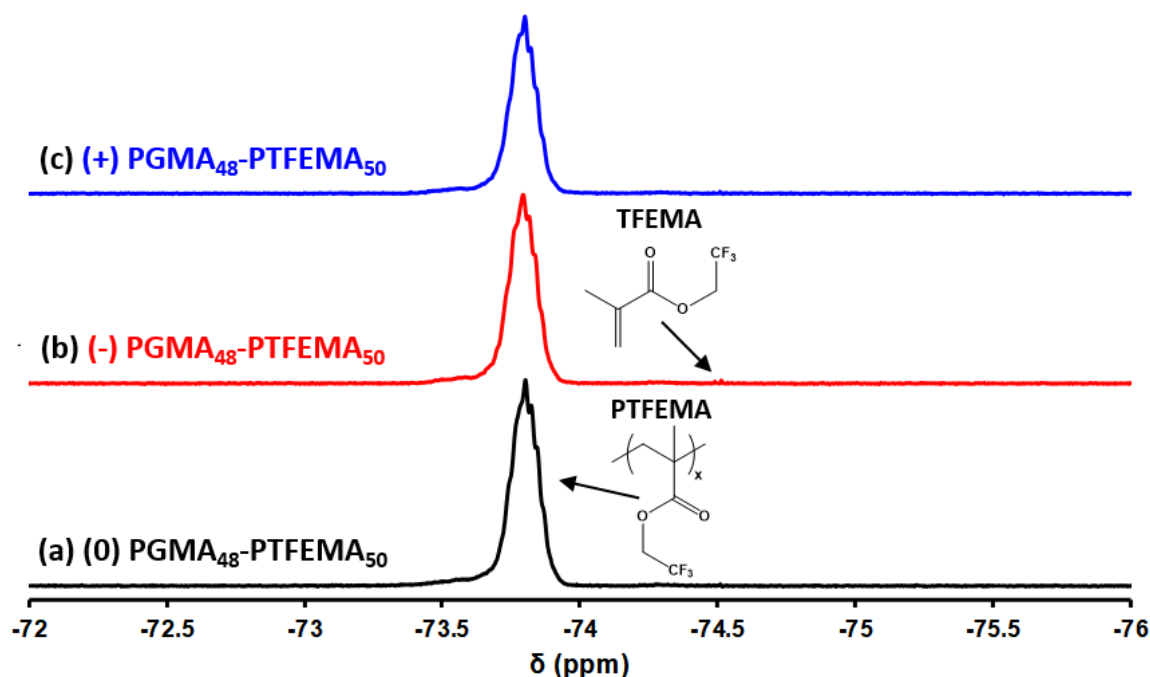


**Figure 2.3.** <sup>19</sup>F NMR spectra recorded for (a) (0) PGMA<sub>48</sub>-PTFEMA<sub>50</sub>, (b) (-) PGMA<sub>48</sub>-PTFEMA<sub>50</sub> and (c) (+) PGMA<sub>48</sub>-PTFEMA<sub>50</sub>.

For (0) PGMA<sub>48</sub>-PTFEMA<sub>50</sub> and (+) PGMA<sub>48</sub>-PTFEMA<sub>50</sub> nanoparticles DMF GPC analysis indicated an identical  $M_n$  of 23 600 g mol<sup>-1</sup> and relatively low  $M_w/M_n$  values of 1.12 and 1.16, respectively (see Figure 2.4). The same technique indicated an  $M_n$  of 29 700 g mol<sup>-1</sup> and an  $M_w/M_n$  of 1.25 for (-) PGMA<sub>48</sub>-PTFEMA<sub>50</sub> nanoparticles. The higher  $M_n$  value is the result of a

## Chapter 2: How do Charged End-Groups on the Steric Stabiliser Block Influence the Formation and Long-Term Stability of Pickering Nanoemulsions Prepared Using Sterically-Stabilised Diblock Copolymer Nanoparticles?

high molecular weight shoulder (see the corresponding GPC trace shown in Figure 2.4b). Nevertheless, these amphiphilic diblock copolymer chains form well-defined sterically-stabilised nanoparticles with comparable mean particle diameters (see Figure 2.5).

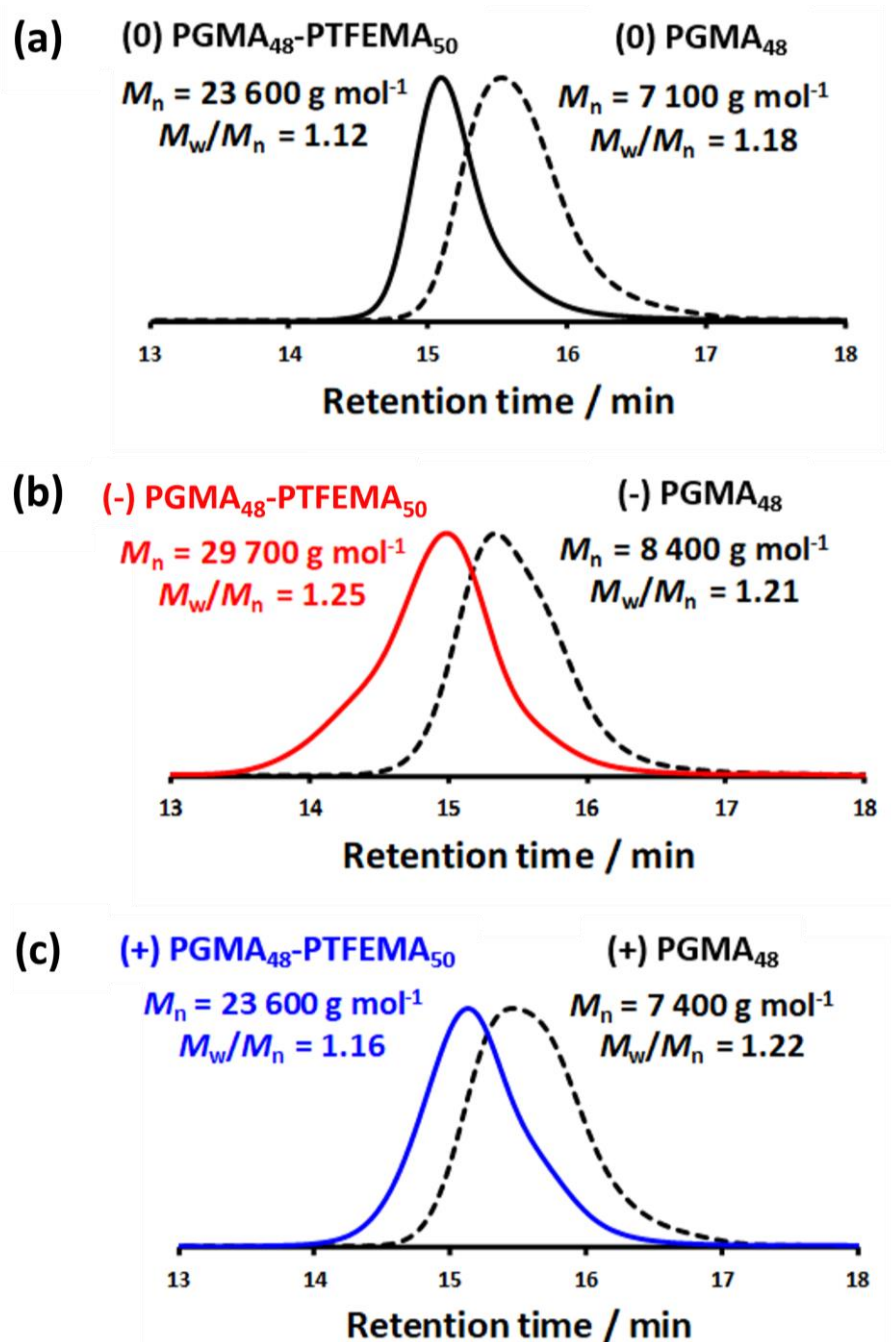


**Figure 2.4.** Overlaid DMF GPC chromatograms obtained for (a) (0) PGMA<sub>48</sub> and (0) PGMA<sub>48</sub>-PTFEMA<sub>50</sub>, (b) (-) PGMA<sub>48</sub> and (-) PGMA<sub>48</sub>-PTFEMA<sub>50</sub>, and (c) (+) PGMA<sub>48</sub> and (+) PGMA<sub>48</sub>-PTFEMA<sub>50</sub>.

Transmission electron microscopy (TEM) images confirmed that well-defined spherical nanoparticles were obtained regardless of the nature of the end-group, see Figure 2.5a. DLS was

## **Chapter 2: How do Charged End-Groups on the Steric Stabiliser Block Influence the Formation and Long-Term Stability of Pickering Nanoemulsions Prepared Using Sterically-Stabilised Diblock Copolymer Nanoparticles?**

---

used to determine the  $z$ -average diameters of the three types of nanoparticles, which were in good agreement (see Figure 2.5b). Moreover, the nature of the end-group had minimal effect on the mean nanoparticle diameter, which is an important parameter for the formation of Pickering nanoemulsions using microfluidisation.<sup>44</sup> As the nanoparticle dimensions and chemical compositions are very similar, this enables the effect of varying the nature of the end-group on the non-ionic steric stabiliser chains to be examined for this model system. PGMA<sub>48</sub>-PTFEMA<sub>50</sub> nanoparticles prepared using the PETTC RAFT agent bear carboxylic acid end-groups whereas the same nanoparticles prepared using MPETTC bear tertiary amine end-groups. Therefore, the solution pH at which the nanoemulsions are prepared is expected to influence the Pickering performance of these nanoparticles.

Zeta potential measurements were performed to examine the effect of varying the solution pH on the aqueous electrophoretic behaviour of the nanoparticles (Figure 2.5c). For (0) PGMA<sub>48</sub>-PTFEMA<sub>50</sub> nanoparticles, a modest change in zeta potential from approximately zero to -12 mV was observed on raising the solution pH from 3 to 10. This weakly anionic character may indicate the presence of carboxylic acid end-groups on some of the PGMA stabiliser chains originating from the ACVA initiator used for their RAFT syntheses. Alternatively, this anionic character may simply result from hydroxide ions adsorbing onto the surface of the nanoparticles at high pH.<sup>7</sup> In this context, it is noteworthy that the zeta potential of the (0) PGMA<sub>48</sub>-PTFEMA<sub>50</sub> nanoparticles is comparable to that of (+) PGMA<sub>48</sub>-PTFEMA<sub>50</sub> nanoparticles at pH 10.

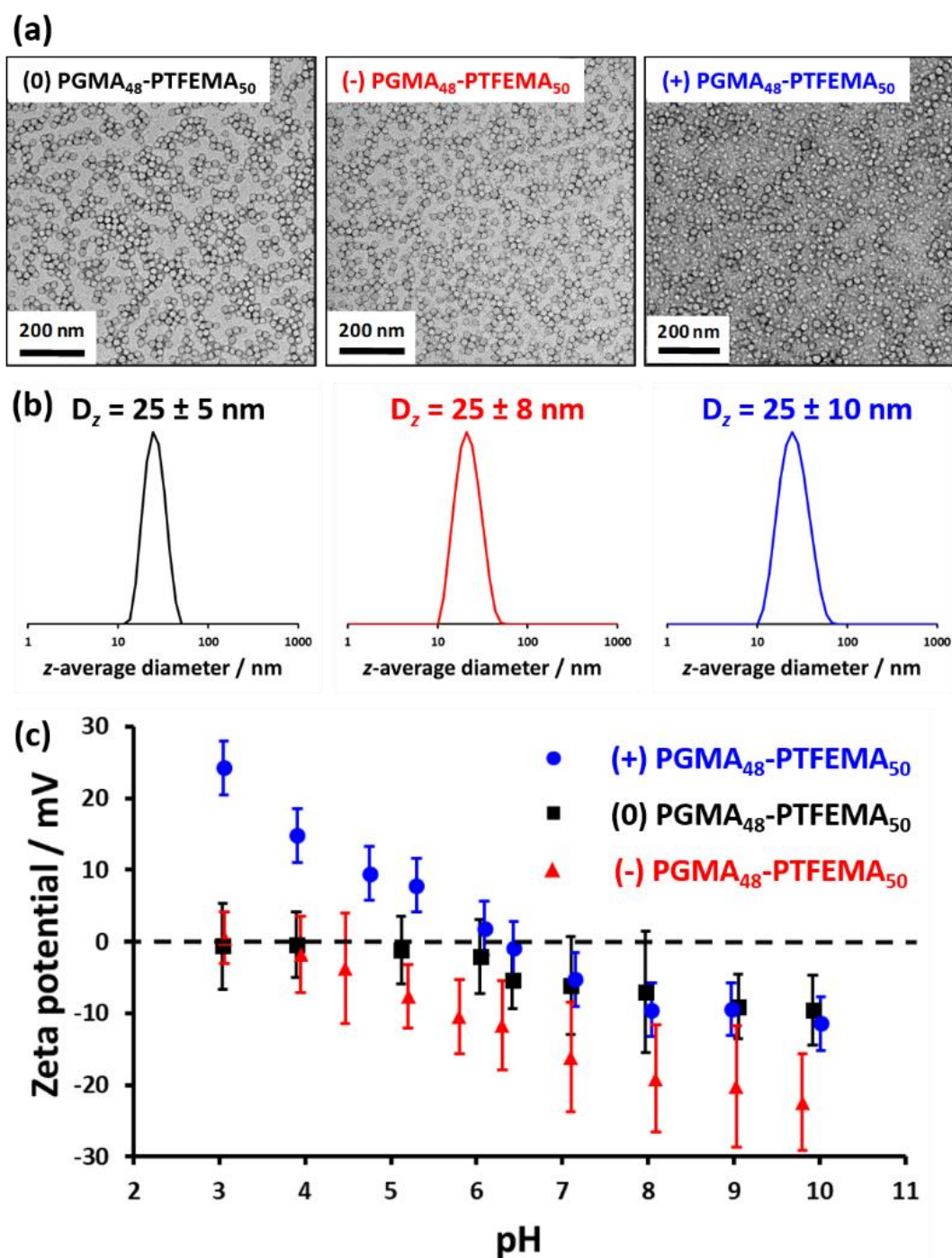


**Figure 2.5** (a) Representative TEM images obtained for PGMA<sub>48</sub>-PTFEMA<sub>50</sub> diblock copolymer nanoparticles prepared by RAFT aqueous emulsion polymerisation of TFEMA, with the PGMA<sub>48</sub> precursor block synthesised using either CPDB (0), PETTC (-) or MPETTC (+) RAFT agents. (b) Corresponding DLS  $z$ -average size distributions and (c) Zeta potential vs. pH curves obtained for (0) PGMA<sub>48</sub>-PTFEMA<sub>50</sub>, (-) PGMA<sub>48</sub>-PTFEMA<sub>50</sub> and (+) PGMA<sub>48</sub>-PTFEMA<sub>50</sub> pH to low pH. The error bars shown for the zeta potential data are equivalent to one standard deviation. Measurements are reported for 0.1% w/w copolymer dispersions prepared in the presence of 1 mM KCl. All pH titrations were performed from high pH to low pH. The error bars shown for the zeta potential data are equivalent to one standard deviation.

## Chapter 2: How do Charged End-Groups on the Steric Stabiliser Block Influence the Formation and Long-Term Stability of Pickering Nanoemulsions Prepared Using Sterically-Stabilised Diblock Copolymer Nanoparticles?

For (+) PGMA<sub>48</sub>-PTFEMA<sub>50</sub> nanoparticles, a significant increase in zeta potential from approximately zero to +25 mV occurs on lowering the solution pH from 6 to 3. These observations are consistent with aqueous electrophoresis data reported by Penfold *et al.* for morpholine-functionalised PGMA<sub>50</sub>-PHPMA<sub>140</sub> diblock copolymer nano-objects.<sup>51</sup> The cationic zeta potentials observed on lowering the solution pH indicate protonation of the terminal morpholine group located on the PGMA<sub>50</sub> stabiliser chains, for which acid titration studies indicate a conjugate acid dissociation constant pK<sub>a</sub> of approximately 6.3.<sup>51</sup> Thus the aqueous electrophoretic behaviour of these three types of diblock copolymer nanoparticles can be adjusted simply by changing the solution pH.

As discussed in Chapter 1, SAXS is a powerful tool for characterising both the diblock copolymer nanoparticles and the Pickering (nano)emulsions.<sup>56</sup> Figure 2.6 shows representative scattering patterns recorded for the three different types of spherical diblock copolymer nanoparticles at either pH 3 or pH 7. Such SAXS patterns can be satisfactorily fitted using a spherical form factor.<sup>57</sup> The resulting volume-average nanoparticle radii  $R_s$  were calculated to be around 11 nm in each case (see Table 2.1 for further information), which are consistent with the  $z$ -average diameters of around 25 nm reported by DLS.

**Table 2.1.** Structural parameters obtained by SAXS analysis of 1.0% w/w either neutral (0) PGMA<sub>48</sub>-PTFEMA<sub>50</sub>, anionic (-) PGMA<sub>48</sub>-PTFEMA<sub>50</sub> or cationic (+) PGMA<sub>48</sub>-PTFEMA<sub>50</sub> nanoparticles at either pH 3 or pH 7.<sup>a</sup>

End-group type	pH 3				pH 7			
	$R_s$ / nm	$\sigma_s$ / nm	$R_{py}$ / nm	$f_{py}$	$R_s$ / nm	$\sigma_s$ / nm	$R_{py}$ / nm	$f_{py}$
Neutral	10.7	1.3	-	-	10.7	1.0	-	-
Anionic	10.8	1.4	-	-	11.1	1.7	23.1	0.03
Cationic	11.5	2.4	22.7	0.02	11.6	2.6	-	-

<sup>a</sup> $R_s$  = mean sphere radius;  $\sigma_s$  = standard deviation of the sphere radius;  $R_{py}$  = hard-sphere interaction radius;  $f_{py}$  = effective volume fraction.

In some cases, a structure factor was included in the model to account for the repulsive interactions arising from the anionic carboxylate or cationic morpholine end-groups located on the PGMA<sub>48</sub> chains. More specifically, a hard-sphere structure factor (solved using the Percus-

## Chapter 2: How do Charged End-Groups on the Steric Stabiliser Block Influence the Formation and Long-Term Stability of Pickering Nanoemulsions Prepared Using Sterically-Stabilised Diblock Copolymer Nanoparticles?

Yevick closure relation) was introduced.<sup>58, 59</sup> This enabled the interaction radius  $R_{PY}$  and the effective volume fraction  $f_{PY}$  to be determined.<sup>60</sup>

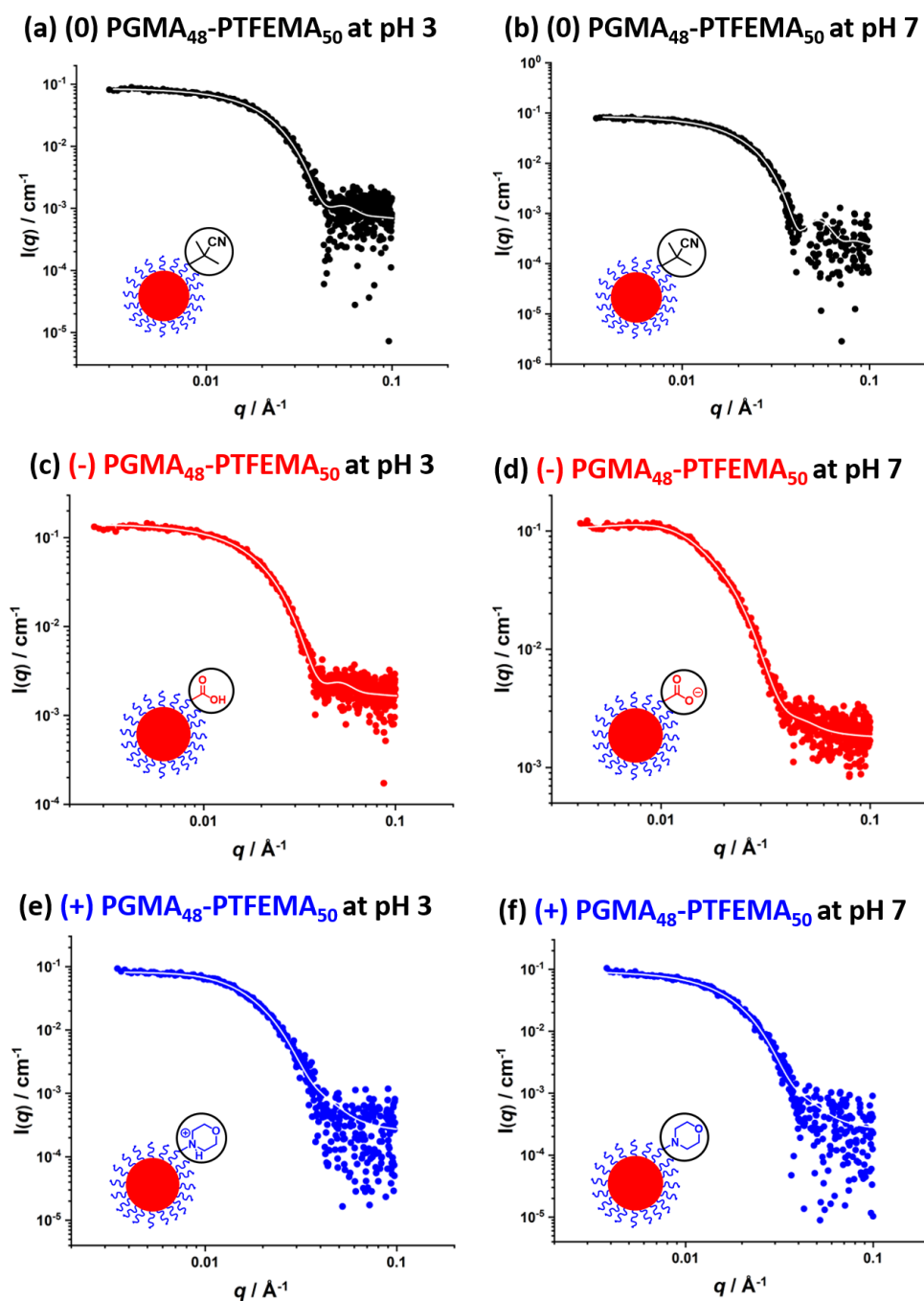


**Figure 2.6.** Experimental SAXS patterns (circles) and calculated data fits (white lines) obtained for 1.0% w/w PGMA<sub>48</sub>-PTFEMA<sub>50</sub> diblock copolymer nanoparticles with a (a) CPDB end-group at pH 3 (neutral nanoparticles); (b) a CPDB end-group at pH 7 (weakly anionic nanoparticles); (c) PETTC end-group at pH 3 (neutral nanoparticles); (d) PETTC end-group at pH 7 (strongly anionic nanoparticles); (e) MPETTC end-group at pH 3 (strongly cationic nanoparticles); (f) MPETTC end-group at pH 7 (neutral nanoparticles).

### 2.3.2 Effect of End-Group Charge on the Formation of Pickering Nanoemulsions

Initially, 7.0% w/v aqueous dispersions of PGMA<sub>48</sub>-PTFEMA<sub>50</sub> nanoparticles were prepared, and the solution pH was adjusted to either 3 or 7 using 1 M HCl or NaOH, respectively. These dispersions were then used to prepare precursor Pickering macroemulsions with a mean droplet diameter of around 20-30  $\mu\text{m}$  *via* high-shear homogenisation. Such precursor macroemulsions were then processed using a commercial LV1 microfluidiser to produce Pickering nanoemulsions, as depicted in Figure 2.7.

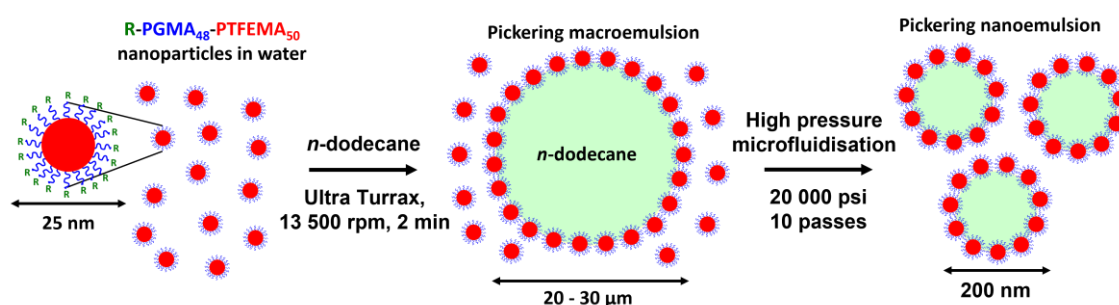


**Figure 2.7.** Schematic representation of the two-step preparation of Pickering nanoemulsions. First, a 7.0 % w/v aqueous dispersion of PGMA<sub>48</sub>-PTFEMA<sub>50</sub> nanoparticles at either pH 3 or pH 7 are homogenised with *n*-dodecane to form an *n*-dodecane-in-water Pickering macroemulsion of around 20-30  $\mu\text{m}$  diameter using conventional high-shear homogenisation at 13 500 rpm for 2 min at 20 °C. This relatively coarse precursor emulsion is then refined *via* ten passes through a commercial LV1 microfluidiser at 20 000 psi to obtain the final Pickering nanoemulsions of approximately 200 nm diameter that are used in this study. (See Figure 2.2 for details of each of the three terminal R groups on the end of the PGMA stabiliser chains).

The latter step had been previously optimised by Thompson and co-workers, who found that a substantial excess of PGMA<sub>48</sub>-PTFEMA<sub>50</sub> nanoparticles should be present after formation of the initial macroemulsion.<sup>44</sup> This is because these non-adsorbed nanoparticles are required to stabilise the additional oil/water interface generated during high-pressure microfluidisation.<sup>44, 61</sup> Furthermore, it was empirically established that an applied pressure of 20 000 psi was optimal for the preparation of stable Pickering nanoemulsions.<sup>44</sup> Lower pressures led to larger, more polydisperse droplets, whereas higher pressures led to *in situ* dissociation of the PGMA<sub>48</sub>-PTFEMA<sub>50</sub> nanoparticles to form individual diblock copolymer chains, which then acted as amphiphilic copolymer surfactant to form non-Pickering nanoemulsions.<sup>44</sup>

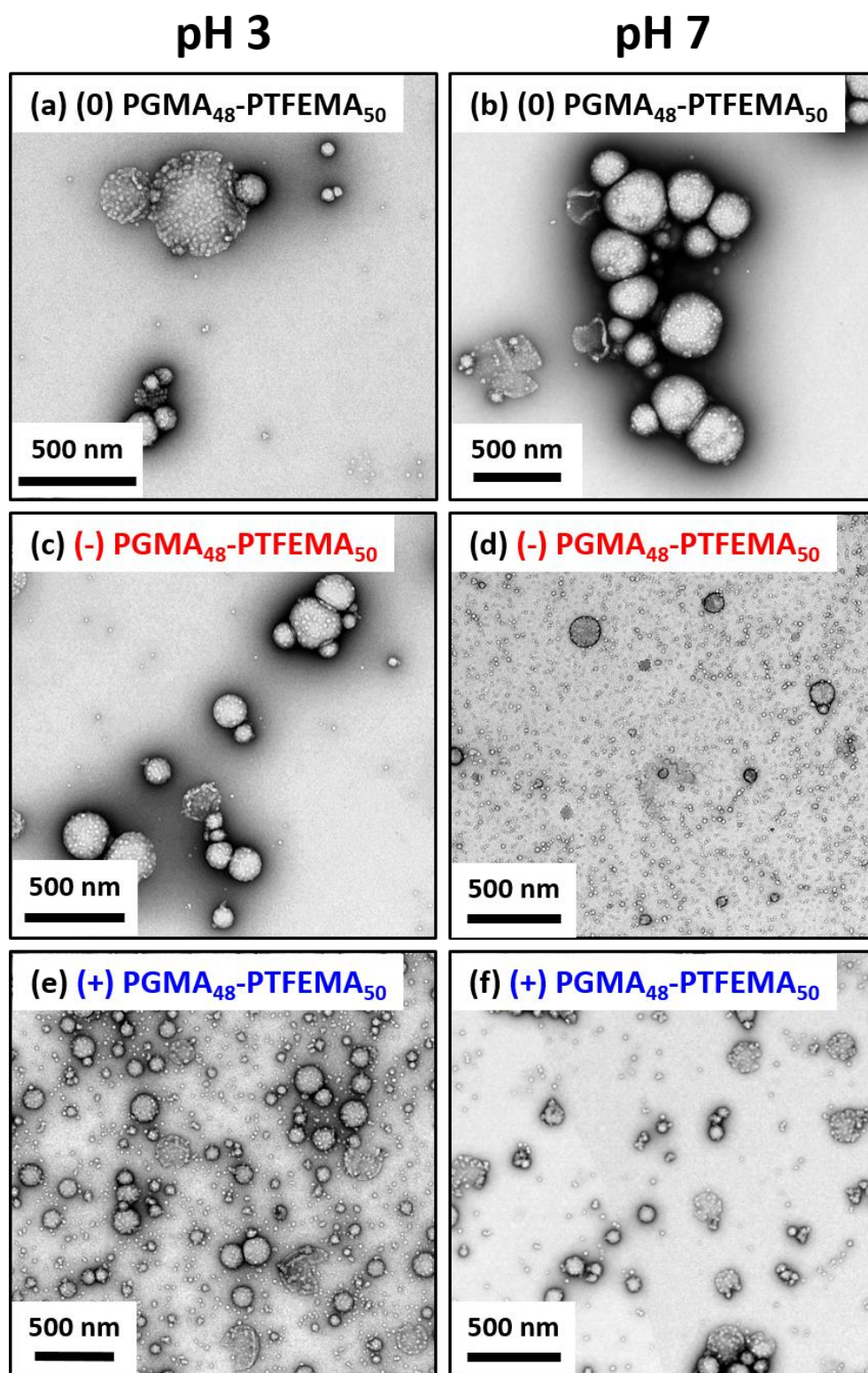


**Figure 2.8.** Representative TEM images obtained for dried *n*-dodecane-in-water Pickering nanoemulsions prepared with 7.0% w/w PGMA<sub>48</sub>-PTFEMA<sub>50</sub> diblock copolymer nanoparticles synthesised using (a) CPDB at pH 3 (neutral); (b) CPDB at pH 7 (weakly anionic); (c) PETTC at pH 3 (neutral); (d) PETTC at pH 7 (strongly anionic); (e) MPETTC at pH 3 (strongly cationic); (f) MPETTC at pH 7 (neutral). The nanoemulsions were prepared using an LV1 microfluidiser at an applied pressure of 20 000 psi for 10 passes.

## Chapter 2: How do Charged End-Groups on the Steric Stabiliser Block Influence the Formation and Long-Term Stability of Pickering Nanoemulsions Prepared Using Sterically-Stabilised Diblock Copolymer Nanoparticles?

---

TEM images were obtained for dried freshly-prepared Pickering nanoemulsions, see Figure 2.8. Although the volatile droplet phase is no longer present under the ultrahigh vacuum conditions required for TEM, some of the original superstructure of the adsorbed PGMA<sub>48</sub>-PTFEMA<sub>50</sub> nanoparticles is preserved. Such *postmortem* studies suggest that spherical oil droplets with nanoscale dimensions corresponding to that indicated by DLS studies were indeed formed when using each of the three nanoparticles as a Pickering emulsifier. It is perhaps worth highlighting that no salt was added to these oil-in-water Pickering macroemulsions prior to their microfluidisation. The hydrodynamic forces generated during this processing step are sufficient to form nanoemulsion droplets, despite the presence of charged end-groups on the steric stabiliser chains under certain conditions. Moreover, these TEM images provide useful qualitative indication of the adsorption efficiency of these nanoparticle emulsifiers when varying the solution pH. More specifically, when the aqueous dispersion pH is adjusted to generate either cationic or anionic end-groups, fewer nanoparticles are adsorbed at the oil/water interface, so the fraction of free (non-adsorbed) nanoparticles increases (compare Figures 2.8d and 2.8e with Figures 2.8c and 2.8f, respectively). In order to confirm that these observations are not simply a drying artefact during the TEM sample preparation, nanoparticle adsorption efficiencies were determined quantitatively using GPC. In addition, these Pickering nanoemulsions were analysed by SAXS.

Table 2.2 summarises the *z*-average droplet diameters  $D_z$ , nanoparticle adsorption efficiencies  $A_{\text{eff}}$ , nanoparticle packing efficiencies  $P_{\text{eff}}$  and zeta potentials determined for freshly-prepared Pickering nanoemulsions using each of the three types of nanoparticles at either pH 3 or 7. DLS studies indicate that changing the aqueous dispersion pH prior to microfluidisation leads to no systematic variation in the initial droplet diameter. However, varying this parameter leads to the steric stabiliser chain-ends acquiring charge, which has a significant effect on the nanoparticle adsorption efficiency, packing efficiency and zeta potential of the Pickering nanoemulsions. For nanoemulsions prepared using (-) PGMA<sub>48</sub>-PTFEMA nanoparticles, negative zeta potentials were obtained regardless of the pH. Thus a zeta potential of -7 mV is observed at

## Chapter 2: How do Charged End-Groups on the Steric Stabiliser Block Influence the Formation and Long-Term Stability of Pickering Nanoemulsions Prepared Using Sterically-Stabilised Diblock Copolymer Nanoparticles?

pH 3 whereas at pH 7 the zeta potential is -48 mV, which is more than twice that of the nanoparticles alone at the same pH (-22 mV). This is attributed to the formation of anionic carboxylate end-groups on the PGMA<sub>48</sub> steric stabiliser chains. In contrast, the (+) PGMA<sub>48</sub>-PTFEMA<sub>50</sub>-stabilised nanoemulsion exhibits minimal anionic character (-6 mV) at pH 7, whereas the zeta potential is strongly cationic (+27 mV) at pH 3 owing to protonation of the morpholine end-groups. This value is comparable to that exhibited by the (+) PGMA<sub>48</sub>-PTFEMA<sub>50</sub> nanoparticles alone at the same pH (+24 mV).

**Table 2.2.** Summary of the Pickering nanoemulsions prepared using either neutral (0) PGMA<sub>48</sub>-PTFEMA<sub>50</sub>, anionic (-) PGMA<sub>48</sub>-PTFEMA<sub>50</sub> or cationic (+) PGMA<sub>48</sub>-PTFEMA<sub>50</sub> diblock copolymer nanoparticles at either pH 3 or 7. <sup>a</sup>

End-group type	pH 3				pH 7			
	$D_z$ / nm	$A_{\text{eff}}$ / %	$P_{\text{eff}}$ / %	Zeta potential / mV	$D_z$ / nm	$A_{\text{eff}}$ / %	$P_{\text{eff}}$ / %	Zeta potential / mV
Neutral	197 ± 56	93	49	0 ± 3	200 ± 72	90	47	-14 ± 4
Anionic	215 ± 74	90	52	-7 ± 4	212 ± 60	49	27	-48 ± 5
Cationic	198 ± 56	63	33	+27 ± 4	204 ± 61	93	50	-6 ± 5

<sup>a</sup> $D_z$  =  $z$ -average droplet diameter;  $A_{\text{eff}}$  = Adsorption efficiency;  $P_{\text{eff}}$  = Packing efficiency.

The effect of varying the solution pH on the nanoparticle adsorption efficiency was assessed by GPC using a UV detector, see Table 2.2. Analysis of UV chromatograms recorded after serial dilution of the original aqueous nanoparticle dispersions enabled construction of a calibration plot of integrated UV signal against copolymer concentration at a wavelength of 305 nm (see Figure 7.1). This linear plot was used to quantify the concentration of non-adsorbed nanoparticles remaining in the aqueous phase after microfluidisation (after using centrifugation to remove the creamed oil droplets) and the extent of nanoparticle adsorption was calculated by difference. Figure 2.9 shows DLS  $z$ -average size distributions recorded for a Pickering nanoemulsion prepared before and after centrifugation. There is a minimal change in the  $z$ -average droplet diameter, indicating that centrifugation does not affect the number of non-adsorbed nanoparticles.

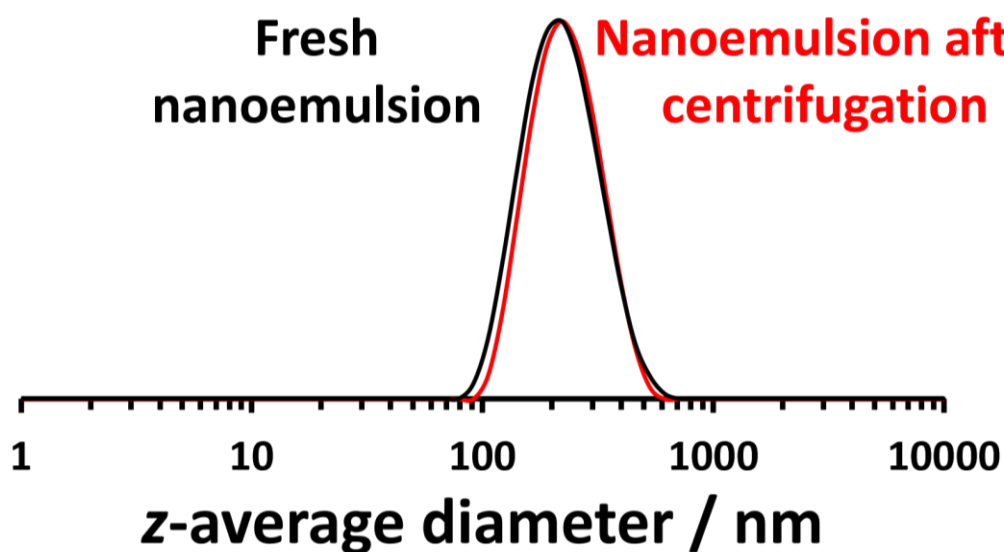


**Figure 2.9.** Overlaid DLS  $z$ -average size distributions recorded for a fresh Pickering nanoemulsion stabilised using (0) PGMA<sub>48</sub>-PTFEMA<sub>50</sub> nanoparticles (black trace) and the same Pickering nanoemulsion after being subjected to five centrifugation-redispersion cycles (red trace).

Figure 2.10 shows a UV GPC curve recorded for a 7% w/w aqueous dispersion of carboxylic acid-functionalised (-) PGMA<sub>48</sub>-PTFEMA<sub>50</sub> nanoparticles (black trace) overlaid with curves obtained after GPC analysis of the aqueous phase following high-pressure microfluidisation and centrifugation for Pickering nanoemulsions prepared at either pH 3 (red trace) or pH 7 (blue trace). The UV GPC signal is significantly lower for the aqueous dispersion at pH 3 relative to that at pH 7, indicating that significantly fewer nanoparticles are adsorbed under the latter conditions. This is consistent with the corresponding TEM images, which indicate that there are far more excess non-adsorbed nanoparticles present in the aqueous phase when the nanoemulsion is prepared at pH 7 when using (-) PGMA<sub>48</sub>-PTFEMA<sub>50</sub> compared to the other two types of nanoparticles. This suggests that anionic end-groups reduce the extent of nanoparticle adsorption at the oil/water interface, which is in agreement with the nanoparticle adsorption efficiency determined using UV GPC. In a complementary experiment, the solution pH of each 7% w/w aqueous dispersion of nanoparticles was adjusted to pH 3 prior to homogenisation. In this case, the adsorption efficiency of the (0) PGMA<sub>48</sub>-PTFEMA<sub>50</sub> nanoparticles remained almost

## Chapter 2: How do Charged End-Groups on the Steric Stabiliser Block Influence the Formation and Long-Term Stability of Pickering Nanoemulsions Prepared Using Sterically-Stabilised Diblock Copolymer Nanoparticles?

unchanged, whereas that of the carboxylic acid-functionalised (-) PGMA<sub>48</sub>-PTFEMA<sub>50</sub> nanoparticles increased significantly from 49% to 90%. On the other hand, the efficiency of the morpholine-functionalised (+) PGMA<sub>48</sub>-PTFEMA<sub>50</sub> nanoparticles was substantially reduced from 93% to 63%. Thus the introduction of surface charge clearly hinders efficient nanoparticle adsorption at the oil/water interface.

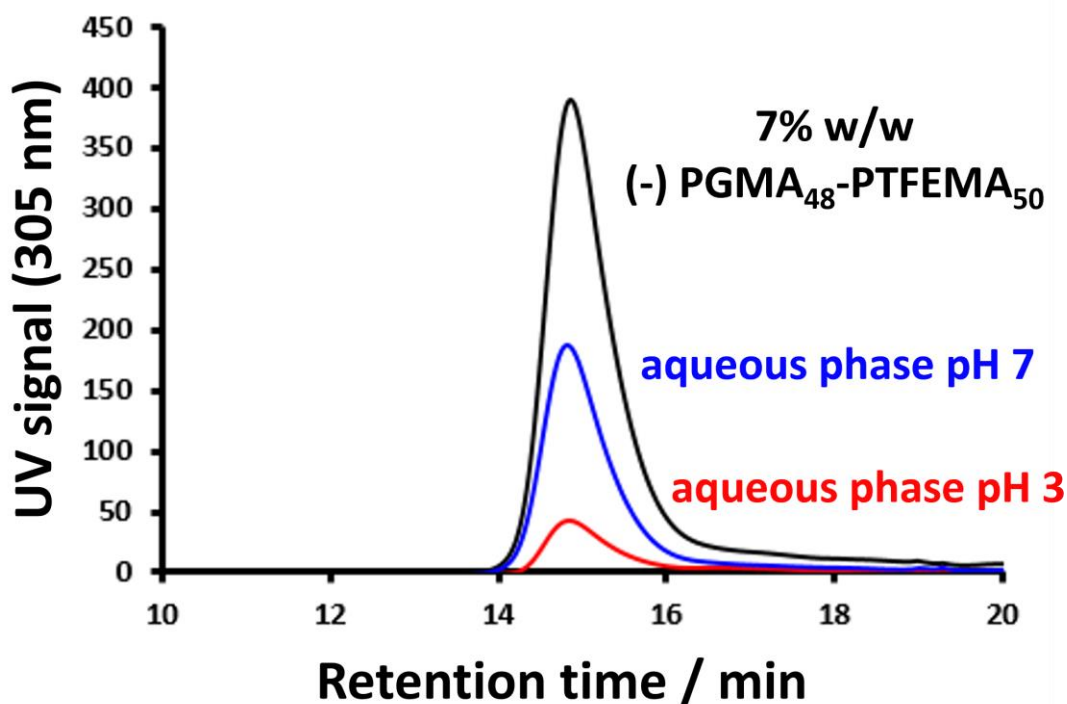


**Figure 2.10.** Overlaid DMF UV GPC curves obtained for a 7% w/w aqueous dispersion of (-) PGMA<sub>48</sub>-PTFEMA<sub>50</sub> nanoparticles (black trace), the aqueous phase after microfluidisation and centrifugation of nanoemulsions prepared using a 7% w/w aqueous dispersion of (-) PGMA<sub>48</sub>-PTFEMA<sub>50</sub> nanoparticles at either pH 7 (blue trace) or pH 3 (red trace). The UV signal is significantly lower for pH 3 compared to pH 7, which indicates that more nanoparticles have adsorbed at the oil/water interface at pH 3.

It has been previously reported that both anionic<sup>4, 8, 13</sup> and cationic<sup>4</sup> particles can be excluded from the oil/water interface owing to strong inter-particle repulsion, image charge effects<sup>4</sup> and, in the case of anionic particles, repulsion from the anionic oil/water interface.<sup>8</sup> However, interfacial adsorption can be achieved by either adjusting the solution pH or increasing the ionic strength to suppress surface charge.<sup>5</sup> In the current study, fewer nanoparticles are adsorbed at the oil/water interface during microfluidisation if they possess cationic or anionic

## Chapter 2: How do Charged End-Groups on the Steric Stabiliser Block Influence the Formation and Long-Term Stability of Pickering Nanoemulsions Prepared Using Sterically-Stabilised Diblock Copolymer Nanoparticles?

---

end-groups. Electrostatic repulsions between neighbouring copolymer nanoparticles suppresses their interfacial adsorption (FLUID-CHARGE REPULSION) This is because charged nanoparticles are more hydrophilic and thus are less strongly adsorbed at the oil/water interface.

As previously described, there is no discernible change in the  $z$ -average diameter of nanoemulsions at either pH 3 or 7. However, the nanoparticle adsorption efficiency differs significantly under such conditions. Since the volume of the oil phase is equal in each case, this implies substantial differences in the nanoparticle packing efficiency at the surface of the oil droplets.

Figure 2.11 shows volume-average cumulative size distributions recorded for each of the freshly-made nanoemulsions prepared at either pH 3 or 7, as determined by analytical centrifugation. In contrast to the  $z$ -average size distributions reported by DLS, there are clear differences in size for Pickering nanoemulsions prepared at pH 3 and pH 7. As noted by Thompson and co-workers, analytical centrifugation has a much higher resolution compared to DLS because droplet fractionation occurs prior to detection.<sup>45</sup> However, one drawback of the former technique is that the *effective particle density* is required to obtain an accurate particle size.<sup>33</sup> This parameter was estimated to be  $0.81 \text{ g cm}^{-3}$  for a PGMA<sub>48</sub>-PTFEMA<sub>50</sub> stabilised *n*-dodecane-in-water nanoemulsion. This value is higher than that of *n*-dodecane ( $0.75 \text{ g cm}^{-3}$ ) because the nanoparticle density is approximately  $1.15 \text{ g cm}^{-3}$ , as previously determined by Armes and co-workers.<sup>33</sup> Moreover, undersizing can be observed if the droplet concentration is too high owing to the phenomenon of hindered creaming.<sup>45, 62</sup> However, using droplet concentrations that are too low is also problematic: such dilute emulsions scatter light only rather weakly and hence fall outside of the optimum transmission range required for the LUMiSizer instrument (i.e. below 30 % transmission). Given these conflicting requirements, a droplet concentration of 1.0% v/v was found to be optimal.<sup>44</sup> In the current study, this concentration was used for all analytical centrifugation measurements. A further complication for this sizing technique is that a density distribution is superimposed on the droplet size distribution, as discussed by Thompson and co-

## Chapter 2: How do Charged End-Groups on the Steric Stabiliser Block Influence the Formation and Long-Term Stability of Pickering Nanoemulsions Prepared Using Sterically-Stabilised Diblock Copolymer Nanoparticles?

---

workers.<sup>45</sup> Overall, this means that analytical centrifugation is best utilised for monitoring *relative* changes in the droplet size distribution during long-term ageing of these Pickering nanoemulsions, rather than for determining *absolute* droplet diameters.

The volume-average cumulative size distributions shown in Figure 2.11 demonstrate that Pickering nanoemulsions prepared using nanoparticles that possess charged end-groups leads to the formation of larger, more polydisperse droplets. For example, nanoemulsions prepared using (-) PGMA<sub>48</sub>-PTFEMA<sub>50</sub> nanoparticles exhibited an initial volume-average droplet diameter of  $159 \pm 54$  nm at pH 3, whereas nanoemulsions prepared using the same nanoparticles at pH 7 had a significantly larger droplet diameter of  $218 \pm 169$  nm. This size difference can be correlated with the substantially different nanoparticle adsorption efficiencies noted above. More specifically, only 49% of the (-) PGMA<sub>48</sub>-PTFEMA<sub>50</sub> nanoparticles are adsorbed on the surface of the oil droplets at pH 7 compared to 90% at pH 3. Because there are far fewer nanoparticles adsorbed at the oil/water interface at pH 7, only relatively large oil droplets can be stabilised at the same copolymer concentration. A similar effect is observed for (+) PGMA<sub>48</sub>-PTFEMA<sub>50</sub> nanoparticles. Protonation of the morpholine end-groups at pH 3 leads to a 30% reduction in nanoparticle adsorption efficiency compared to the neutral form of such nanoparticles at pH 7. Thus interfacial adsorption of the nanoparticles is again suppressed, despite the favourable electrostatic attraction between the cationic nanoparticles and the anionic oil/water interface. These results demonstrate the importance of the choice of RAFT agent (which dictates the nature of the stabiliser end-groups) when designing diblock copolymer nanoparticles for use as Pickering emulsifiers.

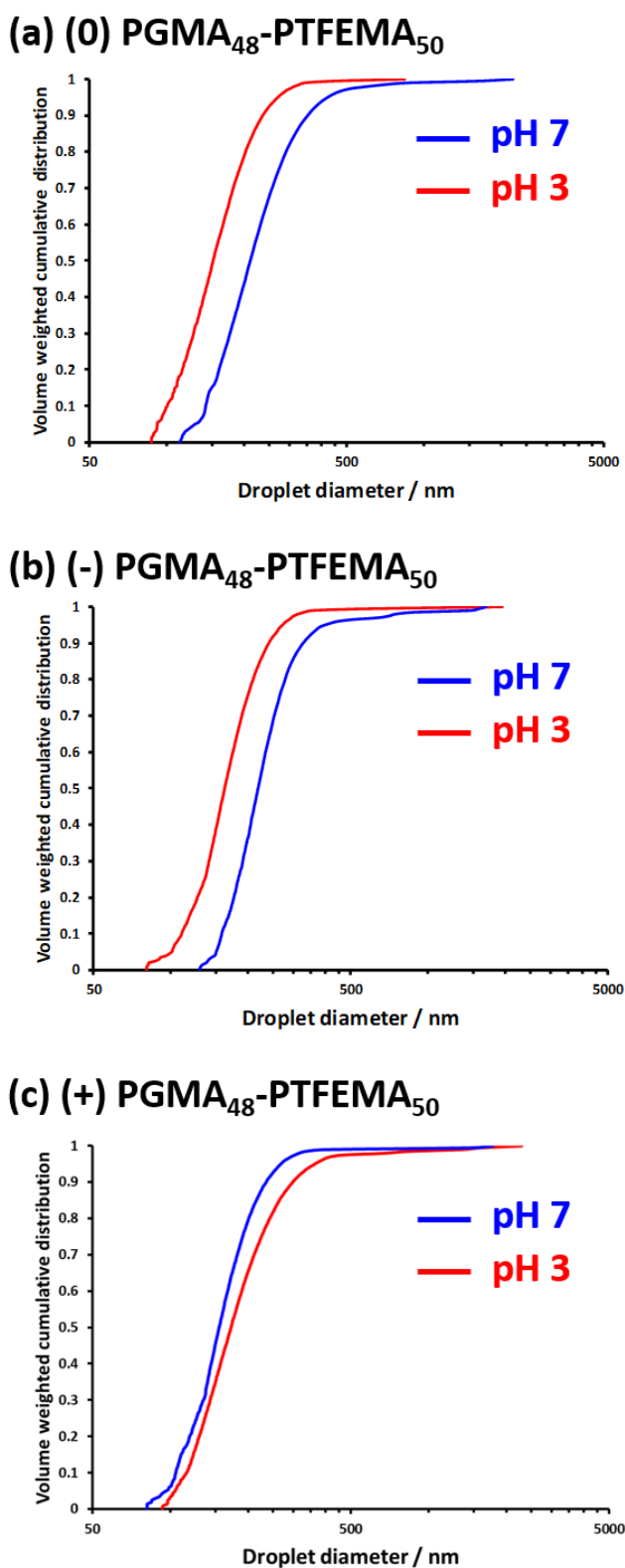


**Figure 2.11.** Volume-weighted cumulative size distributions determined by analytical centrifugation (LUMiSizer instrument) obtained for *n*-dodecane-in-water nanoemulsions prepared with 7.0% w/w PGMA<sub>48</sub>-PTFEMA<sub>50</sub> diblock copolymer nanoparticles synthesised using: (a) CPDB (0), (b) PETTC (-) or (c) MPETTC (+) as the RAFT agent. Microfluidisation conditions: applied pressure = 20 000 psi, ten passes and a solution pH of either 3 or 7.

## Chapter 2: How do Charged End-Groups on the Steric Stabiliser Block Influence the Formation and Long-Term Stability of Pickering Nanoemulsions Prepared Using Sterically-Stabilised Diblock Copolymer Nanoparticles?

---

TEM studies suggest that these Pickering nanoemulsions possess a core-shell morphology with a particulate shell. However, this technique cannot be used to assess the surface coverage of the *n*-dodecane droplets by the adsorbed layer of nanoparticles. Prior studies indicate that scattering techniques should provide useful information in this context.<sup>63</sup> Thus SAXS patterns were recorded for freshly-prepared Pickering nanoemulsions after dilution to 1.0% v/v (Figure 2.12). Following our prior study of the characterisation of core-shell nanocomposite particles comprising polymer latex cores and particulate silica shells,<sup>64</sup> the SAXS data were analysed using a two-population model (see Chapter 7). Population 1 is represented by core-shell spheres, where the cores comprise the oil droplets and the adsorbed layer of nanoparticles form the shell (see Equation 7.2). The particulate nature of the shell is described by small homogeneous spheres which corresponds to population 2 (see Equation 7.6). The packing of the block copolymer spheres within the shell is described by a hard-sphere structure factor (solved using the Percus-Yevick closure relation).<sup>58, 64</sup> First, SAXS patterns recorded for the nanoparticles (see Figure 2.6) were fitted using a spherical form factor<sup>57</sup>. The resulting mean particle radius  $R_s$  and its associated standard deviation  $\sigma_s$  (Table 2.1) were consistent with those obtained by DLS and TEM studies (Figure 2.5). These two parameters were subsequently fixed when fitting the SAXS patterns of the Pickering nanoemulsions using the two-population model (see Table 2.3). The scattering length density for each component of the Pickering nanoemulsions (oil core  $\zeta_c$ , particulate shell  $\zeta_{\text{shell}}$  and surrounding liquid  $\zeta_{\text{solvent}}$ ) was calculated based on their respective known chemical compositions and mass densities (see Table 2.3). These three parameters were also fixed for the subsequent SAXS data fitting. The packing efficiency for the nanoparticles within the particulate shell surrounding the oil droplets was included in such calculations (see Table 2.2). The structure of these Pickering nanoemulsions can be described by the mean core radius  $R_c$  and its standard deviation  $\sigma_c$ , the mean shell thickness  $T_s$ , the hard-sphere interaction radius  $R_{\text{PY}}$  and its effective volume fraction  $f_{\text{PY}}$  and two scaling factors (volume fraction  $\varphi_1$  for population 1 and volume fraction  $\varphi_2$  for population, respectively). These seven parameters were allowed to vary when fitting the SAXS data.

**Chapter 2: How do Charged End-Groups on the Steric Stabiliser Block Influence the Formation and Long-Term Stability of Pickering Nanoemulsions Prepared Using Sterically-Stabilised Diblock Copolymer Nanoparticles?**

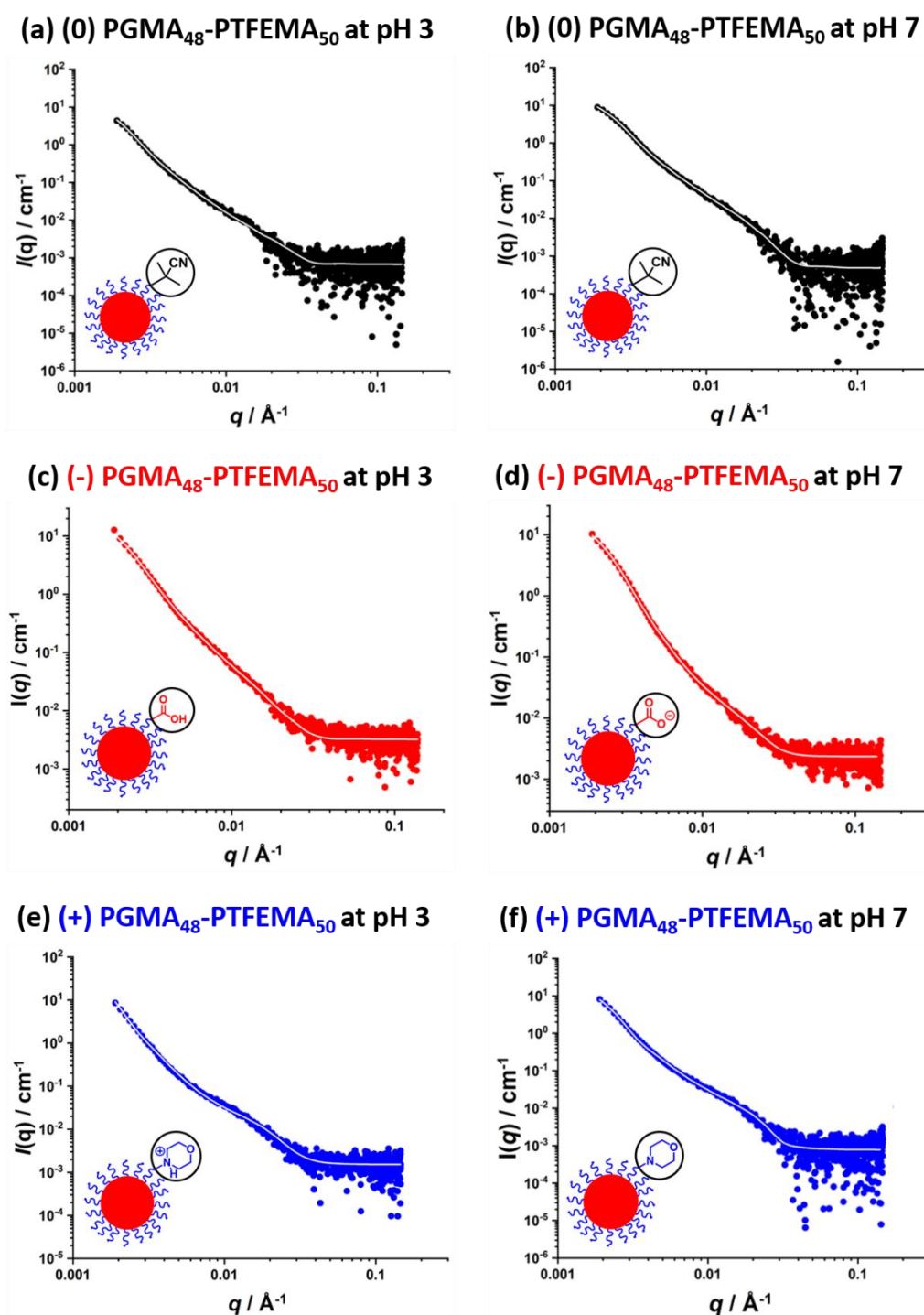


**Figure 2.12.** Experimental SAXS patterns (circles) and calculated data fits (white lines) obtained for 1.0% v/v nanoemulsions prepared using (a) CPDB at pH 3 (neutral nanoparticles); (b) CPDB at pH 7 (weakly anionic nanoparticles); (c) PETTC at pH 3 (neutral nanoparticles); (d) PETTC at pH 7 (strongly anionic nanoparticles); (e) MPETTC at pH 3 (strongly cationic nanoparticles); (f) MPETTC at pH 7 (neutral nanoparticles). Each nanoemulsion was prepared using an LV1 microfluidiser at an applied pressure of 20 000 psi for ten passes. The two-population core-shell structural model used for the SAXS analysis of such Pickering nanoemulsions comprises large oil droplet cores coated with a layer (or shell) of adsorbed spherical nanoparticles.<sup>64</sup>

## Chapter 2: How do Charged End-Groups on the Steric Stabiliser Block Influence the Formation and Long-Term Stability of Pickering Nanoemulsions Prepared Using Sterically-Stabilised Diblock Copolymer Nanoparticles?

---

SAXS patterns for the nanoemulsions comprised three distinct regions: (i) relatively intense scattering at low  $q$  arising from the nanoemulsion droplets (where close inspection reveals a subtle change in gradient at low  $q$ , indicating cross-over from the Porod region to the Guinier region); (ii) additional scattering intensity at intermediate  $q$  corresponding to the copolymer nanoparticle form factor (Figure 2.6) and (iii) relatively weak scattering at high  $q$ , which is most likely associated with thermal fluctuations in the oil density and copolymer components (accordingly, constant background scattering has been incorporated into the model to account for this feature). The two-population model produced a reasonably good fit to the experimental SAXS pattern obtained for each Pickering nanoemulsion. The lack of well-defined minima in these scattering curves suggests that the nanoemulsion droplets are somewhat polydisperse in terms of their size, which is consistent with TEM and DLS studies. Mean droplet radii calculated using the two-population model (Table 2.2) were consistent with those reported by DLS and analytical centrifugation (Table 2.2 and Figure 2.11, respectively). However, these values are not particularly accurate owing to our laboratory-based SAXS instrument, which has limited resolution at low  $q$ . The mean apparent thickness of the shell of adsorbed nanoparticles calculated for these Pickering nanoemulsions was approximately 12 - 15 nm in each case, which is less than the mean diameter of an individual nanoparticle ( $\sim 22$  nm, Table 2.1). This is reasonably consistent with the relatively low surface coverage of the oil droplets by the nanoparticles, which exhibit packing efficiencies of 27 - 52% (Table 2.2). Furthermore,  $T_s$  varied with solution pH for the Pickering nanoemulsions prepared with (-) and (+) PGMA<sub>48</sub>-PTFEMA<sub>50</sub> nanoparticles (Table 2.3). For example,  $T_s$  was calculated to be 11.9 nm for nanoemulsions prepared using (-) PGMA<sub>48</sub>-PTFEMA<sub>50</sub> nanoparticles at pH 7, whereas those prepared using the same nanoparticles at pH 3 had a significantly thicker shell of 14.7 nm. This is consistent with a higher packing efficiency under the latter conditions when the nanoparticles are in their neutral form (Table 2.2). In contrast,  $T_s$  decreases for the (+) PGMA<sub>48</sub>-PTFEMA<sub>50</sub> nanoparticles on switching from pH 7 to pH 3 (Table 2.3). Finally, the  $T_s$  values determined for Pickering nanoemulsions stabilised using the neutral nanoparticles are essentially independent of solution pH, indicating no significant change in the

## Chapter 2: How do Charged End-Groups on the Steric Stabiliser Block Influence the Formation and Long-Term Stability of Pickering Nanoemulsions Prepared Using Sterically-Stabilised Diblock Copolymer Nanoparticles?

nanoparticle packing efficiency under such conditions. The hard-sphere interaction radius  $R_{PY}$  and its effective volume fraction  $f_{PY}$  calculated from the two-population model are reasonable. However, it would be difficult to correlate these data with the structural arrangement of the block copolymer nanoparticles within the shell. This is because this hard-sphere model does not account for the spherical geometry of the core-shell structure. Nevertheless, for the nanoparticles distributed within the shell by repulsive interactions,  $R_{PY}$  correlates well with the thickness of the shell  $T_s$  (Table 2.3). Using nanoparticles with charged end-groups necessarily increases the particle-particle separation distance within the shell, leading to a lower packing efficiency and lower  $T_s$ .

**Table 2.3.** Structural parameters obtained by SAXS analysis of 1.0% v/v Pickering nanoemulsions comprising *n*-dodecane droplets prepared using either neutral (0) PGMA<sub>48</sub>-PTFEMA<sub>50</sub>, (-) PGMA<sub>48</sub>-PTFEMA<sub>50</sub> or (+) PGMA<sub>48</sub>-PTFEMA<sub>50</sub> diblock copolymer nanoparticles at either pH 3 or 7.<sup>a</sup>

End-group type	pH 3						pH 7					
	$R_c$ / nm	$\sigma_c$ / nm	$T_s$ / nm	$\zeta_{shell} \times 10^{-10}$ cm <sup>-2</sup>	$R_{PY}$ / nm	$f_{PY}$	$R_c$ / nm	$\sigma_c$ / nm	$T_s$ / nm	$\zeta_{shell} \times 10^{-10}$ cm <sup>-2</sup>	$R_{PY}$ / nm	$f_{PY}$
Neutral	127	41	14.9	10.85	24	0.15	118	35	14.4	10.79	25	0.17
Anionic	104	41	14.7	10.93	27	0.13	94	36	11.9	10.21	30	0.17
Cationic	162	47	12.2	10.38	32	0.17	128	32	14.2	10.88	25	0.15

<sup>a</sup> $R_c$  = mean core radius;  $\sigma_c$  = standard deviation of the core radius;  $T_s$  = mean shell thickness;  $\zeta_{shell}$  = effective scattering length density of the particulate shell;  $R_s$  = copolymer nanoparticle radius,  $\sigma_s$  = standard deviation of the copolymer nanoparticle radius;  $R_{PY}$  = hard-sphere interaction radius;  $f_{PY}$  = effective volume fraction. Parameters used for modelling are as follows:  $\zeta_{solvent} = 9.42 \times 10^{10}$  cm<sup>-2</sup>;  $\zeta_c = 7.32 \times 10^{10}$  cm<sup>-2</sup>; neutral  $R_s = 10.7$  nm,  $\sigma_s = 1.3$  nm; anionic  $R_s = 10.8$  nm,  $\sigma_s = 1.4$  nm; cationic  $R_s = 11.5$  nm,  $\sigma_s = 2.5$  nm. The  $\zeta_{shell}$  was calculated by averaging the scattering length densities of the PGMA stabiliser block ( $11.94 \times 10^{10}$  cm<sup>-2</sup>), the PTFEMA core-forming block ( $12.76 \times 10^{10}$  cm<sup>-2</sup>) and the solvent (water) based on the copolymer composition and packing efficiency of the copolymer nanoparticles at the surface of the oil droplets.

### 2.3.3 Effect of End-Group Charge on the Stability of Pickering Nanoemulsions

To examine the effect of the stabiliser end-groups on the long-term stability of the nanoemulsions, analytical centrifugation was used to determine the mean droplet size after ageing for both one week and six weeks at 20 °C. Volume-weighted cumulative size distributions for freshly-prepared and one-week-old nanoemulsions at pH 7 and pH 3 are shown in Figure 2.13.

## Chapter 2: How do Charged End-Groups on the Steric Stabiliser Block Influence the Formation and Long-Term Stability of Pickering Nanoemulsions Prepared Using Sterically-Stabilised Diblock Copolymer Nanoparticles?

Nanoemulsions stabilised by nanoparticles with anionic or cationic end-groups (see Figure 2.13b and 2.13c) displayed the greatest rate of droplet growth within one week. The droplet size distributions of such aged nanoemulsions are relatively unimodal. In contrast, nanoemulsions stabilised by nanoparticles prepared with neutral end-groups (see Figures 2.13a and 2.13d) possess distinctly bimodal size distributions after ageing for one week, with the minor population corresponding to the original droplets.

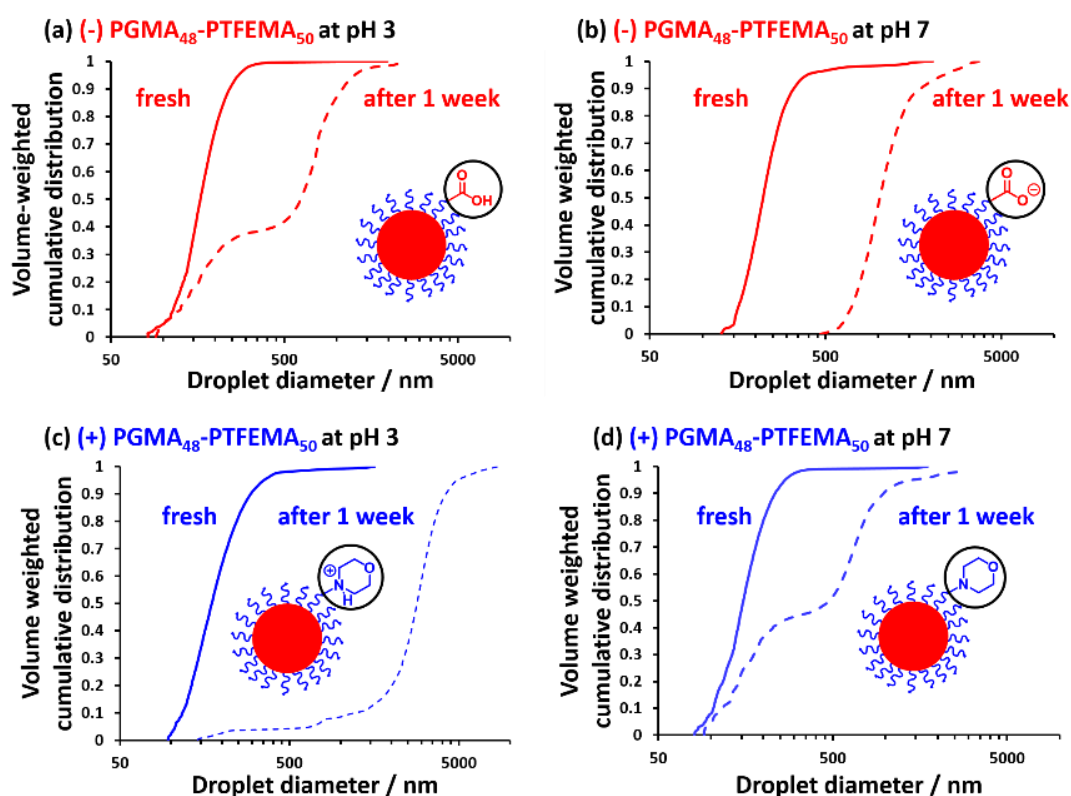


**Figure 2.13.** Volume-weighted cumulative size distributions determined by analytical centrifugation (LUMiSizer instrument) for fresh (solid line) and aged (for one week at 20 °C, dashed line) *n*-dodecane-in-water Pickering nanoemulsions prepared using 7.0% w/w PGMA<sub>48</sub>-PTFEMA<sub>50</sub> diblock copolymer nanoparticles synthesised with the following RAFT agents: (a) PETTC, aged at pH 3; (b) PETTC, aged at pH 7; (c) MPETTC, aged at pH 3; (d) MPETTC, aged at pH 7. Microfluidiser conditions: 20 000 psi; ten passes.

The extent of Ostwald ripening is similar for nanoemulsions stabilised by either (+) PGMA<sub>48</sub>-PTFEMA<sub>50</sub> or (-) PGMA<sub>48</sub>-PTFEMA<sub>50</sub>: around 60% of the oil droplets exceed approximately 500 nm after ageing for one week at 20 °C. As shown above, using neutral nanoparticles as Pickering emulsifiers leads to adsorption efficiencies of around 90%. According to UV GPC studies, the nanoparticle adsorption efficiency for the charged nanoparticles is

## Chapter 2: How do Charged End-Groups on the Steric Stabiliser Block Influence the Formation and Long-Term Stability of Pickering Nanoemulsions Prepared Using Sterically-Stabilised Diblock Copolymer Nanoparticles?

significantly lower than that for the corresponding neutral nanoparticles. Moreover, a somewhat lower droplet surface coverage is anticipated in the former case because of lateral electrostatic repulsion between neighbouring adsorbed nanoparticles: this is also expected to facilitate faster droplet growth *via* coalescence.<sup>65</sup> In practice, the calculated packing efficiencies for anionic or cationic nanoparticles adsorbed onto the oil droplets are 27% or 33% respectively, which are significantly lower than those observed for the adsorbed neutral nanoparticles (~ 47 - 49%) (Table 2.2). These lower surface coverages mean that the adsorbed layers of charged nanoparticles provide a somewhat less effective barrier towards droplet coalescence.<sup>15, 66, 67</sup> Thus the corresponding nanoemulsions exhibit inferior long-term stability with respect to Ostwald ripening.<sup>44, 45, 61, 68, 69</sup> Similar observations have been reported in the literature for surfactant-stabilised nanoemulsions.<sup>70</sup>

**Table 2.4.** Variation in mean droplet diameter with ageing time as determined by analytical centrifugation for Pickering nanoemulsions stabilised using nanoparticles with either neutral, anionic or cationic end-groups.

End-group type	Mean droplet diameter determined by analytical centrifugation (nm)					
	pH 3			pH 7		
	fresh	1 week	6 weeks	fresh	1 week	6 weeks
<b>Neutral</b>	176 ± 130	177 ± 142	177 ± 419	207 ± 162	208 ± 314	184 ± 411
<b>Anionic</b>	159 ± 108	292 ± 425	868 ± 1326	218 ± 169	1005 ± 524	2017 ± 886
<b>Cationic</b>	171 ± 136	1283 ± 1691	1937 ± 2938	140 ± 118	257 ± 500	323 ± 1246

Table 2.4 reports the mean volume-average droplet diameter determined by analytical centrifugation for Pickering nanoemulsions prepared using each of the three types of nanoparticles after ageing at 20 °C for up to six weeks. In each case, there is evidence for Ostwald ripening but nanoemulsions prepared using nanoparticles bearing charged end-groups undergo substantially greater ripening compared to those prepared using approximately neutral nanoparticles. Nanoparticles prepared using the CPDB RAFT agent formed the most stable nanoemulsions: the mean droplet diameter actually remains roughly constant, but the width of the size distribution increases significantly. Nanoemulsions prepared using (+) PGMA<sub>48</sub>-PTFEMA<sub>50</sub> nanoparticles at pH 3 grew from 171 ± 135 μm to 1937 ± 2938 μm, whereas the mean droplet

## Chapter 2: How do Charged End-Groups on the Steric Stabiliser Block Influence the Formation and Long-Term Stability of Pickering Nanoemulsions Prepared Using Sterically-Stabilised Diblock Copolymer Nanoparticles?

---

diameter only increased from  $140 \pm 118 \text{ nm}$  to  $323 \pm 1246 \text{ nm}$  at pH 7. Perhaps surprisingly, nanoemulsions prepared using the (-) PGMA<sub>48</sub>-PTFEMA<sub>50</sub> nanoparticles proved to be relatively unstable with respect to ageing regardless of the solution pH. Overall, it is clear that using charged nanoparticles as Pickering emulsifiers produces nanoemulsions with inferior long-term stability. Interestingly, the nanoemulsion zeta potential cannot be used to reliably predict the long-term stability of such Pickering nanoemulsions.

## 2.4 Conclusions

The effect of charged end-groups on the formation and long-term stability of Pickering nanoemulsions has been explored using model sterically-stabilised diblock copolymer nanoparticles prepared by PISA. More specifically, such nanoparticles were prepared by chain-extending a water-soluble non-ionic PGMA<sub>48</sub> precursor *via* RAFT aqueous emulsion polymerisation of TFEMA to produce well-defined spherical nanoparticles of approximately 20 nm diameter in each case, as judged by DLS, TEM and SAXS studies. Aqueous electrophoresis studies indicated that nanoparticles prepared using PGMA chains with terminal carboxylic acid end-groups displayed strong anionic character at pH 7, whereas those containing a terminal tertiary amine end-group exhibited strong cationic character at pH 3. On the other hand, nanoparticles prepared using a neutral RAFT agent displayed only weakly anionic character at pH 7, most likely owing to hydroxide ion adsorption. These three types of sterically-stabilised nanoparticles were used in turn to prepare *n*-dodecane-in-water nanoemulsions *via* high-pressure microfluidisation at either pH 3 or pH 7. DLS studies confirmed that mean droplet diameters of approximately 200 nm can be readily obtained. TEM studies indicated that the nanoparticle superstructure remained intact on drying, thus providing evidence for the Pickering nature of these nanoemulsions. Mean droplet diameters obtained for the fresh nanoemulsions using analytical centrifugation were all equal to or less than 200 nm. UV GPC analysis of the aqueous phase enabled quantification of the excess non-adsorbed nanoparticles. In the absence of any charged end-groups, the nanoparticle adsorption efficiency was calculated to be approximately 90%.

## Chapter 2: How do Charged End-Groups on the Steric Stabiliser Block Influence the Formation and Long-Term Stability of Pickering Nanoemulsions Prepared Using Sterically-Stabilised Diblock Copolymer Nanoparticles?

---

However, the presence of charged end-groups significantly reduced the nanoparticle adsorption efficiency. This is because electrostatic repulsions between neighbouring copolymer nanoparticles suppresses their interfacial adsorption and reduces their packing efficiency at the oil/water interface. This was confirmed by analysing SAXS patterns recorded for the Pickering nanoemulsions using a two-population model. Furthermore, long-term stability studies using analytical centrifugation revealed significantly faster droplet coarsening *via* Ostwald ripening for the latter Pickering nanoemulsions compared to those prepared using neutral nanoparticles under comparable conditions. This was attributed to the lower packing efficiencies for oil droplets stabilised by nanoparticles bearing charged end-groups compared to those observed for neutral nanoparticles.

## 2.5 References

1. B. P. Binks, *Curr. Opin. Colloid Interface Sci.*, 2002, **7**, 21-41.
2. B. P. Binks, *Langmuir*, 2017, **33**, 6947-6963.
3. O. S. Deshmukh, D. van den Ende, M. C. Stuart, F. Mugele and M. H. G. Duits, *Adv. Colloid Interface Sci.*, 2015, **222**, 215-227.
4. H. Wang, V. Singh and S. H. Behrens, *J. Phys. Chem. Lett.*, 2012, **3**, 2986-2990.
5. J. Vialetto and M. Anyfantakis, *Langmuir*, 2021, **37**, 9302-9335.
6. J. N. Israelachvili, *Intermolecular and Surface Forces*, Academic Press, San Diego, Third edn., 2011.
7. K. G. Marinova, R. G. Alargova, N. D. Denkov, O. D. Velev, D. N. Petsev, I. B. Ivanov and R. P. Borwankar, *Langmuir*, 1996, **12**, 2045-2051.
8. K. Roger and B. Cabane, *Angew. Chem. Int. Ed.*, 2012, **51**, 5625-5628.
9. B. P. Binks and C. P. Whitby, *Colloids Surf., A*, 2005, **253**, 105-115.
10. F. Reincke, S. G. Hickey, W. K. Kegel and D. Vanmaekelbergh, *Angew. Chem. Int. Ed.*, 2004, **43**, 458-462.
11. B. P. Binks and S. O. Lumsdon, *Phys. Chem. Chem. Phys.*, 1999, **1**, 3007-3016.
12. K. Golemanov, S. Tcholakova, P. A. Kralchevsky, K. P. Ananthapadmanabhan and A. Lips, *Langmuir*, 2006, **22**, 4968-4977.
13. S. Tcholakova, N. D. Denkov and A. Lips, *Phys. Chem. Chem. Phys.*, 2008, **10**, 1608-1627.
14. D. E. Tambe and M. M. Sharma, *J. Colloid Interface Sci.*, 1993, **157**, 244-253.
15. L. Ridel, M.-A. Bolzinger, N. Gilon-Delepine, P.-Y. Dugas and Y. Chevalier, *Soft Matter*, 2016, **12**, 7564-7576.
16. J. Frelichowska, M.-A. Bolzinger and Y. Chevalier, *Colloids Surf., A*, 2009, **343**, 70-74.

## Chapter 2: How do Charged End-Groups on the Steric Stabiliser Block Influence the Formation and Long-Term Stability of Pickering Nanoemulsions Prepared Using Sterically-Stabilised Diblock Copolymer Nanoparticles?

---

17. C. J. Mable, K. L. Thompson, M. J. Derry, O. O. Mykhaylyk, B. P. Binks and S. P. Armes, *Macromolecules*, 2016, **49**, 7897-7907.
18. S. L. Kettlewell, A. Schmid, S. Fujii, D. Dupin and S. P. Armes, *Langmuir*, 2007, **23**, 11381-11386.
19. V. Mikulcová, R. Bordes, A. Minařík and V. Kašpárková, *Food Hydrocolloids*, 2018, **80**, 60-67.
20. Y. Chai, A. Lukito, Y. Jiang, P. D. Ashby and T. P. Russell, *Nano Letters*, 2017, **17**, 6453-6457.
21. B. J. Park, J. P. Pantina, E. M. Furst, M. Oettel, S. Reynaert and J. Vermant, *Langmuir*, 2008, **24**, 1686-1694.
22. S. Reynaert, P. Moldenaers and J. Vermant, *Langmuir*, 2006, **22**, 4936-4945.
23. J. I. Amalvy, S. P. Armes, B. P. Binks, J. A. Rodrigues and G. F. Unali, *Chem. Commun.*, 2003, 1826-1827.
24. N. P. Ashby and B. P. Binks, *Phys. Chem. Chem. Phys.*, 2000, **2**, 5640-5646.
25. V. Garbin, J. C. Crocker and K. J. Stebe, *J. Colloid Interface Sci.*, 2012, **387**, 1-11.
26. S. Shahid and M. G. Basavaraj, *J. Colloid Interface Sci.*, 2021, **597**, 409-421.
27. T. Nallamilli, B. P. Binks, E. Mani and M. G. Basavaraj, *Langmuir*, 2015, **31**, 11200-11208.
28. Z. Liu, M. Hu, S. Zhang, L. Jiang, F. Xie and Y. Li, *J. Sci. Food Agric.*, 2021, **101**, 3003-3012.
29. S. L. Canning, G. N. Smith and S. P. Armes, *Macromolecules*, 2016, **49**, 1985-2001.
30. V. J. Cunningham, A. M. Alswieleh, K. L. Thompson, M. Williams, G. J. Leggett, S. P. Armes and O. M. Musa, *Macromolecules*, 2014, **47**, 5613-5623.
31. E. R. Jones, M. Semsarilar, A. Blanazs and S. P. Armes, *Macromolecules*, 2012, **45**, 5091-5098.
32. N. J. Warren and S. P. Armes, *J. Am. Chem. Soc.*, 2014, **136**, 10174-10185.
33. B. Akpınar, L. A. Fielding, V. J. Cunningham, Y. Ning, O. O. Mykhaylyk, P. W. Fowler and S. P. Armes, *Macromolecules*, 2016, **49**, 5160-5171.
34. F. L. Hatton, J. R. Lovett and S. P. Armes, *Polym. Chem.*, 2017, **8**, 4856-4868.
35. C. J. Ferguson, R. J. Hughes, B. T. T. Pham, B. S. Hawkett, R. G. Gilbert, A. K. Serelis and C. H. Such, *Macromolecules*, 2002, **35**, 9243-9245.
36. C. J. Ferguson, R. J. Hughes, D. Nguyen, B. T. T. Pham, R. G. Gilbert, A. K. Serelis, C. H. Such and B. S. Hawkett, *Macromolecules*, 2005, **38**, 2191-2204.
37. D. E. Ganeva, E. Sprong, H. de Bruyn, G. G. Warr, C. H. Such and B. S. Hawkett, *Macromolecules*, 2007, **40**, 6181-6189.
38. I. Chaduc, A. Crepet, O. Boyron, B. Charleux, F. D'Agosto and M. Lansalot, *Macromolecules*, 2013, **46**, 6013-6023.
39. I. Chaduc, W. Zhang, J. Rieger, M. Lansalot, F. D'Agosto and B. Charleux, *Macromol. Rapid Commun.*, 2011, **32**, 1270-1276.
40. I. Chaduc, M. Girod, R. Antoine, B. Charleux, F. D'Agosto and M. Lansalot, *Macromolecules*, 2012, **45**, 5881-5893.
41. C. K. Poon, O. Tang, X.-M. Chen, B. T. T. Pham, G. Gody, C. A. Pollock, B. S. Hawkett and S. Perrier, *Biomacromolecules*, 2016, **17**, 965-973.

## Chapter 2: How do Charged End-Groups on the Steric Stabiliser Block Influence the Formation and Long-Term Stability of Pickering Nanoemulsions Prepared Using Sterically-Stabilised Diblock Copolymer Nanoparticles?

---

42. P. B. Zetterlund, S. C. Thickett, S. Perrier, E. Bourgeat-Lami and M. Lansalot, *Chem. Rev.*, 2015, **115**, 9745-9800.
43. C. J. Mable, N. J. Warren, K. L. Thompson, O. O. Mykhaylyk and S. P. Armes, *Chem. Sci.*, 2015, **6**, 6179-6188.
44. K. L. Thompson, N. Cinotti, E. R. Jones, C. J. Mable, P. W. Fowler and S. P. Armes, *Langmuir*, 2017, **33**, 12616-12623.
45. K. L. Thompson, M. J. Derry, F. L. Hatton and S. P. Armes, *Langmuir*, 2018, **34**, 9289-9297.
46. J. Tan, H. Sun, M. Yu, B. S. Sumerlin and L. Zhang, *ACS Macro Lett.*, 2015, **4**, 1249-1253.
47. M. Li, P. De, S. R. Gondi and B. S. Sumerlin, *J. Polym. Sci., Part A: Polym. Chem.*, 2008, **46**, 5093-5100.
48. S. Perrier and P. Takolpuckdee, *J. Polym. Sci., Part A: Polym. Chem.*, 2005, **43**, 5347-5393.
49. J. R. Lovett, N. J. Warren, L. P. D. Ratcliffe, M. K. Kocik and S. P. Armes, *Angew. Chem. Int. Ed.*, 2015, **54**, 1279-1283.
50. J. R. Lovett, N. J. Warren, S. P. Armes, M. J. Smallridge and R. B. Cracknell, *Macromolecules*, 2016, **49**, 1016-1025.
51. N. J. W. Penfold, J. R. Lovett, N. J. Warren, P. Verstraete, J. Smets and S. P. Armes, *Polym. Chem.*, 2016, **7**, 79-88.
52. N. J. W. Penfold, J. R. Lovett, P. Verstraete, J. Smets and S. P. Armes, *Polym. Chem.*, 2017, **8**, 272-282.
53. R. R. Gibson, S. P. Armes, O. M. Musa and A. Fernyhough, *Polym. Chem.*, 2019, **10**, 1312-1323.
54. J. Ilavsky and P. R. Jemian, *J. Appl. Crystallogr.*, 2009, **42**, 347-353.
55. J. A. Balmer, S. P. Armes, P. W. Fowler, T. Tarnai, Z. Gáspár, K. A. Murray and N. S. J. Williams, *Langmuir*, 2009, **25**, 5339-5347.
56. K. L. Thompson, L. A. Fielding, O. O. Mykhaylyk, J. A. Lane, M. J. Derry and S. P. Armes, *Chem. Sci.*, 2015, **6**, 4207-4214.
57. R.-J. Roe, *Methods of X-ray and Neutron Scattering in Polymer Science*, Oxford University Press, New York, 2000.
58. J. K. Percus and G. J. Yevick, *Physical Review*, 1958, **110**, 1-13.
59. J. S. Pedersen, *J. Chem. Phys.*, 2001, **114**, 2839-2846.
60. T. J. Neal, D. L. Beattie, S. J. Byard, G. N. Smith, M. W. Murray, N. S. J. Williams, S. N. Emmett, S. P. Armes, S. G. Spain and O. O. Mykhaylyk, *Macromolecules*, 2018, **51**, 1474-1487.
61. K. H. Persson, I. A. Blute, I. C. Mira and J. Gustafsson, *Colloids Surf., A*, 2014, **459**, 48-57.
62. J. Walter, T. Thajudeen, S. Su, D. Segets and W. Peukert, *Nanoscale*, 2015, **7**, 6574-6587.
63. K. Larson-Smith, A. Jackson and D. C. Pozzo, *Langmuir*, 2012, **28**, 2493-2501.
64. J. A. Balmer, O. O. Mykhaylyk, A. Schmid, S. P. Armes, J. P. A. Fairclough and A. J. Ryan, *Langmuir*, 2011, **27**, 8075-8089.
65. J. A. Juárez and C. P. Whitby, *J. Colloid Interface Sci.*, 2012, **368**, 319-325.

## Chapter 2: How do Charged End-Groups on the Steric Stabiliser Block Influence the Formation and Long-Term Stability of Pickering Nanoemulsions Prepared Using Sterically-Stabilised Diblock Copolymer Nanoparticles?

---

66. A. B. Pawar, M. Caggioni, R. Ergun, R. W. Hartel and P. T. Spicer, *Soft Matter*, 2011, **7**, 7710-7716.
67. S. Fouilloux, F. Malloggi, J. Daillant and A. Thill, *Soft Matter*, 2016, **12**, 900-904.
68. A. Gupta, H. B. Eral, T. A. Hatton and P. S. Doyle, *Soft Matter*, 2016, **12**, 2826-2841.
69. G. Rodriguez-Lopez, Y. O'Neil Williams and J. Toro-Mendoza, *Langmuir*, 2019, **35**, 5316-5323.
70. E. Nazarzadeh, T. Anthonypillai and S. Sajjadi, *J. Colloid Interface Sci.*, 2013, **397**, 154-162.

# **Chapter 3:**

## **Effect of Salt on the Formation and Stability of Water-in-Oil Pickering Nanoemulsions Stabilised by Diblock Copolymer Nanoparticles**

Reproduced in part with permission from:

[S. J. Hunter, E. J. Cornel, O. O. Mykhaylyk and S. P. Armes, *Langmuir*, 2020, **36**, 15523-15535]

## **1.1 Introduction**

Nanoemulsions comprise very fine droplets with a mean diameter of no more than 200 nm.<sup>1-15</sup> They are much less prone to creaming or sedimentation than conventional emulsions because their Brownian motion is sufficient to overcome gravitational forces. Nanoemulsion droplets are also resistant to coalescence.<sup>1</sup> Flocculating droplets aggregate together but retain their individual structure, whereas two or more coalescing droplets merge to form larger droplets (see Figure 1.22). For macroemulsions, the mean thickness of the adsorbed layer of emulsifier is typically 0.01 – 1  $\mu\text{m}$ , which is usually significantly smaller than the mean droplet diameter (1 – 100  $\mu\text{m}$ ). Therefore, the emulsifier provides insufficient steric stabilisation to prevent flocculation and/or coalescence. In contrast, the mean emulsifier thickness for nanoemulsion droplets is 2 – 30 nm, which is more comparable to the droplet diameter. This means that steric stabilisation is highly effective for nanoemulsions and prevents even weak flocculation. However, both o/w and w/o nanoemulsions tend to suffer from Ostwald ripening.<sup>7, 16-18</sup>

In principle, Ostwald ripening can be suppressed by adding a suitable species to the droplet phase that is highly insoluble in the continuous phase.<sup>19-21</sup> For example, the addition of a relatively long hydrocarbon (or wax) to oil droplets enhances the stability of o/w nanoemulsions towards Ostwald ripening.<sup>22-24</sup> Similarly, the addition of salt to the aqueous phase is known to inhibit inter-droplet mass transfer in the case of w/o emulsions.<sup>25-27</sup> This is because the less soluble and the more soluble components exhibit different rates of transfer between droplets owing to their differing solubilities within the continuous phase (see Equation 1.21).<sup>19</sup> The more soluble component can diffuse between droplets much faster than the insoluble component. Over time, the larger droplets predominantly comprise the soluble component, whereas the smaller droplets become enriched with the insoluble component (see Figure 3.1). This is entropically less favourable than an ideally mixed system, so Ostwald ripening is suppressed.

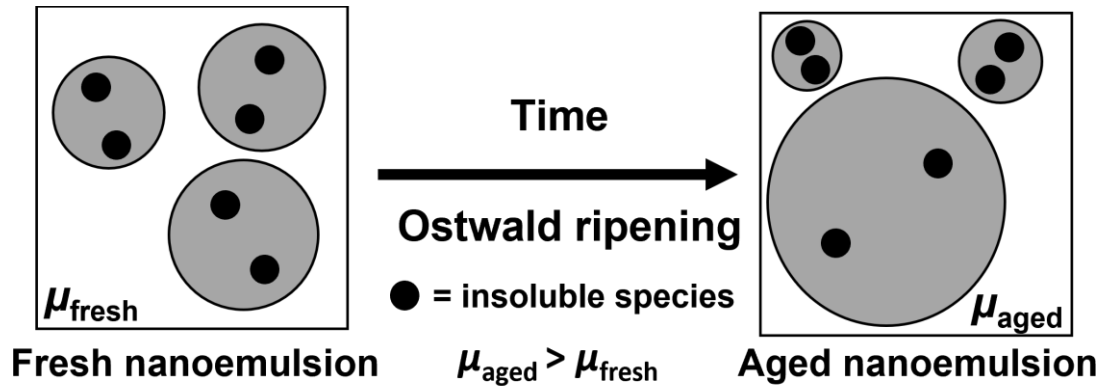


**Figure 3.1.** Schematic representation of the suppression of Ostwald ripening of a fresh nanoemulsion by adding an insoluble species (black) to droplets that are composed of a more soluble component (grey). If this nanoemulsion undergoes Ostwald ripening, then the larger droplets grow at the expense of the smaller ones. Over time, this increases the concentration of the insoluble species within the smaller droplets and hence enriches the larger droplets with the more soluble species, which increases the overall chemical potential of the emulsion.

This so-called ‘trapped species’ concept was first proposed by Higuchi and Misra,<sup>28</sup> and a theoretical analysis was later developed by Kabalnov.<sup>21</sup> In the latter case, the following assumptions were made for a mixed nanoemulsion system: (i) the insoluble component within the droplet phase cannot diffuse into the continuous phase, (ii) the two components have identical molar volumes, (iii) the interfacial tension is independent of composition and (iv) the insoluble and soluble components are infinitely miscible with each other. For these approximations, the chemical potential of the soluble component  $\mu_1$  can be described using Equation 3.1:

$$\mu_1(R, x_2) = \mu_1(R = \infty, x_2 = 0) + \frac{2\gamma V_m}{R} + RT \ln(1 - x_2) \quad 3.1$$

where  $x_2$  is the mole fraction of the insoluble component within the droplet phase. The first two terms of Equation 3.1 describe the positive chemical potential of an emulsion comprising a soluble component (in the absence of any insoluble component), and the final term represents the entropy of mixing, which is negative if  $x_2 > 0$ .

Kabalnov also explained how the excess chemical potential  $\Delta\mu$  depends on the mean droplet radius  $R$ , as described by Equation 3.2:<sup>21</sup>

$$\Delta\mu = -x_2 \left(\frac{R_i}{r}\right)^3 + \frac{2\gamma V_m}{r} \quad 3.2$$

where  $R_i$  represents the initial mean droplet radius. Equation 3.2 indicates that there are three stability regimes: stable, metastable and unstable. The mixed nanoemulsion is stable ( $\Delta\mu < 0$ ) when  $x_2$  is high (i.e. if there is a large fraction of insoluble component in the droplet phase) or when  $r$  is sufficiently small (i.e. for a microemulsion).<sup>2</sup> At intermediate  $x$  and  $r$ , the entropy of mixing term becomes less significant, and the nanoemulsion is metastable (i.e. only kinetically stable). At low  $x$  and large  $r$ , the nanoemulsion is unstable and tends to undergo phase separation. Interestingly, Kabalnov's analysis suggests that, if the droplet phase contains a sufficient proportion of an insoluble component, then a *thermodynamically stable* nanoemulsion can be prepared.

Many experimental studies have explored the effect of adding a highly water-insoluble long-chain hydrocarbon to the droplet phase for oil-in-water emulsions.<sup>23, 24, 29-32</sup> For example, Wooster *et al.* prepared SDS-stabilised triglyceride-in-water nanoemulsions containing mixed oil droplets composed of varying proportions of relatively soluble tricaprylin and relatively insoluble peanut oil.<sup>23</sup> At lower peanut oil volume fractions ( $x_2 \leq 0.20$ ), such nanoemulsions exhibited a linear relationship between the cube of the particle radius  $r^3$ , and time (see Figure 3.2), indicating an Ostwald ripening mechanism (see Equation 1.22).<sup>31, 33, 34</sup> As expected, lower rates of Ostwald ripening were observed at higher peanut oil volume fractions. At intermediate volume fractions ( $x_2 = 0.30 - 0.50$ ), the  $r^3$  initially increased linearly over time, but eventually attained a plateau value. Shorter time scales were required for such plateaus when using higher amounts of peanut oil. Wooster *et al.*<sup>23</sup> accounted for these two regimes in terms of Kabalnov's theory.<sup>21</sup> Initially, the mixed oil droplets undergo Ostwald ripening, causing a reduction in the Laplace pressure within the droplets. However, there is a concomitant reduction in the entropy of mixing owing to enrichment of the larger droplets with the more soluble triglyceride. Therefore,  $\Delta\mu$  becomes negative and the mixed droplets eventually become stable.

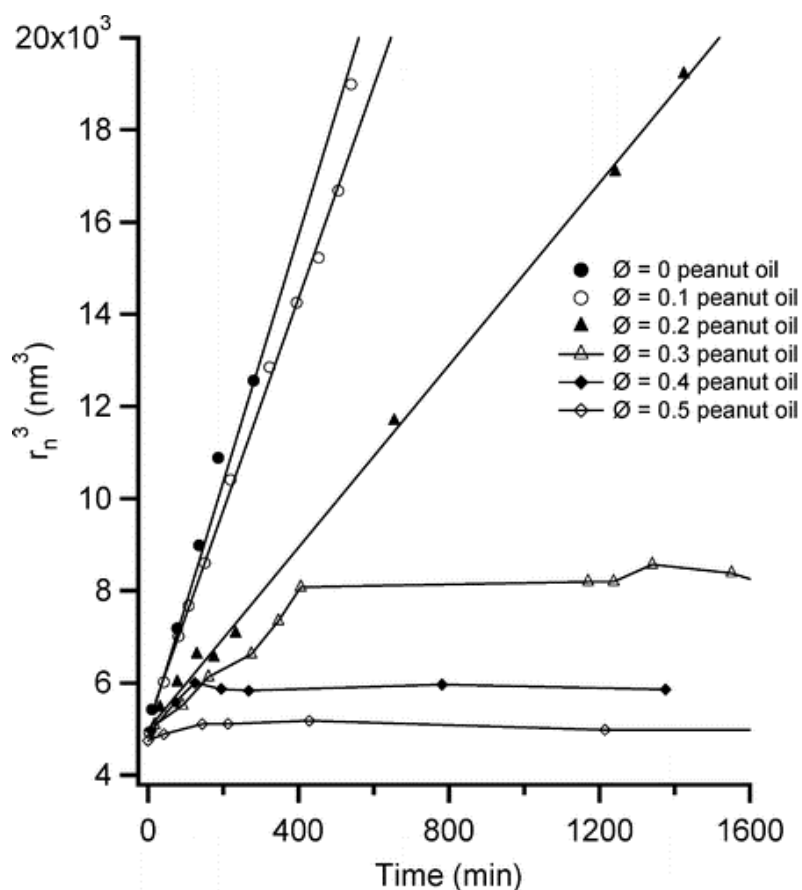


**Figure 3.2.** Effect of insoluble oil (peanut oil) fraction on the rate of Ostwald ripening of 15% v/v tricaprylin nanoemulsions stabilised by SDS (5.6 wt % SDS, continuous phase contains 16.6 wt % PEG with an  $M_n$  of 6600).

There have been a number of studies exploring the effect of the addition of salt to the aqueous phase on the formation of w/o nanoemulsions.<sup>10, 26, 35, 36</sup> In general, increasing the ionic strength of the aqueous droplet phase reduces the mean droplet diameter of the nanoemulsion.<sup>10, 26</sup> Notably, a limiting aqueous droplet diameter is attained at a critical salt concentration.<sup>26</sup> Increasing the salt concentration above this critical value has no discernible effect on the mean aqueous droplet diameter. Salt has also been shown to suppress Ostwald ripening in w/o emulsions owing to its insolubility within the oil continuous phase.<sup>26</sup> In particular, Koroleva and Yurtov studied the effect of varying the NaCl concentration within the aqueous phase of water-in-mineral oil nanoemulsions.<sup>26</sup> Nanoemulsions prepared using less than 0.188 M NaCl were unstable with respect to Ostwald ripening, resulting in larger droplets that became susceptible to

coalescence. However, nanoemulsions exhibited resistance to Ostwald ripening when prepared using higher NaCl concentrations.

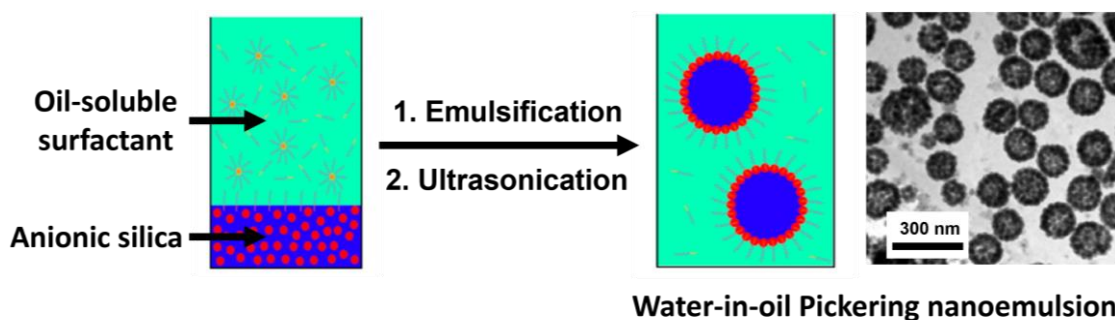


**Figure 3.3.** Schematic representation of the formation of sub-micron water-in-oil Pickering emulsions using hydrophilic anionic silica that is hydrophobised *in situ* using oil-soluble surfactant (poly(ethylene-co-butylene)-block-poly(ethylene oxide)).<sup>37</sup>

In recent years, there has been growing interest in o/w Pickering nanoemulsions.<sup>16, 38-45</sup> However, there have been rather fewer reports of the analogous w/o Pickering nanoemulsions.<sup>37, 46, 47</sup> In one notable example, Bollhorst *et al.*<sup>47</sup> prepared submicrometer-sized colloidosomes *via* self-assembly of metal oxide nanoparticles around water droplets in *n*-decane. Sihler and co-workers<sup>47</sup> utilised ultrasonication to prepare relatively fine w/o emulsions of less than 500 nm diameter using anionic silica nanoparticles, which were rendered sufficiently hydrophobic by adsorption of either cationic or non-ionic surfactants (see Figure 3.3).<sup>37</sup> Moreover, nanoparticle adsorption at the oil-water interface was relatively inefficient, with many nanoparticles remaining within the interior of the aqueous droplets.

Over the past decade or so, PISA has enabled the convenient synthesis of many examples of well-defined diblock copolymer nanoparticles.<sup>48-52</sup> In particular, this versatile technique enables the efficient preparation of 20-30 nm sterically-stabilised spheres in the form of a concentrated dispersion using RAFT dispersion polymerisation.<sup>49, 52, 53</sup> Such nanoparticles exhibit sufficient surface activity to stabilise both Pickering macroemulsions<sup>49, 54</sup> and nanoemulsions.<sup>17, 39</sup> Furthermore, such nanoparticles can be prepared in non-polar solvents such as *n*-alkanes<sup>55-63</sup> or mineral oil.<sup>59, 64</sup> Thus they are suitable for the efficient preparation of Pickering w/o emulsions.<sup>63,</sup>

In this Chapter, we report the production of relatively stable w/o Pickering nanoemulsions using hydrophobic diblock copolymer nanoparticles prepared *via* RAFT dispersion polymerisation in *n*-dodecane. This was achieved by first preparing a w/o Pickering macroemulsion *via* conventional high-shear homogenisation using a large excess of nanoparticles, followed by high-pressure microfluidisation to generate the desired w/o Pickering nanoemulsion. Such nanoemulsions are complementary to the o/w Pickering nanoemulsions previously reported by Thompson and co-workers.<sup>17, 39</sup> The effect of systematically increasing the concentration of added salt within the dispersed phase on the *z*-average diameter of the aqueous droplets is examined. Subsequently, the effect of varying the initial nanoparticle concentration, the number of passes through a high-pressure microfluidiser and the applied pressure during microfluidisation on the final nanoemulsion droplet diameter is investigated. Finally, the effect of varying the amount of salt dissolved in the aqueous dispersed phase on the long-term stability of these w/o Pickering nanoemulsions is explored.

## **3.2 Experimental**

### **3.2.1 Materials**

Stearyl methacrylate (SMA), 2,2,2-trifluoroethyl methacrylate (TFEMA), *n*-dodecane, trimethylamine, butylhydroxytoluene (BHT) tetrahydrofuran (THF), toluene, ruthenium(IV) oxide hydrate and sodium periodate were all purchased from Sigma-Aldrich (UK). Monomers were passed through basic alumina in order to remove inhibitor prior to use. Tert-Butyl peroxy-2-ethylhexanoate (Trigonox 21S, or T21s) initiator was supplied by AkzoNobel (The Netherlands). *d*-Chloroform (CDCl<sub>3</sub>) was purchased from VWR (UK), *d*<sub>2</sub>-dichloromethane (CD<sub>2</sub>Cl<sub>2</sub>) was obtained from Cambridge Isotope Laboratory (USA) and the 4-cyano-4-((2-phenylethanesulfonyl)thiocarbonylsulfanyl)pentanoic acid (PETTC) RAFT agent was prepared in-house according to a previously reported protocol.<sup>65</sup> Unless stated otherwise, deionised water (pH 6) was used for all experiments.

### **3.2.2 Synthesis of a PSMA<sub>32</sub> Precursor *via* RAFT Solution Polymerisation in Toluene**

A PSMA<sub>32</sub> precursor was prepared *via* RAFT solution polymerisation of SMA in toluene using a trithiocarbonate-based PETTC RAFT agent, as previously described.<sup>66</sup> A mean DP of 32 was determined *via* <sup>1</sup>H NMR analysis in CD<sub>2</sub>Cl<sub>2</sub>; the integrated aromatic PETTC signals at 7.1–8.1 ppm were compared to that of the oxymethylene signal at 3.7 – 4.2 ppm. THF GPC studies (refractive index detector; using a series of eight near-monodisperse poly(methyl methacrylate) calibration standards) indicated an  $M_n$  of 12 300 g mol<sup>-1</sup> and an  $M_w/M_n$  of 1.13.

### **3.2.3 Synthesis of PSMA<sub>32</sub>-PTFEMA<sub>53</sub> Diblock Copolymer Nanoparticles *via* RAFT Dispersion Polymerisation of TFEMA in *n*-Dodecane**

The synthesis of PSMA<sub>32</sub>-PTFEMA<sub>53</sub> spheres at 20% w/w solids was conducted as follows: a PSMA<sub>32</sub> precursor (2.01 g, 0.18 mmol), T21s (77 mg, 0.036 mmol), and *n*-dodecane (14.6 g, 19.5 ml) were added in turn to a glass vial and the resulting solution was degassed with N<sub>2</sub> gas for 30 min at 20 °C. TFEMA was degassed separately in ice to minimise evaporation. This monomer (1.95 ml, 9.82 mmol; target DP = 55) was then added *via* syringe to the reaction mixture, which was subsequently heated to 80 °C for 16 h by immersing the vial in an oil bath. <sup>19</sup>F NMR spectroscopy analysis of the copolymer dissolved in CDCl<sub>3</sub> indicated 97% TFEMA conversion under these conditions. THF GPC studies (refractive index detector; using a series of eight near-monodisperse polymethyl methacrylate calibration standards) indicated an  $M_n$  of 18 000 g mol<sup>-1</sup> and an  $M_w/M_n$  of 1.23.

### **3.2.4 Preparation of PSMA<sub>32</sub>-PTFEMA<sub>53</sub>-Stabilised Pickering Macroemulsions Using High-Shear Homogenisation**

A 5.0% w/w dispersion of PSMA<sub>32</sub>-PTFEMA<sub>53</sub> nanoparticles in *n*-dodecane (4.5 mL) was added to a 14 mL glass vial. This was then homogenised with various aqueous solutions (prepared

using deionised water at around pH 6, unless stated otherwise) (0.5 mL; containing 0 - 0.43 M NaCl) for 2 min at 20 °C using an IKA Ultra-Turrax T-18 homogeniser equipped with a 10 mm dispersing tool and operating at 13 500 rpm.

### **3.2.5 Preparation of PSMA<sub>32</sub>-PTFEMA<sub>53</sub>-Stabilised Pickering Nanoemulsions Using High-Pressure Microfluidisation**

A Pickering macroemulsion (5.0 mL, initial nanoparticle concentration in the *n*-dodecane phase = 5.0% w/w) was further processed using an LV1 microfluidiser (Microfluidics, USA). The pressure was fixed at 10 000 psi and each emulsion was passed five times through the LV1 unit to produce unimodal w/o Pickering nanoemulsions.

### **3.2.6 Characterisation**

<sup>19</sup>F NMR spectroscopy.

<sup>19</sup>F NMR spectra were recorded in CDCl<sub>3</sub> using a Bruker Avance III HD spectrometer operating at 400.23 MHz (<sup>1</sup>H frequency). Spectra were recorded using 16 transients with an acquisition window of 89.3 kHz, 128 points and a relaxation delay of 1 s. Spectra were analysed using TopSpin version 3.1 software. TFEMA conversions were determined by comparing the integrated intensities of signals assigned to residual monomer and the corresponding polymer.

Gel Permeation Chromatography (GPC)

Molecular weight distributions were assessed by GPC using THF as an eluent. The GPC set-up comprised an Agilent 1260 Infinity series degasser and pump, two Agilent PLgel 5 µm Mixed C columns in series and a refractive index detector. The mobile phase contained 2.0% v/v trimethylamine and 0.05% w/w butylhydroxytoluene (BHT) and the flow rate was fixed at 1.0 ml min<sup>-1</sup>. Copolymer samples were dissolved in THF containing 0.50% v/v toluene as a flow-rate marker prior to GPC analysis. A series of eight near-monodisperse PMMA standards (*M<sub>p</sub>* values

ranging from 580 to 552 500 g mol<sup>-1</sup>) were used for calibration using either a refractive index detector or a UV detector operating at 260 nm.

#### Transmission Electron Microscopy (TEM)

The staining agent was prepared by dissolving ruthenium(IV) oxide hydrate (0.30 g) and sodium periodate (2.00 g) in 50 ml water. Nanoemulsion samples were diluted to 1.0% v/v and nanoparticle dispersions were diluted to 0.1% w/w using *n*-dodecane. A droplet (10 µL) was then placed on a carbon-coated copper TEM grid with the aid of a micropipet. The loaded grid was stained for 7 min by exposure to the heavy metal stain within a desiccator. TEM images were recorded using a Tecnai Spirit T12 TEM instrument operating at 80 kV and equipped with an Orius SC1000B S4 CCD camera (2672 x 4008 pixels; 9 µm each).

#### Scanning electron microscopy (SEM)

The nanoemulsion was diluted to 1.0% v/v using *n*-dodecane and one droplet was placed on a glass slide, which was then left to dry overnight. The glass slide was then mounted onto an SEM stub using an electrically conductive adhesive pad. The stub was gold-coated for 2 min prior to analysis. SEM studies were performed using an Inspect F field emission microscope operating at 5 kV.

#### Dynamic Light Scattering (DLS)

hydrodynamic *z*-average diameters were obtained by DLS using a Malvern Zetasizer NanoZS instrument at a fixed scattering angle of 173°. Dispersions of 0.1% w/w nanoemulsions or nanoparticles were analysed using disposable cuvettes, and the results were averaged over three consecutive runs, each comprising ten analyses. The *n*-dodecane used to dilute each sample was ultrafiltered through a 0.20 µm membrane to remove extraneous dust.

#### Analytical Centrifugation (LUMiSizer)

Aqueous droplet size distributions were assessed using a LUMiSizer analytical photocentrifuge (LUM GmbH, Berlin, Germany) at 20 °C. Measurements were conducted on diluted Pickering nanoemulsions (1.0 - 10.0% v/v water) using 2 mm pathlength polyamide cells at 400 rpm for 200 profiles (allowing 10 s between profiles) and then the rate of centrifugation was increased up to 4000 rpm for a further 800 profiles. The slow initial rate of centrifugation enabled detection of any larger oil droplets that might be present within the nanoemulsion. Overall, the measurement time is approximately 135 min. The LUMiSizer instrument employs space- and time-resolved extinction profiles (STEP) technology to measure the intensity of transmitted near-infrared light as a function of time and position simultaneously over the entire length of the cell. The gradual progression of these transmission profiles provides information on the rate of sedimentation of the aqueous droplets and hence enables assessment of the droplet size distribution. The particle density is an essential input parameter for analytical centrifugation studies. The droplet density used for the nanoemulsion ageing studies was either the density of pure water or the appropriate density for a given aqueous salt solution (which is 1.016 g cm<sup>-3</sup> for the highest NaCl concentration (0.43 M) used in this study).<sup>67</sup> This ignores any contribution to the droplet density from the adsorbed PSMA<sub>32</sub>-PTFEMA<sub>53</sub> nanoparticles, but this approximation is reasonable given that we merely wish to assess *relative* changes in the droplet size distribution over time.

#### Small-Angle X-ray Scattering (SAXS)

Small-angle X-ray scattering (SAXS) patterns were recorded using a laboratory SAXS beamline (Xeuss 2.0, Xenocs, France) equipped with a liquid gallium MetalJet X-ray source (Excillum, Sweden) (wavelength  $\lambda = 0.134$  nm), two sets of motorised scatterless slits for beam collimation, and a Pilatus 1M two-dimensional pixel SAXS detector (Dectris, Switzerland). A flow-through glass capillary (2 mm diameter) was connected to an injector syringe and a waste container *via* plastic tubing and mounted horizontally on the beamline stage; this set-up was used

as a sample holder. SAXS patterns were recorded over a  $q$  range of 0.01–1.4 nm<sup>-1</sup>, where  $q = (4\pi \sin \theta)/\lambda$  is the length of the scattering vector, and  $\theta$  is a half of the scattering angle. Two-dimensional SAXS patterns were reduced to one-dimensional curves using the Foxtrot software package supplied with the instrument and further analysed (background subtraction and data modelling) using Irena SAS macros<sup>68</sup> for Igor Pro.

Packing efficiency calculation

The nanoparticle packing efficiency was estimated by first calculating the number of nanoparticles  $N$ , adsorbed onto an individual aqueous droplet using Equation 3.3:<sup>17</sup>

$$N = \frac{\text{total number of nanoparticles}}{\text{total number of droplets}} = \frac{m_p N_A / (N_s M_n)}{V_{\text{water}} / (\frac{4}{3} \pi R_{\text{water}})^3} \quad 3.3$$

Here,  $m_{\text{particles}}$  is the mass of nanoparticles used to prepare the nanoemulsion,  $M_n$  is the number-average molecular weight of the PSMA<sub>32</sub>–PTFEMA<sub>53</sub> chains,  $V_{\text{water}}$  is the total volume of water used to prepare each nanoemulsion, and  $R_{\text{water}}$  is the mean radius of bare aqueous droplets. Finally,

$N_s$  is the number of PSMA<sub>32</sub>–PTFEMA<sub>53</sub> chains per nanoparticle determined as  $N_s = \frac{\frac{4}{3} \pi R_s^3}{V_{\text{PTFEMA}}}$

where  $R_s$  is the mean radius of the PTFEMA cores measured by SAXS and  $V_{\text{PTFEMA}}$  is volume of the core-forming block of a copolymer molecule. We calculate  $R_{\text{water}}$  to be equal to the  $z$ -average radius  $R_{\text{DLS}}$  of the overall nanoemulsion droplets minus the diameter of the adsorbed nanoparticles (or  $R_{\text{water}} = R_{\text{DLS}} - 2R_{\text{particle}}$ ). The volume-average diameter of the nanoparticles could be calculated from SAXS measurements of the nanoparticles as  $2R_s + 4R_g$ , where  $R_g$  is radius of gyration of the micelle PSMA<sub>32</sub> corona block. However, we contend that the *effective* diameter  $2R_{\text{particle}}$  of the PSMA<sub>32</sub>–PTFEMA<sub>53</sub> nanoparticles adsorbed at the oil-water interface is actually given by  $2R_s + 2R_g$ .<sup>17</sup> This is because the non-solvated PSMA<sub>32</sub> stabiliser chains that are in direct contact with the aqueous phase are most likely collapsed and hence occupy negligible volume at the oil-water interface.

Assuming that an area of a large spherical particle covered by small spheres can be represented by the total area of projection of the small spheres on the large particle surface,<sup>69</sup> the packing efficiency  $P_{\text{eff}}$ , of the small spheres in the large particle shell is given by Equation 2.2. We make the same assumptions in our nanoparticle packing efficiency calculations as those outlined in Chapter 2. However, we assume that all of the nanoparticles adsorb at the surface of the aqueous droplets. Therefore, the calculated nanoparticle packing efficiency should be regarded as an upper limit value.

### 3.3 Results and Discussion

#### 3.3.1 Synthesis and Characterisation of PSMA<sub>32</sub>-PTFEMA<sub>53</sub> Diblock Copolymer Nanoparticles

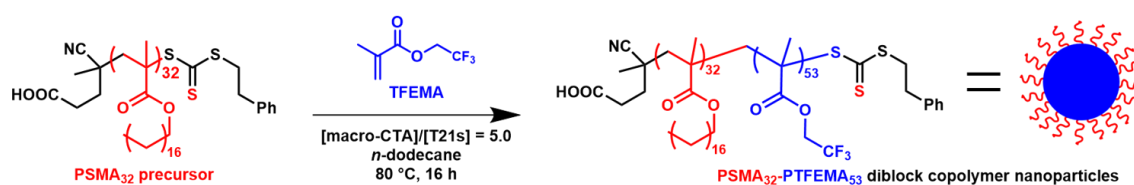


**Figure 3.4.** Synthesis of PSMA<sub>32</sub>-PTFEMA<sub>53</sub> nanoparticles *via* RAFT dispersion polymerisation of TFEMA in *n*-dodecane at 80 °C using a PSMA<sub>32</sub> precursor.

The sterically-stabilised diblock copolymer nanoparticles used in this study were prepared by chain-extending an oil-soluble PSMA precursor with TFEMA *via* RAFT dispersion polymerisation, as previously described by Cornel and co-workers (see Figure 3.4 above).<sup>66</sup> Provided that a relatively short PTFEMA block of 55 is targeted, this PISA formulation enables the preparation of PTFEMA-core spherical nanoparticles with a mean diameter of less than 30 nm,<sup>66</sup> which is expected to be small enough to enable the stabilisation of Pickering nanoemulsions.<sup>16, 39</sup> <sup>119</sup>F NMR spectroscopy studies indicated that the TFEMA polymerisation proceeded to relatively high monomer conversion (~97%) within 16 h at 80 °C (see Figure 3.5).

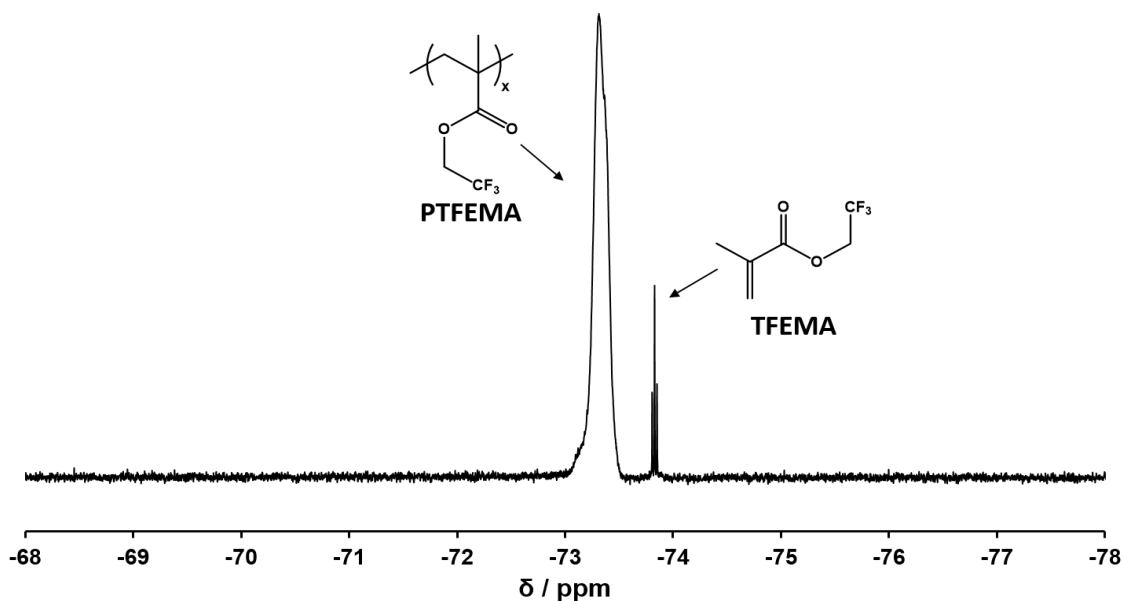


**Figure 3.5.**  $^{19}\text{F}$  NMR spectrum recorded for PSMA<sub>32</sub>-PTFEMA<sub>53</sub> diblock copolymer dissolved in  $\text{CDCl}_3$ . From the residual monomer signal observed at -73.8 ppm, a final TFEMA conversion of 97% can be calculated.

THF GPC analysis indicated a relatively narrow molecular weight distribution ( $M_w/M_n = 1.23$ ), suggesting that this RAFT dispersion polymerisation was well-controlled (see Figure 3.6a). The  $z$ -average diameter of the sterically-stabilised nanoparticles determined by DLS is  $28 \pm 6$  nm (Figure 3.6b), which is consistent with the number-average diameter of  $24 \pm 4$  nm estimated from TEM analysis (based on analysis of more than 100 nanoparticles; see Figure 3.16a). The SAXS pattern recorded for these nanoparticles was fitted using a spherical micelle form factor (see Equation 7.9).<sup>70</sup> This approach indicated a mean PTFEMA core radius  $R_s$  of 6.5 nm (and an associated standard deviation,  $\sigma_s$ , of 1.3 nm) and a radius of gyration  $R_g$  for the PSMA corona block of 1.7 nm, resulting in a volume-average diameter  $D_{\text{SAXS}}(2R_s + 4R_g)$  of 19.9 nm (see Figure 3.6c). This is somewhat smaller than the nanoparticle dimensions indicated by DLS and TEM. However, DLS reports a hydrodynamic  $z$ -average diameter while TEM analysis suffers from poor statistics, so both techniques overestimate the effective particle dimensions indicated by SAXS.

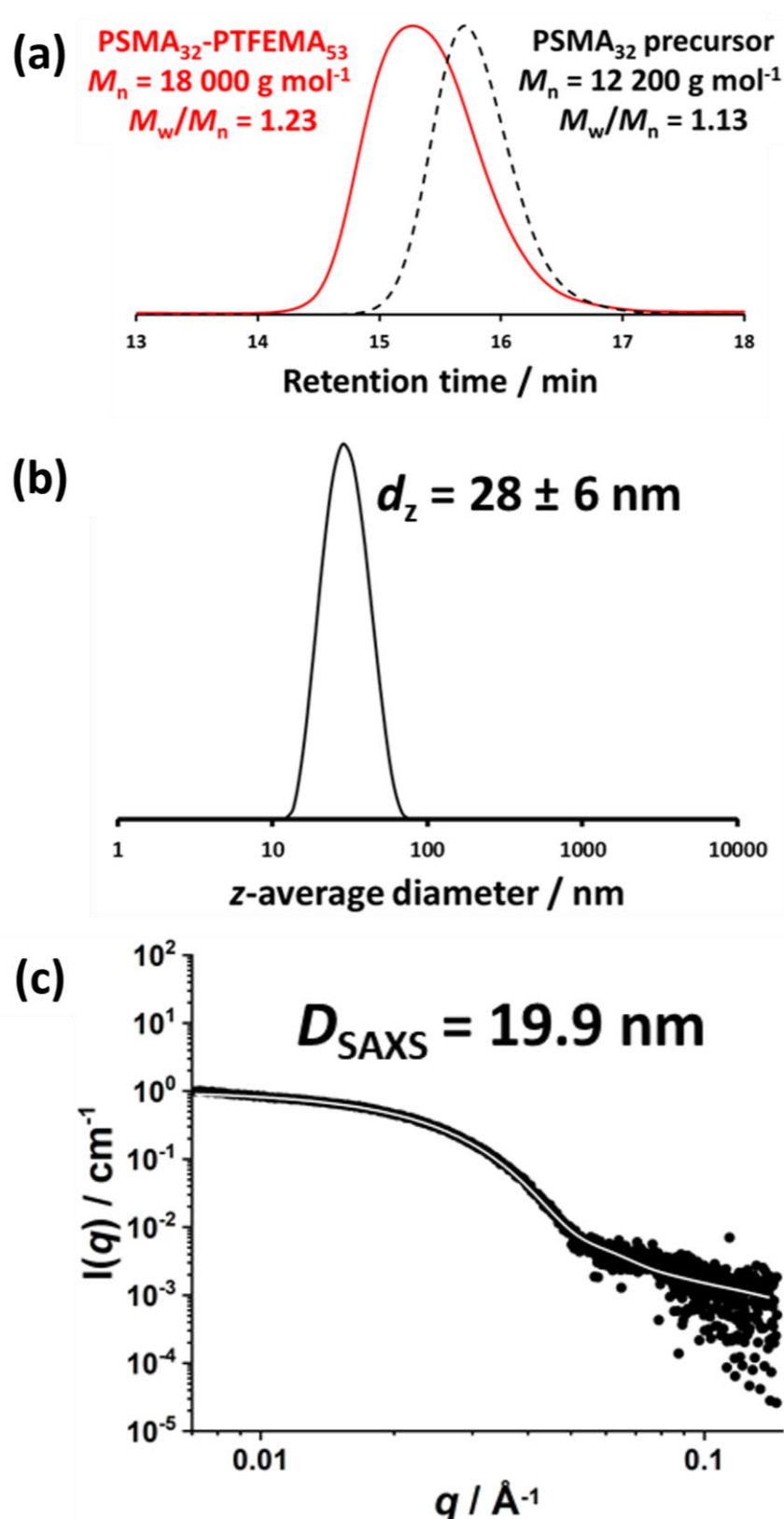


**Figure 3.6.** (a) Overlaid DMF GPC curves obtained for a PSMA<sub>32</sub> precursor and the corresponding PSMA<sub>32</sub>-PTFEMA<sub>53</sub> diblock copolymer; (b) z-average particle size distribution determined by DLS; (c) Experimental SAXS pattern (black circles) recorded for a 1.0% w/w dispersion of PSMA<sub>32</sub>-PTFEMA<sub>53</sub> diblock copolymer nanoparticles in *n*-dodecane. A satisfactory data fit was obtained using a spherical micelle model (white line).

### 3.3.2 Effect of Salt on the Formation of w/o Pickering Nanoemulsions

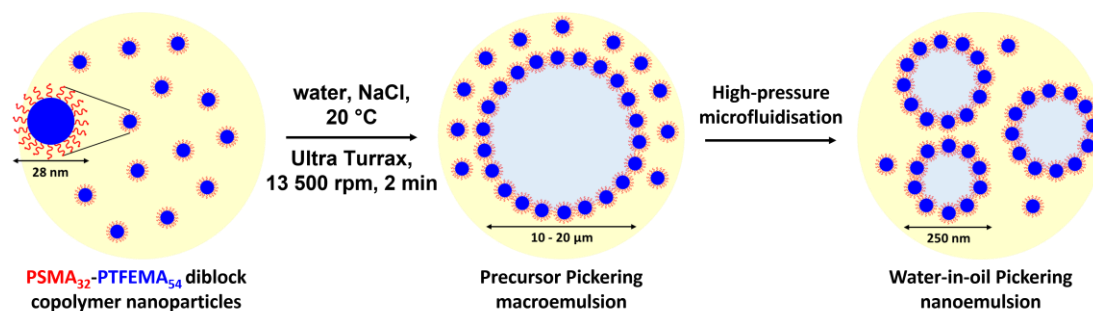


**Figure 3.7.** Schematic representation of the preparation of water-in-oil (w/o) Pickering nanoemulsions reported in this study. A precursor Pickering macroemulsion was prepared using high-shear homogenisation, and then further processed using the LV1 microfluidiser to produce a w/o Pickering nanoemulsion. A large excess of non-adsorbed nanoparticles co-exist with the macroemulsion but very few non-adsorbed nanoparticles remain in the continuous phase after high-pressure microfluidisation.

PSMA<sub>32</sub>-PTFEMA<sub>53</sub> nanoparticles were used to prepare a Pickering precursor macroemulsion of approximately 10 - 20 µm diameter *via* high-shear homogenisation (13 500 rpm, 2 min) using an Ultra-Turrax homogeniser (see Figure 3.7). A water volume fraction of 0.10 and a nanoparticle concentration of 5.0% w/w was used to prepare this macroemulsion. These conditions were deliberately selected because a large excess of non-adsorbed nanoparticles is required to stabilise the substantial increase in interfacial area that is generated during the subsequent high-pressure microfluidisation to produce the much finer Pickering nanoemulsion.<sup>16</sup>

39

In initial microfluidisation experiments, no salt was added to the aqueous phase. A precursor macroemulsion prepared using 5.0% w/w PSMA<sub>32</sub>-PTFEMA<sub>53</sub> nanoparticles was subjected to repeated passes through an LV1 microfluidiser at various applied pressures, with the mean droplet diameter being assessed by DLS after each pass. At an applied pressure of 5000 psi, the mean droplet diameter was reduced significantly between the first and tenth pass (Figure 3.8). However, there was no further change when using higher applied pressures (e.g. 10 000 or 20 000 psi) and *larger* droplets were observed at 30 000 psi owing to over-shearing. The mean droplet diameters for such emulsions exceeded 600 nm, which is significantly greater than those reported

by Thompson and co-workers for o/w nanoemulsions prepared using PGMA<sub>48</sub>-PTFEMA<sub>50</sub> diblock copolymer nanoparticles.<sup>17, 39</sup> Moreover, such coarse droplets do not correspond to nanoemulsions, which should be less than 200 nm diameter.<sup>71</sup>

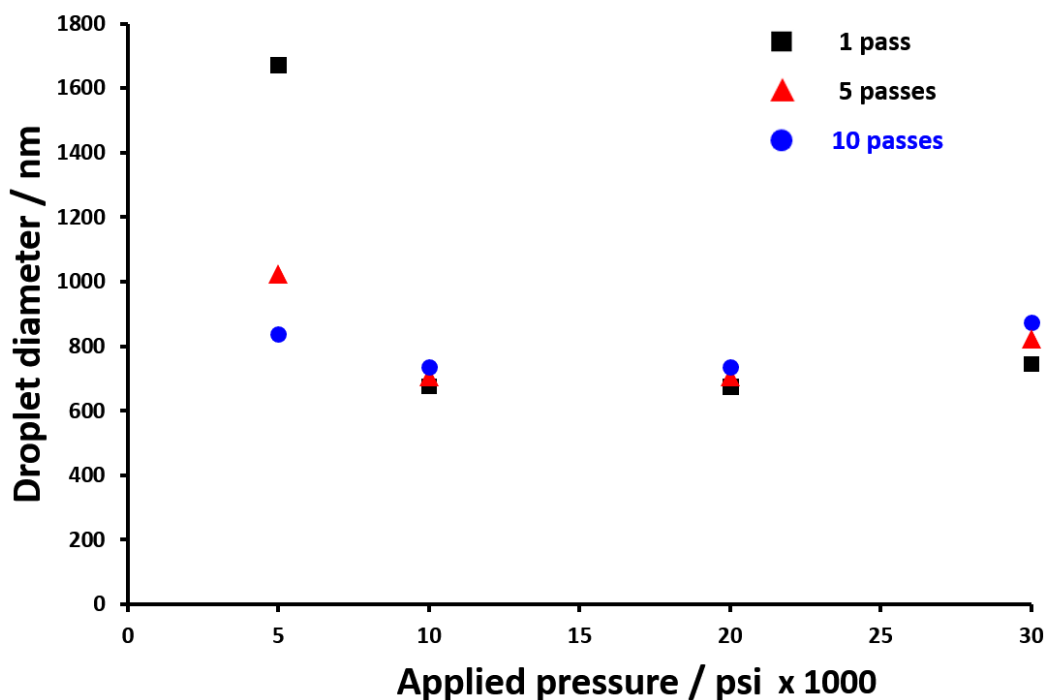


**Figure 3.8.** Effect of varying the applied pressure and number of passes during microfluidisation on the initial *z*-average aqueous droplet diameter of w/o Pickering nanoemulsions prepared using 5.0% w/w PSMA<sub>32</sub>-PTFEMA<sub>53</sub> nanoparticles at a fixed water volume fraction of 0.10, as determined by DLS.

Based on the conclusions from Chapter 2, the ionisation of the carboxylic acid end-groups on the PSMA<sub>32</sub> stabiliser chains might occur at the *n*-dodecane-water interface. To examine this hypothesis, we prepared two Pickering nanoemulsions using an aqueous 0.11 M NaCl solution adjusted to either pH 7 or pH 2. In the former case, the formation of anionic carboxylate groups at the *n*-dodecane-water interface was anticipated, whereas in the latter case no such ionisation should occur. DLS studies of the nanoemulsion at pH 7 indicated a droplet diameter of  $268 \pm 96$  nm, which is comparable to the nanoemulsion using deionised water at pH 6 (see entry 2 in Table 3.1). On the other hand, the Pickering nanoemulsion prepared at pH 2 had a droplet diameter of  $217 \pm 92$  nm, see Figure 3.19. These observations indicate that ionisation of the carboxylic acid end-groups on the steric stabiliser chains of these nanoparticles leads to the

formation of a slightly larger nanoemulsion than that formed when using neutral nanoparticles. However, further work would be required to establish whether such end-group ionisation also affected the nanoparticle adsorption efficiency, the nanoparticle packing efficiency at the oil-water interface, and the long-term stability of such nanoemulsions.

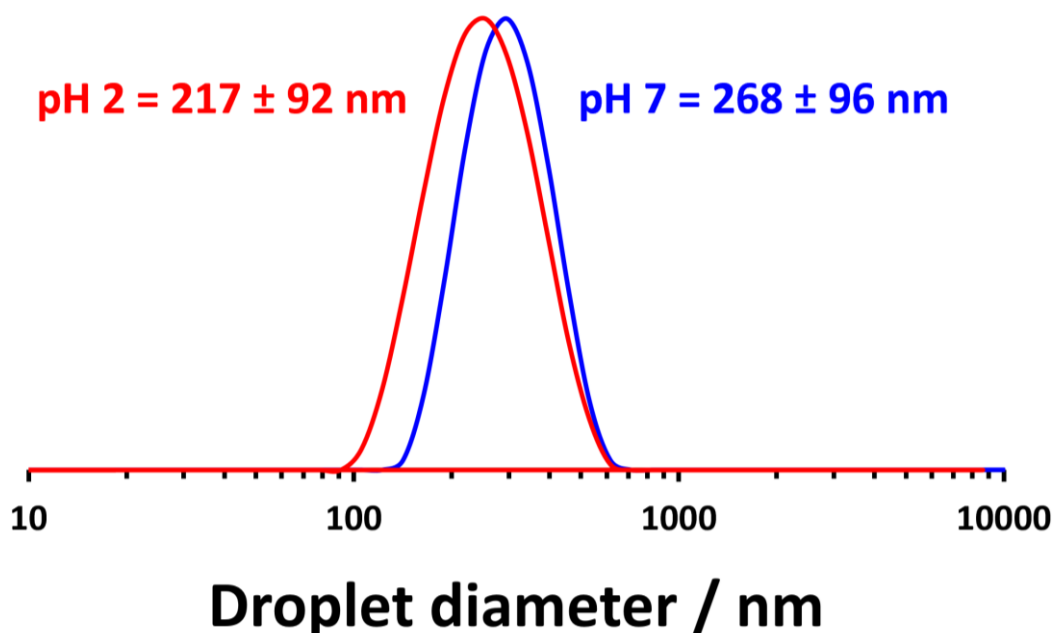


**Figure 3.9.** *z*-average droplet size distributions recorded by DLS for Pickering nanoemulsions prepared using either a neutral (pH 7) or acidic (pH 2) aqueous solution containing 0.11 M NaCl.

In the case of surfactant-stabilised w/o nanoemulsions, it is well-known that addition of electrolyte to the aqueous phase prior to emulsification results in the formation of smaller, more stable droplets.<sup>10, 72</sup> Therefore, aqueous solutions containing up to 0.43 M NaCl were used to prepare w/o Pickering nanoemulsions using 5.0% w/w PSMA<sub>32</sub>-PTFEMA<sub>53</sub> nanoparticles at an applied pressure of 10 000 psi with 5 passes through the LV1 microfluidiser. Figure 3.10 shows the effect of varying the NaCl concentration on the mean droplet diameter, as indicated by DLS studies. The droplet diameter and polydispersity index are both reduced significantly at higher salt concentrations. A limiting droplet diameter of around 250 nm is achieved at 0.43 M NaCl. This *overall* diameter necessarily includes the thickness of the adsorbed PSMA<sub>32</sub>-PTFEMA<sub>53</sub> nanoparticle layer. If this nanoparticle contribution is subtracted then the mean diameter for the

underlying ‘naked’ aqueous droplet is less than 200 nm, which meets the criterion for a nanoemulsion according to the literature.<sup>1</sup>

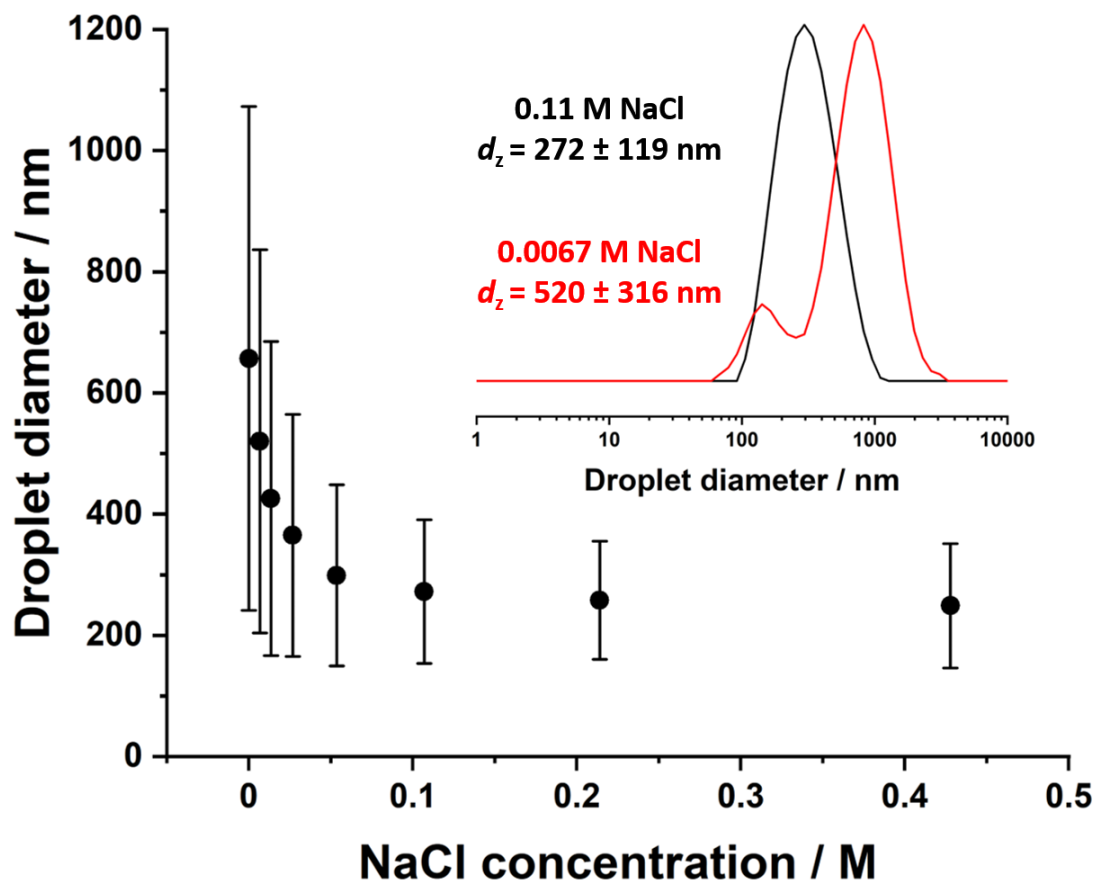


**Figure 3.10.** Systematic reduction in  $z$ -average droplet diameter observed for a w/o Pickering nanoemulsion prepared at a water volume fraction of 0.10 using 5.0% w/w PSMA<sub>32</sub>-PTFEMA<sub>53</sub> nanoparticles in *n*-dodecane while varying the NaCl concentration. Error bars represent the standard deviation of the droplet size distributions, rather than the experimental error associated with repeated measurements. Inset:  $z$ -average droplet size distributions determined by DLS for Pickering nanoemulsions prepared with either 0.11 M or 0.0067 M NaCl dissolved within the aqueous phase (deionised water at pH 6).

Below the critical concentration of 0.11 M NaCl, visual inspection confirmed that coarser nanoemulsion droplets sediment on standing overnight at 20 °C (see Figure 3.11). Moreover, bimodal droplet size distributions are observed for such nanoemulsions. In contrast, nanoemulsions possess unimodal droplet size distributions when prepared in the presence of at least 0.11 M NaCl and do not undergo sedimentation under the same conditions. Similar observations were made by Koroleva and Yurtov for surfactant stabilised mineral-in-water

nanoemulsions.<sup>26</sup> They demonstrated that emulsions prepared with a salt concentration below critical concentration undergo fast rates of Ostwald ripening. This leads to a lower number of larger droplets, since the smaller droplets vanish. Therefore, the droplets undergo to sedimentation and coalescence, since steric stabilisation conferred by the surfactant becomes less effective.

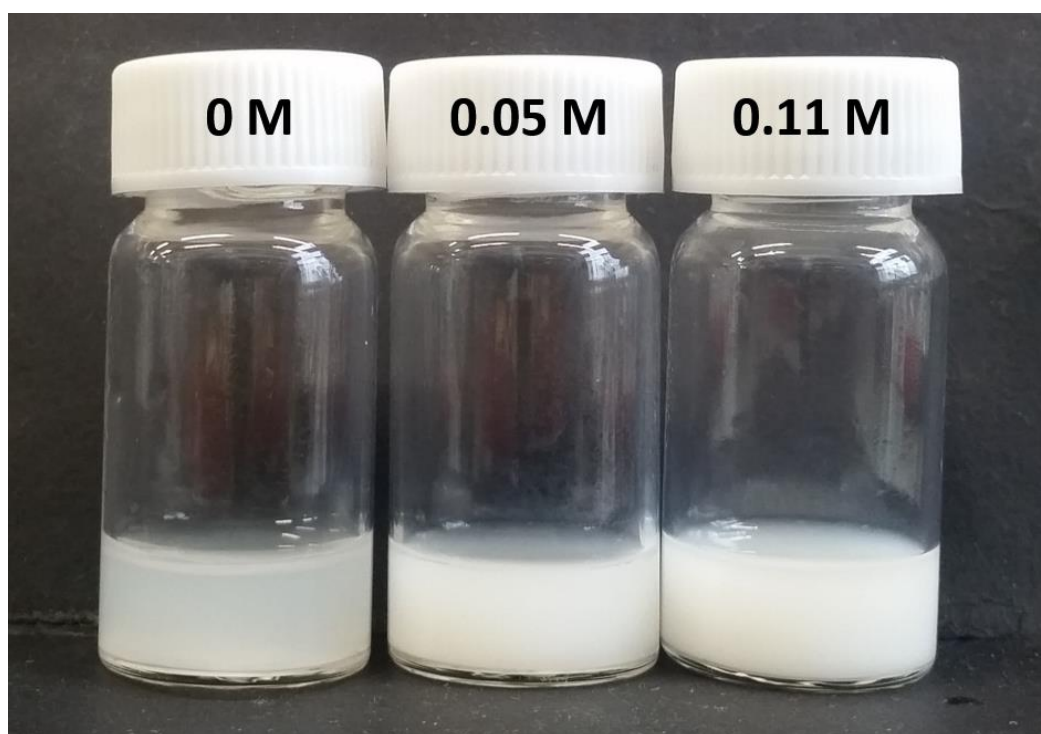


**Figure 3.11.** Digital photographs recorded for one-day-old w/o Pickering nanoemulsions prepared using various NaCl concentrations (0, 0.05 or 0.11 M) at a constant nanoparticle concentration of 5.0% w/w and a water volume fraction of 0.10. Microfluidisation conditions: applied pressure = 10 000 psi; 5 passes.

In order to assess whether high-pressure microfluidisation induced nanoparticle dissociation or degradation, a control experiment was performed in which a 5.0% w/w dispersion of PSMA<sub>32</sub>-PTFEMA<sub>53</sub> nanoparticles in *n*-dodecane was subjected to the above optimised processing conditions (applied pressure = 10 000 psi, number of passes = 5) *in the absence of any aqueous solution*. DLS studies conducted before and after microfluidisation confirmed that the *z*-average diameter of the nanoparticles (and DLS polydispersity) remained essentially unchanged (see Figure 3.12). Thus the PSMA<sub>32</sub>-PTFEMA<sub>53</sub> nanoparticles survive the high-pressure microfluidisation conditions intact.

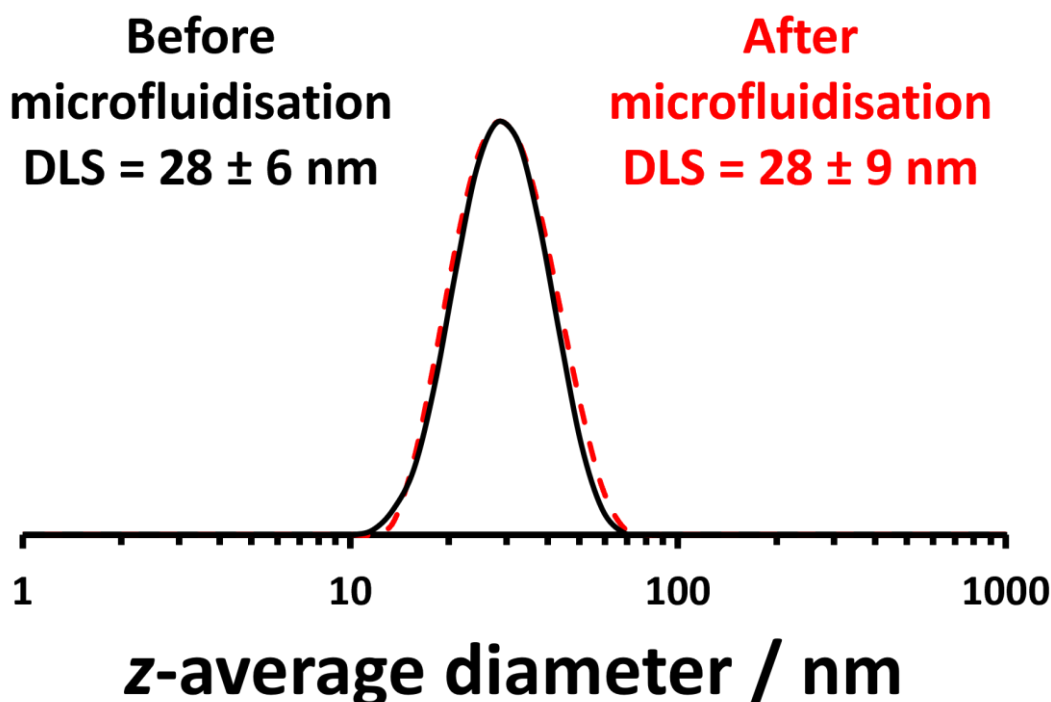


**Figure 3.12.** Overlaid  $z$ -average particle size distributions determined by DLS for PSMA<sub>32</sub>-PTFEMA<sub>53</sub> diblock copolymer nanoparticles before and after microfluidisation (10 000 psi; 5 passes).

The mean packing efficiency  $P_{\text{eff}}$  for the adsorbed layer of nanoparticles surrounding each aqueous droplet was calculated for fresh Pickering nanoemulsions prepared in the presence of added salt (0.05 M to 0.43 M NaCl) (Table 3.1) using a core-shell model originally developed by Balmer *et al.* to study the adsorption of 20 nm silica nanoparticles onto large polymer latexes.<sup>69</sup> This model was recently applied to oil-in-water Pickering nanoemulsions by Thompson *et al.*<sup>17</sup> For the latter system, an effective contact angle of  $\theta_w 0^\circ$  was assumed for nanoparticle adsorption at the oil-water interface and the same assumption was made in the present study (see Figure 1.25). Increasing the NaCl concentration within the aqueous phase leads to a higher droplet density and a gradual reduction in the  $z$ -average droplet diameter, as expected. This size reduction necessarily reduces the number of nanoparticles adsorbed onto each droplet but the nanoparticle packing efficiency is also reduced from 75% to 58% on raising the NaCl concentration from 0.05 M to 0.43 M NaCl. One possible explanation for this reduction in packing efficiency might be a lower three-phase particle contact angle  $\theta_w$  in the presence of additional salt. In principle, the

hydrophobic PSMA<sub>32</sub>-PTFEMA<sub>53</sub> nanoparticles adsorbed at the surface of the aqueous droplets should exhibit reduced wettability at higher NaCl concentrations.

**Table 3.1.** Summary of droplet density, droplet diameter, number of nanoparticles per droplet and packing efficiency for four Pickering nanoemulsions prepared using 5.0% w/w PSMA<sub>32</sub>-PTFEMA<sub>53</sub> diblock copolymer nanoparticles with 0.05 M to 0.43 M NaCl dissolved in the aqueous phase.<sup>a</sup>

NaCl concentration / M	$\rho$ / g cm <sup>-3</sup>	$D_z$ / nm	$N$	$P_{\text{eff}}$ / %
0.05	1.0003	299 ± 150	362	75
0.11	1.003	272 ± 119	257	66
0.21	1.007	258 ± 97	211	61
0.43	1.016	249 ± 103	185	58

<sup>a</sup> $\rho$  = aqueous droplet density;  $D_z$  = initial  $z$ -average diameter;  $N$  = number of nanoparticles per droplet;  $P_{\text{eff}}$  = packing efficiency.

The packing efficiencies calculated herein are broadly comparable to those determined by Thompson *et al.* for *n*-dodecane-in-water Pickering nanoemulsions, which were stabilised using hydrophilic 25 nm PGMA<sub>48</sub>-PTFEMA<sub>50</sub> diblock copolymer nanoparticles prepared *via* RAFT aqueous emulsion polymerisation.<sup>17</sup> More specifically, in this prior study the number of adsorbed nanoparticles per droplet  $N$  and the  $P_{\text{eff}}$  were calculated to be 438 and 74% for *n*-dodecane droplets with a  $z$ -average diameter of 257 ± 93 nm. In the present study, a water-in-oil Pickering nanoemulsion prepared with a similar mean droplet diameter using 0.21 M NaCl at pH 6 had  $N = 211$  and  $P_{\text{eff}} = 61\%$ , respectively (see entry 3 in Table 3.1).

The PSMA<sub>32</sub>-PTFEMA<sub>53</sub> nanoparticle concentration was systematically varied at a fixed 0.11 M NaCl, which corresponds to the minimum salt concentration required to prepare well-defined Pickering nanoemulsion droplets with a  $z$ -average diameter of 274 ± 119 nm. A significant reduction in the mean droplet diameter was observed when increasing the nanoparticle concentration from 1.0 to 4.0% w/w (see Figure 3.13). However, preparing nanoemulsions under the same conditions using higher nanoparticle concentrations (up to 7.0% w/w) did not result in a further reduction in droplet size. Such behaviour is typical for Pickering nanoemulsions and have been previously reported when using other particulate emulsifiers.<sup>16, 37, 39, 41, 73</sup> This provides strong (albeit indirect) evidence that the PSMA<sub>32</sub>-PTFEMA<sub>53</sub> nanoparticles survive the high-

pressure microfluidisation required to generate nano-sized droplets. Moreover, the mean droplet diameter reaches a minimum value at a copolymer concentration of 4.0% w/w. Assuming that all the nanoparticles are adsorbed onto the aqueous droplets and an effective nanoparticle density of approximately  $1 \text{ g cm}^{-3}$ , we estimate that  $N = 211$  and  $P_{\text{eff}} = 53\%$  under such conditions. Such values seem to be physically reasonable given the data reported in Table 3.1. Thus the initial limiting droplet diameter appears to correspond to maximum overall efficiency; i.e. the smallest possible aqueous droplets coated with all (or almost all) of the nanoparticles present in the formulation.

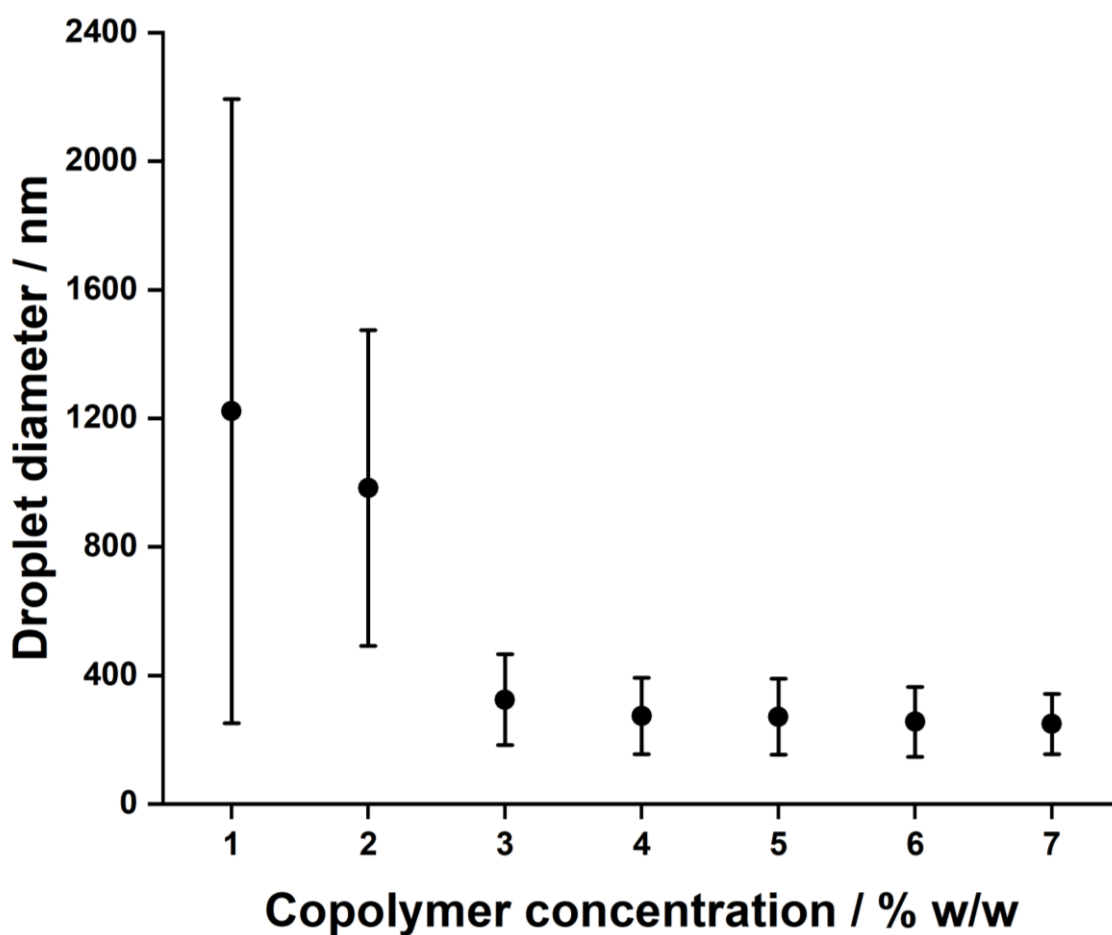


**Figure 3.13.** Variation in the  $z$ -average aqueous droplet diameter with nanoparticle concentration for w/o Pickering nanoemulsions prepared using PSMA<sub>32</sub>-PTFEMA<sub>53</sub> nanoparticles after five passes through an LV1 microfluidiser. Conditions: water volume fraction = 0.10; 0.11 M NaCl; applied pressure = 10 000 psi. Errors bars represent standard deviations for the DLS droplet size distributions, rather than the experimental error associated with repeated measurements.

A precursor w/o Pickering macroemulsion prepared using 5.0% w/w PSMA<sub>32</sub>-PTFEMA<sub>53</sub> nanoparticles was subjected to up to 10 passes through the LV1 microfluidiser at various applied pressures. The mean droplet diameter was assessed using DLS after 1, 5 and 10 passes (see Figure 3.14). At 5 000 psi, a significant reduction in emulsion droplet diameter was observed between the first and tenth passes. When the applied pressure was raised to 10 000 psi, the mean droplet diameter was reduced from 683 ± 382 nm to 268 ± 95 nm. However, for applied pressures ranging from 10 000 to 30 000 psi, only rather subtle changes in the mean droplet diameter were observed. Furthermore, only modest changes in droplet diameter were observed after each pass. In view of these empirical observations, an applied pressure of 10 000 psi and 5 passes was used to prepare w/o Pickering nanoemulsions in all subsequent experiments.

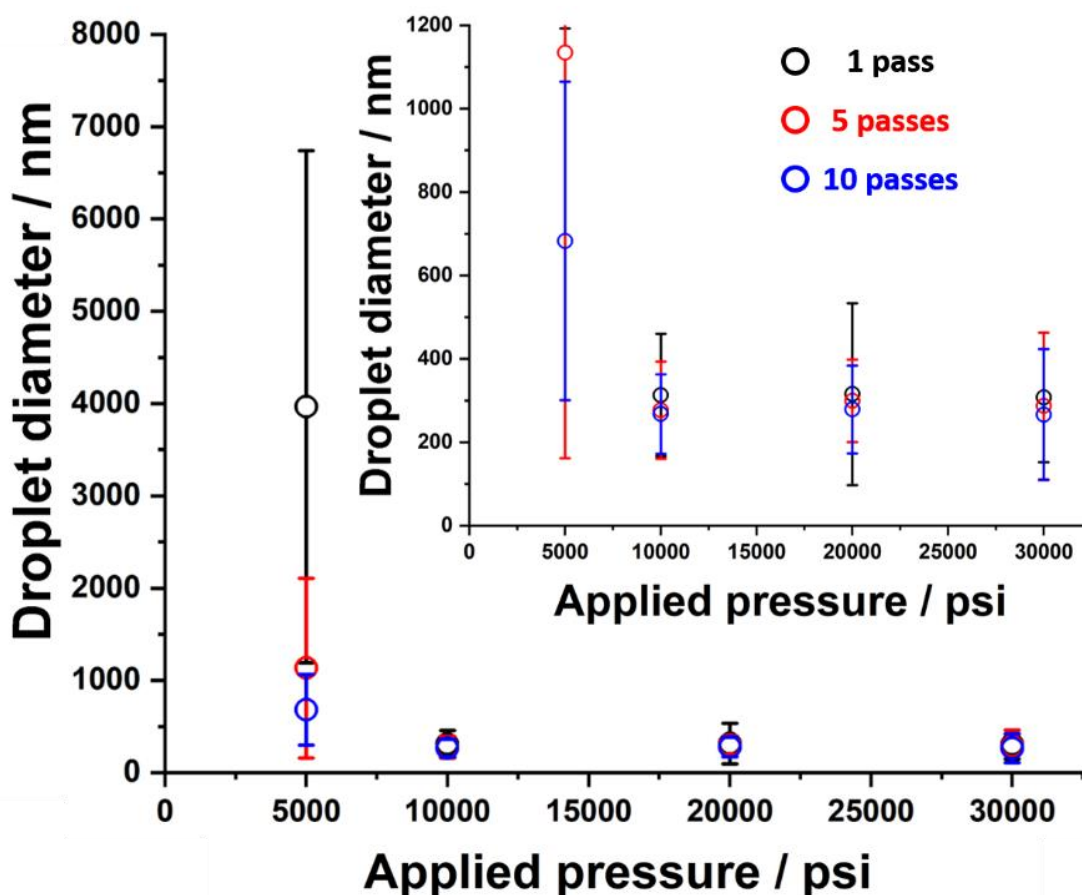


**Figure 3.14.** Variation in the *z*-average droplet diameter with applied pressure when preparing w/o Pickering nanoemulsions using an LV1 microfluidiser with 1, 5 or 10 pass(es). Conditions: water volume fraction = 0.10; 5.0% w/w PSMA<sub>32</sub>-PTFEMA<sub>53</sub> nanoparticles; 0.11 M NaCl. Error bars represent standard deviations for the DLS droplet size distributions rather than the experimental error associated with repeated measurements. The data shown in the inset are replotted over a narrower range of droplet diameters for the sake of clarity.

### 3.3.3 Characterisation of w/o Pickering Nanoemulsions

A w/o Pickering nanoemulsion was prepared under optimised conditions (10 000 psi, 5 passes, 5.0% w/w PSMA<sub>32</sub>-PTFEMA<sub>53</sub> nanoparticles) to visualise the remnants of dried droplets (i.e. the remaining nanoparticle superstructure) using TEM and SEM (see Figure 3.16b). As expected, the number-average droplet diameter of  $168 \pm 73$  nm (estimated from analysis of 50 droplets) is somewhat lower than the  $z$ -average diameter reported by DLS ( $272 \pm 119$  nm). On close inspection (see inset), it is clear that the spherical nanoparticles have survived the high-pressure microfluidisation conditions intact. Thus the w/o nanoemulsion is a genuine Pickering nanoemulsion, rather than simply a nanoemulsion that is stabilised by molecularly-dissolved diblock copolymer chains acting as a polymeric surfactant. This was not unexpected, because the PSMA<sub>32</sub> and PTFEMA<sub>53</sub> blocks are both hydrophobic, so the diblock copolymer chains do not possess any amphiphilic character with respect to water. SEM images recorded for the same nanoemulsion also indicated that spherical aqueous droplets were produced (see Figure 3.15b).

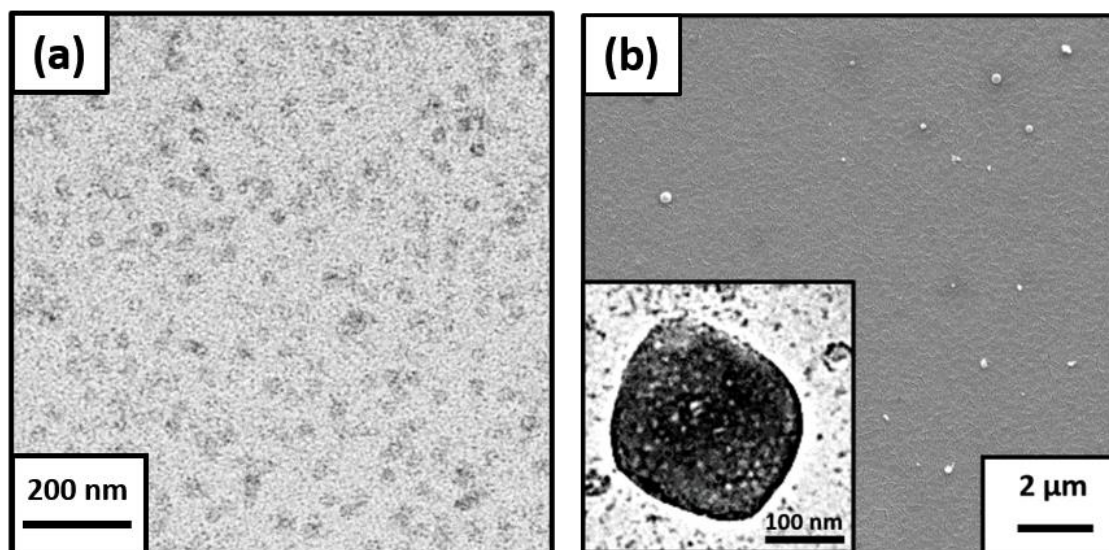


**Figure 3.15.** (a) TEM image recorded for a dried dilute dispersion of sterically-stabilised PSMA<sub>32</sub>-PTFEMA<sub>53</sub> nanoparticles. (b) Representative SEM and (inset) TEM images recorded for dried water-in-*n*-dodecane Pickering nanoemulsions prepared using 5.0% w/w PSMA<sub>32</sub>-PTFEMA<sub>53</sub> nanoparticles with 0.11 M NaCl dissolved in the aqueous phase. Conditions: microfluidisation pressure = 10 000 psi; 5 passes.

To determine the mean thickness of the nanoparticles adsorbed at the surface of the aqueous droplets, a SAXS pattern was recorded for a freshly-prepared Pickering nanoemulsion immediately after dilution to 1.0% v/v (Figure 3.16). Following our recent study of the characterisation of complementary *n*-dodecane-in-water Pickering nanoemulsions, this SAXS pattern was analysed using a two-population model. Population 1 is represented by core-shell spheres, where the core comprises the aqueous droplet and the shell is composed of an adsorbed monolayer of spherical micelles (see Equation 7.2). The particulate nature of the shell is described by the spherical micelles with a hard-sphere structure factor<sup>74</sup> to account for inter-particle interactions at the oil-water interface, which corresponds to population 2 (see Equation 7.9). In order to minimise the number of fitting parameters, the mean micelle core radius  $R_s$  and its associated standard deviation  $\sigma_s$  determined by analysis of the nanoparticles alone (Figure 3.6c) were used and these values were held constant when analysing the SAXS pattern of the Pickering nanoemulsion using the two-population model. The scattering length density for each component of the Pickering nanoemulsion [aqueous droplet core ( $\zeta_{core} = 9.42 \times 10^{10} \text{ cm}^{-2}$ ), particulate shell ( $\zeta_{shell} = 10.34 \times 10^{10} \text{ cm}^{-2}$ ), and the *n*-dodecane continuous phase ( $\zeta_{sol} = 7.63 \times 10^{10} \text{ cm}^{-2}$ )] was calculated based on their respective chemical compositions and mass densities. These three parameters were also fixed for the subsequent data fit to the SAXS pattern recorded for the Pickering nanoemulsion, whose structure can be described by the mean core radius  $R_c$  and its standard deviation  $\sigma_c$ , the mean shell thickness  $T_{shell}$ , and two scaling factors (volume fraction  $\varphi_1$  for population 1 and volume fraction  $\varphi_2$  for population). Two additional parameters were required to account for the packing of spherical micelles at the surface of the aqueous droplets: the micelle interaction radius,  $R_{PY}$ , and the effective volume fraction,  $f_{PY}$ . These seven parameters were used to fit the SAXS data.

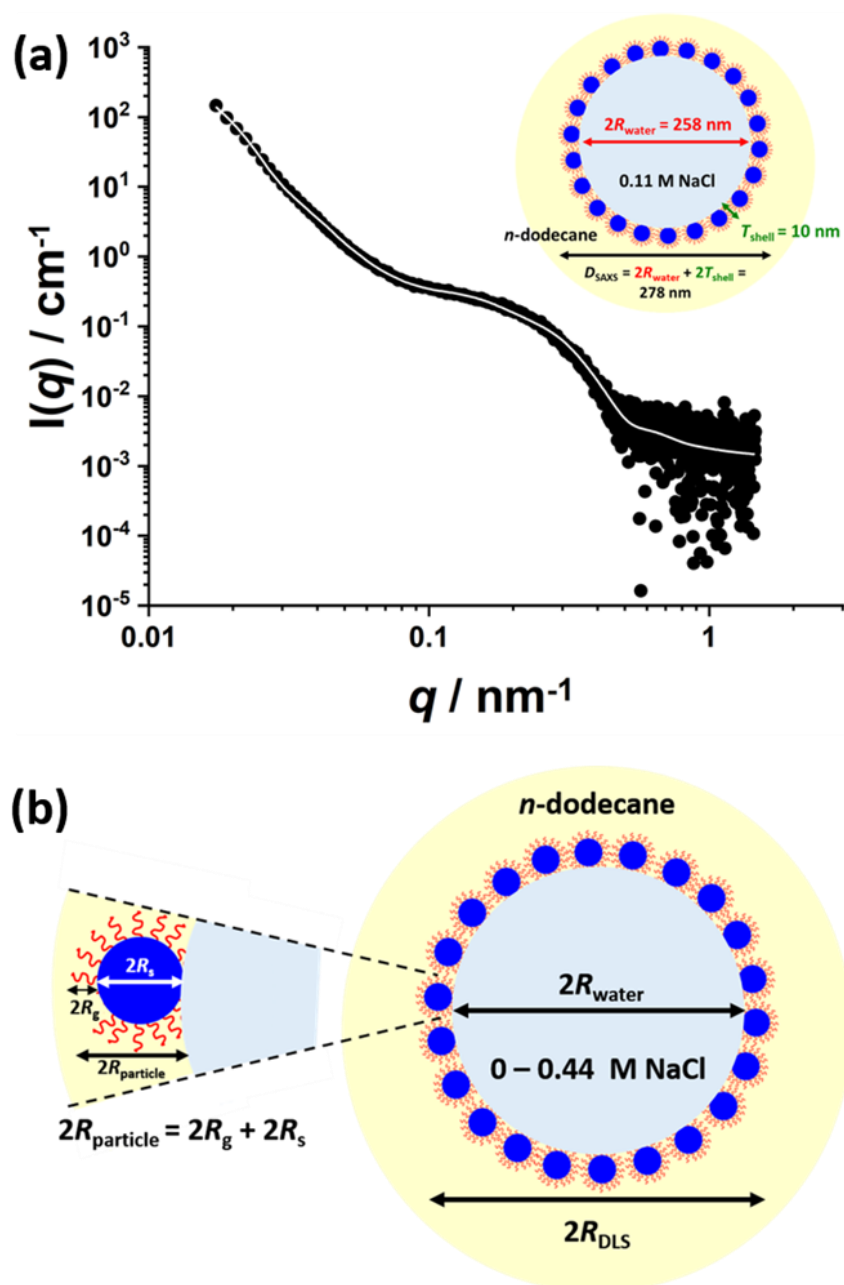


**Figure 3.16.** (a) SAXS pattern (circles) and corresponding data fit (white line) obtained for a 1.0% v/v Pickering nanoemulsion prepared using 5.0% w/w PSMA<sub>32</sub>-PTFEMA<sub>53</sub> nanoparticles and an aqueous phase containing 0.11 M NaCl (pH 6). This nanoemulsion was prepared using an LV1 microfluidiser at an applied pressure of 10 000 psi for 5 passes. The two-population core–shell structural model used for the SAXS analysis of this Pickering nanoemulsion comprises aqueous droplet cores coated with an adsorbed layer of PSMA<sub>32</sub>-PTFEMA<sub>53</sub> spherical nanoparticles. (b) Schematic representation of the adsorption of such nanoparticles at the *n*-dodecane/water interface. It is assumed that (i) these nanoparticles are adsorbed with an effective contact angle of 0° and (ii) PSMA<sub>32</sub> stabiliser chains in direct contact with the *n*-dodecane/water interface are fully collapsed and hence do not contribute to the adsorbed nanoparticle radius. Thus given that the effective thickness of these adsorbed sterically-stabilised nanoparticles is given by  $2R_s + 2R_g$  (rather than  $2R_s + 4R_g$ ), the approximate effective sphere radius,  $R_{\text{particle}}$ , is given by  $R_{\text{particle}} = R_s + R_g = 8.2$  nm. Experimental values for  $R_s$  and  $R_g$  were obtained from SAXS analysis of the PSMA<sub>32</sub>-PTFEMA<sub>53</sub> nanoparticles prior to emulsification, see the main text.

The shape of the SAXS pattern (Figure 3.16a) is similar to that previously reported in Chapter 2 for *n*-dodecane-in-water Pickering nanoemulsions prepared using hydrophilic PGMA<sub>48</sub>-PTFEMA<sub>50</sub> nanoparticles. Again, three main regions can be discerned: (i) relatively intense scattering at low  $q$  arising from the nanoemulsion droplets (close inspection reveals a subtle change in the gradient at low  $q$ , indicating cross-over from the Guinier region to the Porod region); (ii) additional scattering intensity at intermediate  $q$  corresponding to the nanoparticle form factor (see Figure 3.6c); (iii) relatively weak scattering at high  $q$ , which is associated with both scattering from the stabiliser chains forming the micelle corona (as described by the Debye function within the scattering model).

The two-population model produced a satisfactory fit to the nanoemulsion SAXS pattern (Figure 3.16a). The lack of a well-defined minimum in the scattering curve suggests that the aqueous droplets are polydisperse in size, which is consistent with DLS and analytical centrifugation studies (see Table 3.1, entry e and Table 3.2, entry 3, respectively). A mean droplet diameter  $D_{\text{SAXS}}$ , of  $278 \pm 68$  nm was calculated using the two-population model from the core droplet diameter  $2R_c$  and mean shell thickness  $T_{\text{shell}}$  (Figure 3.16b). Bearing in mind the limited resolution at low  $q$ , this droplet diameter is in reasonably good agreement with DLS and analytical centrifugation data ( $272 \pm 119$  nm and  $341 \pm 326$  nm, respectively). The mean apparent thickness of the adsorbed layer of nanoparticles  $T_{\text{shell}}$ , obtained for this Pickering nanoemulsion was approximately 10 nm. Given that the PSMA<sub>32</sub> chains in direct contact with the surface of the aqueous droplets are most likely in their collapsed state, we estimate the effective thickness of an individual adsorbed nanoparticle to be 16.4 nm ( $2R_{\text{particle}} = 2R_s + 2R_g$ ) (see Figure 3.16b). Moreover, the micelle interaction radius obtained from SAXS analysis ( $R_{\text{PY}} = 20.7$  nm) suggests that the nanoparticles are not in particularly close proximity to their neighbours, which results in an effective adsorbed layer thickness ( $T_{\text{shell}}$ ) that is somewhat lower than the nanoparticle diameter. Thus the SAXS data are consistent with the formation of a loosely packed monolayer of adsorbed nanoparticles surrounding each aqueous droplet, as expected for such a Pickering nanoemulsion.

### **3.3.4 Effect of Salt on the Stability of w/o Pickering Nanoemulsions**

It is well-known that o/w nanoemulsions undergo droplet growth predominantly *via* Ostwald ripening.<sup>16-18</sup> This phenomenon has also been reported for surfactant-stabilised w/o nanoemulsions.<sup>4</sup> To investigate the effect of varying the initial salt concentration on the rate of Ostwald ripening, Pickering nanoemulsions were prepared using zero, 0.11 M or 0.44 M NaCl dissolved in the aqueous phase. DLS was used to monitor the number-average droplet radius ( $R_n$ ) for the aged nanoemulsions. According to Lifshitz, Slyozov<sup>33</sup> and Wagner<sup>34</sup> (LSW theory), if the droplet growth mechanism occurs *via* Ostwald ripening then a plot of  $R_n^3$  against time should be linear (see Equation 1.22). This plot is shown in Figure 3.17a for a w/o Pickering nanoemulsion prepared in the absence of any added salt.

Two distinct linear regimes are observed, with the rate of droplet growth increasing by an order of magnitude within 2 h. In contrast,  $R_n^3$  increased linearly over time when the same w/o nanoemulsion was prepared using either 0.11 M or 0.43 M NaCl, indicating that droplet growth occurs *via* Ostwald ripening under such conditions (see Figure 3.17). In each case, the fresh Pickering w/o nanoemulsion had an initial droplet diameter of approximately 250 nm. This is important when comparing such data, because the initial droplet diameter (and polydispersity) is known to affect the rate of Ostwald ripening.<sup>3</sup> From the gradients of these linear plots, the Ostwald ripening rates were calculated to be 147 and 91 nm<sup>3</sup> s<sup>-1</sup> for 0.11 M and 0.43 M NaCl, respectively. Thus using a higher salt concentration leads to a slower rate of Ostwald ripening, as expected. This is because the salt ions are completely insoluble in the *n*-dodecane continuous phase and therefore remain within the aqueous droplets. Thus if water molecules were to diffuse from small to large droplets, the salt concentration in the former droplets increases, which inevitably leads to a higher chemical potential. This retards the rate of mass transport of water from small to large aqueous droplets and explains why the addition of salt reduces the rate of Ostwald ripening of the aqueous droplets.<sup>25-27</sup>

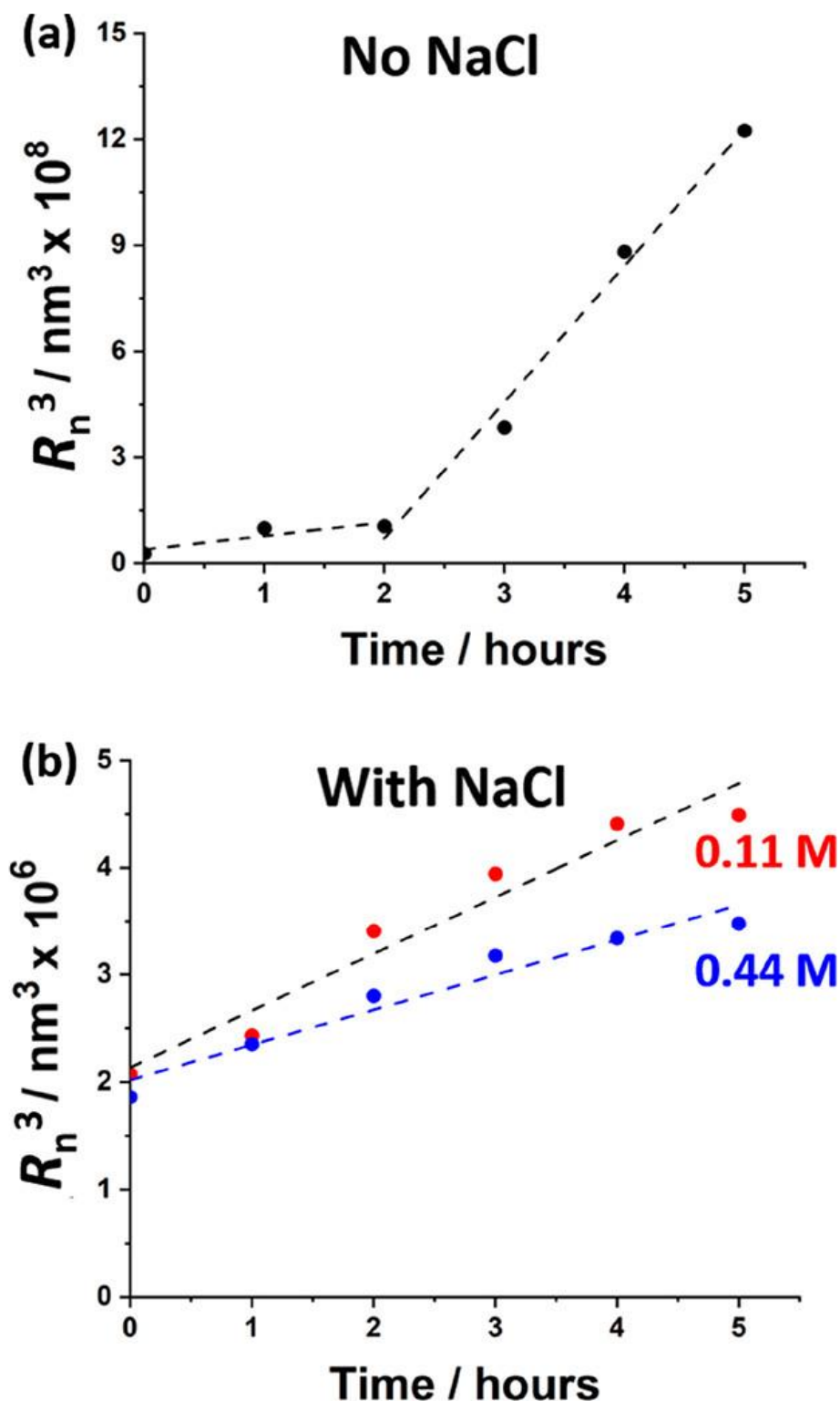


**Figure 3.17.** Variation in the cube of the mean droplet number-average radius ( $R_n$ ) as determined by DLS over time at 20 °C for aged water-in-*n*-dodecane Pickering nanoemulsions prepared either (a) in the absence of NaCl or (b) using 0.11 M or 0.43 M NaCl dissolved in the aqueous phase prior to emulsification. In the absence of any salt, the growth of  $R_n^3$  exhibits strongly non-linear behaviour, with a clear breakpoint being observed after 2 h. However, a relatively linear relationship is observed in the presence of salt, suggesting that droplet growth under such conditions involves Ostwald ripening.

Increasing the amount of added NaCl in the aqueous phase prior to high-shear homogenisation leads to the formation of finer droplets and narrower size distributions. However, a limiting overall droplet diameter of around 250 nm is obtained at a critical concentration of 0.43 M NaCl. Thus the effect of varying the NaCl concentration can be examined for w/o Pickering nanoemulsions with essentially the same initial mean droplet diameter.

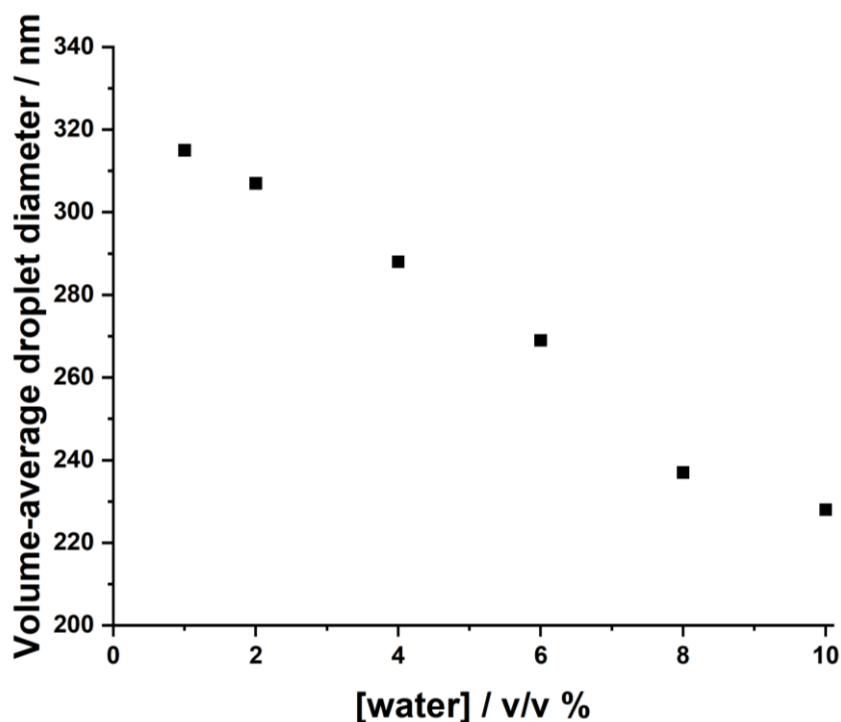


**Figure 3.18.** Effect of varying the aqueous droplet concentration on the apparent droplet diameter of a water-in-*n*-dodecane Pickering nanoemulsion as determined by analytical centrifugation (LUMiSizer instrument). This so-called ‘hindrance’ function indicates that the optimum droplet concentration for such analyses is approximately 1.0% v/v, with higher concentrations leading to hindered creaming and hence undersizing.

Analytical centrifugation was used to characterise both fresh and ageing nanoemulsions prepared using various salt concentrations. As noted by Thompson and co-workers, analytical centrifugation has a much higher resolution compared to DLS because droplet fractionation occurs prior to detection.<sup>17</sup> However, undersizing can be observed if the droplet concentration is too high as a result of hindered creaming.<sup>17, 75</sup> Moreover, using droplet concentrations that are too low can also be problematic: dilute emulsions scatter light only rather weakly and hence can fall outside of the optimum range required for the LUMiSizer instrument (i.e. below 30 %

### Chapter 3: Effect of Salt on the Formation and Stability of Water-in-Oil Pickering Nanoemulsions Stabilised by Diblock Copolymer Nanoparticles

transmission). Given these conflicting requirements, Thompson and co-workers found that a droplet concentration of 1.0% v/v was optimal.<sup>17</sup> In the present study, the aqueous droplet concentration (or water volume fraction) used for analytical centrifugation studies was systemically reduced. As shown in Figure 3.18, this led to a reduction in the apparent nanoemulsion droplet diameter, with a plateau value being observed at approximately 1.0% v/v. Analysing more concentrated nanoemulsions leads to a significantly smaller apparent droplet diameter owing to hindered sedimentation. Therefore, each nanoemulsion was diluted to an aqueous droplet concentration of 1.0% v/v prior to analytical centrifugation experiments.

**Table 3.2.** Variation in mean droplet diameter with ageing time as determined by analytical centrifugation analysis of Pickering nanoemulsions prepared using 5.0% w/w PSMA<sub>9</sub>-PTFEMA<sub>50</sub> diblock copolymer nanoparticles with 0.05 M to 0.43 M NaCl dissolved in the aqueous phase.

NaCl concentration / M	Volume-average droplet diameter by analytical centrifugation / nm				
	Fresh	1 week	2 weeks	3 weeks	4 weeks
0.43	259 ± 154	283 ± 220	276 ± 610	225 ± 227	229 ± 555
0.21	261 ± 178	297 ± 282	325 ± 872	342 ± 370	247 ± 566
0.11	341 ± 326	346 ± 1120	351 ± 1036	301 ± 537	257 ± 1128
0.05	463 ± 2522	918 ± 2395	828 ± 4225	522 ± 2901	498 ± 2103

Table 3.2 shows the mean volume-average diameters determined by analytical centrifugation for a series of w/o Pickering nanoemulsions prepared using 0.05 M to 0.43 M NaCl after ageing for up to 4 weeks at 20 °C. Unimodal droplet size distributions were observed for three of the four fresh nanoemulsions. The exception was the nanoemulsion prepared using 0.05 M NaCl, which exhibited a bimodal droplet size distribution. However, analysis of the latter fresh nanoemulsion by DLS indicated a unimodal droplet size distribution. In principle, this apparent discrepancy may simply reflect the inherently lower resolution of DLS compared to analytical centrifugation. Alternatively, Ostwald ripening may commence immediately after preparation of this relatively unstable nanoemulsion, with DLS merely offering a shorter analysis time. Nevertheless, aqueous droplets prepared using 0.05 M NaCl coarsened at a significantly faster rate relative to that observed for nanoemulsions prepared at higher salt concentrations. In all cases, both the volume-average droplet diameter and the corresponding polydispersity increased over a three-week period. However, a lower volume-average droplet diameter was observed after four

weeks, along with a concomitant increase in polydispersity. An apparent reduction in volume-average diameter was also reported by Thompson *et al.* during long-term ageing studies of o/w Pickering nanoemulsions stabilised by diblock copolymer nanoparticles, which was attributed to the increasingly skewed nature of the droplet size distribution.<sup>17</sup>

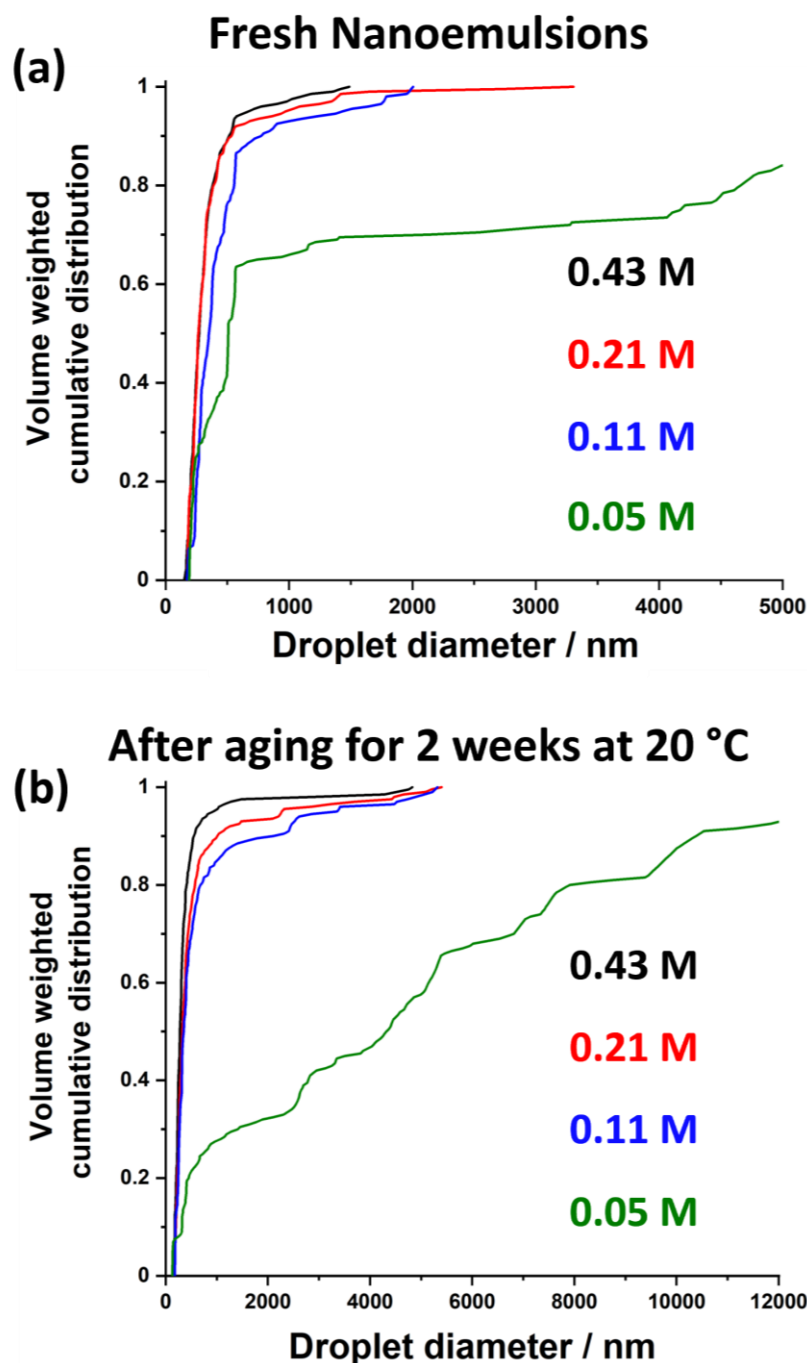


**Figure 3.19.** Volume-weighted cumulative distributions determined by analytical centrifugation (LUMiSizer instrument) for *n*-dodecane-in-water Pickering nanoemulsions prepared using various amounts of NaCl dissolved in the aqueous phase: (a) fresh nanoemulsions and (b) after aging for 2 weeks at 20 °C.

Figure 3.19a shows the volume-average cumulative distributions recorded for each of the four Pickering nanoemulsions after aging for 2 weeks at 20 °C. The greatest extent of Ostwald ripening is observed for the nanoemulsion prepared using 0.05 M NaCl, with more than 40% of the aqueous droplets now exceeding 2 µm diameter. In contrast, fewer than 5% of aqueous droplets exceed 2 µm after the same ageing time if they contained 0.11 M NaCl. Interestingly, no improvement in droplet stability was observed when using higher salt concentrations. After ageing for 2 weeks at 20 °C, most nanoemulsions exhibited bimodal droplet size distributions (see Figure 3.19b). Nanoemulsions prepared using 0.11 M NaCl or higher contain a minor population of larger droplets exceeding 2 µm diameter. For the least stable nanoemulsion prepared in the presence of 0.05 M NaCl, two approximately equal droplet populations are initially observed.

After ageing, the population of larger droplets has increased relative to that of the smaller droplets. Such observations are consistent with an Ostwald ripening mechanism and also account for the apparent reduction in droplet diameter that is observed after 4 weeks ageing at 20 °C (see Figure 3.20). Analytical centrifugation studies indicate that a critical NaCl concentration of 0.11 M is required to substantially suppress Ostwald ripening. Using NaCl concentrations greater than 0.11 M provides little improvement in terms of stability. According to Kabalnov, this salt concentration corresponds to the fraction of insoluble component for which the nanoemulsions are in their (meta)stable regime (see Equation 3.2).<sup>21</sup> More explicitly, the entropy of mixing is sufficiently negative to overcome the Laplace pressure that drives Ostwald ripening. Over time, the smaller droplets become enriched with salt, which is entropically less favourable than a perfectly mixed system, therefore Ostwald ripening is suppressed.

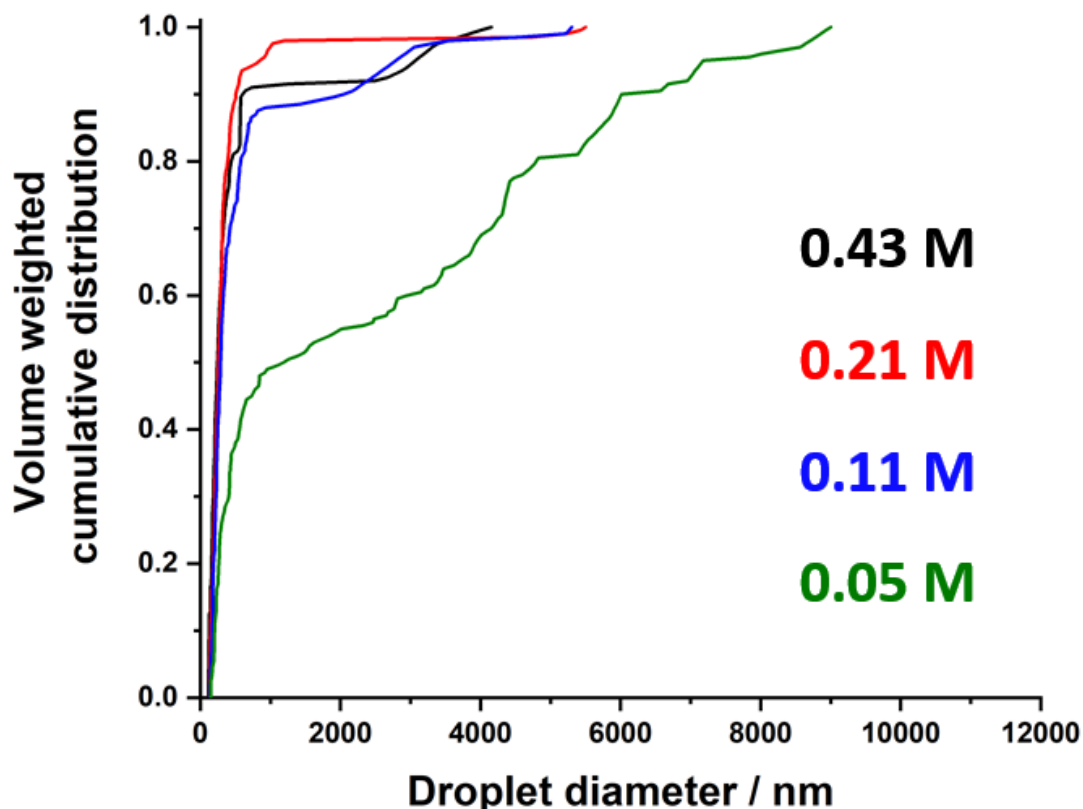


**Figure 3.20.** Volume-weighted cumulative distributions determined by analytical centrifugation (LUMiSizer instrument) for *n*-dodecane-in-water Pickering nanoemulsions prepared using various amounts of NaCl dissolved in the aqueous phase) after ageing for 4 weeks at 20 °C.

### 3.4 Conclusions

RAFT dispersion polymerisation of TFEMA enables the convenient synthesis of sterically-stabilised PSMA<sub>32</sub>-PTFEMA<sub>53</sub> spherical nanoparticles of  $28 \pm 6$  nm diameter in *n*-dodecane at 80 °C. Such diblock copolymer nanoparticles have been used as an emulsifier to prepare a water-in-oil Pickering nanoemulsions for the first time. In the absence of any added salt in the dispersed aqueous phase, only relatively coarse droplets of more than 600 nm diameter could be produced *via* high-pressure microfluidisation. However, increasing the NaCl concentration in the aqueous phase prior to emulsification led to a systematic reduction in the  $z$ -average droplet diameter, as judged by DLS studies. A limiting aqueous droplet diameter of around 250 nm was obtained when using 0.11 M NaCl. Furthermore, this droplet diameter could be tuned by varying the applied pressure and the number of passes through the microfluidiser. Increasing the PSMA<sub>32</sub>-PTFEMA<sub>53</sub>

nanoparticle concentration produced finer aqueous droplets, suggesting that such nanoparticles survive the microfluidisation conditions intact. Furthermore, TEM studies conducted on the dried droplets indicate that the PSMA<sub>32</sub>-PTFEMA<sub>53</sub> nanoparticles retain their original spherical morphology and adsorb intact at oil-water interface. SAXS studies conducted on such nanoemulsions confirm the formation of a loosely-packed monolayer of adsorbed nanoparticles surrounding the aqueous droplets. DLS studies indicate that the long-term stability of the aqueous droplets is enhanced at higher NaCl concentrations. The cube of the droplet radius of Pickering nanoemulsions prepared using an aqueous solution containing either 0.11 or 0.43 M NaCl increased linearly over time, suggesting that droplet growth involves an Ostwald ripening mechanism. In contrast, when such Pickering nanoemulsion were prepared in the absence of NaCl, they proved to be significantly less stable. Analytical centrifugation was used to conduct longer-term stability studies on such nanoemulsions. Ostwald ripening was substantially suppressed in the presence of 0.05 M NaCl, with volume-average diameters remaining below 300 nm after 4 weeks storage at 20 °C. However, using 0.11 M NaCl led to no discernible improvement in the nanoemulsion stability.

### **3.5 References**

1. C. Solans, P. Izquierdo, J. Nolla, N. Azemar and M. J. Garcia-Celma, *Curr. Opin. Colloid Interface Sci.*, 2005, **10**, 102-110.
2. D. J. McClements, *Soft Matter*, 2012, **8**, 1719-1729.
3. A. Gupta, H. B. Eral, T. A. Hatton and P. S. Doyle, *Soft Matter*, 2016, **12**, 2826-2841.
4. J.-H. Sommerling, M. B. C. de Matos, E. Hildebrandt, A. Dessy, R. J. Kok, H. Nirschl and G. Leneweit, *Langmuir*, 2018, **34**, 572-584.
5. V. Massel, M. Alexander and M. Corredig, *Food Biophysics*, 2015, **10**, 57-65.
6. Q. Zhu, F. Wu, M. Saito, E. Tatsumi and L. Yin, *Food Chemistry*, 2016, **201**, 197-204.
7. L.-C. Peng, C.-H. Liu, C.-C. Kwan and K.-F. Huang, *Colloids Surf., A*, 2010, **370**, 136-142.
8. A. H. E. Machado, D. Lundberg, A. J. Ribeiro, F. J. Veiga, B. Lindman, M. G. Miguel and U. Olsson, *Langmuir*, 2012, **28**, 4131-4141.
9. M. Chiesa, J. Garg, Y. T. Kang and G. Chen, *Colloids Surf., A*, 2008, **326**, 67-72.
10. L. Lee, R. Hancocks, I. Noble and I. T. Norton, *J. Food Eng.*, 2014, **131**, 33-37.

11. A. Orte, M. J. Ruedas-Rama, J. M. Paredes, L. Crovetto and J. M. Alvarez-Pez, *Langmuir*, 2011, **27**, 12792-12799.
12. H. Kumar and V. Kumar, *Ultrason. Sonochem.*, 2018, **49**, 79-88.
13. I. F. Guha, S. Anand and K. K. Varanasi, *Nat. Commun.*, 2017, **8**, 1371.
14. G. C. Kini, S. L. Biswal, M. S. Wong and C. A. Miller, *J. Colloid Interface Sci.*, 2012, **385**, 111-121.
15. N. Anton and P. Saulnier, *Soft Matter*, 2013, **9**, 6465-6474.
16. K. H. Persson, I. A. Blute, I. C. Mira and J. Gustafsson, *Colloids Surf., A*, 2014, **459**, 48-57.
17. K. L. Thompson, M. J. Derry, F. L. Hatton and S. P. Armes, *Langmuir*, 2018, **34**, 9289-9297.
18. G. Rodriguez-Lopez, Y. O'Neil Williams and J. Toro-Mendoza, *Langmuir*, 2019, **35**, 5316-5323.
19. A. S. Kabal'nov, A. V. Pertzov and E. D. Shchukin, *Colloids Surf.*, 1987, **24**, 19-32.
20. A. J. Webster and M. E. Cates, *Langmuir*, 1998, **14**, 2068-2079.
21. A. Kabalnov, *J. Dispers. Sci. Technol.*, 2001, **22**, 1-12.
22. H. Egger and K. M. McGrath, *J. Colloid Interface Sci.*, 2006, **299**, 890-899.
23. T. J. Wooster, M. Golding and P. Sanguansri, *Langmuir*, 2008, **24**, 12758-12765.
24. T. Delmas, H. Piraux, A.-C. Couffin, I. Texier, F. Vinet, P. Poulin, M. E. Cates and J. Bibette, *Langmuir*, 2011, **27**, 1683-1692.
25. J. Kizling and B. Kronberg, *Colloids Surf.*, 1990, **50**, 131-140.
26. M. Y. Koroleva and E. V. Yurtov, *Colloid Journal*, 2003, **65**, 40-43.
27. M. P. Aronson and M. F. Petko, *J. Colloid Interface Sci.*, 1993, **159**, 134-149.
28. W. I. Higuchi and J. Misra, *J. Pharm. Sci.*, 1962, **51**, 459-466.
29. R. Buscall, S. S. Davis and D. C. Potts, *Colloid. Polym. Sci.*, 1979, **257**, 636-644.
30. S. S. Davis, H. P. Round and T. S. Purewal, *J. Colloid Interface Sci.*, 1981, **80**, 508-511.
31. P. Taylor and R. H. Ottewill, *Colloids Surf., A*, 1994, **88**, 303-316.
32. P. Taylor, *Adv. Colloid Interface Sci.*, 1998, **75**, 107-163.
33. I. M. Lifshitz and V. V. Slyozov, *J. Phys. Chem. Solids*, 1961, **19**, 35-50.
34. C. Wagner, *Zeitschrift für Elektrochemie, Berichte der Bunsengesellschaft für physikalische Chemie*, 1961, **65**, 581-591.
35. H. L. Rosano, F. G. Gandolfo and J.-D. P. Hidrot, *Colloids Surf., A*, 1998, **138**, 109-121.
36. Q. Zhu, Y. Pan, X. Jia, J. Li, M. Zhang and L. Yin, *Compr. Rev. Food Sci. Food Saf.*, 2019, **18**, 1660-1675.
37. S. Sihler, A. Schrade, Z. Cao and U. Ziener, *Langmuir*, 2015, **31**, 10392-10401.
38. N. G. Eskandar, S. Simovic and C. A. Prestidge, *J. Colloid Interface Sci.*, 2011, **358**, 217-225.
39. K. L. Thompson, N. Cinotti, E. R. Jones, C. J. Mable, P. W. Fowler and S. P. Armes, *Langmuir*, 2017, **33**, 12616-12623.
40. C. Jiménez Saelices and I. Capron, *Biomacromolecules*, 2018, **19**, 460-469.

41. D. J. Kang, H. Bararnia and S. Anand, *ACS Appl. Mater. Interfaces*, 2018, **10**, 21746-21754.
42. Z. Du, Q. Li, J. Li, E. Su, X. Liu, Z. Wan and X. Yang, *J. Agr. Food Chem.*, 2019, **67**, 11728-11740.
43. S. M. Dieng, N. Anton, P. Bouriat, O. Thioune, P. M. Sy, N. Massaddeq, S. Enharrar, M. Diarra and T. Vandamme, *Soft Matter*, 2019, **15**, 8164-8174.
44. Z. Xiao, Y. Liu, Y. Niu and X. Kou, *Colloids Surf., A*, 2020, **588**, 124367.
45. T. Okada and T. Koide, *Langmuir*, 2018, **34**, 9500-9506.
46. H. Jiang, L. Hong, Y. Li and T. Ngai, *Angew. Chem. Int. Ed.*, 2018, **57**, 11662-11666.
47. T. Bollhorst, T. Grieb, A. Rosenauer, G. Fuller, M. Maas and K. Rezwani, *Chem. Mater.*, 2013, **25**, 3464-3471.
48. S. L. Canning, G. N. Smith and S. P. Armes, *Macromolecules*, 2016, **49**, 1985-2001.
49. V. J. Cunningham, A. M. Alswieleh, K. L. Thompson, M. Williams, G. J. Leggett, S. P. Armes and O. M. Musa, *Macromolecules*, 2014, **47**, 5613-5623.
50. E. R. Jones, M. Semsarilar, A. Blanazs and S. P. Armes, *Macromolecules*, 2012, **45**, 5091-5098.
51. N. J. Warren and S. P. Armes, *J. Am. Chem. Soc.*, 2014, **136**, 10174-10185.
52. B. Akpınar, L. A. Fielding, V. J. Cunningham, Y. Ning, O. O. Mykhaylyk, P. W. Fowler and S. P. Armes, *Macromolecules*, 2016, **49**, 5160-5171.
53. F. L. Hatton, J. R. Lovett and S. P. Armes, *Polym. Chem.*, 2017, **8**, 4856-4868.
54. C. J. Mable, N. J. Warren, K. L. Thompson, O. O. Mykhaylyk and S. P. Armes, *Chem. Sci.*, 2015, **6**, 6179-6188.
55. L. Houillot, C. Bui, M. Save, B. Charleux, C. Farcet, C. Moire, J.-A. Raust and I. Rodriguez, *Macromolecules*, 2007, **40**, 6500-6509.
56. L. A. Fielding, M. J. Derry, V. Ladmiral, J. Rosselgong, A. M. Rodrigues, L. P. D. Ratcliffe, S. Sugihara and S. P. Armes, *Chem. Sci.*, 2013, **4**, 2081-2087.
57. M. J. Derry, L. A. Fielding and S. P. Armes, *Prog. Polym. Sci.*, 2016, **52**, 1-18.
58. L. A. Fielding, J. A. Lane, M. J. Derry, O. O. Mykhaylyk and S. P. Armes, *J. Am. Chem. Soc.*, 2014, **136**, 5790-5798.
59. M. J. Derry, L. A. Fielding and S. P. Armes, *Polym. Chem.*, 2015, **6**, 3054-3062.
60. Y. Pei, O. R. Sugita, L. Thurairajah and A. B. Lowe, *RSC Advances*, 2015, **5**, 17636-17646.
61. Y. Pei, L. Thurairajah, O. R. Sugita and A. B. Lowe, *Macromolecules*, 2015, **48**, 236-244.
62. L. P. D. Ratcliffe, B. E. McKenzie, G. M. D. Le Bouëdec, C. N. Williams, S. L. Brown and S. P. Armes, *Macromolecules*, 2015, **48**, 8594-8607.
63. M. J. Rymaruk, S. J. Hunter, C. T. O'Brien, S. L. Brown, C. N. Williams and S. P. Armes, *Macromolecules*, 2019, **52**, 2822-2832.
64. C. György, S. J. Hunter, C. Girou, M. J. Derry and S. P. Armes, *Polym. Chem.*, 2020, **11**, 4579-4590.
65. M. Semsarilar, V. Ladmiral, A. Blanazs and S. P. Armes, *Langmuir*, 2012, **28**, 914-922.
66. E. J. Cornel, S. van Meurs, T. Smith, P. S. O'Hora and S. P. Armes, *J. Am. Chem. Soc.*, 2018, **140**, 12980-12988.

67. J. A. Gates and R. H. Wood, *J. Chem. Eng. Data*, 1985, **30**, 44-49.
68. J. Ilavsky and P. R. Jemian, *J. Appl. Crystallogr.*, 2009, **42**, 347-353.
69. J. A. Balmer, S. P. Armes, P. W. Fowler, T. Tarnai, Z. Gáspár, K. A. Murray and N. S. J. Williams, *Langmuir*, 2009, **25**, 5339-5347.
70. J. S. Pedersen and M. C. Gerstenberg, *Macromolecules*, 1996, **29**, 1363-1365.
71. D. J. McClements and J. Rao, *Crit. Rev. Food Sci. Nutr.*, 2011, **51**, 285-330.
72. A. Pawlik, P. W. Cox and I. T. Norton, *J. Colloid Interface Sci.*, 2010, **352**, 59-67.
73. I. Kalashnikova, H. Bizot, P. Bertoncini, B. Cathala and I. Capron, *Soft Matter*, 2013, **9**, 952-959.
74. D. J. Kinning and E. L. Thomas, *Macromolecules*, 1984, **17**, 1712-1718.
75. J. Walter, T. Thajudeen, S. Su, D. Segets and W. Peukert, *Nanoscale*, 2015, **7**, 6574-6587.

## Chapter 4:

# Synthesis of Diblock Copolymer Spheres, Worms and Vesicles *via* RAFT Aqueous Emulsion Polymerisation of Hydroxybutyl Methacrylate

Reproduced in part with permission from:

[S. J. Hunter, J. R. Lovett, O. O. Mykhaylyk, E. R. Jones and S. P. Armes, *Polym. Chem.*, 2021, **12**, 3629-3639]

## 4.1 Introduction

It is well known that water possesses extensive intermolecular forces known as hydrogen bonds.<sup>1</sup> The act of dissolution of a solute involves disrupting hydrogen bonds and also forming new hydrogen bonds. The overall energetic balance dictates the behaviour of the solute. If the solute is incapable of hydrogen bonding, then it may not be soluble. To maximise the number of interactions, the water molecules rearrange to form a cage-like structure around each solute molecule.<sup>2, 3</sup> This is known as the hydrophobic effect and is entropically unfavourable.<sup>4</sup> This explains why some liquids are immiscible with water; such molecules are characterised as being hydrophobic. Hydrophobic interactions depend on the temperature, pressure, ionic strength, solute size, shape, and type.<sup>5-7</sup> Moreover, the concept of hydrophobicity can be applied to either a whole molecule or to specific regions within a molecule.<sup>8</sup> In principle, the hydrophobicity of a small molecule can be assessed using octanol-water partition coefficients, otherwise known as  $\text{Log } P$ .<sup>9, 10</sup> However, estimating the theoretical hydrophobicity of macromolecules has proven to be much more challenging,<sup>11-13</sup> although models suggest that hydrophobicity scales with surface area.<sup>2</sup>

The self-assembly of amphiphilic diblock copolymers in aqueous solution is driven by the hydrophobic effect.<sup>14, 15</sup> To minimise interfacial energy, the hydrophobic blocks aggregate together to form discrete domains that are stabilised by the hydrophilic block. The shape adopted by the aggregates is related to the amphiphile geometry by the so-called packing parameter  $P$  (see Figure 1.8).<sup>16, 17</sup> However, this empirical geometric parameter cannot be used to predict the copolymer morphology because it cannot account for either kinetics or thermodynamics.<sup>18, 19</sup> Under equilibrium conditions, the tendency for a diblock copolymer to self-assemble into higher-order morphologies is expected to be greater for more hydrophobic core-forming blocks.<sup>13</sup> For example, Ratcliffe *et al.* reported that chain extension of a carboxylic acid-functionalised hydrophilic HOOC-PGMA<sub>60</sub> precursor with 2-hydroxyethyl methacrylate (HEMA) led to no self-assembly at all, which was attributed to the insufficiently hydrophobic character of the PHEMA

block.<sup>20</sup> However, when HEMA was replaced with the more hydrophobic HPMA then the resulting PGMA-HPMA diblock copolymers self-assembled to form the expected range of copolymer morphologies (i.e. spheres, worms or vesicles). Ratcliffe *et al.* also briefly examined the RAFT aqueous emulsion homopolymerisation of HBMA as part of a broader study of the statistical copolymerisation of HBMA with HEMA.<sup>20</sup> However, only kinetically-trapped spheres were obtained. More specifically, a HOOC-PGMA<sub>60</sub> precursor was chain-extended with HBMA at 70 °C to prepare a series of HOOC-PGMA<sub>60</sub>-PHBMA<sub>x</sub> spheres ( $x = 75 - 500$ ) at around pH 5 - 6. In a subsequent study, Lovett *et al.* reported that terminal anionic charge introduced into the steric stabiliser chains *via* ionisation of carboxylic acid end-groups was sufficient to drive a worm-to-sphere transition.<sup>21</sup> In retrospect, this explains why only kinetically-trapped spheres were observed by Ratcliffe *et al.*<sup>20</sup>

In principle, RAFT aqueous emulsion polymerisation formulations provide a convenient surfactant-free route for the synthesis of sterically-stabilised nano-objects with various morphologies.<sup>22-24</sup> In practice, there are many literature examples of such syntheses that are restricted to kinetically-trapped spheres.<sup>25-34</sup> However, in 2017 Cockram *et al.* reported that the RAFT aqueous emulsion polymerisation of HBMA using a partially ionised PMAA stabiliser block at pH 5 produced a new non-spherical ‘monkey nut’ morphology.<sup>35</sup> It was hypothesised that the relatively high aqueous monomer solubility of HBMA (estimated to be 20 g dm<sup>-3</sup> at the reaction temperature of 70 °C) allowed more effective plasticisation of the core-forming block during the polymerisation. In turn, this facilitated sphere-sphere fusion to produce ‘monkey nuts’, rather than merely kinetically-trapped spheres (see Figure 1.16). Similarly, Hatton *et al.* explored the RAFT aqueous emulsion polymerisation of GlyMA (aqueous solubility ~ 18 - 20 g dm<sup>-3</sup> at the reaction temperature of 50 °C)<sup>36</sup> using a non-ionic PGMA precursor as a steric stabiliser block.<sup>33, 37, 38</sup> Well-defined diblock copolymer worms or vesicles were obtained when the PGMA stabiliser block was sufficiently short, which is known to promote access to higher order morphologies.<sup>37-40</sup> More recently, Brotherton and co-workers reported the RAFT aqueous emulsion polymerisation of MOEMA, a third methacrylic monomer with moderate aqueous

solubility ( $19.6 \text{ g dm}^{-3}$  at the reaction temperature of  $70 \text{ }^\circ\text{C}$ ).<sup>40</sup> In this case, synchrotron SAXS was used to monitor the *in situ* evolution in copolymer morphology from spheres to worms to vesicles during this aqueous PISA synthesis.<sup>40</sup> Interesting, relatively small vesicles were obtained when targeting a sufficiently asymmetric diblock composition for either  $\text{PGMA}_{28}\text{-PGlyMA}_x$  or  $\text{PGMA}_{29}\text{-PMOEMA}_x$  (see Figure 4.1).<sup>38, 40</sup> In fact, SAXS was required to verify the vesicular nature of such nano-objects since they resisted collapse under ultrahigh vacuum conditions, leading them to be incorrectly assigned as spheres during preliminary TEM studies.

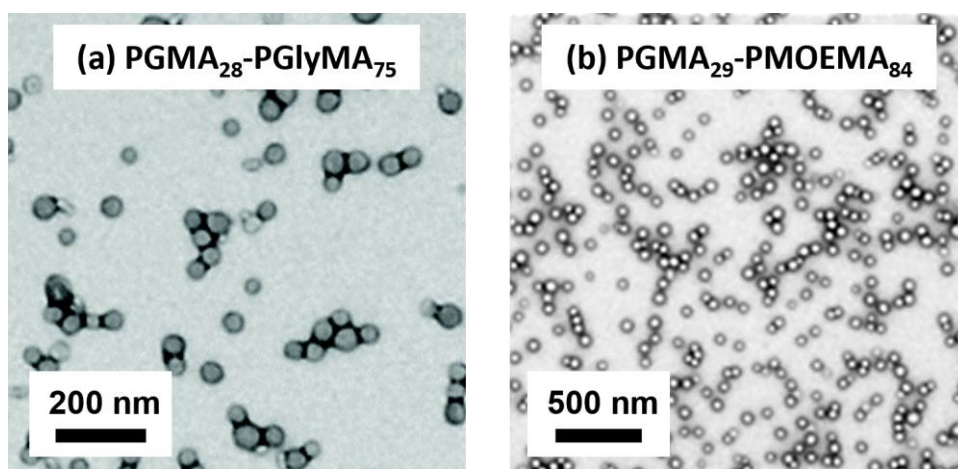


**Figure 4.1.** Representative TEM images recorded for (a)  $\text{PGMA}_{28}\text{-PGlyMA}_{75}$  and (b)  $\text{PGMA}_{29}\text{-PGlyMA}_{84}$  vesicles.<sup>38, 40</sup>

O'Reilly and co-workers reported an *in silico* method to predict novel monomers that are suitable for RAFT aqueous dispersion polymerisation. More specifically, the variance in  $\text{Log } P$  was normalised with respect to the surface area  $SA$  as a function of  $DP$  for a range of oligomers, as shown in Figure 4.2. Oligomers with positive  $\text{Log } P/SA$  values indicate that the monomer should serve as a suitable core-forming block. The magnitude of  $\text{Log } P/SA$  also provided an assessment of the hydrophobic character of the latter. This new approach was used to calculate the effect of oligomer hydrophobicity on the onset of nucleation during PISA and the final copolymer morphology. More specifically, a water-soluble  $\text{PEG}_{113}$  precursor was chain-extended (target  $DP = 100$  in each case) using the following five vinyl monomers of increasing  $\text{Log } P/SA$  (DAAm, 3-HPMA, 2-HPMA, 2-HBA and HBMA) under the same experimental conditions. Kinetic data indicated that a shorter critical core-forming block  $DP$  was required to form nascent

micelles when examining more hydrophobic oligomers. Moreover, oligomers generated from monomers with higher Log  $P$ /SA values resulted in higher-order morphologies compared to diblock copolymers of the same DP exhibiting lower Log  $P$ /SA values. Interestingly, cryo-TEM studies revealed that the resulting PEG<sub>113</sub>-PHBMA<sub>100</sub> diblock copolymers possessed a mixture of worm-like and vesicular morphologies.<sup>13</sup>

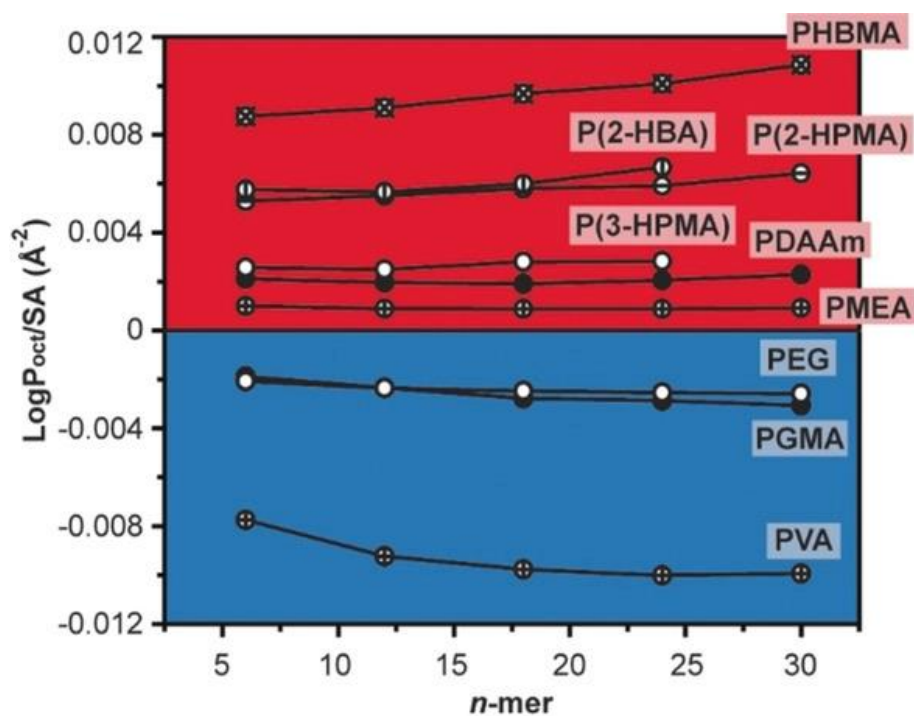


**Figure 4.2.** Oligomer hydrophobicity as a function of the length of the oligomer. Log  $P_{\text{oct}}$  values normalised by surface area SA. Blue region indicates stabiliser blocks and red region indicates core-forming blocks in aqueous PISA.<sup>13</sup>

In the current Chapter, the above PGMA-PHBMA formulation is revisited using a relatively short PGMA<sub>41</sub> precursor to gain access to spheres, worms and vesicles. A pseudo-phase diagram is constructed to enable the reproducible targeting of pure copolymer morphologies. Furthermore, monitoring the evolution in copolymer morphology by TEM when targeting vesicles for this formulation reveals various transient intermediates similar to those observed during the RAFT aqueous dispersion polymerisation of HPMA by Blanzas *et al.*<sup>41</sup> Finally, the performance of linear PGMA<sub>41</sub>-PHBMA<sub>110</sub> vesicles as a Pickering emulsifier for *n*-dodecane droplets is critically compared to that previously reported for the analogous linear PGMA<sub>45</sub>-PHPMA<sub>200</sub> vesicles.<sup>42</sup>

## 4.2 Experimental

### 4.2.1 Materials

Glycerol monomethacrylate (GMA) was kindly donated by GEO Specialty Chemicals (Hythe, UK) and used without further purification. Hydroxybutyl methacrylate (HBMA; 94% purity; comprising a 1:1 mixture of 4-hydroxybutyl methacrylate and 2-hydroxybutyl methacrylate) and 4,4'-azobis(4-cyanopentanoic acid) (ACVA; 99%) and tolylene 2,4-diisocyanate-terminated poly(propylene glycol) (PPG-TDI) were purchased from Sigma-Aldrich (UK) and were used as received. 2,2'-Azobis[2-(2-imidazolin-2-yl)propane] dihydrochloride (VA-044;  $\geq 97\%$ ) and 2-cyano-2-propyl dithiobenzoate (CPDB) were purchased from Strem Chemicals Ltd. (Cambridge, UK) and used as received. Deuterated methanol ( $\text{CD}_3\text{OD}$ ) was purchased from Goss Scientific Instruments Ltd. (Cheshire, UK). All other solvents were purchased from Fisher Scientific (Loughborough, UK) and were used as received. Deionised water was used for all experiments.

### 4.2.2 Synthesis of a PGMA<sub>41</sub> precursor *via* RAFT Solution Polymerisation in Ethanol

A round-bottomed flask was charged with GMA (20.00 g, 0.126 mol), CPDB (0.614 g, 2.22 mmol; target DP = 57), ACVA (0.124 g, 0.444 mmol; CPDB/ACVA molar ratio = 5.0), and anhydrous ethanol (30.9 g) to afford a 40% w/w solution. The resulting pink solution was purged with  $\text{N}_2$  gas for 30 min before the sealed flask was immersed into an oil bath set at 70 °C. After 140 min (70% conversion as judged by  $^1\text{H}$  NMR spectroscopy), the GMA polymerisation was quenched by immersion of the flask into an ice bath and subsequently exposing the reaction mixture to air. The crude polymer was then precipitated twice into excess dichloromethane and washed three times with this solvent before being freeze-dried overnight.  $^1\text{H}$  NMR studies indicated a mean degree of polymerisation of 41 *via* end-group analysis (by comparing the integrated aromatic RAFT end-group signals at 7.1 – 7.4 ppm to those assigned to the two

oxymethylene protons at 3.5–4.4 ppm). DMF GPC studies indicated an  $M_n$  of 13 900 g mol<sup>-1</sup> and an  $M_w/M_n$  of 1.18.

#### **4.2.3 Synthesis of PGMA<sub>41</sub>-PHBMA<sub>x</sub> Diblock Copolymer Nano-Objects by RAFT Aqueous Emulsion Polymerisation of HBMA**

The following example is representative of the general protocol. PGMA<sub>41</sub> precursor (0.149 g, 21.9 μmol), HBMA monomer (0.417 g, 2.63 mmol; target DP = 120), VA-044 initiator (1.77 mg, 52.3 μmol; PGMA<sub>41</sub>/VA-044 molar ratio = 4.0), and deionised water (5.11 g, 10% w/w solids) were added to a 14 mL sample vial. This reaction solution was purged using N<sub>2</sub> gas for 30 min at 20 °C prior to immersing the flask into an oil bath set at 50 °C. After 2 h, the HBMA polymerisation was quenched by exposing the contents of the flask to air, followed by cooling to ambient temperature.

#### **4.2.4 Preparation of Pickering Emulsions Stabilised by PGMA<sub>41</sub>-PHBMA<sub>110</sub> Diblock Copolymer Vesicles**

*n*-Dodecane (2.0 ml) was homogenised at 20 °C with a 0.06 – 2.00% w/w aqueous dispersion of linear PGMA<sub>41</sub>-PHBMA<sub>110</sub> vesicles (2.0 ml) for 2 min at 12 000 rpm using a IKA Ultra-Turrax T-18 homogeniser equipped with a 10 mm dispersing tool. After appropriate dilution, the resulting oil droplets were imaged by optical microscopy and their volume-average droplet diameter was determined by laser diffraction.

#### **4.2.5 Preparation of Colloidosomes Stabilised by PGMA<sub>41</sub>-PHBMA<sub>110</sub> Diblock Copolymer Vesicles**

PPG-TDI (20.0 g dm<sup>-3</sup>) was weighed into a sample vial and then dissolved in *n*-dodecane (2.0 ml) prior to homogenisation with 2.0 ml of a 0.25% w/w aqueous dispersion of linear PGMA<sub>41</sub>-PHBMA<sub>110</sub> vesicles for 2 min at 20 °C using a IKA Ultra-Turrax T-18 homogeniser equipped with a 10 mm dispersing tool operating at 12 000 rpm. The resulting stable milky-white

emulsion was allowed to stand at 20 °C for several hours to allow the urethane cross-linking reaction to proceed.

#### **4.2.6 Characterisation**

##### <sup>1</sup>H NMR spectroscopy

Spectra were recorded in CD<sub>3</sub>OD at 20 °C using a Bruker Avance III HD 400 MHz spectrometer with 64 scans being averaged per spectrum.

##### Gel permeation chromatography (GPC)

Copolymer molecular weight distributions were assessed using the following GPC set-up. Two Agilent PL gel 5 µm Mixed-C columns and a guard column were connected in series to an Agilent 1260 Infinity GPC system equipped with both refractive index and UV–vis detectors (only the refractive index detector was used in the present study) operating at 60 °C. The GPC eluent was HPLC-grade DMF containing 10 mM LiBr at a flow rate of 1.0 mL min<sup>-1</sup>. Calibration was achieved using a series of ten near-monodisperse PMMA standards ( $M_p$  ranging from 625 to 618 000 g mol<sup>-1</sup>). Chromatograms were analysed using Agilent GPC/SEC software provided by the manufacturer.

##### Dynamic light scattering (DLS)

Hydrodynamic  $z$ -average diameters  $D_z$  and polydispersity indices PDI were determined by DLS utilising the cumulants method a Malvern Zetasizer NanoZS instrument. All measurements were performed on 0.10% copolymer dispersions (prepared by dilution using deionised water) using disposable plastic cuvettes. All data were averaged over three consecutive runs.

##### Transmission electron microscopy (TEM)

Copper/palladium TEM grids (Agar Scientific, UK) were coated in-house to yield a thin film of amorphous carbon. The grids were subjected to a plasma glow discharge for 30 s. One

droplet of each dilute aqueous copolymer dispersion (or aqueous emulsion) (10  $\mu\text{L}$ , 0.1% w/w copolymer concentration or 0.5% oil droplets, respectively) was placed in turn on a freshly-treated grid for 1 min and then carefully blotted with filter paper to remove excess solution. To ensure sufficient electron contrast, a droplet of uranyl formate (10  $\mu\text{L}$  of a 0.75% w/w solution) was placed on the sample-loaded grid for 20 s and then blotted to remove excess stain. Each grid was carefully dried using a vacuum hose. Imaging was performed using a FEI Tecnai Spirit 2 microscope operating at 80 Kv and fitted with an Orius SC1000B camera.

#### Optical Microscopy (OM)

Optical microscopy images of Pickering emulsions were recorded using a Cole-Palmer compound optical microscope equipped with an LCD tablet display and a Moticam BTW digital camera.

#### Laser Diffraction

Each Pickering emulsion was sized by laser diffraction using a Malvern Mastersizer 3000 instrument equipped with a Hydro EV wet sample dispersion unit, a red HeNe laser operating at 633 nm and a LED blue light source operating at 470 nm. The stirring rate was adjusted to 1500 rpm in order to avoid creaming of the emulsion droplets during analysis. After each measurement, the cell was rinsed once with ethanol and three times with deionised water and the laser was aligned centrally to the detector prior to data acquisition.

#### Small Angle X-ray scattering (SAXS)

SAXS patterns were recorded for selected 1.0% w/w aqueous dispersions of PGMA<sub>41</sub>-PHBMA<sub>x</sub> nano-objects at the European Synchrotron Radiation Facilities (ESRF, station ID02, Grenoble, France) using monochromatic X-ray radiation ( $\lambda = 0.0995$  nm;  $q$  range = 0.002 to 0.15  $\text{\AA}^{-1}$ , where  $q$  is the length of the scattering vector and  $\theta$  is one-half of the scattering angle, such that  $q = 4\pi\sin\theta/\lambda$ ) and a Rayonix MX-170HS CCD detector. A flow-through horizontal capillary

set-up was used as the sample holder, with a 2.0 mm diameter glass capillary. Scattering data were reduced using standard routines from the beamline and were further analysed using Irena SAS macro<sup>43</sup> for Igor Pro. Water was used for absolute intensity calibration.

## 4.3 Results and Discussion

### 4.3.1 Synthesis of PGMA<sub>41</sub>-PHBMA<sub>x</sub> Diblock Copolymer Nano-Objects *via* RAFT Aqueous Emulsion Polymerisation of HBMA

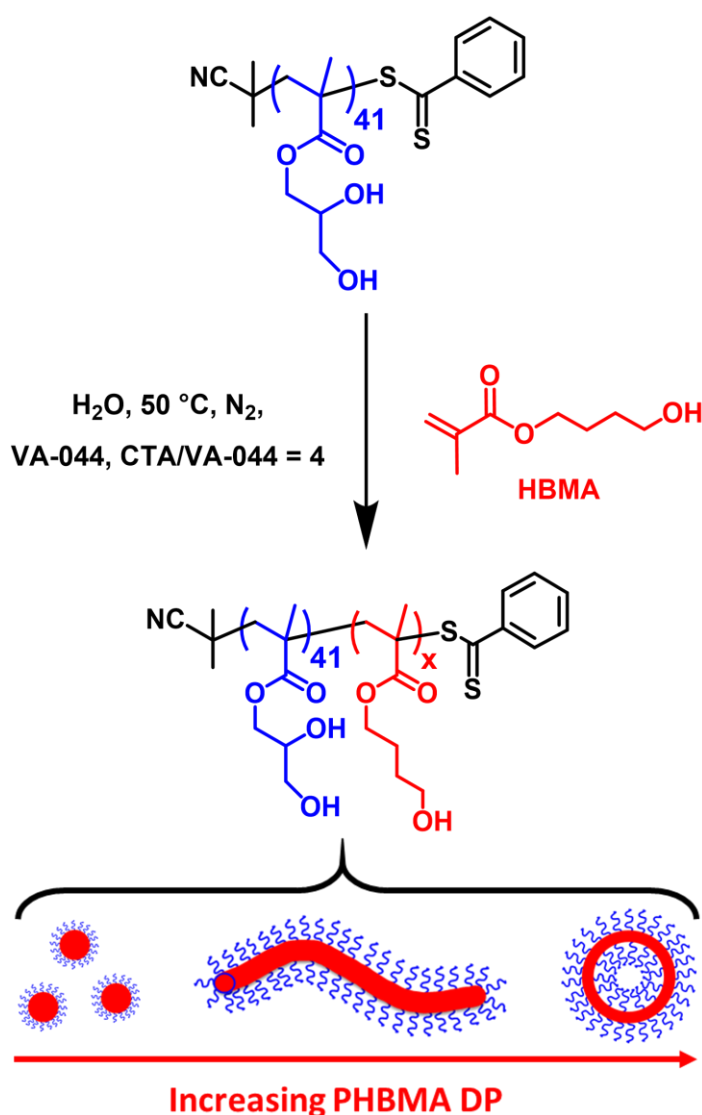


**Figure 4.3.** RAFT aqueous emulsion polymerisation of HBMA (N.B. this monomer comprises a 1:1 mixture of the 2- and 4-isomers) using a PGMA<sub>41</sub> precursor provides convenient access to diblock copolymer spheres, worms or vesicles depending on the target degree of polymerisation  $x$  for the PHBMA block.

A PGMA precursor with a mean DP of 41 was synthesised *via* RAFT ethanolic solution polymerisation of GMA using a CPDB at 70 °C, as previously described.<sup>30</sup> This PGMA precursor was then chain-extended *via* RAFT aqueous emulsion polymerisation of HBMA at 50 °C, as shown in Figure 4.3. The mean target DP of the core-forming PHBMA block was systematically varied between 10 and 120 for copolymer concentrations ranging between 5% and 20% w/w. High HBMA conversions ( $\geq 99\%$ ) were achieved for all PISA syntheses, as confirmed by <sup>1</sup>H NMR spectroscopy studies (see Figure 4.4).

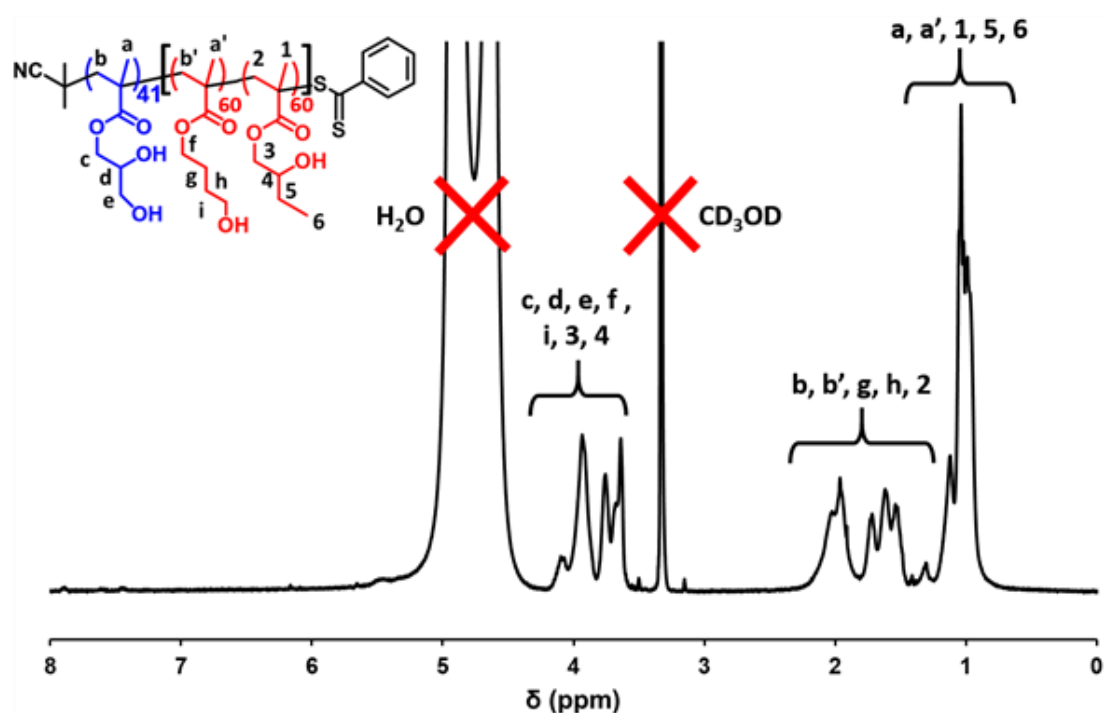


**Figure 4.4.** Assigned <sup>1</sup>H NMR spectrum (CD<sub>3</sub>OD) recorded for a PGMA<sub>48</sub>-PHBMA<sub>120</sub> diblock copolymer after reaching more than 99 % conversion within 120 min at 50°C. Both isomeric forms of the HBMA monomer, which are present in a 1:1 molar ratio, are depicted in the chemical structure.

DMF GPC studies of a series of five PGMA<sub>41</sub>-PHBMA<sub>x</sub> diblock copolymers indicated relatively narrow, unimodal molecular weight distributions (dispersities ranging from 1.18 to 1.37) and high blocking efficiencies (see Figure 4.5 and Table 4.1). It is worth noting that similar dispersities ( $M_w/M_n = 1.16$  to 1.32 when targeting PHBMA DPs between 75 and 175, respectively) were reported by Ratcliffe *et al.* for PGMA<sub>60</sub>-PHBMA<sub>x</sub> spheres.<sup>36</sup> In striking contrast, Cockram and co-workers obtained dispersities ranging from 1.93 to 6.13 for methylated

PMAA<sub>56</sub>-PHBMA<sub>x</sub> diblock copolymers when targeting PHBMA DPs between 130 and 300, respectively.<sup>35</sup> There are several reasons for these differences. Firstly, the batch of HBMA monomer used in the present study may contain significantly less dimethacrylate impurity than that used by Cockram and co-workers.<sup>35</sup> Secondly, the non-ionic PGMA<sub>41</sub>-PHBMA<sub>x</sub> diblock copolymer chains prepared herein do not require any methylation prior to GPC analysis, unlike the anionic PMAA-PHBMA copolymer chains prepared by Cockram and co-workers.<sup>35</sup> It is known that in that exhaustive methylation of acidic blocks can introduce GPC artefacts.<sup>35</sup> Thirdly, rather lower PHBMA DPs are required to target spheres, worms and vesicles in the present study, which should minimise the light branching resulting from any dimethacrylate impurities.<sup>44</sup>

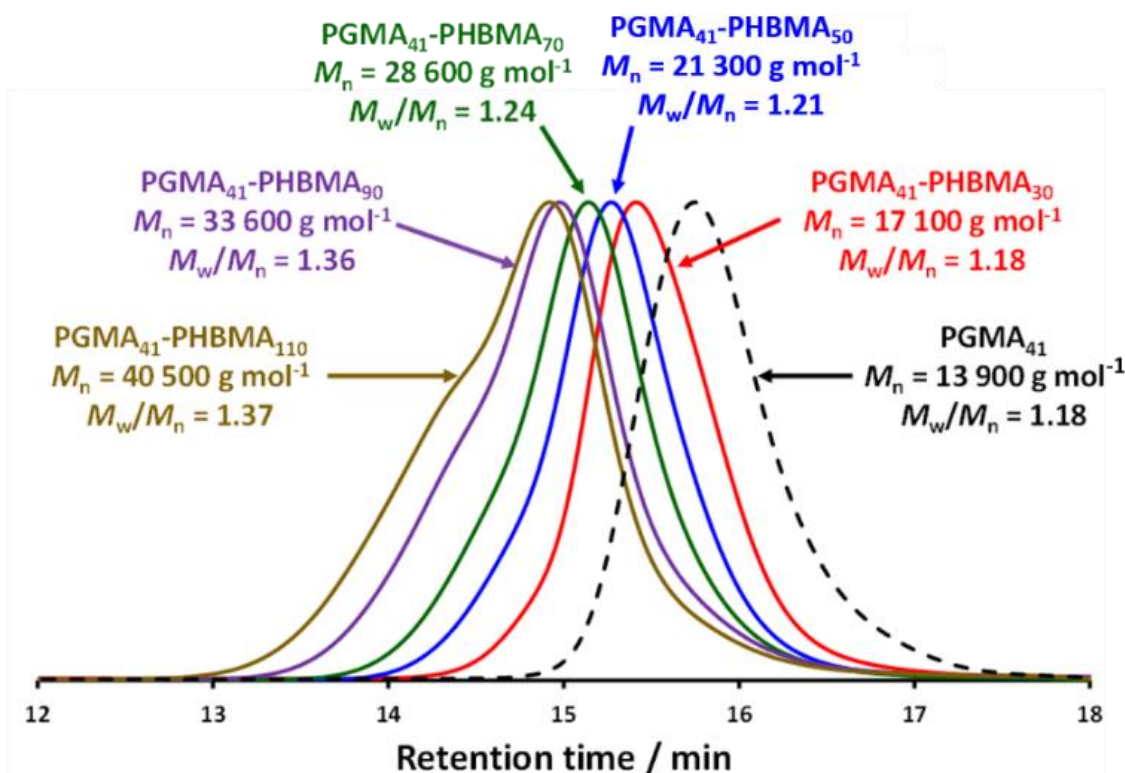


**Figure 4.5.** Overlaid DMF GPC traces recorded for a series of five PGMA<sub>41</sub>-PHBMA<sub>x</sub> diblock copolymers prepared by RAFT aqueous emulsion polymerisation of HBMA (conditions: 10% w/w, 50 °C, 2 h) for x = 30, 50, 70, 90 and 110. The GPC curve for the PGMA<sub>41</sub> precursor is also shown as a reference. Molecular weight data are expressed relative to a series of near-monodisperse PMMA calibration standards.

## Chapter 4: Synthesis of Diblock Copolymer Spheres, Worms and Vesicles *via* RAFT Aqueous Emulsion Polymerisation of Hydroxybutyl Methacrylate

**Table 4.1.** Summary of target DPs, molecular weight data and final copolymer morphology for the synthesis of PGMA<sub>41</sub>-PHBMA<sub>x</sub> diblock copolymer nano-objects at 5 - 20% w/w solids *via* RAFT aqueous emulsion polymerisation of HBMA at 50 °C using a PGMA<sub>41</sub> precursor.

Copolymer concentration / % w/w	Target HBMA DP	<sup>a</sup> DMF GPC $M_n$ / g mol <sup>-1</sup>	<sup>a</sup> $M_w/M_n$	<sup>b</sup> Morphology
5	10	15 400	1.14	C
5	20	17 000	1.14	C
5	30	18 200	1.14	S
5	40	19 000	1.19	S
5	50	21 000	1.19	S
5	60	23 100	1.19	S
5	70	24 900	1.25	S
5	75	26 700	1.24	S
5	80	30 700	1.25	S + W + V
5	85	33 400	1.28	S + W + V
5	90	33 500	1.31	S + W + V
5	100	34 500	1.33	S + W + V
5	110	40 100	1.36	V
10	10	15 500	1.15	C
10	20	16 300	1.15	C
10	30	17 100	1.18	S
10	35	19 500	1.18	S + W
10	40	20 000	1.18	S + W
10	50	21 300	1.21	S + W
10	55	22 400	1.24	S + W
10	60	26 200	1.24	S + W
10	65	27 800	1.25	W
10	70	28 600	1.24	W
10	75	29 700	1.28	W + V
10	80	31 300	1.29	W + V
10	85	32 900	1.29	W + V
10	90	33 600	1.36	W + V
10	95	34 100	1.30	W + V
10	100	36 100	1.34	V
10	110	40 500	1.37	V
15	20	15 800	1.17	C
15	30	16 900	1.17	S
15	35	18 100	1.17	S + W
15	40	22 300	1.20	S + W
15	45	24 600	1.20	W
15	50	25 000	1.19	W
15	60	27 100	1.25	W
15	65	26 600	1.26	W + V
15	70	28 900	1.26	W + V
15	80	33 100	1.26	W + V
15	85	33 300	1.27	V
15	90	34 800	1.32	V
15	100	36 200	1.34	V
20	10	14 700	1.16	C
20	20	15 700	1.16	C
20	30	17 100	1.16	S
20	35	18 100	1.18	S + W
20	40	21 200	1.19	S + W
20	45	23 300	1.22	W
20	50	25 200	1.22	W
20	55	25 800	1.25	W
20	60	26 100	1.24	W + V
20	70	27 600	1.24	W + V
20	80	29 300	1.28	W + V
20	85	33 100	1.28	V
20	90	34 200	1.32	V
20	100	37 100	1.36	V

<sup>a</sup>Determined by DMF GPC vs. PMMA standards. <sup>b</sup>Determined by TEM studies of 0.1 % w/w aqueous dispersions. C = chains; S = pure spheres; S+W = mixed phase of spheres and worms; W = pure worms; S+W+V = mixed phase of spheres, worms and vesicles; W+V = mixed phase of worms and vesicles; and V = pure vesicles.

A pseudo-phase diagram was constructed for a series of PGMA<sub>41</sub>-PHBMA<sub>x</sub> diblock copolymer nano-objects using morphology assignments based on TEM studies (Figure 4.6. and Figure 4.7.)

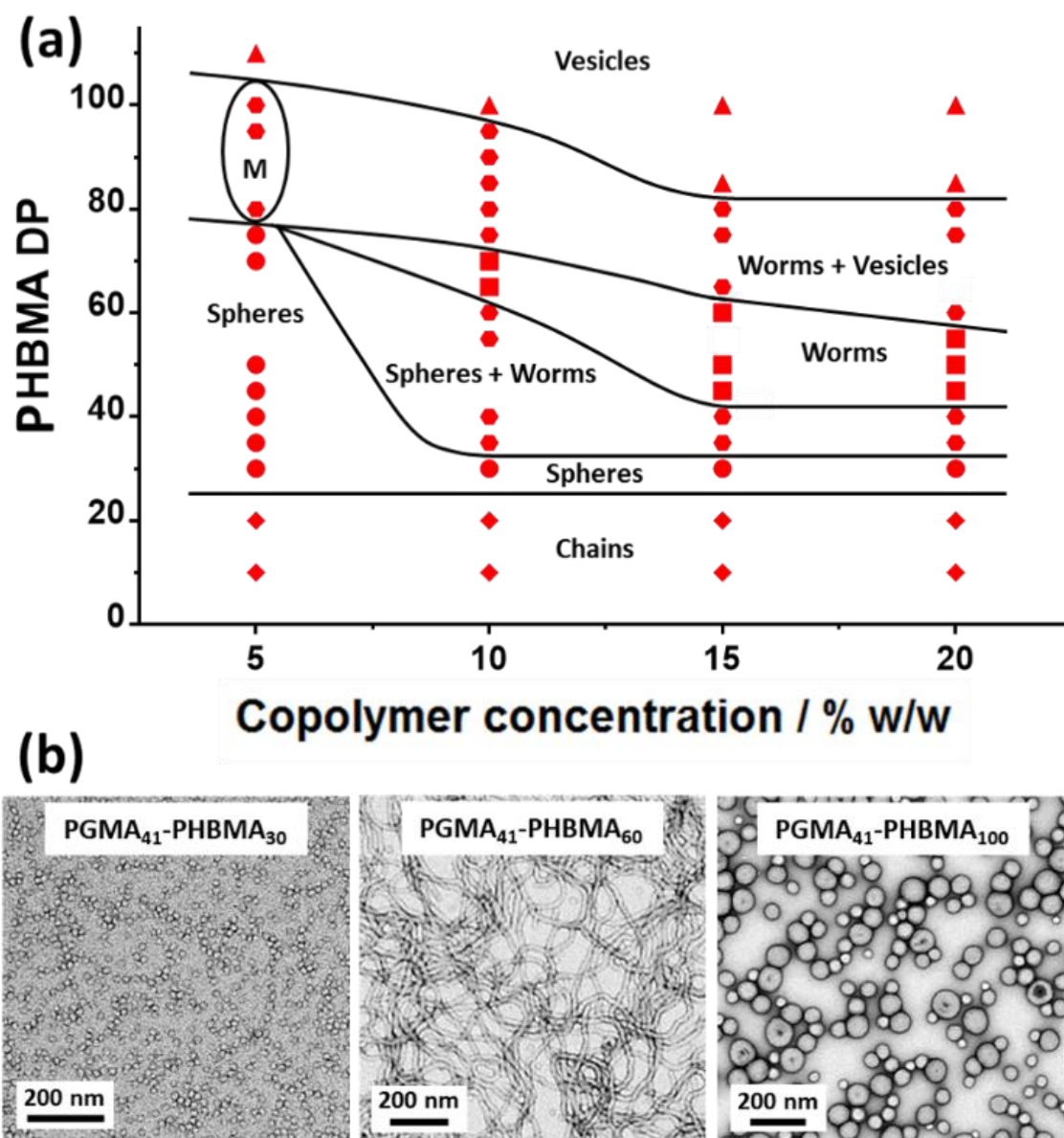


**Figure 4.6.** Pseudo-phase diagram constructed for a series of PGMA<sub>41</sub>-PHBMA<sub>x</sub> diblock copolymer nano-objects prepared by RAFT aqueous emulsion polymerisation of HBMA using a PGMA<sub>41</sub> precursor at a copolymer concentration of 5 - 20% w/w [N.B. 'M' denotes a mixed phase comprising spheres, worms and vesicles]. Representative TEM images are shown for PGMA<sub>41</sub>-PHBMA<sub>x</sub> nano-objects prepared at 15% w/w, where x = 30 (spheres), 60 (worms) and 100 (vesicles).

In general, the nanoparticle morphology depends on the copolymer concentration, with lower concentrations favouring the formation of spherical nano-objects. For example, the PISA synthesis of PGMA<sub>41</sub>-PHBMA<sub>60</sub> at 15% w/w produces a pure worm phase (Figure 4.6b), whereas targeting the same composition at 5% w/w produces only spheres. The sphere phase is unusually narrow at copolymer concentrations of 10 - 20% w/w. Furthermore, increasing the copolymer concentration enables access to worm and vesicle phases even when targeting relatively short PHBMA blocks. In contrast, for the synthesis of PGMA<sub>28</sub>-PMOEMA<sub>x</sub> nano-objects *via* RAFT aqueous emulsion polymerisation, shorter hydrophobic PMOEMA blocks were required to access vesicles at *lower* copolymer concentrations.<sup>40</sup> In the current study, pure vesicles can be obtained at each of the copolymer concentrations investigated, even at 5% w/w. In contrast, pure worms can only be obtained at a minimum copolymer concentration of 10% w/w.

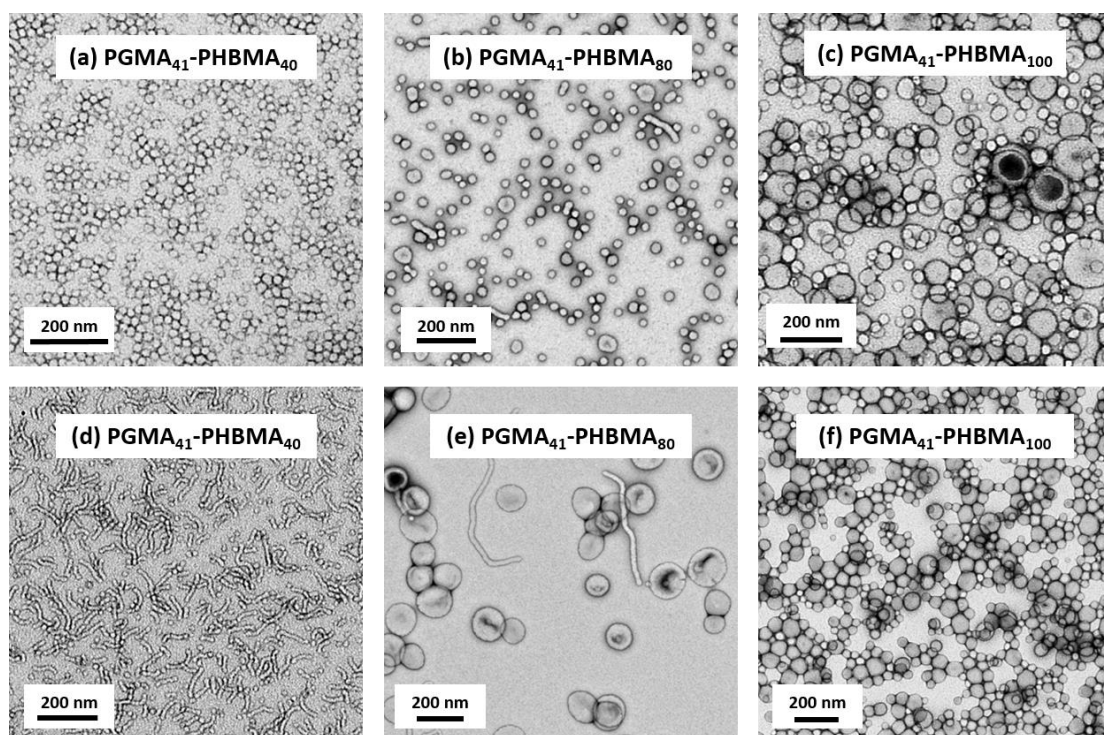


**Figure 4.7.** Representative TEM images obtained for various diblock copolymer nano-objects prepared *via* RAFT aqueous emulsion polymerisation of HBMA at 50 °C: (a) PGMA<sub>41</sub>-PHBMA<sub>40</sub> spheres synthesised at 5% w/w, (b) PGMA<sub>41</sub>-PHBMA<sub>80</sub> spheres, worms and vesicles synthesised at 5% w/w, (c) PGMA<sub>41</sub>-PHBMA<sub>100</sub> vesicles synthesised at 5% w/w, (d) PGMA<sub>41</sub>-PHBMA<sub>40</sub> spheres and worms synthesised at 20% w/w, (e) PGMA<sub>41</sub>-PHBMA<sub>80</sub> vesicles (plus a few worms) synthesised at 20% w/w and (f) PGMA<sub>41</sub>-PHBMA<sub>100</sub> vesicles synthesised at 20% w/w.

Clearly, the problem of kinetically-trapped spheres that is often encountered for RAFT aqueous emulsion polymerisation formulations can be overcome by appropriate monomer selection. More specifically, the water-immiscible monomer (e.g. GlyMA, MOEMA or HBMA) should exhibit moderate aqueous solubility ( $\sim 20 \text{ g m}^{-3}$ ).<sup>38, 40</sup> This ensures enhanced polymer chain mobility within the growing monomer-swollen nanoparticle cores within the relatively short time scale of the polymerisation, thus enabling evolution of the copolymer morphology. In this context, it is perhaps also noteworthy that pure worms and vesicles can be obtained with a somewhat longer steric stabiliser block (PGMA<sub>41</sub>) when using HBMA compared to GlyMA (PGMA<sub>28</sub>) and MOEMA (PGMA<sub>29</sub>), respectively.<sup>38, 40</sup>

SAXS patterns were recorded for 1.0% w/w aqueous dispersions of PGMA<sub>41</sub>-PHBMA<sub>x</sub> spheres, worms and vesicles prepared at 10% w/w, see Figure 4.8e. This ten-fold dilution ensures that the structure factor can be assumed to be unity, which simplifies the data analysis.<sup>45</sup> The SAXS pattern obtained for PGMA<sub>41</sub>-PHBMA<sub>30</sub> can be satisfactorily fitted using a spherical micelle model<sup>46</sup> (see Figure 4.8a, Table 4.2, and Equation 7.9 for more details). This approach enables a volume-average core diameter of 12.2 nm to be calculated. Assuming that the mean radius of gyration  $R_g$  of the PGMA<sub>41</sub> stabiliser chains is 2.2 nm, the overall volume-average diameter calculated from this fit is 21 nm. Bearing in mind the effect of polydispersity, this is consistent with the  $z$ -average diameter of  $25 \pm 8$  nm reported by DLS. Moreover, this scattering pattern has a low  $q$  gradient of approximately zero, which is consistent with the morphology indicated by TEM studies (Figure 4.6b) and further indicates non-interacting spheres. The SAXS pattern recorded for PGMA<sub>41</sub>-PHBMA<sub>70</sub> diblock copolymer can be fitted using a worm-like micelle model (see Equation 7.16),<sup>46</sup> where the low  $q$  gradient of approximately -1 (see Figure 4.8b) is consistent with the highly anisotropic worm morphology indicated by the corresponding TEM image (see Figure 4.6b).<sup>47, 48</sup> SAXS patterns recorded for PGMA<sub>41</sub>-PHBMA<sub>100</sub> and PGMA<sub>41</sub>-PHBMA<sub>120</sub> could each be fitted using a vesicle model (see Equation 7.22);<sup>49</sup> a low  $q$  gradient of approximately -2 was observed in each case, which is consistent with the presence of bilayers (see Figure 4.8c and 4.8d). These analyses indicated volume-average diameters of 108

nm and 75 nm, respectively. Given that such small vesicles are much less prone to collapse under ultrahigh vacuum conditions, this morphology could be incorrectly assigned as spheres based on TEM analysis alone. Similar observations have been reported for PGMA<sub>28</sub>-PGlyMA<sub>75</sub> and PGMA<sub>29</sub>-PMOEMA<sub>84</sub> vesicles prepared *via* RAFT aqueous emulsion polymerisation (see Figure 4.1).<sup>38, 40</sup> Such situations serve to highlight the value of performing SAXS studies, which readily enable discrimination between spheres and vesicles. Similar observations have been made for relatively small vesicles prepared *via* RAFT aqueous emulsion polymerisation of MOEMA<sup>40</sup> and GlyMA.<sup>33</sup>

**Table 4.2.** Structural parameters obtained from SAXS analysis of four 1.0% w/w aqueous dispersions of PGMA<sub>41</sub>-PHBMA<sub>x</sub> diblock copolymer nano-objects using sphere, worm or vesicle models, where appropriate. Representative parameters are denoted as follows:  $V_{\text{PHBMA}}$  is the volume of the PHBMA block,  $\phi$  is the volume fraction of copolymers forming nano-objects,  $R_s$  represents the mean sphere core volume-average radius,  $R_w$  is the mean worm micelle radius,  $R_m$  is the mean radius from the centre of the vesicle to the centre of the membrane,  $T_m$  is the mean vesicle membrane thickness (i.e. the hydrophobic part of the membrane). Here  $\sigma_x$  denotes the standard deviation of the relevant parameter ( $x = R_s, R_w, R_m$  or  $T_m$ ).  $R_g$  represents the radius of gyration of the PGMA<sub>41</sub> stabiliser block,  $D_s$  represents the sphere volume-average diameter,  $D_w$  is the worm cross-sectional volume-average diameter and  $D_v$  represents the vesicle volume-average diameter.  $x_{\text{sol}}$  is the volume fraction of water within the hydrophobic core/membrane and  $N_{\text{agg}}$  is the mean aggregation number for each type of nano-object. The volume of the PGMA block,  $V_{\text{PGMA}}$ , used for fitting these SAXS patterns was 8.23 nm<sup>3</sup> in all cases.

Diblock Copolymer Composition	Model used for fitting <sup>a</sup>	$V_{\text{PHBMA}} / \text{nm}^3$	$\phi^b$	$R_s / \sigma_{R_s} / \text{nm}$ or $R_w / \sigma_{R_w} / \text{nm}$	$R_m / \sigma_{R_m} (\text{nm})$	$T_m / \sigma_{T_m} / \text{nm}$	$R_g / \text{nm}$	$D_s, D_w$ or $D_v / \text{nm}^b$	$x_{\text{sol}}$	$N_{\text{agg}}$
PGMA <sub>41</sub> -PHBMA <sub>30</sub>	S	6.57	0.0004	6.1 / 0.66	-	-	2.20	21.0	0.0008	145
PGMA <sub>41</sub> -PHBMA <sub>70</sub>	W	15.85	0.0010	7.9 / 0.80	-	-	1.98	19.8	0.0003	3828
PGMA <sub>41</sub> -PHBMA <sub>100</sub>	V	22.00	0.0012	-	43.7 / 7.6	13.8 / 2.0	1.76	108.2	0.03	14429
PGMA <sub>41</sub> -PHBMA <sub>120</sub>	V	25.15	0.0046	-	27.3 / 6.2	12.2 / 2.3	2.09	75.2	0.01	4727

<sup>a</sup>Where S denotes a spherical micelle model, W denotes a worm model and V denotes a vesicle model. <sup>b</sup>When fitted using a spherical micelle model, the sphere volume-average diameter,  $D_s$ , was calculated using  $D_s = 2R_s + 4R_g$ . When fitted using a worm model, the worm cross-sectional volume-average diameter,  $D_w$ , was calculated using  $D_w = 2R_s + 4R_g$ . When fitted using a vesicle model, the vesicle volume-average diameter,  $D_v$ , was calculated using  $D_v = 2R_m + T_m + 4R_g$ .

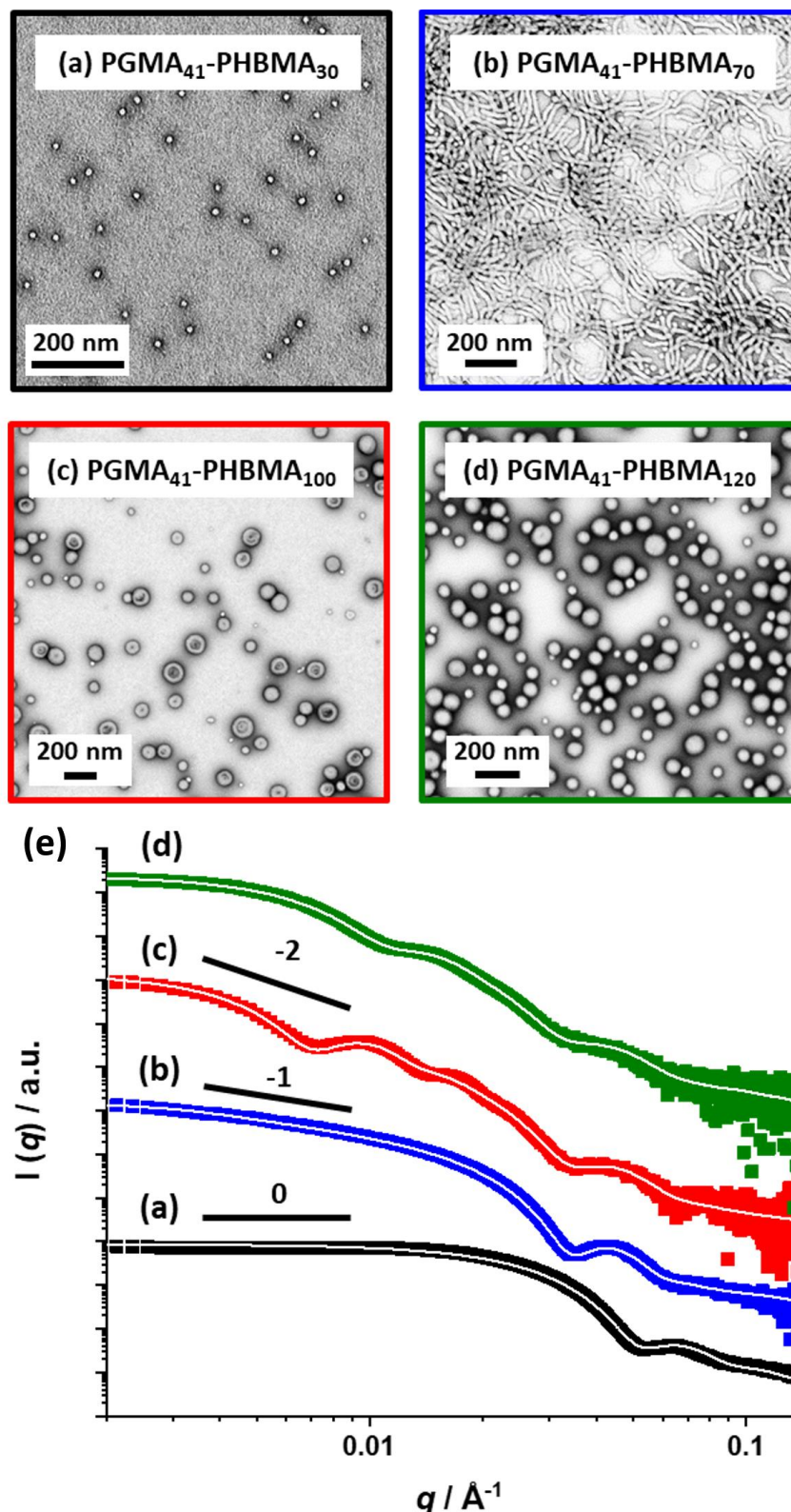


**Figure 4.8.** TEM images obtained for (a) PGMA<sub>41</sub>-PHBMA<sub>30</sub> spheres, (b) PGMA<sub>41</sub>-PHBMA<sub>70</sub> worms, (c) relatively large PGMA<sub>41</sub>-PHBMA<sub>100</sub> vesicles and (d) relatively small PGMA<sub>41</sub>-PHBMA<sub>120</sub> vesicles. (e) Corresponding SAXS patterns recorded at 1.0% w/w for the same four copolymer dispersions, which were each originally prepared at 10% w/w. White solid lines show the data fits obtained for each SAXS pattern using an appropriate spherical micelle, worm-like micelle or vesicle model. Each low  $q$  gradient is consistent with the corresponding TEM image.

The kinetics of polymerisation for the RAFT aqueous emulsion polymerisation of HBMA was assessed at a copolymer concentration of 10% w/w. A PHBMA DP of 120 was targeted and more than 99% HBMA conversion was achieved within 70 min at 50 °C (see Figure 4.9). Intermediate conversions were determined by periodically withdrawing small aliquots of the reaction mixture and quenching the polymerisation in each case, and subsequent analysis by <sup>1</sup>H NMR spectroscopy and with DLS and TEM studies were also performed on each aliquot. A two-fold increase in the rate of HBMA polymerisation was observed after around 30 min, which corresponds to approximately 15% conversion and a PHBMA DP of 18.

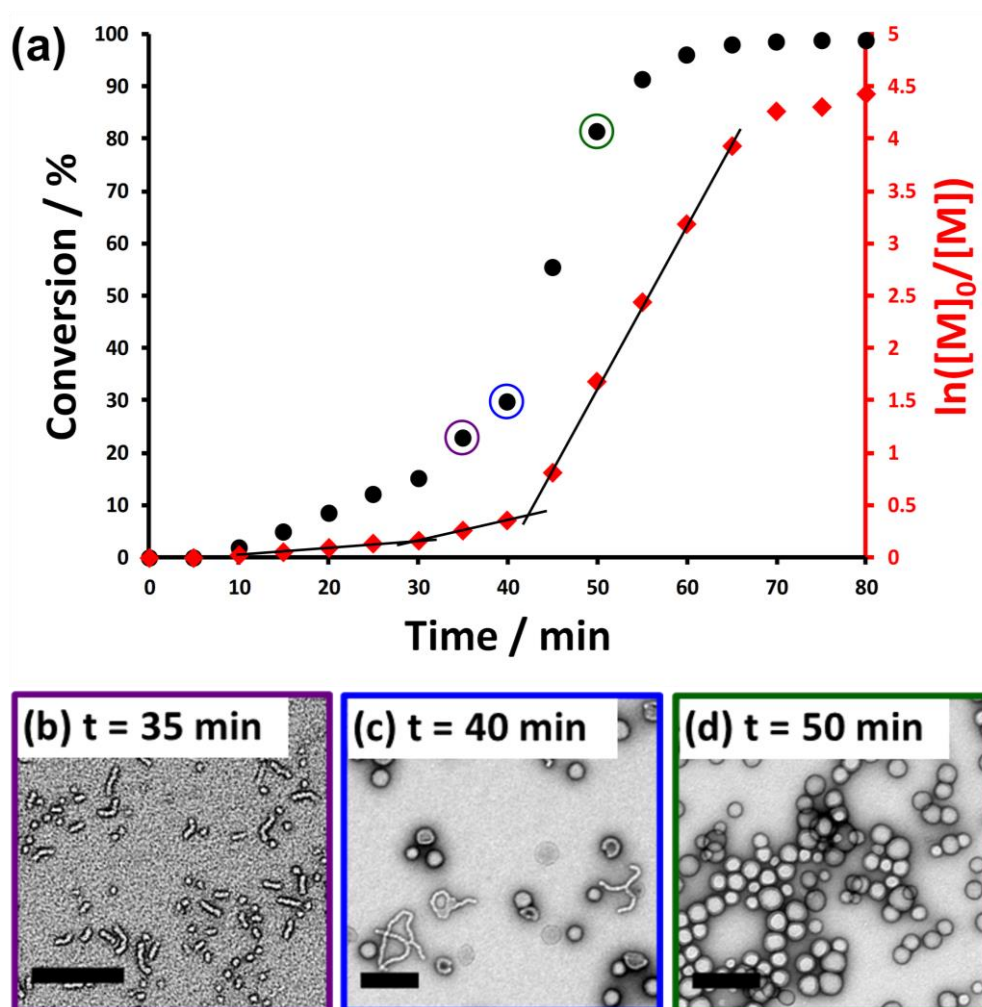


**Figure 4.9.** (a) Kinetic studies during the synthesis of PGMA<sub>41</sub>-PHBMA<sub>120</sub> vesicles *via* RAFT aqueous emulsion polymerisation of HBMA at a copolymer concentration of 10% w/w: conversion vs time curve (black circles) and its corresponding semi-logarithmic plot (red diamonds). Bottom: representative TEM images recorded for intermediate copolymer morphologies observed after (b) 35 min (23% conversion; PHBMA DP = 28), (c) 40 min (36% conversion; PHBMA DP = 43), and (d) 50 min (81% conversion; PHBMA DP = 97). Each scale bar = 200 nm.

This rate enhancement is attributed to micellar nucleation, or the point at which the growing diblock copolymer chains begin to form nascent nuclei. This interpretation is supported by the substantial increase observed in the scattered light intensity (derived count rate) from 70 to 700 kcps and a DLS diameter of around 20 nm (see Figure 4.10). Similar rate acceleration effects have been reported for both RAFT dispersion polymerisation<sup>41, 50</sup> and also for other RAFT aqueous emulsion polymerisation formulations.<sup>40, 51</sup> TEM images recorded after 35 min indicate the presence of spheres and short worms (see Figure 4.9b). A further three-fold rate enhancement was observed at 40 min (36% conversion). This corresponds to a PHBMA DP of 43, which is consistent with a sphere/worm mixed phase as indicated by the phase diagram. This suggests that this second rate acceleration is associated with the formation of worm-like nano-objects. Similar two-stage rate enhancements are not well-understood but have been recently observed for RAFT aqueous emulsion polymerisation of MOEMA<sup>40</sup> and also for RAFT dispersion polymerisations conducted in non-polar media.<sup>50</sup> Finally, the polymerisation proceeds more slowly after 55 min, presumably owing to the gradual depletion of unreacted HBMA within the monomer-swollen vesicle membranes. TEM studies conducted during this HBMA polymerisation reveal intermediate morphologies (e.g. spheres and worms) that are strikingly similar to those observed during RAFT aqueous *dispersion* polymerisation of HPMA when targeting vesicles.<sup>41, 52, 53</sup> These observations suggest that the mechanism for vesicle formation is likely to be the same (or at least very similar) for RAFT aqueous *dispersion* polymerisation and RAFT aqueous *emulsion* polymerisation.

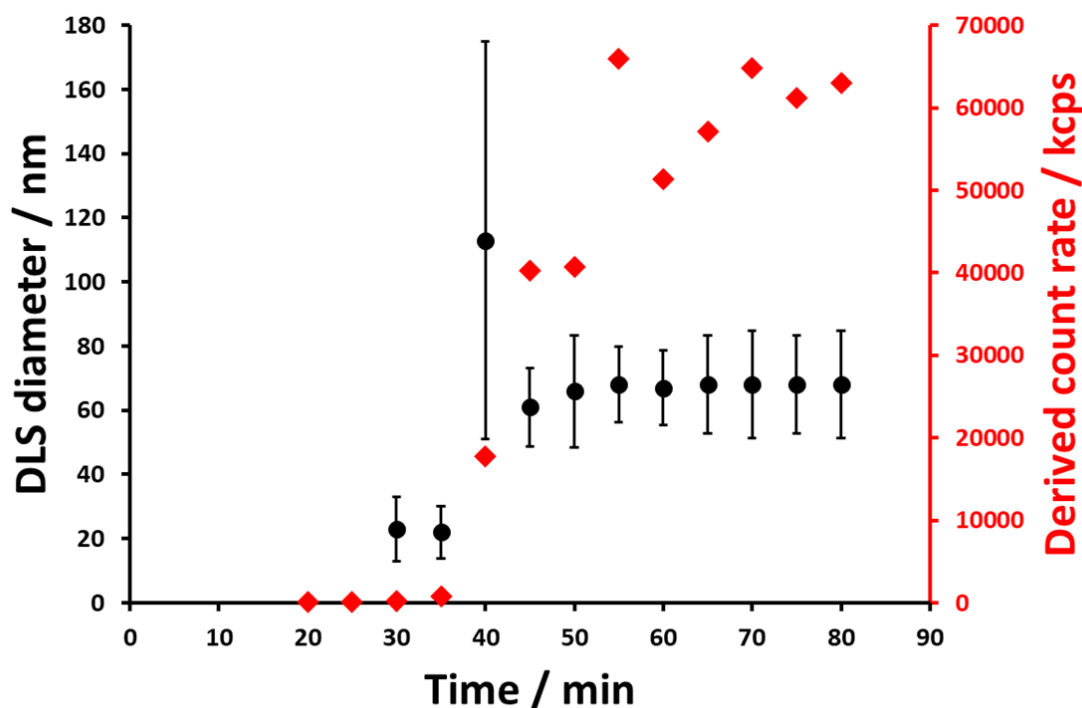


**Figure 4.10.** DLS studies of the evolution in particle diameter during the synthesis of PGMA<sub>41</sub>-PHBMA<sub>120</sub> vesicles *via* RAFT aqueous emulsion polymerisation targeting 10% w/w solids. DLS diameter data are indicated by black circles while the corresponding derived count rate data are indicated by red diamonds.

### 4.3.2 Preparation of Pickering Emulsions Stabilised by Diblock Copolymer Vesicles

RAFT-mediated PISA enables the design of a wide range of surface-active block copolymer nano-objects that can stabilise either oil<sup>30, 42, 54, 55</sup> or water droplets.<sup>56-58</sup> Particular attention has been paid to vesicles since they were the initial diblock copolymer nano-objects to be utilised as Pickering emulsifiers.<sup>42, 59-61</sup> In such study, Thompson *et al.*<sup>42</sup> attempted the preparation of oil-in-water Pickering emulsions using linear PGMA<sub>45</sub>-PHPMA<sub>200</sub> vesicles. However, these nano-objects did not withstand the high-shear homogenisation conditions required to generate the oil droplets, instead *in situ* dissociation occurred to form individual diblock copolymer chains.<sup>42</sup> Such dissociation was attributed to the weakly hydrophobic nature of the core-forming PHPMA block. Since these PGMA<sub>45</sub>-PHPMA<sub>200</sub> chains were amphiphilic, a stable emulsion was obtained but it was not a genuine Pickering emulsion.<sup>62</sup> To ensure that the

original vesicle morphology survived homogenisation, a small amount of ethylene glycol dimethacrylate (EGDMA) crosslinker could be added as a third block to form covalently-stabilised vesicles.<sup>62</sup> Alternatively, PGMA<sub>63</sub>-PHPMA<sub>350</sub>-PBzMA<sub>x</sub> triblock copolymer framboidal vesicles can be prepared *via* aqueous PISA, with the third PBzMA block being sufficiently hydrophobic to prevent *in situ* dissociation during high shear homogenisation.<sup>59</sup>

The aqueous solubility of HPMA monomer is  $\sim 100 \text{ g dm}^{-3}$  at  $70 \text{ }^\circ\text{C}$ , whereas that for HBMA is only  $\sim 20 \text{ g dm}^{-3}$  at the same temperature.<sup>35</sup> On this basis, PHBMA homopolymer is expected to be significantly more hydrophobic than PHPMA homopolymer, which should in principle lead to stronger van de Waals interactions between such water-insoluble chains in an aqueous environment. The scientific question addressed herein is whether these stronger attractive forces are actually sufficient to enable *linear* PGMA<sub>41</sub>-PHBMA<sub>110</sub> vesicles to serve as an emulsifier for the production of oil-in-water Pickering emulsions *via* high-shear homogenisation.

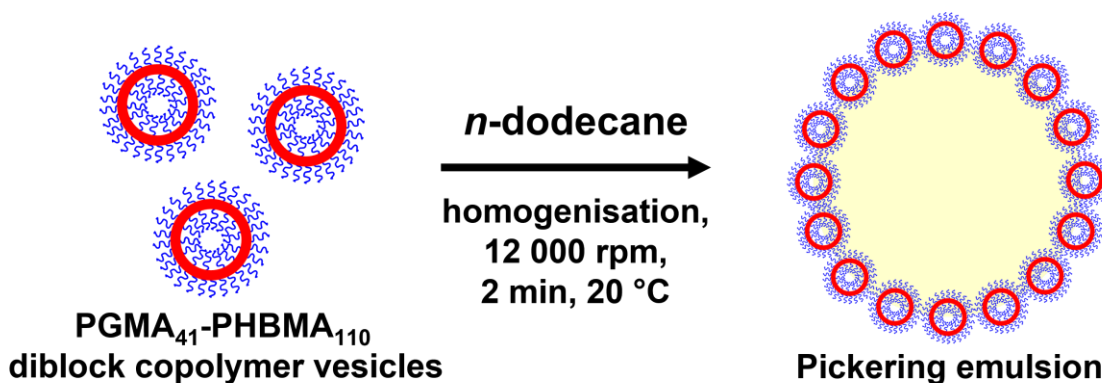


**Figure 4.11.** Schematic preparation of an oil-in-water Pickering emulsion prepared *via* high-shear homogenisation of *n*-dodecane with an equal volume of an aqueous dispersion of linear PGMA<sub>41</sub>-PHBMA<sub>110</sub> vesicles at 12 000 rpm for 2 min at  $20 \text{ }^\circ\text{C}$ . The copolymer concentration was systematically varied from 0.063% to 2.00% w/w during such experiments.

To examine this hypothesis, a PHBMA DP of 110 was targeted at a copolymer concentration of 10% w/w to produce PGMA<sub>41</sub>-PHBMA<sub>110</sub> vesicles. These vesicles were then evaluated as putative Pickering emulsifiers for the stabilisation of *n*-dodecane droplets in water for copolymer concentrations ranging from 0.063% to 2.00% w/w. Thus a series of such aqueous

dispersions of vesicles were homogenised with an equal volume of *n*-dodecane at 12 000 rpm for 2 min at 20 °C to produce *n*-dodecane-in-water emulsions, as depicted in Figure 4.11.

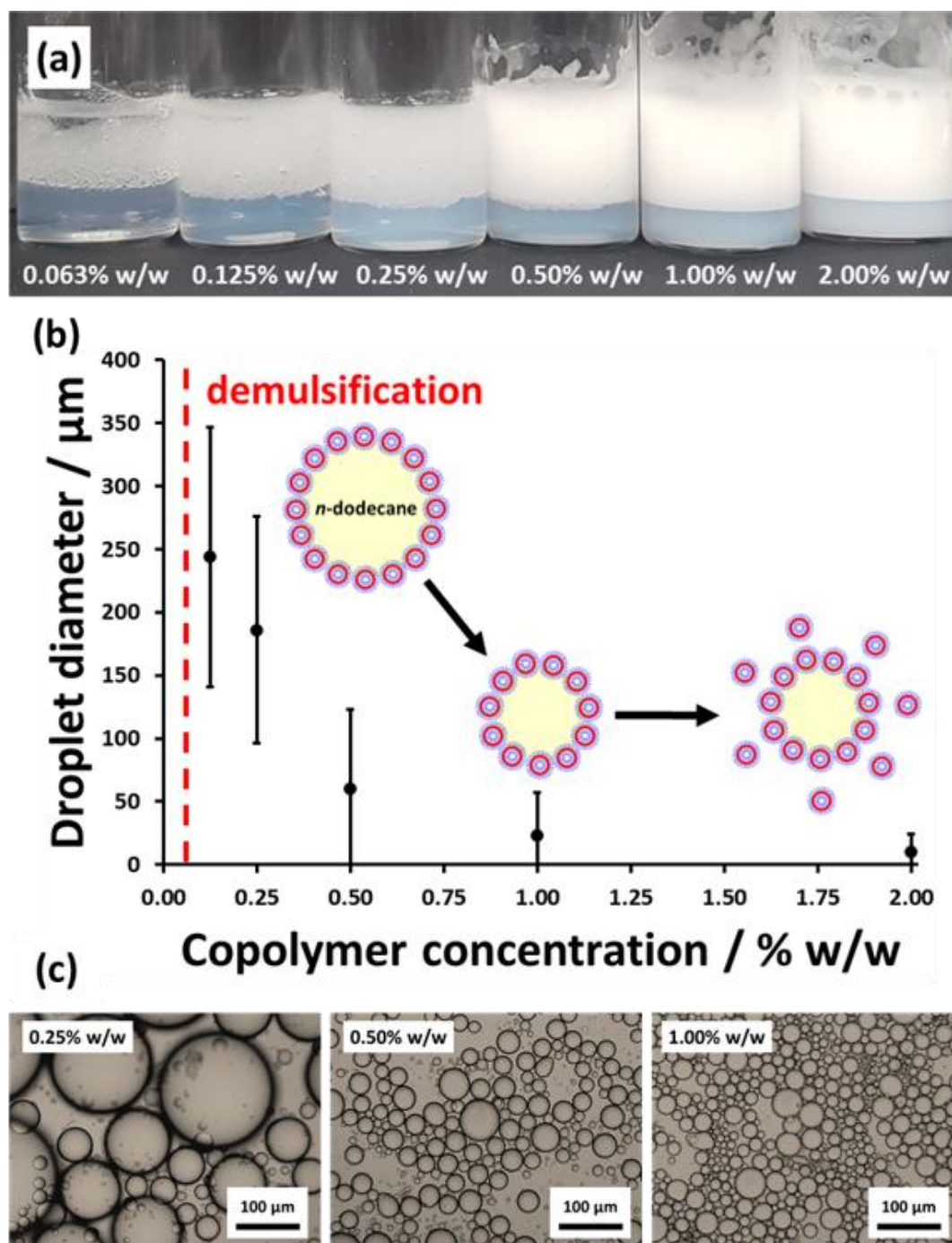


**Figure 4.12.** Digital photographs obtained for the Pickering emulsions prepared using PGMA<sub>41</sub>-PHBMA<sub>110</sub> vesicles at various copolymer concentrations. (b) Relationship between volume-average droplet diameter (determined by laser diffraction) and copolymer concentration after high-shear homogenisation of *n*-dodecane with aqueous dispersions of PGMA<sub>41</sub>-PHBMA<sub>110</sub> diblock copolymer vesicles of varying concentration. The upturn in droplet size at low copolymer concentration is consistent with the formation of a series of *n*-dodecane-in-water Pickering emulsions. (c) Optical microscopy images recorded for the *n*-dodecane droplets prepared at various copolymer concentrations. Emulsification conditions: 12 000 rpm for 2 min at 20 °C.

Figure 4.12 shows a digital photograph, laser diffraction data and optical microscopy images obtained for the emulsions produced at various copolymer concentrations. Lowering the copolymer concentration leads to a reduction in turbidity for the lower aqueous phase because it contains fewer excess non-adsorbed vesicles. There is a corresponding gradual increase in the volume-average droplet diameter because using fewer vesicles reduces the total surface area of the oil phase that can be coated with a monolayer of adsorbed vesicles, which in turn leads to coarser droplets. This is consistent with the formation of genuine Pickering emulsions and has been reported by various research groups.<sup>42, 63, 64</sup> In contrast, Thompson and co-workers reported essentially no change in the mean droplet diameter with copolymer concentration when using linear PGMA<sub>45</sub>-PHPMA<sub>300</sub> vesicles, which is consistent with the *in situ* break-up of these more delicate nano-objects during high-shear homogenisation.<sup>42, 62</sup>

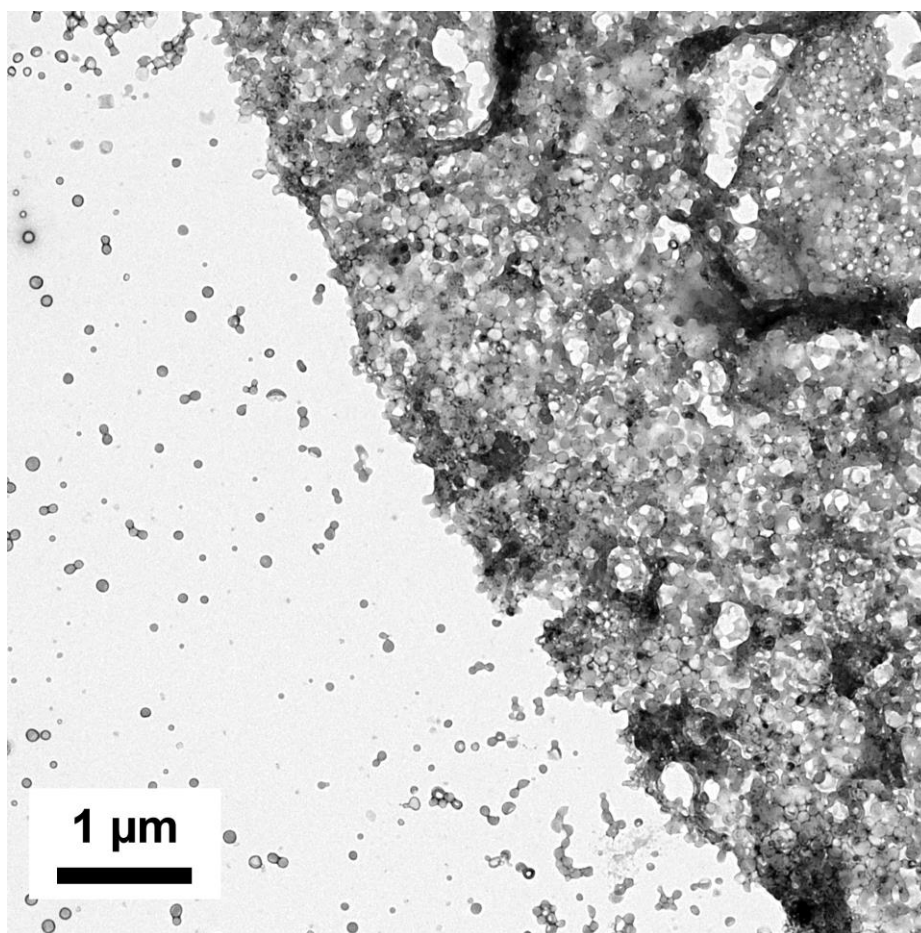


**Figure 4.13.** TEM image obtained for a single dried *n*-dodecane Pickering droplet prepared using a 0.25% w/w aqueous dispersion of PGMA<sub>41</sub>-PHBMA<sub>110</sub> vesicles. Emulsification conditions: 12 000 rpm for 2 min at 20 °C.

TEM studies of the dried emulsion droplets (see Figure 4.13) confirmed that *linear* PGMA<sub>41</sub>-PHBMA<sub>110</sub> vesicles do indeed remain intact after high-shear homogenisation. More specifically, a densely packed monolayer of adsorbed vesicles is observed after evaporation of both the oil and aqueous phases under the ultrahigh vacuum conditions required for TEM studies. This residual superstructure provides direct evidence for the formation of genuine Pickering emulsions. It is perhaps worth emphasising that the difference in chemical structure between the PHPMA and PHBMA core-forming blocks is rather subtle: the latter possess just one extra methylene group per monomer repeat unit. Nevertheless, this is sufficient to ensure survival of PGMA<sub>41</sub>-PHBMA<sub>110</sub> vesicles without requiring a third block for either covalent stabilisation (PEGDMA) or physical reinforcement *via* stronger attractive inter-chain forces (PBzMA).<sup>42, 59, 62</sup>

PGMA<sub>58</sub>-PHPMA<sub>350</sub>-PEGDMA<sub>20</sub> *cross-linked* vesicles have been previously examined by Thompson *et al.* for the preparation of colloidosomes.<sup>42</sup> This protocol involved using diisocyanate-capped poly(propylene glycol) (PPG-TDI), which is an oil-soluble polymeric cross-linker that readily reacts with the hydroxyl groups on the PGMA stabiliser chains (and perhaps also the PHBMA core-forming chains) to convert the precursor Pickering emulsions into covalently cross-linked colloidosomes.

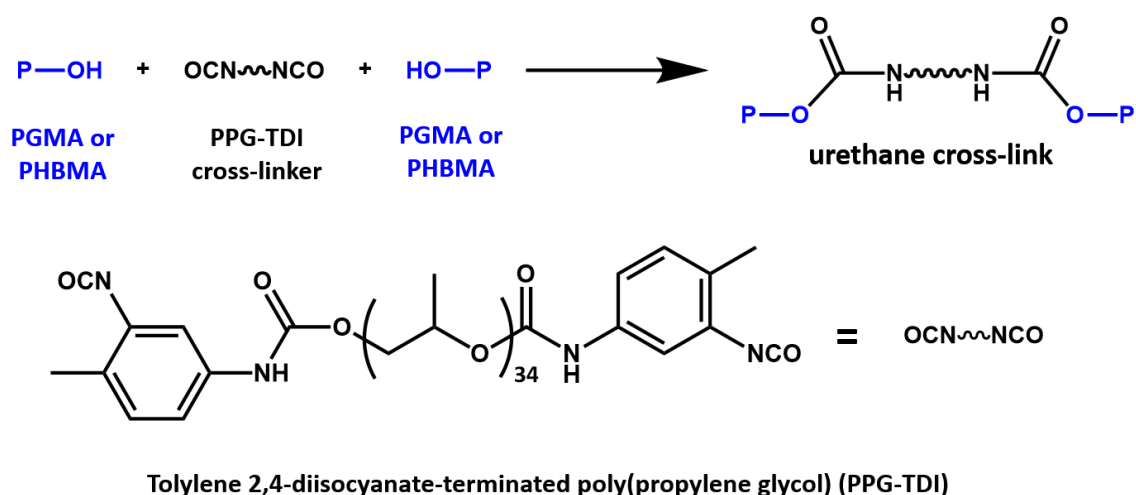


**Figure 4.14.** Chemical structure of the oil-soluble polymeric cross-linker (PPG-TDI) used in this Chapter (top). Schematic representation of the reaction between the terminal isocyanate groups on this PPG-TDI crosslinker with the pendent hydroxyl groups (P-OH) on either the PGMA or PHBMA chains to form urethane cross-links.<sup>42</sup>

In the current study, the preparation of colloidosomes involved homogenisation of a 0.25% w/w aqueous dispersion of *linear* PGMA<sub>41</sub>-PHBMA<sub>110</sub> vesicles with an equal volume of *n*-dodecane containing 20.0 g dm<sup>-3</sup> PPG-TDI cross-linker at 12 000 rpm for 2 min at 20 °C. The initial Pickering emulsion was allowed to stand at 20 °C for several hours to allow the urethane cross-linking reaction to proceed (see Figure 4.14). The resulting colloidosomes were imaged using optical microscopy and TEM (see Figure 4.15a and 4.15c). To evaluate their structural integrity, these colloidosomes were subjected to an alcohol challenge whereby excess methanol was added to remove the oil phase prior to TEM studies. As shown in Figure 4.15b, such colloidosomes were sufficiently cross-linked to withstand this alcohol challenge. However, TEM studies (see Figure 4.15d) suggest that the vesicles break up to form ill-defined aggregates in the presence of methanol.

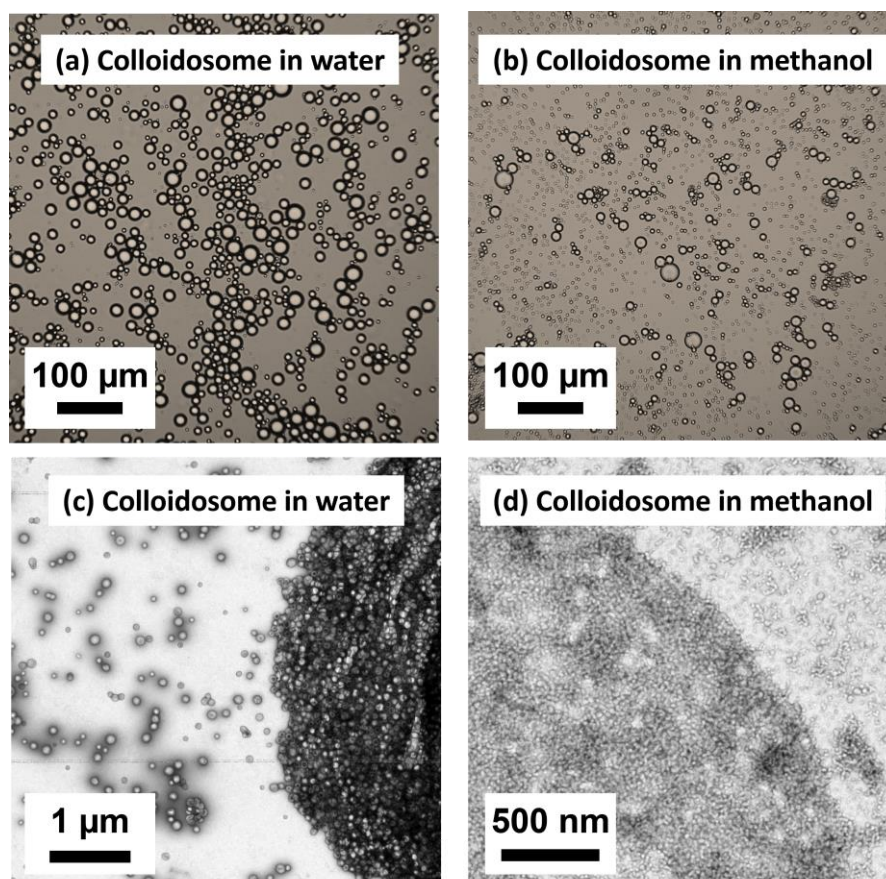


**Figure 4.15.** Representative optical microscopy images recorded for PPG-TDI cross-linked colloidosomes prepared *via* high-shear homogenisation (12 000 rpm for 2 min at 20 °C) of a 0.25% w/w aqueous dispersion of PGMA<sub>41</sub>-PHBMA<sub>110</sub> vesicles with *n*-dodecane followed by dilution using either (a) water or (b) methanol. TEM image recorded for a single colloidosome after dilution using (c) water or (d) methanol.

## 4.4 Conclusions

In summary, a rather subtle change in monomer structure leads to the aqueous solubility of HBMA being approximately four times lower than that of HPMA, which represents the difference between aqueous emulsion polymerisation and aqueous dispersion polymerisation, respectively. Interestingly, chain-extending a non-ionic PGMA<sub>41</sub> steric stabiliser *via* RAFT aqueous emulsion polymerisation of HBMA provides convenient access to diblock copolymer spheres, worms or vesicles. Thus HBMA exhibits sufficient aqueous solubility to avoid the problem of kinetically-trapped spheres that is observed for so many RAFT aqueous emulsion polymerisation formulations. More than 99% HBMA conversion can be achieved within 2 h at 50 °C using a low-temperature azo initiator, with GPC analysis indicating relatively low dispersities ( $M_w/M_n < 1.37$ ) when targeting PHBMA DPs up to 110. A pseudo-phase diagram was constructed for the synthesis of PGMA<sub>41</sub>-PHBMA<sub>x</sub> nano-objects at copolymer concentrations ranging from 5% to 20% w/w when targeting  $x = 10$  to 120. Given the observed concentration-dependent copolymer morphologies and the presence of mixed phases, this systematic approach is essential to ensure reproducible targeting of pure spheres, worms or vesicles. Pure vesicles could be obtained at just 5% w/w, whereas pure worms required higher copolymer concentrations. <sup>1</sup>H NMR spectroscopy was used to perform kinetic studies when targeting PGMA<sub>41</sub>-PHBMA<sub>120</sub> vesicles. A significant rate acceleration was observed at two separate stages, with TEM and DLS studies suggesting that the first stage heralds the onset of micellar nucleation while the second stage corresponds to the sphere-to-worm transition. This study provides useful insights regarding the mechanism of vesicle formation *via* RAFT aqueous emulsion polymerisation, which appears to be similar to that reported for RAFT aqueous *dispersion* polymerisation of HPMA when using essentially the same non-ionic PGMA stabiliser block. Finally, the Pickering emulsifier performance of linear PGMA<sub>41</sub>-PHBMA<sub>110</sub> vesicles was assessed. Laser diffraction and TEM studies suggest that such vesicles survive intact when exposed to the high-shear conditions required for homogenisation, unlike the linear PGMA<sub>45</sub>-PHPMA<sub>300</sub> vesicles previously reported by Thompson and co-workers.<sup>42</sup> This is attributed to the greater hydrophobic character of the PHBMA chains, which

leads to stronger inter-chain attractive forces and hence enables retention of the original vesicle morphology after emulsification.

## 4.5 References

1. L. Slade, H. Levine and D. S. Reid, *Crit. Rev. Food Sci. Nutr.*, 1991, **30**, 115-360.
2. D. Chandler, *Nature*, 2005, **437**, 640-647.
3. H. Schober, H. Itoh, A. Klapproth, V. Chihaiia and W. F. Kuhs, *Eur. Phys. J. E*, 2003, **12**, 41-49.
4. C. Tanford, *Science*, 1978, **200**, 1012-1018.
5. Q. Sun, *Chemical Physics Letters*, 2017, **672**, 21-25.
6. N. T. Southall and K. A. Dill, *J. Phys. Chem. B*, 2000, **104**, 1326-1331.
7. N. T. Southall, K. A. Dill and A. D. J. Haymet, *J. Phys. Chem. B*, 2002, **106**, 521-533.
8. N. U. Dharmaratne, T. M. M. Jouaneh, M. K. Kiesewetter and R. T. Mathers, *Macromolecules*, 2018, **51**, 8461-8468.
9. C. A. Lipinski, F. Lombardo, B. W. Dominy and P. J. Feeney, *Adv Drug Deliv Rev*, 2001, **46**, 3-26.
10. C. C. Bannan, G. Calabró, D. Y. Kyu and D. L. Mobley, *Journal of Chemical Theory and Computation*, 2016, **12**, 4015-4024.
11. S. Venkatram, C. Kim, A. Chandrasekaran and R. Ramprasad, *Journal of Chemical Information and Modeling*, 2019, **59**, 4188-4194.
12. J. C. Foster, I. Akar, M. C. Grocott, A. K. Pearce, R. T. Mathers and R. K. O'Reilly, *ACS Macro Lett.*, 2020, **9**, 1700-1707.
13. J. C. Foster, S. Varlas, B. Couturaud, J. R. Jones, R. Keogh, R. T. Mathers and R. K. O'Reilly, *Angew. Chem. Int. Ed.*, 2018, **57**, 15733-15737.
14. Y. Mai and A. Eisenberg, *Chem. Soc. Rev.*, 2012, **41**, 5969-5985.
15. A. Sánchez-Iglesias, M. Grzelczak, T. Altantzis, B. Goris, J. Pérez-Juste, S. Bals, G. Van Tendeloo, S. H. Donaldson, B. F. Chmelka, J. N. Israelachvili and L. M. Liz-Marzán, *ACS Nano*, 2012, **6**, 11059-11065.
16. J. N. Israelachvili, D. J. Mitchell and B. W. Ninham, *J. Chem. Soc., Trans.*, 1976, **72**, 1525-1568.
17. M. Antonietti and S. Förster, *Adv. Mater.*, 2003, **15**, 1323-1333.
18. H. Cui, Z. Chen, S. Zhong, K. L. Wooley and D. J. Pochan, *Science*, 2007, **317**, 647-650.
19. Y. Yan, J. Huang and B. Z. Tang, *Chem. Commun.*, 2016, **52**, 11870-11884.
20. L. P. D. Ratcliffe, A. Blanz, C. N. Williams, S. L. Brown and S. P. Armes, *Polym. Chem.*, 2014, **5**, 3643-3655.
21. J. R. Lovett, N. J. Warren, L. P. D. Ratcliffe, M. K. Kocik and S. P. Armes, *Angew. Chem. Int. Ed.*, 2015, **54**, 1279-1283.
22. S. L. Canning, G. N. Smith and S. P. Armes, *Macromolecules*, 2016, **49**, 1985-2001.

23. B. Charleux, G. Delaittre, J. Rieger and F. D'Agosto, *Macromolecules*, 2012, **45**, 6753-6765.
24. X. Dai, L. Yu, Y. Zhang, L. Zhang and J. Tan, *Macromolecules*, 2019, **52**, 7468-7476.
25. J. Rieger, F. Stoffelbach, C. Bui, D. Alaimo, C. Jérôme and B. Charleux, *Macromolecules*, 2008, **41**, 4065-4068.
26. J. Rieger, G. Osterwinter, C. Bui, F. Stoffelbach and B. Charleux, *Macromolecules*, 2009, **42**, 5518-5525.
27. J. Rieger, W. Zhang, F. Stoffelbach and B. Charleux, *Macromolecules*, 2010, **43**, 6302-6310.
28. W. Zhang, F. D'Agosto, O. Boyron, J. Rieger and B. Charleux, *Macromolecules*, 2011, **44**, 7584-7593.
29. I. Chaduc, M. Girod, R. Antoine, B. Charleux, F. D'Agosto and M. Lansalot, *Macromolecules*, 2012, **45**, 5881-5893.
30. V. J. Cunningham, A. M. Alswieleh, K. L. Thompson, M. Williams, G. J. Leggett, S. P. Armes and O. M. Musa, *Macromolecules*, 2014, **47**, 5613-5623.
31. N. P. Truong, M. V. Dussert, M. R. Whittaker, J. F. Quinn and T. P. Davis, *Polym. Chem.*, 2015, **6**, 3865-3874.
32. B. Akpınar, L. A. Fielding, V. J. Cunningham, Y. Ning, O. O. Mykhaylyk, P. W. Fowler and S. P. Armes, *Macromolecules*, 2016, **49**, 5160-5171.
33. F. L. Hatton, J. R. Lovett and S. P. Armes, *Polym. Chem.*, 2017, **8**, 4856-4868.
34. O. J. Deane, O. M. Musa, A. Fernyhough and S. P. Armes, *Macromolecules*, 2020, **53**, 1422-1434.
35. A. A. Cockram, T. J. Neal, M. J. Derry, O. O. Mykhaylyk, N. S. J. Williams, M. W. Murray, S. N. Emmett and S. P. Armes, *Macromolecules*, 2017, **50**, 796-802.
36. L. P. D. Ratcliffe, A. J. Ryan and S. P. Armes, *Macromolecules*, 2013, **46**, 769-777.
37. F. L. Hatton, A. M. Park, Y. Zhang, G. D. Fuchs, C. K. Ober and S. P. Armes, *Polym. Chem.*, 2019, **10**, 194-200.
38. F. L. Hatton, M. J. Derry and S. P. Armes, *Polym. Chem.*, 2020, **11**, 6343-6355.
39. A. Blanazs, A. J. Ryan and S. P. Armes, *Macromolecules*, 2012, **45**, 5099-5107.
40. E. E. Brotherton, F. L. Hatton, A. A. Cockram, M. J. Derry, A. Czajka, E. J. Cornel, P. D. Topham, O. O. Mykhaylyk and S. P. Armes, *J. Am. Chem. Soc.*, 2019, **141**, 13664-13675.
41. A. Blanazs, J. Madsen, G. Battaglia, A. J. Ryan and S. P. Armes, *J. Am. Chem. Soc.*, 2011, **133**, 16581-16587.
42. K. L. Thompson, P. Chambon, R. Verber and S. P. Armes, *J. Am. Chem. Soc.*, 2012, **134**, 12450-12453.
43. J. Ilavsky and P. R. Jemian, *J. Appl. Crystallogr.*, 2009, **42**, 347-353.
44. I. Bannister, N. C. Billingham, S. P. Armes, S. P. Rannard and P. Findlay, *Macromolecules*, 2006, **39**, 7483-7492.
45. J. S. Pedersen and C. Svaneborg, *Curr. Opin. Colloid Interface Sci.*, 2002, **7**, 158-166.
46. J. Pedersen, *J. Appl. Crystallogr.*, 2000, **33**, 637-640.
47. A. Blanazs, R. Verber, O. O. Mykhaylyk, A. J. Ryan, J. Z. Heath, C. W. I. Douglas and S. P. Armes, *J. Am. Chem. Soc.*, 2012, **134**, 9741-9748.

48. V. J. Cunningham, L. P. D. Ratcliffe, A. Blanz, N. J. Warren, A. J. Smith, O. O. Mykhaylyk and S. P. Armes, *Polym. Chem.*, 2014, **5**, 6307-6317.
49. J. Bang, S. Jain, Z. Li, T. P. Lodge, J. S. Pedersen, E. Kesselman and Y. Talmon, *Macromolecules*, 2006, **39**, 1199-1208.
50. E. J. Cornel, S. van Meurs, T. Smith, P. S. O'Hora and S. P. Armes, *J. Am. Chem. Soc.*, 2018, **140**, 12980-12988.
51. W. Zhang, F. D'Agosto, P.-Y. Dugas, J. Rieger and B. Charleux, *Polymer*, 2013, **54**, 2011-2019.
52. M. J. Derry, L. A. Fielding, N. J. Warren, C. J. Mable, A. J. Smith, O. O. Mykhaylyk and S. P. Armes, *Chem. Sci.*, 2016, **7**, 5078-5090.
53. A. Czajka and S. P. Armes, *Chem. Sci.*, 2020, **11**, 11443-11454.
54. C. J. Mable, K. L. Thompson, M. J. Derry, O. O. Mykhaylyk, B. P. Binks and S. P. Armes, *Macromolecules*, 2016, **49**, 7897-7907.
55. Y. Zhang, L. Yu, X. Dai, L. Zhang and J. Tan, *ACS Macro Lett.*, 2019, **8**, 1102-1109.
56. K. L. Thompson, L. A. Fielding, O. O. Mykhaylyk, J. A. Lane, M. J. Derry and S. P. Armes, *Chem. Sci.*, 2015, **6**, 4207-4214.
57. K. L. Thompson, C. J. Mable, J. A. Lane, M. J. Derry, L. A. Fielding and S. P. Armes, *Langmuir*, 2015, **31**, 4137-4144.
58. M. J. Rymaruk, K. L. Thompson, M. J. Derry, N. J. Warren, L. P. D. Ratcliffe, C. N. Williams, S. L. Brown and S. P. Armes, *Nanoscale*, 2016, **8**, 14497-14506.
59. C. J. Mable, N. J. Warren, K. L. Thompson, O. O. Mykhaylyk and S. P. Armes, *Chem. Sci.*, 2015, **6**, 6179-6188.
60. Q. Xu, Y. Zhang, X. Li, J. He, J. Tan and L. Zhang, *Polym. Chem.*, 2018, **9**, 4908-4916.
61. Z. P. Wang, M. C. M. van Oers, F. Rutjes and J. C. M. van Hest, *Angew. Chem. Int. Edit.*, 2012, **51**, 10746-10750.
62. K. L. Thompson, C. J. Mable, A. Cockram, N. J. Warren, V. J. Cunningham, E. R. Jones, R. Verber and S. P. Armes, *Soft Matter*, 2014, **10**, 8615-8626.
63. R. Aveyard, B. P. Binks and J. H. Clint, *Adv. Colloid Interface Sci.*, 2003, **100**, 503-546.
64. B. P. Binks and C. P. Whitby, *Langmuir*, 2004, **20**, 1130-1137.

## **Chapter 5:**

# **Synthesis of Thermoresponsive Diblock Copolymer Nano-Objects *via* RAFT Aqueous Emulsion Polymerisation of Hydroxybutyl Methacrylate**

## 5.1 Introduction

It is well-known that PISA enables the convenient and efficient preparation of a wide range of block copolymer nano-objects in the form of concentrated dispersions.<sup>1-26</sup> In the case of aqueous PISA formulations, if the vinyl monomer used to grow the hydrophobic second block is water-miscible this corresponds to an aqueous dispersion polymerisation.<sup>3, 17, 21, 27-35</sup> On the other hand, if the monomer is water-immiscible – which is much more common – this corresponds to an aqueous emulsion polymerisation.<sup>36, 37</sup> In the PISA literature, there has been substantial interest in the rational design of aqueous dispersions of thermoresponsive ‘shape-shifting’ diblock copolymer nano-objects over the past decade.<sup>17, 38-45</sup> In practice, such nano-objects are invariably prepared *via* RAFT aqueous dispersion polymerisation.<sup>3, 46-49</sup> This is because water-miscible vinyl monomers such as HPMA,<sup>27, 50-53</sup> HBA,<sup>35, 45, 54</sup> NIPAM<sup>17, 41</sup> or 2-methoxyethyl acrylate (MEA)<sup>29, 31</sup> produce homopolymers that are only weakly hydrophobic. In particular, their degree of hydration is temperature-dependent, which affects the relative volume fraction of such hydrophobic blocks.<sup>38, 45</sup> This induces a subtle change in the fractional packing parameter  $P$  (see Figure 1.8),<sup>55, 56</sup> which is sufficient to drive various morphological transitions for the corresponding diblock copolymer nano-objects when adjusting the solution temperature.<sup>38, 44, 45, 54, 55, 62-66</sup> For example, Ratcliffe and co-workers reported that a PHPMAC-PPMA diblock copolymer formed spheres at 4 °C, worms at 22 °C and vesicles at 50 °C.<sup>44</sup>

Recently, we have reported three distinct examples of HBA-based thermoresponsive diblock copolymer of fixed composition that can form spheres, worms or vesicles in aqueous solution simply by adjusting the solution temperature.<sup>45, 57, 58</sup> Initially, Byard *et al.* prepared thermoresponsive PDMAC<sub>56</sub>-PHBA<sub>218-269</sub> diblock copolymer worms *via* RAFT dispersion polymerisation of HBA at 20% w/w solids.<sup>59</sup> Spheres were formed upon cooling to 3 °C, whereas heating to 50 °C led to the formation of vesicles. Variable temperature <sup>1</sup>H NMR studies indicated that the weakly hydrophobic HBA repeat units became *more* hydrated at elevated temperature. This is in striking contrast to the behaviour observed for PHPMA-based diblock copolymers, where the HPMA repeat units become

less hydrated on heating.<sup>38, 52, 53, 60-64</sup> Such behaviour is somewhat counter-intuitive given that HPMA and HBA are structural isomers. Unfortunately, the relatively low  $T_g$  of the PHBA core block led to film formation, which made it impossible to determine copolymer morphologies *via* TEM.<sup>45</sup> Subsequently, Byard *et al.* addressed this technical issue by statistically copolymerising HBA with a crosslinkable DAAM comonomer. Core-crosslinking prevented film formation and hence enabled TEM studies. However, the presence of 20 mol% DAAM comonomer reduced the thermoresponsive behaviour exhibited by the HBA-rich structure-directing block. Recently, this problem was overcome by Deane *et al.*, who prepared PNAEP<sub>85</sub>-PHBA<sub>x</sub> diblock copolymer nano-objects.<sup>57</sup> In this case, glutaraldehyde was employed to covalently stabilise the nanoparticles and hence enable high-quality TEM images to be obtained without requiring a crosslinkable comonomer to be incorporated within the structure-directing block (see Figure 5.1). This enabled direct evaluation of the thermoresponsive behaviour of PNAEP<sub>85</sub>-PHBA<sub>295</sub> nano-objects. More specifically, raising the temperature drives morphological transitions from spheres (5 °C) to worms (23 °C) to vesicles (31 °C) and finally lamellae (41 °C). Moreover, such morphological transitions proved to be fully reversible on cooling.

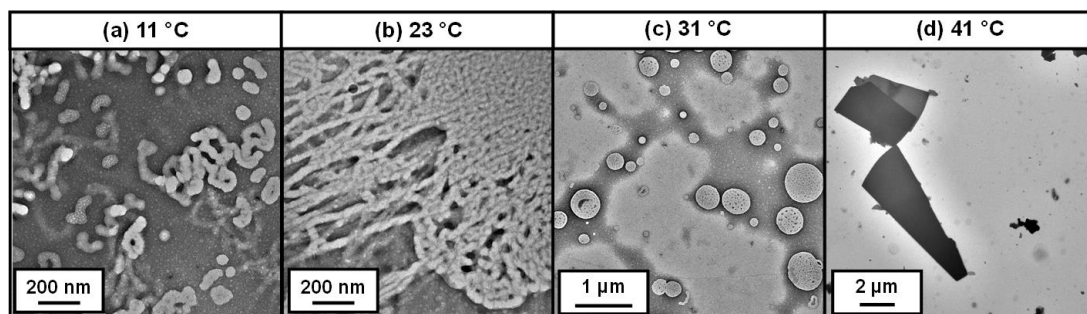


**Figure 5.1.** Representative TEM images obtained for dilute aqueous dispersions of PNAEP<sub>85</sub>-PHBA<sub>295</sub> nanoparticles after reacting with glutaraldehyde crosslinker for 24 h at (a) 11 °C, (b) 23 °C, (c) 31 °C or (d) 41 °C.<sup>57</sup>

The RAFT aqueous emulsion polymerisation of vinyl monomers such as styrene,<sup>65-71</sup> MMA,<sup>72-74</sup> BzMA,<sup>75, 76</sup> nBA,<sup>70, 72, 77</sup> phenyl acrylate,<sup>78</sup> VAc<sup>79-82</sup> or TFEMA<sup>83-86</sup> invariably leads to the formation of block copolymer nano-objects that do *not* exhibit thermoresponsive behaviour. Moreover, such formulations often lead to kinetically-trapped spheres as the sole accessible morphology, although there are a few well-known counter-examples to this restrictive

paradigm.<sup>20, 66, 67, 87, 88</sup> Recently, Armes and co-workers have explored the RAFT aqueous emulsion polymerisation of vinyl monomers such as GlyMA,<sup>89-91</sup> MEOMA<sup>92</sup> and HBMA<sup>93</sup> that exhibit moderately high aqueous solubilities ( $\sim 15 - 20 \text{ g dm}^{-3}$ ). This has enabled the problem of kinetically-trapped spheres to be avoided and hence provide access to well-defined worms and vesicles, as explored in Chapter 4.

In the present Chapter, we demonstrate that the RAFT aqueous emulsion polymerisation of HBMA using a trithiocarbonate-capped PEG precursor provides the first example of thermoresponsive diblock copolymer nano-objects to be prepared using such an aqueous PISA formulation. Moreover, this system can form spheres, worms or vesicles reversibly in aqueous solution simply by varying the solution temperature.

## **5.2 Experimental**

### **5.2.1 Materials**

Hydroxybutyl methacrylate (HBMA; 94% purity; comprising a 1:1 mixture of 4-hydroxybutyl methacrylate and 2-hydroxybutyl methacrylate) was purchased from Sigma-Aldrich (UK) and used as received. A trithiocarbonate-based poly(ethylene glycol) (PEG<sub>45</sub>-TTC) precursor was prepared and purified as reported elsewhere.<sup>61</sup> 2,2'-Azobis[2-(2-imidazolin-2-yl)propane] dihydrochloride (VA-044;  $\geq 97\%$ ) was purchased from Strem Chemicals Ltd. (Cambridge, UK) and used as received. Deuterated methanol (CD<sub>3</sub>OD) was purchased from Goss Scientific Instruments Ltd. (Cheshire, UK). All other solvents were purchased from Fisher Scientific (Loughborough, UK) and were used as received. Deionised water was used for all experiments.

### **5.2.2 Synthesis of PEG<sub>45</sub>-PHBMA<sub>20</sub> Diblock Copolymer Nano-Objects *via* RAFT Aqueous Emulsion Polymerisation of HBMA**

A 14 mL glass vial was charged with PEG<sub>45</sub>-TTC precursor (0.40 g, 157  $\mu\text{mol}$ ), HBMA monomer (0.496 g, 3.13 mmol; target DP = 20), VA-044 initiator (10.1 mg, 31.3  $\mu\text{mol}$ ; PEG<sub>41</sub>/VA-044 molar ratio = 5.0), and deionised water (8.17 g, 10% w/w solids). This reaction solution was purged using N<sub>2</sub> gas for 30 min at 20 °C prior to immersing the vial into an oil bath set at 50 °C. After 1 h, the HBMA polymerisation was quenched by exposing the reaction mixture to air, followed by cooling to ambient temperature. A HBMA conversion of more than 99% was determined *via* <sup>1</sup>H NMR studies (CD<sub>3</sub>OD). THF GPC studies indicated an  $M_n$  of 5 900 g mol<sup>-1</sup> and an  $M_w/M_n$  of 1.11 (vs. a series of PMMA calibration standards).

### 5.2.3 Characterisation

#### <sup>1</sup>H NMR spectroscopy

Spectra were recorded in CD<sub>3</sub>OD at 20 °C using a Bruker Avance III HD 400 MHz spectrometer with 64 scans being averaged per spectrum. Variable temperature <sup>1</sup>H NMR spectra were recorded using a 500 MHz Bruker Avance-500 spectrometer. An outer tube contained a 10% w/w aqueous dispersion of PEG<sub>45</sub>-PHBMA<sub>20</sub> nano-objects prepared in D<sub>2</sub>O and an inner capillary tube contained the pyridine external standard dissolved in C<sub>2</sub>D<sub>2</sub>Cl<sub>4</sub>. Spectra were recorded from 25 °C to 75 °C at 5 °C intervals with an equilibrium time of 10 min at each temperature with 64 scans being averaged per spectrum.

#### Gel permeation chromatography (GPC)

THF GPC was used to assess (co)polymer molecular weight distributions. The GPC set-up comprised two 5  $\mu\text{m}$  (30 cm) mixed C columns and a WellChrom K-2301 refractive index detector operating at 950  $\pm$  30 nm. The THF mobile phase contained 2.0% v/v triethylamine and 0.05% w/v butylhydroxytoluene (BHT) with a toluene flow-rate marker at a flow rate of 1.0 mL min<sup>-1</sup>. A series of eleven near-monodisperse PMMA standards ( $M_p$  values ranging from 800 to 988 000 g mol<sup>-1</sup>) were used for calibration.

### Dynamic light scattering (DLS)

The hydrodynamic  $z$ -average diameter ( $D_z$ ) and polydispersity index (PDI) were determined by DLS using a Malvern Zetasizer NanoZS instrument *via* the cumulants method. All measurements were performed on 0.10% copolymer dispersions (prepared by dilution using deionised water) using disposable plastic cuvettes. All data were averaged over three consecutive runs. The ‘sphere-equivalent’  $z$ -average diameter of diblock copolymer nano-objects was determined using the Stokes-Einstein equation, which assumes perfectly monodisperse, non-interacting spheres. For variable temperature DLS studies, 1.0 mL of a 0.10% w/w aqueous copolymer dispersion in a glass cuvette was heated from 20 °C to 75 °C at 1 °C intervals with 5 min being allowed for thermal equilibration at each temperature, followed by cooling from 75 °C to 20 °C using the same protocol. The hydrodynamic  $z$ -average diameter was determined at each temperature by averaging data over three consecutive runs.

### Transmission electron microscopy (TEM)

Copper/palladium TEM grids (Agar Scientific, UK) were coated in-house to yield a thin film of amorphous carbon and then subjected to a plasma glow discharge for 30 s. One 10  $\mu$ L droplet of each 0.10% w/w aqueous copolymer dispersion was placed in turn on a freshly-treated grid for 1 min and then carefully blotted with filter paper to remove excess solution. To ensure sufficient electron contrast, a 10  $\mu$ L droplet of a 0.75% w/w aqueous uranyl formate solution was placed on the sample-loaded grid for 20 s and then blotted to remove excess stain. Each grid was carefully dried using a vacuum hose. Imaging was performed using a FEI Tecnai Spirit 2 microscope operating at 80 kV and equipped with an Orius SC1000B camera.

### Oscillatory Rheology

An AR-G2 rheometer (TA Instruments, Delaware, USA) equipped with a variable-temperature PeltAier plate and a 40 ml 2° aluminium cone was used for all experiments. Temperature sweeps were conducted using a constant percentage strain of 1.0% and a constant

angular frequency of  $1.0 \text{ rad s}^{-1}$ . Prior to the temperature sweep, the 10% w/w PEG<sub>45</sub>-PHBMA<sub>20</sub> aqueous copolymer dispersion was equilibrated at 20 °C for 5 min. Thermal cycles were conducted between 20 °C and 75 °C at 1 °C intervals.

Shear-induced polarised light imaging (SIPLI).

Polarised light images were recorded at various temperatures using a Physica MCR301 mechano-optical rheometer (Anton Paar, Graz, Austria) equipped with a SIPLI attachment and variable temperature Peltier (bottom plate and hood) heaters. A detailed description of this instrument can be found elsewhere.<sup>94, 95</sup> A plate–plate geometry consisting of a 25 mm polished steel plate fixture and a fused quartz bottom plate with a fixed gap of 1.0 mm was used for these experiments. The angle between the polariser and analyser was 90° and polarised light images were recorded under shear using a colour CCD camera (Lumenera Lu165c) from 20 °C to 75 °C at a ramp rate of 1 °C min<sup>-1</sup> for an 10% w/w aqueous dispersion of PEG<sub>45</sub>-PHBMA<sub>20</sub> nano-objects. A maximum (sample edge) shear rate of  $1.0 \text{ s}^{-1}$  was applied for 250 s in each case.

Small Angle X-ray scattering (SAXS)

SAXS experiments were conducted on 1.0% w/w aqueous dispersion of PEG<sub>45</sub>-PHBMA<sub>20</sub> nano-objects at the European Synchrotron Radiation Facilities (ESRF, station ID02, Grenoble, France) using monochromatic X-ray radiation ( $\lambda = 0.0995 \text{ nm}$ ;  $q$  range = 0.002 to  $0.15 \text{ \AA}^{-1}$ , where  $q$  is the length of the scattering vector and  $\theta$  is one-half of the scattering angle, such that  $q = 4\pi\sin\theta/\lambda$ ) and a Eiger2 4M two-dimensional detector (Dectris, Switzerland). A glass capillary of 1.4 mm diameter was used as a sample holder and the temperature was controlled using a heating/cooling capillary holding stage (Linkam Scientific Instruments Ltd., Tadworth, UK). Measurements were conducted on a 1.0% w/w aqueous dispersion of PEG<sub>45</sub>-PHBMA<sub>20</sub> nano-objects. Scattering patterns were recorded from 20 °C to 75 °C at a heating rate of 1 °C min<sup>-1</sup>. Scattering data were reduced using standard routines provided by the beamline and were further analysed using Irena SAS macro for Igor Pro.<sup>96</sup>

## 5.3 Results and Discussion

### 5.3.1 RAFT Aqueous Emulsion Polymerisation of HBMA Using a PEG<sub>45</sub>-TTC Precursor

#### Precursor

PEG<sub>45</sub>-PHBMA<sub>20</sub> diblock copolymer nano-objects were synthesised by RAFT aqueous emulsion polymerisation of HBMA using a previously reported trithiocarbonate-based PEG<sub>45</sub>-TTC precursor,<sup>61</sup> as shown in Figure 5.2. These syntheses were performed using an azo-based VA-044 initiator at 50 °C using a PEG<sub>45</sub>-TTC/initiator molar ratio of 5.0 and targeting 10% w/w copolymer concentration.

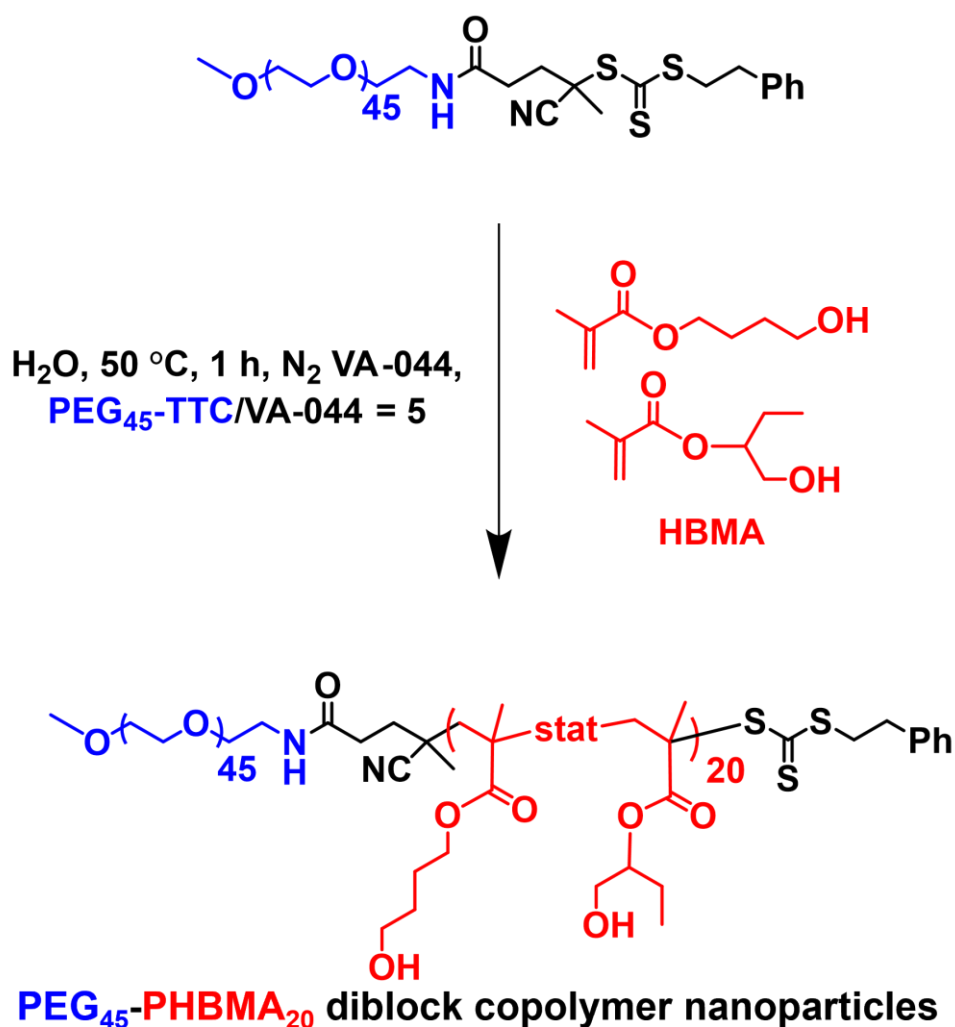


**Figure 5.2.** RAFT aqueous emulsion polymerisation of HBMA (N.B. this monomer comprises a 11:1 mixture of the 2- and 4-isomers; both of the isomers are depicted here) using a trithiocarbonate-based PEG<sub>45</sub>-TTC precursor.

$^1\text{H}$  NMR spectroscopy studies of  $\text{PEG}_{45}\text{-PHBMA}_{20}$  molecularly dissolved in  $\text{CD}_3\text{OD}$  confirmed that a HBMA conversion of more than 99% was achieved within 1 h at  $50^\circ\text{C}$  (see Figure 5.3).

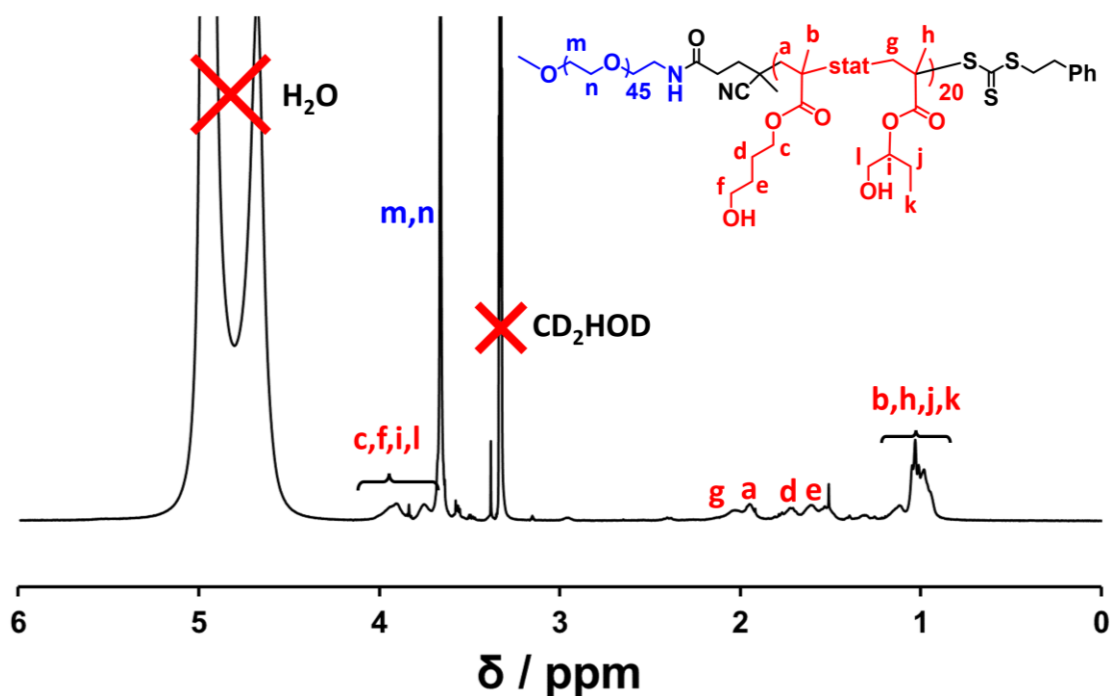


**Figure 5.3.** Assigned  $^1\text{H}$  NMR spectrum ( $\text{CD}_3\text{OD}$ ) recorded for a  $\text{PGMA}_{45}\text{-PHBMA}_{20}$  diblock copolymer obtained *via* RAFT aqueous emulsion polymerisation of HBMA after more than 99% conversion within 60 min at  $50^\circ\text{C}$ . Both isomeric forms of the HBMA repeat units (which are present in a 1:1 molar ratio) are depicted in the chemical structure.

THF GPC analysis of the  $\text{PEG}_{45}\text{-PHBMA}_{20}$  diblock copolymer is shown in Figure 5.4. The GPC trace for this copolymer was shifted relative to its  $\text{PEG}_{45}\text{-TTC}$  precursor, which indicates a relatively high blocking efficiency and minimal homopolymer contamination. Moreover, a relatively narrow molecular weight distribution was obtained ( $M_w/M_n = 1.11$ ). As discussed in Chapter 4, the  $M_w$  and the  $M_w/M_n$  increase as higher DPs of PHBMA are targeted.<sup>54, 93</sup> This is due to the presence of dimethacrylate impurities in the HBMA monomer, which leads to branching and light cross-linking.<sup>97</sup> In the previous Chapter, the target DPs were comparatively lower than Cockram *et al.* and therefore the polydispersities of the final copolymers were lower.<sup>93</sup> In the current Chapter, for a PHBMA target DP of 20, an  $M_w/M_n$  of 1.11 was obtained. This value is consistent with the GPC data obtained  $\text{PGMA-PHBMA}$  diblock copolymers reported in Chapter 4 and previously reported by Ratcliffe *et al.*<sup>54</sup>

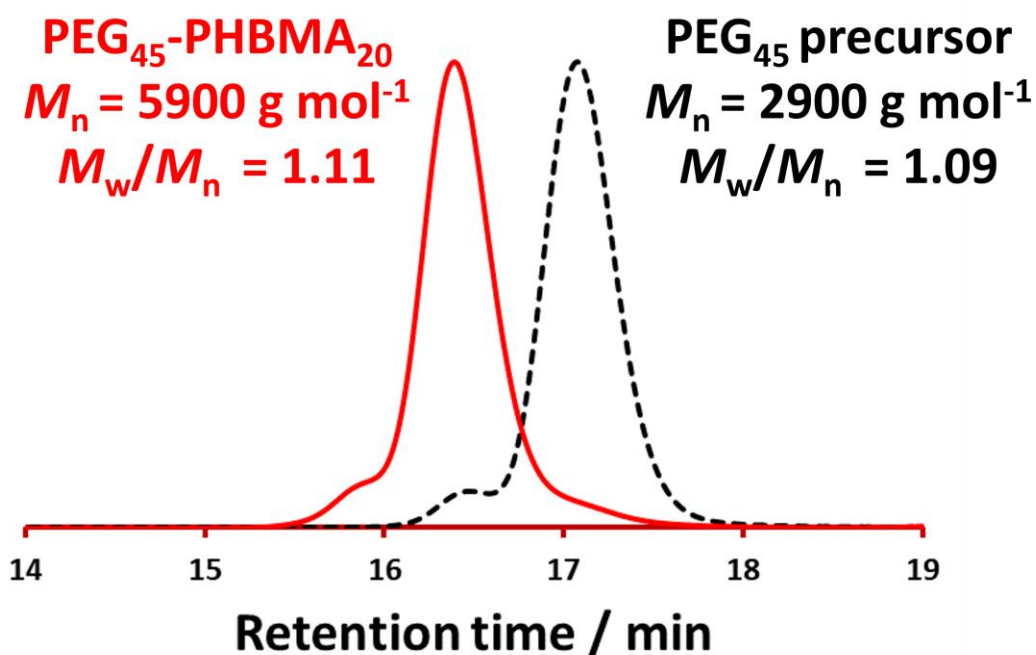


**Figure 5.4.** Overlaid THF GPC traces recorded for a PEG<sub>45</sub>-TTC precursor (black trace) and the corresponding PEG<sub>45</sub>-PHBMA<sub>20</sub> diblock copolymer (red trace) prepared by RAFT aqueous emulsion polymerisation of HBMA (conditions: 10% w/w, 50 °C for 1 h). Molecular weight data are expressed relative to a series of near-monodisperse poly(methyl methacrylate) calibration standards.

The final 10% w/w aqueous dispersion of PEG<sub>45</sub>-PHBMA<sub>40</sub> nano-objects was a transparent free-flowing fluid at 20 °C. This was not unexpected since the relatively short target PHBMA DP should favour the formation of spheres. Indeed, TEM studies confirmed that this diblock copolymer possessed a relatively well-defined spherical morphology (see Figure 5.6a) while DLS studies indicated the formation of nano-objects with a hydrodynamic *z*-average diameter of 17 nm (PDI = 0.09).

### 5.3.2 Characterisation of Thermoresponsive PEG<sub>41</sub>-PHBMA<sub>20</sub> Diblock Copolymer Nano-Objects

Initially, the 10% w/w PEG<sub>45</sub>-PHBMA<sub>20</sub> dispersion was highly viscous on quenching the polymerisation of HBMA at 50 °C. However, a free-flowing dispersion was obtained on cooling to 20 °C (see Figure 5.5). This physical transformation indicated that the PEG<sub>45</sub>-PHBMA<sub>20</sub> nano-

objects may possess thermoresponsive character. To further explore the effect of temperature on its visual appearance, this 10% w/w dispersion was immersed in an oil bath and heated to 25 °C, 55 °C or 65 °C for 10 min while recording digital photographs. On heating to 55 °C, a transparent free-standing gel was obtained. On further heating to 65 °C, degelation occurred to produce a free-flowing transparent dispersion. Such transformations were fully reversible as judged by visual inspection.

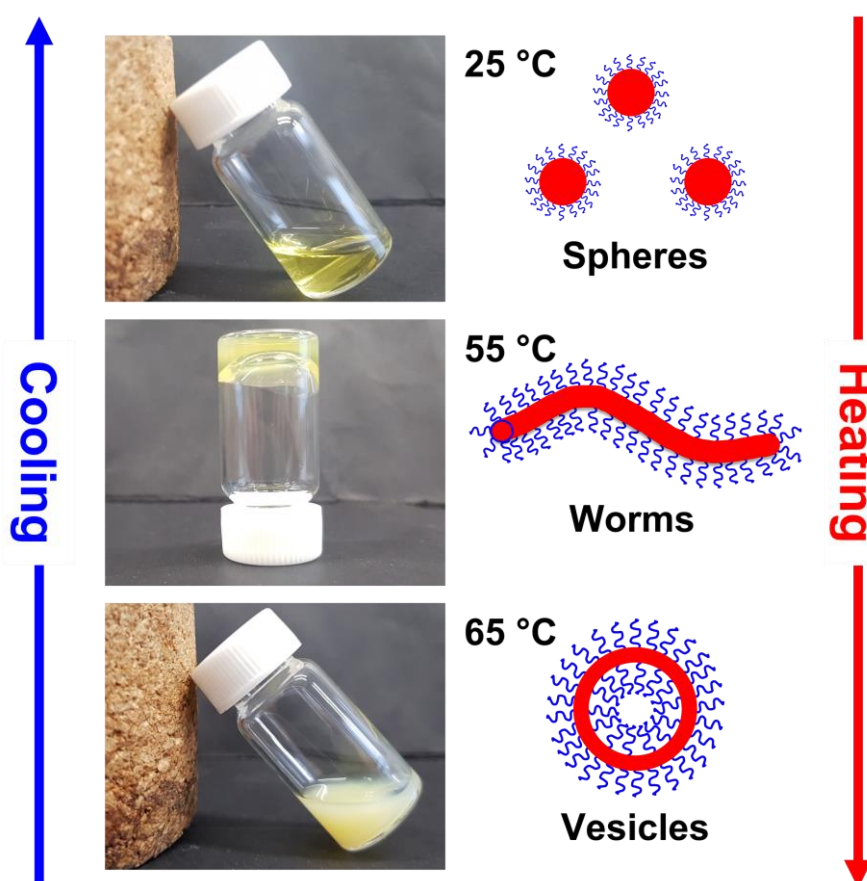


**Figure 5.5.** Digital images (left) illustrating the physical appearance of a 10% w/w PEG<sub>45</sub>-PHBMA<sub>20</sub> aqueous dispersion: (top) at 25 °C, (middle) on heating to 55 °C for 10 min and (bottom) on heating to 65 °C for 10 min. Schematic representation (right) of the likely thermoreversible morphological transitions exhibited by these diblock copolymer nano-objects.

Thermally-driven transitions are often associated with a change in copolymer morphology.<sup>98</sup> To examine whether this was the case for this diblock copolymer system, TEM studies were performed from 25 °C to 75 °C. Unlike previously reported temperature-dependent studies on PHBA-based diblock copolymers,<sup>45</sup> the PEG<sub>45</sub>-PHBMA<sub>20</sub> diblock copolymer studied herein does not require covalent stabilisation prior to visualisation by TEM. This is because the

methacrylic block has a sufficiently high  $T_g$  to prevent film formation during TEM grid preparation. Hence the PEG<sub>45</sub>-PHBMA<sub>20</sub> nano-objects can be analysed directly without covalent stabilisation.<sup>54</sup> TEM studies confirm that PEG<sub>45</sub>-PHBMA<sub>20</sub> undergoes morphological transitions that resemble those reported for PHBA-based diblock copolymers.<sup>45, 57, 58</sup> This is perhaps surprising given the significantly greater hydrophobic character of the PHBMA block. More specifically, TEM studies confirmed that PEG<sub>45</sub>-PHBMA<sub>20</sub> forms spheres at 25 °C, anisotropic worms at 55 °C, vesicles at 65 °C and lamellae at 75 °C (see Figure 5.6). One key difference between the PHBA- and PHBMA-based diblock copolymers is the preferred morphology at ambient temperature. For example, Deane *et al.* reported that PNAEP<sub>85</sub>-PHBA<sub>295</sub> diblock copolymer worms undergo a worm-to-sphere on cooling to 5 °C, whereas on heating to 34 °C they undergo a worm-to-vesicle transition. In contrast, PEG<sub>45</sub>-PHBMA<sub>20</sub> forms spheres at ambient temperature, which undergo a sphere-to-worm and a worm-to-vesicle transition on heating up to 70 °C. Therefore, both diblock copolymers undergo the same thermal transitions, but higher onset temperatures are required to generate worms and vesicles in the case of PEG<sub>45</sub>-PHBMA<sub>20</sub>.

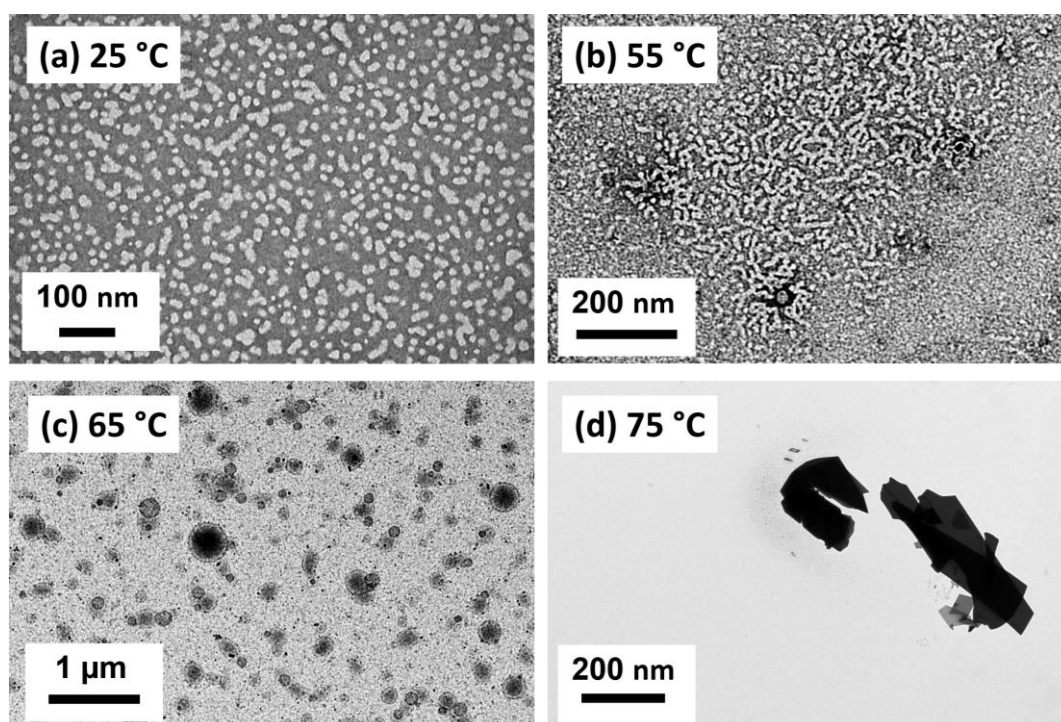


**Figure 5.6.** Representative TEM images obtained for a 0.1% w/w aqueous dispersion of PEG<sub>45</sub>-PHBMA<sub>20</sub> at (a) 25 °C or after heating for 30 min to (b) 55 °C, (c) 65 °C or (d) 75 °C.

DLS was used to determine the sphere-equivalent  $z$ -average diameter for a 0.10% w/w aqueous dispersion of PEG<sub>45</sub>-PHBMA<sub>20</sub> nano-objects during a thermal cycle from 20 °C to 75 °C to 20 °C (Figure 5.7). Initially, this dispersion comprises relatively small spheres (17 nm diameter, PDI = 0.09). At 44 °C, the  $z$ -average diameter and DLS polydispersity both begin to increase rapidly, which are characteristic features of a sphere-to-worm transition.<sup>45,99</sup> A dramatic increase in size and a concomitant reduction in DLS polydispersity occurs above 60 °C, suggesting the formation of relatively small and well-defined vesicles ( $z$ -average diameter = 117 nm, DLS polydispersity = 0.05). Very similar  $z$ -average diameters were recorded during the cooling cycle, which indicates good thermoreversibility even at this relatively low copolymer concentration.

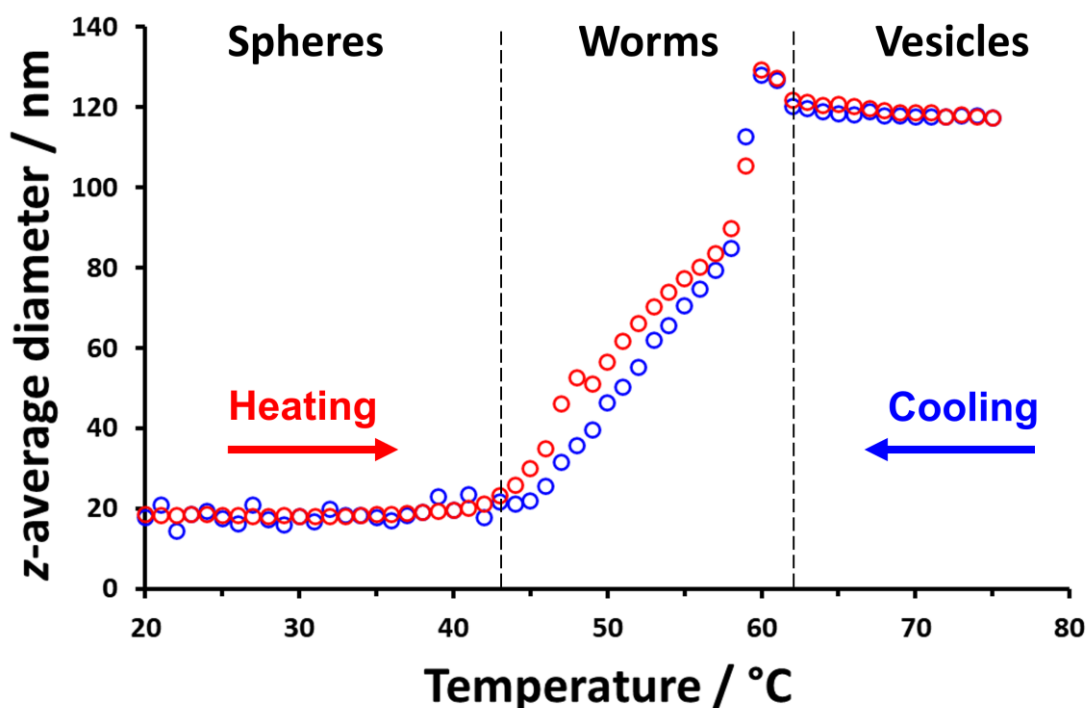


**Figure 5.7.** Apparent sphere-equivalent  $z$ -average diameter determined by DLS as a function of temperature for a 0.1% w/w dispersion of PEG<sub>45</sub>-PHBMA<sub>20</sub> nano-objects. The red data represents the heating cycle from 20 °C to 75 °C. The blue data represents the cooling cycle from 75 °C to 20 °C. The dispersion was equilibrated at each temperature for 5 min prior to DLS measurements. The black dashed lines indicate the likely phase boundaries for the three copolymer morphologies (spheres, worms and vesicles).

Small-angle X-ray scattering (SAXS) studies were conducted on a 1.0% w/w aqueous dispersion of PEG<sub>45</sub>-PHBMA<sub>20</sub> nano-objects as a function of temperature. Figure 5.8 shows a

series of plots of the scattered X-ray intensity  $I(q)$  against  $q$  recorded for such nano-objects from 20 °C to 70 °C at a heating rate of 1 °C min<sup>-1</sup>.

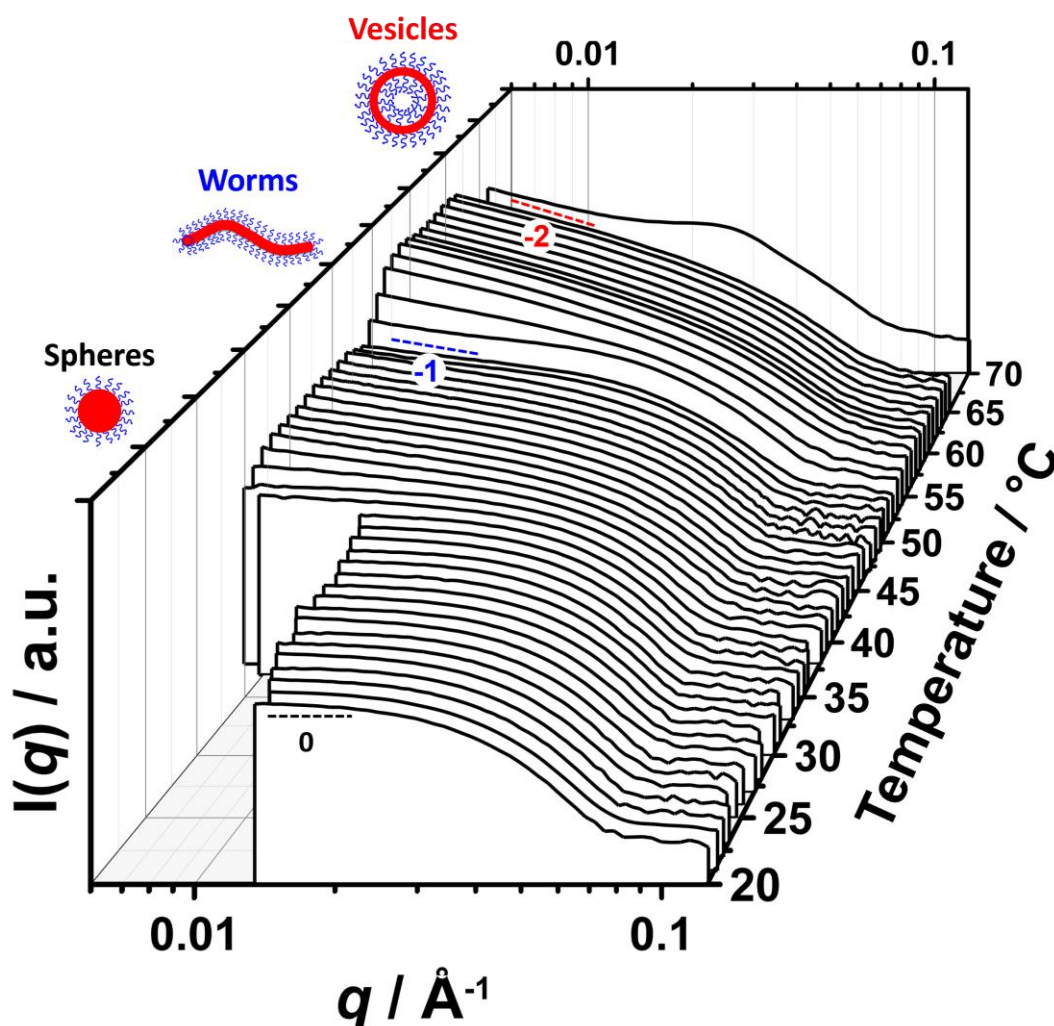


**Figure 5.8.** SAXS patterns recorded for a 1.0% w/w aqueous dispersion of thermoresponsive PEG<sub>45</sub>-PHBMA<sub>20</sub> nano-objects between 20 °C and 70 °C using a heating rate of 1 °C min<sup>-1</sup>. The horizontal dashed lines indicate the characteristic low  $q$  gradients (0, -1 and -2), which are indicative of the presence of spheres, worms and vesicles, respectively.

In each case, the gradient in the low  $q$  region is characteristic of the predominant copolymer morphology, see Figure 5.9.<sup>100</sup> The low  $q$  gradient is close to zero at 20 - 40 °C, suggesting the presence of spheres over this temperature range. At around 50 °C, the low  $q$  gradient tends toward -1, indicating the formation of highly anisotropic worms. At around 65 °C, the low  $q$  gradient is close to -2, which is characteristic of bilayer (or vesicle) formation. At 70 °C, the broad structure factor observed at around 0.024 Å indicates the presence of stacked lamellae

sheets.<sup>45</sup> These SAXS observations are broadly consistent with the copolymer morphologies observed by TEM.

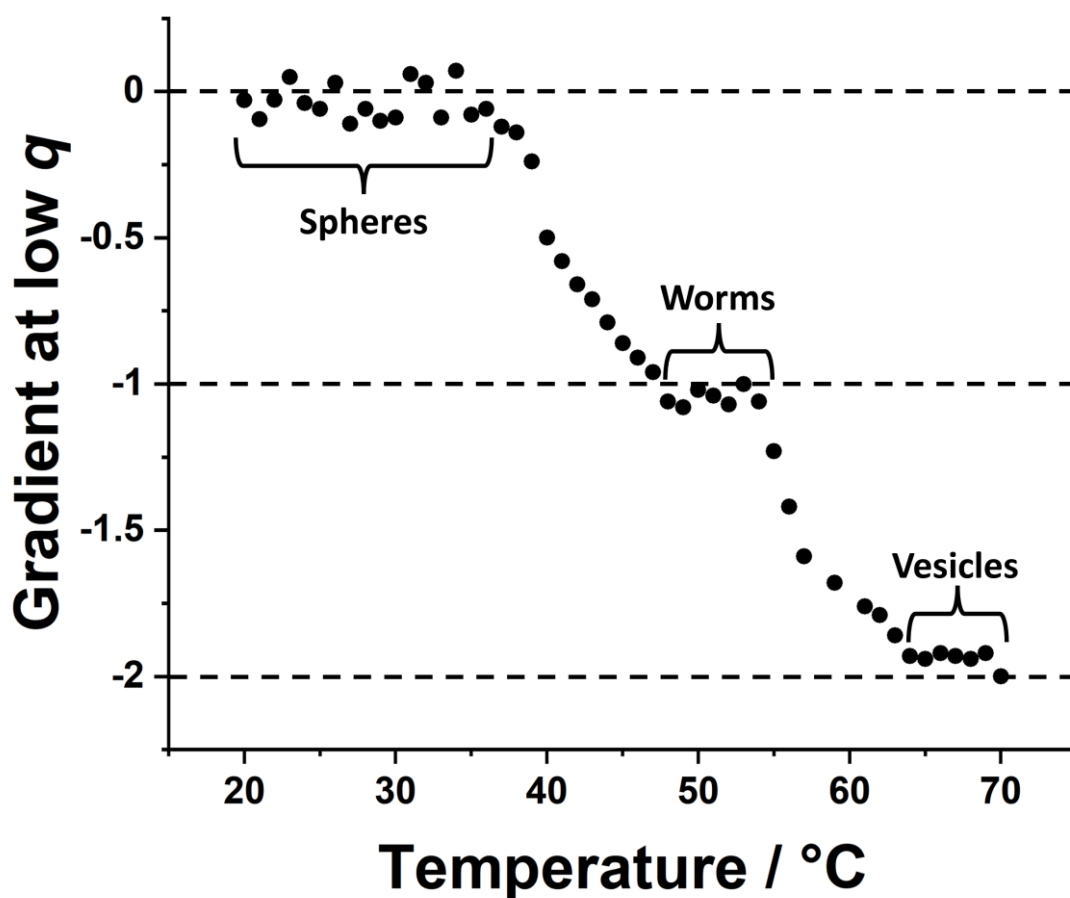


**Figure 5.9.** Variation in the low  $q$  gradient ( $0.006 \leq q \leq 0.015 \text{ \AA}^{-1}$ ) of the SAXS patterns shown in Figure 5.8. as a function of temperature. The horizontal dashed lines indicate the characteristic low  $q$  gradients (0,  $-1$  and  $-2$ ), which are indicative of the presence of spheres, worms and vesicles, respectively.

Figure 5.10 shows selected SAXS patterns recorded at 20, 55, 65 and 70 °C that could be satisfactorily fitted using well-known scattering models (see Chapter 7 for more information).<sup>104</sup>

<sup>105</sup> In each case, the dimensions calculated from these SAXS fits were consistent with those determined by DLS and TEM (see Table 5.1). SAXS analysis of the spheres formed at 20 °C indicated a volume-average core diameter of 13.8 nm, which is consistent with the  $z$ -average diameter of 17.6 nm indicated by DLS. For the anisotropic worms at 55 °C, the core cross-section diameter  $T_w$  was calculated to be 11.5 nm, which is in good agreement with the number-average worm width estimated by TEM ( $11.2 \pm 1.9$  nm).

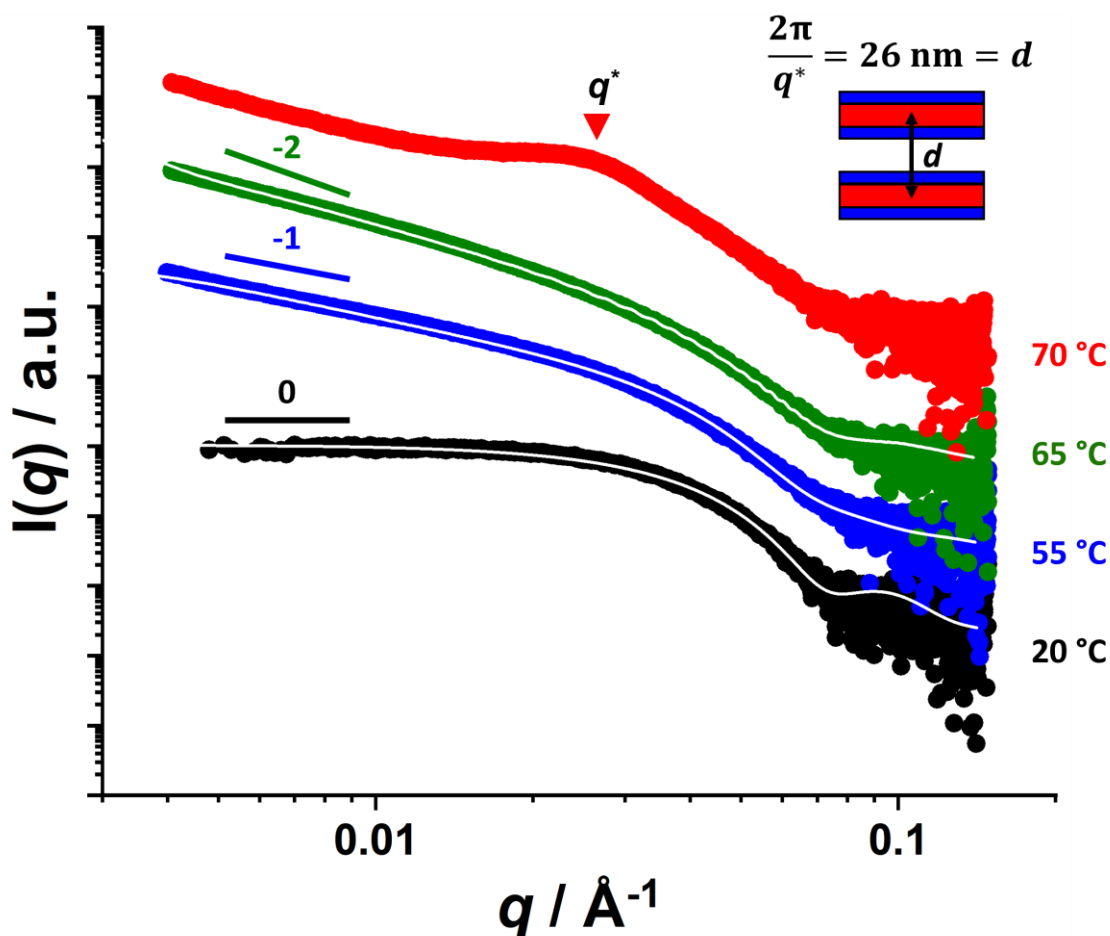


**Figure 5.10.** Representative double-logarithmic plots of SAXS patterns recorded for a 1.0 % w/w aqueous dispersion of thermoresponsive PEG<sub>45</sub>-PHBMA<sub>20</sub> nano-objects at 20 °C (black), 50 °C (blue), 65 °C (green) and 70 °C (red). The solid white line within each pattern indicates the data fits obtained using appropriate scattering models.<sup>101, 102</sup> The characteristic low  $q$  gradients expected for spheres, worms and vesicles (0,  $-1$  and  $-2$ , respectively) are included as a guide for the eye. The mean distance,  $d$ , between the stacked lamellae was calculated from the diffraction peak labelled  $q^*$  using the equation shown in the inset.<sup>45</sup>

The gradual increase in the DLS diameter at around 40 °C (see Figure 5.7) indicates that the formation of these PEG<sub>45</sub>-PHBMA<sub>20</sub> worms involves stochastic 1D fusion of multiple spheres, which has been observed for other PISA formulations.<sup>22, 62, 103</sup> In principle, a small reduction in cross-sectional radius is expected when a worm is formed from the fusion of multiple spheres.<sup>53</sup> This can be rationalised by the change in cross-sectional core radius associated with a sphere-to-cylinder (or worm) transition, while maintaining constant core volume (see Figure 5.11).<sup>53</sup> Under such circumstances, the worm core radius divided by the sphere core radius is equal to

$\sqrt{2/3}$  or  $\approx 0.82$ . There is good agreement for the worm/sphere radius ratio of  $\sim 0.83$  calculated for the PEG<sub>45</sub>-PHBMA<sub>20</sub> nano-objects. At 65 °C, SAXS analysis indicated that relatively small vesicles were formed with a volume-average diameter of 119 nm and a mean hydrophobic membrane thickness of 5.5 nm; the former value is consistent with the *z*-average diameter of 117 nm reported by DLS. The membrane thickness indicates significant interdigitation of the structure-directing hydrophobic chains,<sup>104</sup> which has been observed for thermoresponsive PHBA-based nano-objects.<sup>45, 57, 58</sup> Finally, a relatively broad diffraction peak ( $q^* = 0.024 \text{ \AA}^{-1}$ ) is visible at 75 °C, which suggests the presence of lamellar sheets.<sup>45</sup> This is consistent with TEM studies of the nano-objects that are formed at 75 °C (see Figure 5.6d). From the SAXS pattern, the mean inter-sheet stacking distance was estimated to be 26 nm from the position of the diffraction peak using the equation  $d = 2\pi/q^*$ .<sup>45</sup>

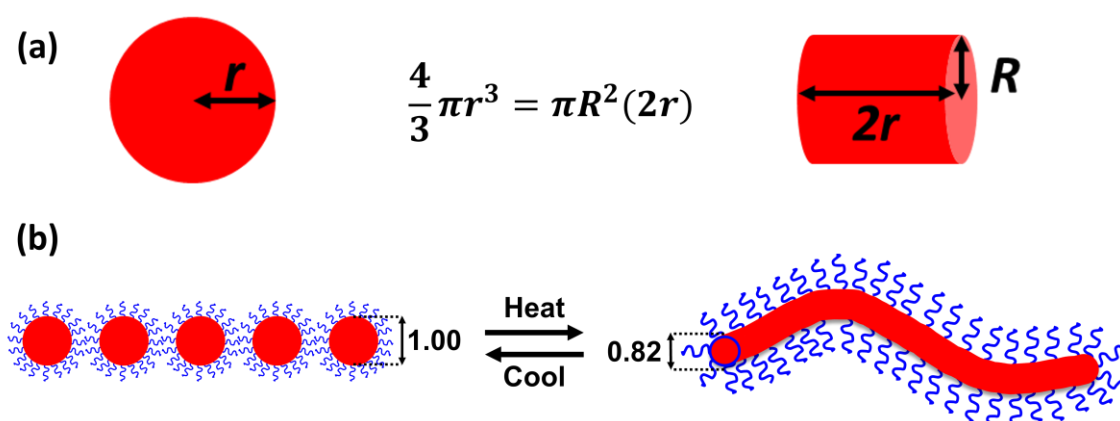


**Figure 5.11.** (a) Mean core-cross sectional radius for a sphere and cylinder of the same core volume. (b) Reduction in mean cross-sectional radius associated with a sphere-to-worm transition while maintaining a constant core volume.<sup>53</sup>

SAXS analysis indicated that the water volume fraction of associated with the core-forming PHBMA block  $x_{\text{sol}}$  remained constant at 0.001 on heating from 20 °C to 50 °C (see Table 5.1). However, on heating further to 65 °C,  $x_{\text{sol}}$  increased significantly to 0.18. This perhaps surprising given that PHBMA block is relatively hydrophobic. Subtle increases in the hydration of core-forming block have previously been shown to be responsible for a thermally-driven morphological transitions observed for block copolymer nano-objects prepared *via* RAFT

aqueous dispersion polymerisation.<sup>38, 45</sup> For example, Deane *et al.* calculated that  $x_{sol}$  associated with HBA repeat units within the PHBA core of PEG<sub>113</sub>-PHBA<sub>260</sub> nano-objects increased from 0.10 to 0.68 on heating on heating from 10 °C to 50 °C.<sup>58</sup> These  $x_{sol}$  values are consistent with those calculated for PEG<sub>45</sub>-PHBMA<sub>20</sub> nano-objects in this Chapter, since PHBA is significantly more hydrophilic than PHBMA.<sup>35</sup> Therefore, PHBMA is expected to have less tendency to become hydrated than PHBA. Nevertheless, the increase in hydration of the PHBMA core-forming block on heating seems to be sufficient to drive morphological transitions.

**Table 5.1.** Summary of the various structural parameters calculated from SAXS analysis of a 1.0% w/w aqueous dispersion of PEG<sub>45</sub>-PHBMA<sub>20</sub> nano-objects at 20, 50 or 65 °C.

Temperature / °C	Morphology	$D_s$ / nm <sup>a</sup>	$D_w$ / nm <sup>b</sup>	$D_v$ / nm <sup>c</sup>	$T_m$ / nm	$x_{sol}$
20	Spheres	13.8 ± 2.2	-	-	-	0.001
55	Worms	-	11.5 ± 2.0	-	-	0.001
65	Vesicles	-	-	119 ± 46	10.7 ± 0.6	0.18

<sup>a</sup>When fitted using a spherical micelle model, the sphere volume-average diameter,  $D_s$ , was calculated using  $D_s = 2R_s + 4R_g$ . <sup>b</sup>When fitted using a worm model, the worm cross-sectional volume-average diameter  $D_w$ , was calculated using  $D_w = 2R_s + 4R_g$ . <sup>c</sup>When fitted using a vesicle model, the vesicle volume-average diameter  $D_v$ , was calculated using  $D_v = 2R_m + T_m + 4R_g$ .  $R_s$  represents the mean sphere core volume-average radius;  $R_w$  is the mean worm micelle radius;  $R_m$  is the mean radius from the centre of the vesicle to the centre of the membrane;  $T_m$  is the mean vesicle membrane thickness;  $R_g$  represents the radius of gyration of the PEG<sub>45</sub> stabiliser block;  $x_{sol}$  is the volume fraction of water within the hydrophobic core/membrane.

Oscillatory rheological studies conducted on a 10% w/w aqueous dispersion of PEG<sub>45</sub>-PHBMA<sub>20</sub> nano-objects confirmed that a low-viscosity fluid was obtained between 20 °C and 50 °C. Further heating of this dispersion resulted in a soft, highly transparent, free-standing gel. More specifically, the storage modulus ( $G'$ ) exceeds the loss modulus ( $G''$ ) at around 52 °C and a maximum  $G'$  value of around 45 Pa is attained at 58 °C (see Figure 5.12). According to Lovett and co-workers, such macroscopic gelation is the result of multiple inter-worm contacts, which leads to the formation of a 3D percolating network.<sup>105</sup> It is perhaps noteworthy that this PEG<sub>45</sub>-PHBMA<sub>20</sub> worm gel is significantly weaker than the PEG<sub>113</sub>-PHBMA<sub>220</sub> worm gel reported by Warren *et al.*<sup>28</sup> ( $G' = 65$  Pa at 11°C). However, a comparison between the PEG<sub>45</sub>-PHBMA<sub>20</sub> worms reported herein and the previously reported PEG<sub>113</sub>-based worms is problematic given the different PEG stabiliser block lengths. This is in also part because the former worms are produced

on heating spheres to around 50 °C, whereas the latter worms are observed at lower temperatures. Furthermore, the PHBMA-based worms require a much shorter core-forming block to access a worm morphology because PHBMA is significantly more hydrophobic than either PHBA or PHBMA. Warming the PEG<sub>45</sub>-PHBMA<sub>20</sub> dispersion above 58 °C resulted in a significant reduction in viscosity, suggesting a worm-to-vesicle transition.<sup>45, 106</sup> Heating to 75 °C led to a second, smaller increase in viscosity, which is likely to correspond to the formation of lamellae.<sup>45</sup> These thermal transitions proved to be remarkably reversible, with relatively little hysteresis being observed at heating/cooling rates of 1 °C min<sup>-1</sup>.

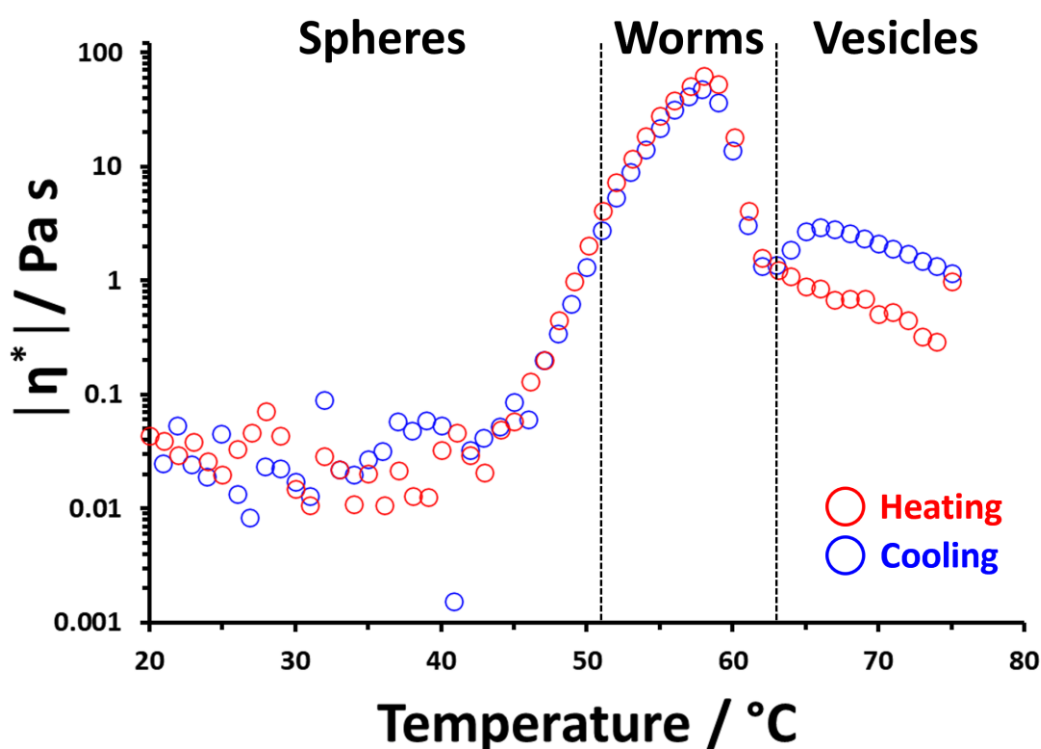


**Figure 5.12.** Complex viscosity  $|\eta^*|$  as a function of temperature for a 20 °C to 75 °C to 20 °C thermal cycle obtained for a 10% w/w aqueous dispersion of PEG<sub>45</sub>-PHBMA<sub>20</sub> nano-objects at an applied strain of 1.0% and an angular frequency of 1.0 rad s<sup>-1</sup>. The dispersion was equilibrated at 20 °C for 10 min prior to a thermal cycle conducted at 1 °C min<sup>-1</sup>. The black dashed lines indicate the sol-gel and gel-sol transitions that occur during this cycle.

Shear-induced polarised light imaging (SIPLI) studies were conducted from 20 °C to 75 °C to provide further evidence for the thermally-induced changes in copolymer morphology. According to Mykhayklyk and co-workers, this optorheological technique enables the alignment of anisotropic nano-objects such as block copolymer worms and lamellae to be visualised at a

certain critical rate of applied shear.<sup>94, 95, 107</sup> At 20 °C, only a dark image was observed for the 10% w/w aqueous dispersion of PEG<sub>45</sub>-PHBMA<sub>20</sub> nano-objects at an applied shear rate of 1.0 s<sup>-1</sup> (see Figure 5.13).

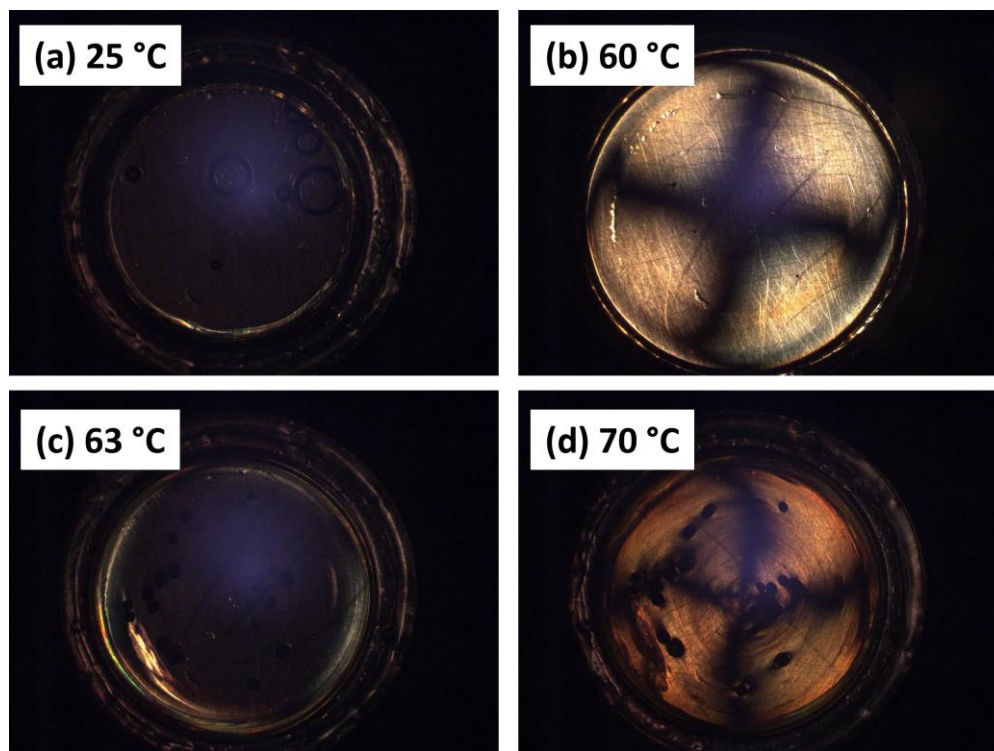


**Figure 5.13.** Shear-induced polarised light images (SIPLI) obtained for a 10% w/w aqueous dispersion of PEG<sub>45</sub>-PHBMA<sub>20</sub> nano-objects at an applied shear rate of 1.0 s<sup>-1</sup> during a temperature ramp experiment conducted at a heating rate of 1.0 °C min<sup>-1</sup>. The initial dark image recorded at 25 °C is consistent with the presence of isotropic spheres. In contrast, the highly anisotropic worms formed at 60 °C exhibit a characteristic Maltese cross owing to birefringence caused by their alignment in the direction of shear flow. This distinctive feature disappears at 63 °C, indicating the formation of isotropic vesicles. A second, weaker Maltese cross is observed at 70 °C, which is consistent with the presence of anisotropic lamellae (platelets).

This indicates the presence of non-birefringent isotropic spheres. At 60 °C, a Maltese cross is observed, which is characteristic of anisotropic worm-like nano-objects.<sup>62, 108</sup> This feature is the result of birefringence produced by *in situ* shear alignment of anisotropic nano-objects.<sup>45</sup> It disappears above 60 °C, which is consistent with a worm-to-vesicle transition, while a new, albeit weaker Maltese cross is observed at 70 °C. The latter feature indicates the presence of anisotropic lamellae that have either a perpendicular or transverse orientation, with the lamellar normal parallel to the neutral or velocity direction of the flow, respectively. However, the onset

temperature required to produce lamellae is lower than that indicated by the oscillatory rheology data shown in Figure 5.12. This is because the applied (continuous) shear is greater in SIPLI, which promotes the transition from vesicles to lamellae.<sup>45</sup>

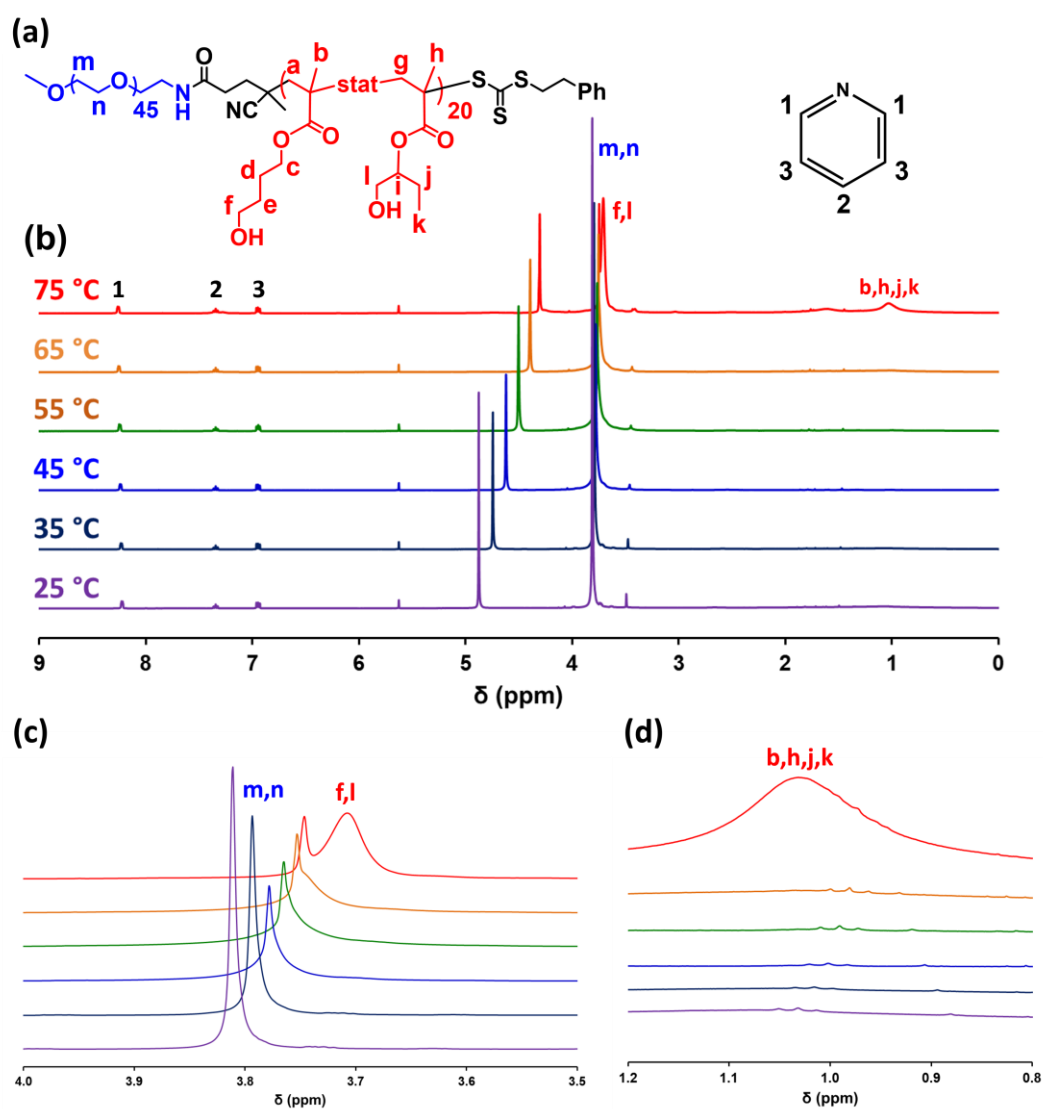


**Figure 5.14.** Variable temperature <sup>1</sup>H NMR studies of thermoresponsive PEG<sub>45</sub>-PHBMA<sub>20</sub> diblock copolymer nano-objects. (a) Chemical structure of the PEG<sub>45</sub>-PHBMA<sub>20</sub> diblock copolymer showing both the 2- and 4-isomers as HBMA repeat units and the pyridine external standard. (b) Normalised (relative to pyridine) <sup>1</sup>H NMR spectra recorded from 25 °C to 75 °C for a 10% w/w aqueous dispersion of PEG<sub>45</sub>-PHBMA<sub>20</sub> nano-objects prepared in D<sub>2</sub>O. (c) Overlaid partial spectra recorded between 25 °C (purple) and 75 °C (red) for the oxymethylene protons (m,n) assigned to the PEG<sub>45</sub> chains. This signal clearly becomes broader and weaker at higher temperatures, suggesting that the stabiliser block becomes less hydrated. (d) Overlaid partial spectra recorded between 25 °C (purple) and 75 °C (red). The signal at around 0.95-1.15 ppm assigned to the methacrylic backbone protons (b,h,j,k) of the PHBMA block becomes visible at higher temperatures, indicating partial solvation of the PHBMA block. In addition, a broad signal at around 3.70-3.75 ppm can be observed as a shoulder on the oxymethylene protons (m,n) assigned to the PEG<sub>45</sub> chains at or above 65 °C. This new signal is assigned to the HO-CH<sub>2</sub>-protons (f,l) of the HBMA repeat units.

Variable temperature  $^1\text{H}$  NMR spectroscopy studies were conducted to examine the molecular mechanism driving the thermoresponsive behaviour observed for PEG<sub>45</sub>-PHBMA<sub>20</sub> nano-objects. A subtle change in the degree of hydration of the core-forming block has been shown to be responsible for the ‘shape-shifting’ behaviour exhibited by various thermoresponsive block copolymers prepared by RAFT aqueous *dispersion* polymerisation.<sup>38, 44, 45</sup> For example, thermoresponsive PHPMA-based worms undergo a worm-to-sphere transition on cooling owing to the hydration of the HPMA repeat units close to the block junction.<sup>38, 44</sup> This ‘LCST-like’ behaviour has been described as *surface* plasticisation. In contrast, PHBA-based nano-objects exhibit ‘UCST-like’ behaviour: an increase in (partial) solvation of the hydrophobic block occurs on heating, which corresponds to *uniform* plasticisation.<sup>45</sup>

Variable temperature  $^1\text{H}$  NMR spectroscopy studies were conducted between 20 and 75 °C on a 10% w/w aqueous dispersion of PEG<sub>45</sub>-PHBMA<sub>20</sub> nano-objects prepared in D<sub>2</sub>O. The full  $^1\text{H}$  NMR spectra normalised relative to an external standard (pyridine) are shown overleaf in Figure 5.14, along with partial spectra highlighting regions of particular interest.  $^1\text{H}$  NMR signals assigned to the PEG<sub>45</sub> stabiliser chains become broader and less prominent at higher temperature, indicating a progressively lower degree of hydration for this water-soluble block. In contrast,  $^1\text{H}$  NMR signals assigned to the oxymethylene and methacrylic backbone signals of the structure-directing PHBMA chains at around 3.7 ppm and 1.0 ppm respectively become progressively more intense on heating (see Figures 5.14c and d). This indicates that this weakly hydrophobic block becomes more hydrated, particularly at higher temperatures. Interestingly, these observations are not inconsistent with the SAXS studies, which indicate a significant increase in the solvent volume fraction,  $x_{\text{sol}}$ , associated with the PHBMA chains between 55 °C and 65 °C (see Table 5.1). However, it is rather surprising that such spectral changes only become apparent above 65 °C, whereas the sphere-to-worm and worm-to-vesicle transitions occur at significantly lower temperatures. Unfortunately, such spectral changes cannot be easily quantified owing to overlap between the PEG and PHBMA signals at 3.7-3.8 ppm. Nevertheless, these  $^1\text{H}$  NMR studies provide direct evidence for significant changes in the degree of hydration of the PEG<sub>45</sub>-PHBMA<sub>20</sub>

chains on heating. One plausible interpretation of the  $^1\text{H}$  NMR spectra shown in Figure 5.14 is that the sphere-to-worm and worm-to-vesicle transitions are mainly driven by (partial) dehydration of the PEG stabiliser block, whereas the vesicle-to-lamellae transition is driven by a greater degree of (partial) hydration of the PHBMA block. This hypothesis is explored below in the context of the packing parameter originally introduced by Israelachvili and co-workers to account for the micellisation of small-molecule surfactants<sup>55</sup> and latterly applied to the self-assembly of amphiphilic diblock copolymers.<sup>56</sup>

It is well-known that aqueous solutions of PEG exhibit LCST-type behaviour.<sup>109-113</sup> In principle, partial dehydration of the PEG stabiliser chains at higher temperatures should lead to an increase in the packing parameter  $P$  (see Figure 5.15 and Equation 5.1), which would account for the observed sphere-to-worm and worm-to-vesicle transitions. However, variable temperature SAXS and  $^1\text{H}$  NMR studies both confirm that there is also a subtle change in the (partial) degree of hydration of the structure-directing PHBMA block between 65 °C and 75 °C. The packing parameter  $P$  is given by the following equation:

$$P = \frac{V}{a_0 l_c} \quad 5.1$$

For the PEG<sub>45</sub>-PHBMA<sub>20</sub> diblock copolymer,  $V$  is the volume occupied by the hydrophobic PHBMA block,  $a_0$  is the optimal area occupied by the head-group (in this case, the PEG stabiliser), and  $l_c$  is the length of the PHBMA block (see Figure 1.8). Since spheres are formed when  $P < 1/3$  and worms are favoured when  $1/3 < P < 1/2$ , an increase in  $P$  must occur to account for the observed sphere-to-worm and worm-to-vesicle transitions. Thus either  $V$  must increase and/or  $a_0$  must decrease. If *surface* plasticisation of the PHBMA block occurred at 75 °C, the HBMA residues near the block junction would become hydrated and  $V$  would decrease, which would lead to a concomitant reduction in  $P$ . However, this is not consistent with the experimental observations. In contrast, *uniform* plasticisation of the PHBMA block increases  $V$  and hence leads to the desired increase in  $P$ . Hence *uniform* plasticisation most likely accounts for the vesicle-to-lamellae transition exhibited by the PEG<sub>45</sub>-PHBMA<sub>20</sub> diblock copolymer. Similar ‘UCST-like’ behaviour

has been reported for PHBA-based diblock copolymers.<sup>45, 57, 58</sup> It is perhaps also worth noting that further dehydration of the PEG stabiliser chains would also lead to an increase in the relative volume fraction of the hydrophobic PHBMA block.

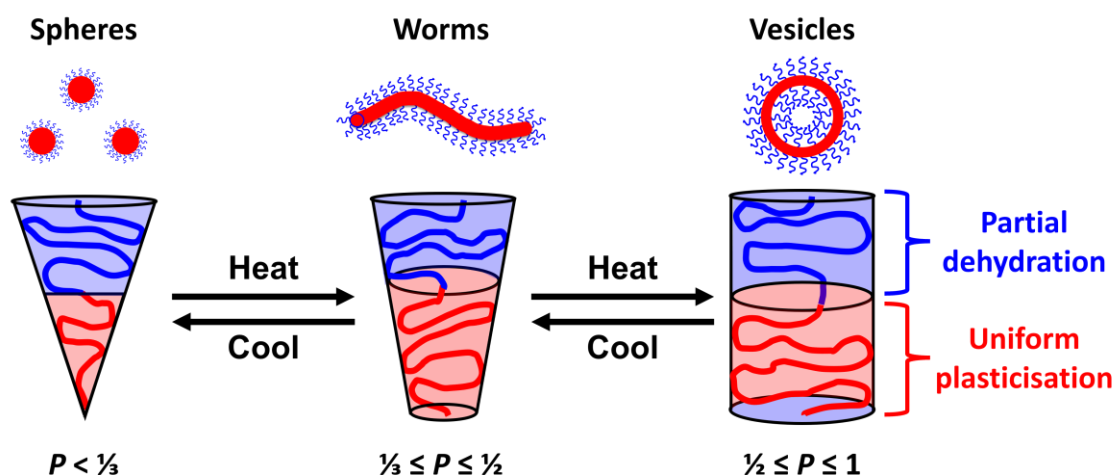


**Figure 5.15.** Schematic representation of the partial hydration of the PEG<sub>45</sub>-TTC stabiliser block and the uniform plasticisation of the core-forming PHBMA block (depicted in red) that occurs on heating an aqueous dispersion of PEG<sub>45</sub>-PHBMA<sub>20</sub> spheres resulting in both sphere-to-worm and worm-to-vesicle transitions.

## 5.4 Conclusions

Amphiphilic PEG<sub>45</sub>-PHBMA<sub>20</sub> diblock copolymer nano-objects have been prepared by chain-extending a water-soluble PEG<sub>45</sub>-TTC precursor *via* RAFT aqueous emulsion polymerisation of HBMA at 50 °C. A high monomer conversion was achieved within 1 h and efficient extension of the PEG<sub>45</sub>-TTC precursor with HBMA was confirmed by THF GPC analysis. Heating a transparent free-flowing 10% w/w dispersion of PEG<sub>45</sub>-PHBMA<sub>20</sub> nano-objects up to 50 °C resulted in a sol-gel transition, which indicates the formation of a worm phase. At 65 °C, this dispersion became opaque and free-flowing, which suggests a worm-to-vesicle transition. Oscillatory rheology studies of these PEG<sub>45</sub>-PHBMA<sub>20</sub> nano-objects as a function of temperature indicated a critical gelation temperature (CGT) of approximately 52 °C and the complex viscosity  $|\eta^*|$  attained its maximum value at 58 °C. Furthermore, these shape-shifting nano-objects exhibit excellent thermoreversibility. As expected, SIPLI studies confirmed the presence of isotropic nano-objects at ambient temperature, the formation of

highly anisotropic nano-objects at around 58 °C and the re-emergence of isotropic nano-objects on further heating. Moreover, SIPLI studies indicated that anisotropic character is regained at 75 °C, which suggests a lamellar phase at this temperature.

TEM studies of a 0.1% w/w aqueous dispersion of PEG<sub>45</sub>-PHBMA<sub>20</sub> nano-objects indicated the presence of spheres, worms, vesicles and lamellae at 25, 55, 65 and 75 °C, respectively. Variable temperature DLS studies confirmed that these morphological transitions are thermoreversible at copolymer concentrations as low as 0.1% w/w. SAXS analysis indicated a significant increase in the degree of hydration of the PHBMA core-forming block above 65 °C. This was confirmed using variable temperature <sup>1</sup>H NMR spectroscopy. Consideration of the packing parameter suggests that the vesicle-to-lamellae transition is driven by an increase in the degree of hydration of the hydrophobic PHBMA block according to a uniform plasticisation mechanism, which is similar to the thermoresponsive behaviour reported for PHBA-based nano-objects.<sup>45, 57, 58</sup> In contrast, <sup>1</sup>H NMR observations suggest that the sphere-to-worm and worm-to-vesicle transitions appear to be driven by dehydration of the PEG stabiliser chains, rather than any discernible changes associated with the hydrophobic PHBMA chains.

This is the first example of any thermoresponsive diblock copolymer nano-objects prepared *via* RAFT aqueous emulsion polymerisation. Moreover, this particular PEG<sub>45</sub>-PHBMA<sub>20</sub> diblock copolymer exhibits three thermoreversible transitions in aqueous solution. No doubt such behaviour is related to the relatively short DP targeted for the hydrophobic PHBMA block. Furthermore, the aqueous solubility of HBMA is relatively high at 25 g dm<sup>-3</sup>, which suggests that the PHBMA block cannot be strongly hydrophobic. Clearly, further studies are warranted to examine whether comparable thermoresponsive behaviour can be achieved when targeting higher DPs for the PEG stabiliser and PHBMA blocks, respectively. However, it seems highly unlikely that such thermoresponsive behaviour could ever be observed for more hydrophobic water-immiscible monomers such as styrene or *n*BA.

## 5.5 References

1. A. Blanazs, S. P. Armes and A. J. Ryan, *Macromolecular rapid communications*, 2009, **30**, 267-277.
2. B. Charleux, G. Delaittre, J. Rieger and F. D'Agosto, *Macromolecules*, 2012, **45**, 6753-6765.
3. N. J. Warren and S. P. Armes, *Journal of the American Chemical Society*, 2014, **136**, 10174-10185.
4. P. B. Zetterlund, S. C. Thickett, S. Perrier, E. Bourgeat-Lami and M. Lansalot, *Chem. Rev.*, 2015, **115**, 9745-9800.
5. J. Rieger, *Macromolecular Rapid Communications*, 2015, **36**, 1458-1471.
6. A. B. Lowe, *Polymer*, 2016, **106**, 161-181.
7. M. J. Derry, L. A. Fielding and S. P. Armes, *Progress in Polymer Science*, 2016, **52**, 1-18.
8. S. L. Canning, G. N. Smith and S. P. Armes, *Macromolecules*, 2016, **49**, 1985-2001.
9. J. Yeow and C. Boyer, *Advanced Science*, 2017, **4**, 1700137.
10. N. J. W. Penfold, J. Yeow, C. Boyer and S. P. Armes, *ACS Macro Letters*, 2019, **8**, 1029-1054.
11. S. Y. Khor, J. F. Quinn, M. R. Whittaker, N. P. Truong and T. P. Davis, *Macromolecular Rapid Communications*, 2019, **40**, 1800438.
12. W. J. Zhang, C. Y. Hong and C. Y. Pan, *Macromolecular Rapid Communications*, 2019, **40**.
13. D. Le, D. Keller and G. Delaittre, *Macromolecular Rapid Communications*, 2019, **40**.
14. F. D'Agosto, J. Rieger and M. Lansalot, *Angewandte Chemie International Edition*, 2020, **59**, 8368-8392.
15. C. Liu, C. Y. Hong and C. Y. Pan, *Polymer Chemistry*, 2020, **11**, 3673-3689.
16. Z. An, W. Tang, C. J. Hawker and G. D. Stucky, *Journal of the American Chemical Society*, 2006, **128**, 15054-15055.
17. Z. An, Q. Shi, W. Tang, C.-K. Tsung, C. J. Hawker and G. D. Stucky, *J. Am. Chem. Soc.*, 2007, **129**, 14493-14499.
18. W.-M. Wan, C.-Y. Hong and C.-Y. Pan, *Chemical Communications*, 2009, 5883-5885.
19. W.-M. Wan, X.-L. Sun and C.-Y. Pan, *Macromol. Rapid Commun.*, 2010, **31**, 399-404.
20. S. Boissé, J. Rieger, K. Belal, A. Di-Cicco, P. Beaunier, M.-H. Li and B. Charleux, *Chemical Communications*, 2010, **46**, 1950-1952.
21. S. Sugihara, S. P. Armes, A. Blanazs and A. L. Lewis, *Soft Matter*, 2011, **7**, 10787-10793.
22. A. Blanazs, J. Madsen, G. Battaglia, A. J. Ryan and S. P. Armes, *Journal of the American Chemical Society*, 2011, **133**, 16581-16587.
23. C.-Q. Huang and C.-Y. Pan, *Polymer*, 2010, **51**, 5115-5121.
24. L. Houillot, C. Bui, M. Save, B. Charleux, C. Farcet, C. Moire, J.-A. Raust and I. Rodriguez, *Macromolecules*, 2007, **40**, 6500-6509.
25. L. A. Fielding, M. J. Derry, V. Ladmiral, J. Rosselgong, A. M. Rodrigues, L. P. D. Ratcliffe, S. Sugihara and S. P. Armes, *Chemical Science*, 2013, **4**, 2081-2087.

26. M. J. Rymaruk, S. J. Hunter, C. T. O'Brien, S. L. Brown, C. N. Williams and S. P. Armes, *Macromolecules*, 2019, **52**, 2822-2832.
27. A. Blanazs, A. J. Ryan and S. P. Armes, *Macromolecules*, 2012, **45**, 5099-5107.
28. N. J. Warren, O. O. Mykhaylyk, D. Mahmood, A. J. Ryan and S. P. Armes, *Journal of the American Chemical Society*, 2014, **136**, 1023-1033.
29. G. Liu, Q. Qiu, W. Shen and Z. An, *Macromolecules*, 2011, **44**, 5237-5245.
30. W. Shen, Y. Chang, G. Liu, H. Wang, A. Cao and Z. An, *Macromolecules*, 2011, **44**, 2524-2530.
31. G. Liu, Q. Qiu and Z. An, *Polymer Chemistry*, 2012, **3**, 504-513.
32. J. Tan, H. Sun, M. Yu, B. S. Sumerlin and L. Zhang, *ACS Macro Letters*, 2015, **4**, 1249-1253.
33. J. Tan, Y. Bai, X. Zhang, C. Huang, D. Liu and L. Zhang, *Macromolecular Rapid Communications*, 2016, **37**, 1434-1440.
34. J. Tan, X. Zhang, D. Liu, Y. Bai, C. Huang, X. Li and L. Zhang, *Macromolecular Rapid Communications*, 2017, **38**, 1600508.
35. J. C. Foster, S. Varlas, B. Couturaud, J. R. Jones, R. Keogh, R. T. Mathers and R. K. O'Reilly, *Angewandte Chemie International Edition*, 2018, **57**, 15733-15737.
36. P. A. Lovell and F. J. Schork, *Biomacromolecules*, 2020, **21**, 4396-4441.
37. J. Zhou, H. Yao and J. Ma, *Polymer Chemistry*, 2018, **9**, 2532-2561.
38. A. Blanazs, R. Verber, O. O. Mykhaylyk, A. J. Ryan, J. Z. Heath, C. W. I. Douglas and S. P. Armes, *Journal of the American Chemical Society*, 2012, **134**, 9741-9748.
39. A. B. Lowe and C. L. McCormick, *Progress in Polymer Science*, 2007, **32**, 283-351.
40. J. Rieger, C. Grazon, B. Charleux, D. Alaimo and C. Jérôme, *Journal of Polymer Science Part A: Polymer Chemistry*, 2009, **47**, 2373-2390.
41. C. A. Figg, A. Simula, K. A. Gebre, B. S. Tucker, D. M. Haddleton and B. S. Sumerlin, *Chemical Science*, 2015, **6**, 1230-1236.
42. X. Wang, J. Zhou, X. Lv, B. Zhang and Z. An, *Macromolecules*, 2017, **50**, 7222-7232.
43. Y. Ma, P. Gao, Y. Ding, L. Huang, L. Wang, X. Lu and Y. Cai, *Macromolecules*, 2019, **52**, 1033-1041.
44. L. P. D. Ratcliffe, M. J. Derry, A. Ianiro, R. Tuinier and S. P. Armes, *Angew. Chem. Int. Ed.*, 2019, **58**, 18964-18970.
45. S. J. Byard, C. T. O'Brien, M. J. Derry, M. Williams, O. O. Mykhaylyk, A. Blanazs and S. P. Armes, *Chemical Science*, 2020, **11**, 396-402.
46. J. Chiefari, Y. K. Chong, F. Ercole, J. Krstina, J. Jeffery, T. P. T. Le, R. T. A. Mayadunne, G. F. Meijs, C. L. Moad, G. Moad, E. Rizzardo and S. H. Thang, *Macromolecules*, 1998, **31**, 5559-5562.
47. G. Moad, E. Rizzardo and S. H. Thang, *Australian Journal of Chemistry*, 2006, **59**, 669-692.
48. G. Moad, E. Rizzardo and S. H. Thang, *Australian Journal of Chemistry*, 2009, **62**, 1402-1472.
49. G. Moad, E. Rizzardo and S. H. Thang, *Aust. J. Chem.*, 2012, **65**, 985-1076.

50. R. R. Gibson, S. P. Armes, O. M. Musa and A. Fernyhough, *Polymer Chemistry*, 2019, **10**, 1312-1323.
51. D. Zhou, S. Dong, R. P. Kuchel, S. Perrier and P. B. Zetterlund, *Polymer Chemistry*, 2017, **8**, 3082-3089.
52. S. M. North and S. P. Armes, *Polymer Chemistry*, 2020, **11**, 2147-2156.
53. D. L. Beattie, O. O. Mykhaylyk, A. J. Ryan and S. P. Armes, *Soft Matter*, 2021, **17**, 5602-5612.
54. L. P. D. Ratcliffe, A. Blanazs, C. N. Williams, S. L. Brown and S. P. Armes, *Polymer Chemistry*, 2014, **5**, 3643-3655.
55. J. N. Israelachvili, D. J. Mitchell and B. W. Ninham, *J. Chem. Soc., Trans.*, 1976, **72**, 1525-1568.
56. M. Antonietti and S. Förster, *Advanced Materials*, 2003, **15**, 1323-1333.
57. O. J. Deane, J. Jennings, T. J. Neal, O. M. Musa, A. Fernyhough and S. P. Armes, *Chemistry of Materials*, 2021, **33**, 7767-7779.
58. O. J. Deane, J. Jennings and S. P. Armes, *Chemical Science*, 2021, **12**, 13719-13729.
59. S. J. Wilson, PhD Thesis, University of Sheffield, 2019.
60. L. Romero-Azogil, N. J. W. Penfold and S. P. Armes, *Polymer Chemistry*, 2020, **11**, 5040-5050.
61. N. J. W. Penfold, J. R. Whatley and S. P. Armes, *Macromolecules*, 2019, **52**, 1653-1662.
62. N. J. Warren, M. J. Derry, O. O. Mykhaylyk, J. R. Lovett, L. P. D. Ratcliffe, V. Ladmiraal, A. Blanazs, L. A. Fielding and S. P. Armes, *Macromolecules*, 2018, **51**, 8357-8371.
63. V. J. Cunningham, L. P. D. Ratcliffe, A. Blanazs, N. J. Warren, A. J. Smith, O. O. Mykhaylyk and S. P. Armes, *Polymer Chemistry*, 2014, **5**, 6307-6317.
64. R. Verber, A. Blanazs and S. P. Armes, *Soft Matter*, 2012, **8**, 9915-9922.
65. W. Zhang, F. D'Agosto, O. Boyron, J. Rieger and B. Charleux, *Macromolecules*, 2011, **44**, 7584-7593.
66. S. Boissé, J. Rieger, G. Pembouong, P. Beaunier and B. Charleux, *Journal of Polymer Science Part A: Polymer Chemistry*, 2011, **49**, 3346-3354.
67. W. Zhang, F. D'Agosto, O. Boyron, J. Rieger and B. Charleux, *Macromolecules*, 2012, **45**, 4075-4084.
68. C. K. Poon, O. Tang, X.-M. Chen, B. T. T. Pham, G. Gody, C. A. Pollock, B. S. Hawkett and S. Perrier, *Biomacromolecules*, 2016, **17**, 965-973.
69. J. Lesage de la Haye, X. Zhang, I. Chaduc, F. Brunel, M. Lansalot and F. D'Agosto, *Angewandte Chemie International Edition*, 2016, **55**, 3739-3743.
70. O. J. Deane, O. M. Musa, A. Fernyhough and S. P. Armes, *Macromolecules*, 2020, **53**, 1422-1434.
71. N. P. Truong, M. V. Dussert, M. R. Whittaker, J. F. Quinn and T. P. Davis, *Polym. Chem.*, 2015, **6**, 3865-3874.
72. J. Rieger, G. Osterwinter, C. Bui, F. Stoffelbach and B. Charleux, *Macromolecules*, 2009, **42**, 5518-5525.
73. W. Zhang, F. D'Agosto, P.-Y. Dugas, J. Rieger and B. Charleux, *Polymer*, 2013, **54**, 2011-2019.

74. D. H. Chan, A. Millet, C. R. Fisher, M. C. Price, M. J. Burchell and S. P. Armes, *ACS Applied Materials & Interfaces*, 2021, **13**, 3175-3185.
75. V. J. Cunningham, A. M. Alswieleh, K. L. Thompson, M. Williams, G. J. Leggett, S. P. Armes and O. M. Musa, *Macromolecules*, 2014, **47**, 5613-5623.
76. A. A. Cockram, R. D. Bradley, S. A. Lynch, P. C. D. Fleming, N. S. J. Williams, M. W. Murray, S. N. Emmett and S. P. Armes, *Reaction Chemistry & Engineering*, 2018, **3**, 645-657.
77. M. Chenal, L. Bouteiller and J. Rieger, *Polymer Chemistry*, 2013, **4**, 752-762.
78. S. L. Canning, V. J. Cunningham, L. P. D. Ratcliffe and S. P. Armes, *Polymer Chemistry*, 2017, **8**, 4811-4821.
79. J. Bernard, M. Save, B. Arathoon and B. Charleux, *Journal of Polymer Science Part A: Polymer Chemistry*, 2008, **46**, 2845-2857.
80. S. Binauld, L. Delafresnaye, B. Charleux, F. D'Agosto and M. Lansalot, *Macromolecules*, 2014, **47**, 3461-3472.
81. L. Etchenausia, A. Khoukh, E. Deniau Lejeune and M. Save, *Polymer Chemistry*, 2017, **8**, 2244-2256.
82. P. Galanopoulo, P.-Y. Dugas, M. Lansalot and F. D'Agosto, *Polymer Chemistry*, 2020, **11**, 3922-3930.
83. B. Akpınar, L. A. Fielding, V. J. Cunningham, Y. Ning, O. O. Mykhaylyk, P. W. Fowler and S. P. Armes, *Macromolecules*, 2016, **49**, 5160-5171.
84. M. J. Rymaruk, K. L. Thompson, M. J. Derry, N. J. Warren, L. P. D. Ratcliffe, C. N. Williams, S. L. Brown and S. P. Armes, *Nanoscale*, 2016, **8**, 14497-14506.
85. K. L. Thompson, N. Cinotti, E. R. Jones, C. J. Mable, P. W. Fowler and S. P. Armes, *Langmuir*, 2017, **33**, 12616-12623.
86. D. H. H. Chan, E. L. Kynaston, C. Lindsay, P. Taylor and S. P. Armes, *ACS Applied Materials & Interfaces*, 2021, **13**, 30235-30243.
87. B. T. T. Pham, D. Nguyen, V. T. Huynh, E. H. Pan, B. Shirodkar-Robinson, M. Carey, A. K. Serelis, G. G. Warr, T. Davey, C. H. Such and B. S. Hawkett, *Langmuir*, 2018, **34**, 4255-4263.
88. D. Nguyen, V. Huynh, N. Pham, B. Pham, A. Serelis, T. Davey, C. Such and B. Hawkett, *Macromolecular Rapid Communications*, 2019, **40**, 1800402.
89. F. L. Hatton, J. R. Lovett and S. P. Armes, *Polymer Chemistry*, 2017, **8**, 4856-4868.
90. F. L. Hatton, A. M. Park, Y. Zhang, G. D. Fuchs, C. K. Ober and S. P. Armes, *Polymer Chemistry*, 2019, **10**, 194-200.
91. F. L. Hatton, M. J. Derry and S. P. Armes, *Polym. Chem.*, 2020, **11**, 6343-6355.
92. E. E. Brotherton, F. L. Hatton, A. A. Cockram, M. J. Derry, A. Czajka, E. J. Cornel, P. D. Topham, O. O. Mykhaylyk and S. P. Armes, *Journal of the American Chemical Society*, 2019, **141**, 13664-13675.
93. A. A. Cockram, T. J. Neal, M. J. Derry, O. O. Mykhaylyk, N. S. J. Williams, M. W. Murray, S. N. Emmett and S. P. Armes, *Macromolecules*, 2017, **50**, 796-802.
94. O. O. Mykhaylyk, *Soft Matter*, 2010, **6**, 4430-4440.
95. O. O. Mykhaylyk, N. J. Warren, A. J. Parnell, G. Pfeifer and J. Laeuger, *Journal of Polymer Science Part B: Polymer Physics*, 2016, **54**, 2151-2170.

96. J. Ilavsky and P. R. Jemian, *J. Appl. Crystallogr.*, 2009, **42**, 347-353.
97. I. Bannister, N. C. Billingham, S. P. Armes, S. P. Rannard and P. Findlay, *Macromolecules*, 2006, **39**, 7483-7492.
98. Y. Pei, A. B. Lowe and P. J. Roth, *Macromolecular Rapid Communications*, 2017, **38**.
99. A. Czajka and S. P. Armes, *Chem. Sci.*, 2020, **11**, 11443-11454.
100. O. Glatter and O. Kratky, *Small-angle X-ray Scattering*, Academic Press, London, 1982.
101. J. S. Pedersen and M. C. Gerstenberg, *Macromolecules*, 1996, **29**, 1363-1365.
102. J. Pedersen, *J. Appl. Crystallogr.*, 2000, **33**, 637-640.
103. L. A. Fielding, J. A. Lane, M. J. Derry, O. O. Mykhaylyk and S. P. Armes, *Journal of the American Chemical Society*, 2014, **136**, 5790-5798.
104. G. Battaglia and A. J. Ryan, *Journal of the American Chemical Society*, 2005, **127**, 8757-8764.
105. J. R. Lovett, M. J. Derry, P. Yang, F. L. Hatton, N. J. Warren, Patrick W. Fowler and S. P. Armes, *Chemical Science*, 2018, **9**, 7138-7144.
106. C. György, S. J. Hunter, C. Girou, M. J. Derry and S. P. Armes, *Polym. Chem.*, 2020, **11**, 4579-4590.
107. O. O. Mykhaylyk, A. J. Parnell, A. Pryke and J. P. A. Fairclough, *Macromolecules*, 2012, **45**, 5260-5272.
108. M. J. Rymaruk, C. T. O'Brien, S. L. Brown, C. N. Williams and S. P. Armes, *Macromolecules*, 2019, **52**, 6849-6860.
109. G. Malcolm and J. Rowlinson, *Transactions of the Faraday Society*, 1957, **53**, 921-931.
110. W. F. Polik and W. Burchard, *Macromolecules*, 1983, **16**, 978-982.
111. F. E. Bailey and R. Callard, *J. Appl. Polym. Sci.*, 1959, **1**, 56-62.
112. E. E. Dormidontova, *Macromolecules*, 2002, **35**, 987-1001.
113. T. Shikata, M. Okuzono and N. Sugimoto, *Macromolecules*, 2013, **46**, 1956-1961.

# Chapter 6:

# Conclusions and Outlook

### 6.1 Conclusions and Outlook

Nanoemulsions is a mature area of research that is of considerable and broad interest.<sup>1,2</sup> Perhaps the most appealing application is their potential use as nanocarriers for hydrophobic drugs and other therapeutics.<sup>3</sup> Furthermore, their high surface area means that they exhibit superior activity when used in cosmetic,<sup>4</sup> food,<sup>5</sup> and agrochemical<sup>6</sup> formulations. However, such nanoemulsions must exhibit good long-term stability. One strategy to improve the stability of nanoemulsions is to employ particulate emulsifiers. However, such particles must be sufficiently small to coat droplets with mean diameters of less than 200 nm. Given this constraint, there are relatively few reports of Pickering nanoemulsions and the various parameters that can affect their long-term stability.<sup>7-9</sup> The revival of academic interest in Pickering emulsions over the past twenty years or so has led to significant advances in this field.<sup>10</sup> Such particle-stabilised emulsions are attractive because they possess several advantages over surfactant-stabilised emulsions.<sup>11</sup> These include, but are not limited to, lower toxicity, enhanced long-term stability and reduced foaming during preparation. The underlying mechanism of Pickering stabilisation is well-understood and has been applied to many different types of inorganic and organic particles.<sup>11</sup> Block copolymer nanoparticles are an example of such an emulsifier that offers the possibility of fine-tuning, especially with regard to particle size<sup>12</sup> and wettability.<sup>13</sup> Moreover, the efficient synthesis of a wide range of hydrophilic and hydrophobic block copolymer nanoparticles *via* PISA over the past decade has undoubtedly provided new opportunities within the field of Pickering nanoemulsions.

Prior to this Thesis, Thompson *et al.*<sup>14</sup> published the first example of a Pickering nanoemulsion stabilised by block copolymer nanoparticles. This study was originally inspired by silica-stabilised nanoemulsions reported by Persson and co-workers.<sup>9</sup> To prepare nanoparticles small enough to stabilise nanoemulsions, a relatively low DP of 50 was targeted for the core-forming block.<sup>14</sup> In order to ensure that the spherical nanoparticles survived high-pressure microfluidisation, a relatively hydrophobic PTFEMA core was selected.<sup>15</sup> Block copolymer nanoparticles that meet these criteria could be conveniently prepared by RAFT

aqueous emulsion polymerisation.<sup>15</sup> The first half of this Thesis focused on examining the various parameters that affect the stability of either o/w or w/o Pickering nanoemulsions prepared using block nanoparticles.

Chapter 2 examined how the introduction of charged end-groups on the steric stabiliser chains of block copolymer nanoparticles affected the formation and long-term stability of Pickering nanoemulsions. Thus three PGMA<sub>48</sub> precursors were prepared using non-ionic CPDB, carboxylic acid-functional PETTC or morpholine-functional MPETTC in turn as the RAFT agent to confer neutral, anionic or cationic end-groups, respectively. Pickering nanoemulsions were then prepared at an aqueous solution of either pH 3 or pH 7. These solution conditions were selected to provide nanoparticles with highly cationic (protonated morpholine end-groups) or highly anionic (ionised carboxylic acid end-groups) surface character, respectively. In principle, intermediate solution pH values could be explored in the future to investigate the effect of systematically varying the degree of surface charge on the formation and long-term stability of Pickering nanoemulsions. In this Thesis, it is shown that the presence of charged end-groups significantly reduces the nanoparticle adsorption efficiency. This was attributed to electrostatic repulsions between neighbouring copolymer nanoparticles, which suppresses their interfacial adsorption and reduces their packing efficiency at the oil/water interface. The latter was confirmed by using a two-population model to analyse SAXS patterns recorded for the Pickering nanoemulsions.<sup>16</sup> The mean apparent thickness of the shell of adsorbed nanoparticles calculated for Pickering nanoemulsions was significantly lower for those prepared using nanoparticles with charged end-groups. This indicates lower surface coverage of the oil droplets when employing such nanoparticles. Nanoemulsions prepared using nanoparticles with charged end-groups exhibited inferior long-term stability compared to those prepared with nanoparticles possessing neutral end-groups. Literature precedent indicates that *surfactant* micelles can mediate the transport of oil between droplets through the aqueous phase.<sup>17, 18</sup> Preparing Pickering nanoemulsions using nanoparticles with charged end-groups leads to an excess of non-adsorbed *block copolymer* micelles in the aqueous phase. Such excess micelles most likely

facilitate oil diffusion through the continuous aqueous phase. In principle, this explains the enhanced rate of Ostwald ripening observed for nanoemulsions stabilised by nanoparticles bearing charged end-groups. This hypothesis could be explored by addition of varying amounts of nanoparticles to the aqueous phase of Pickering nanoemulsions. Measuring the evolution in the droplet diameter over time should enable assessment as to whether the presence of excess nanoparticles adversely affects the long-term stability of nanoemulsions.

In Chapter 3, w/o nanoemulsions stabilised by block copolymer nanoparticles were prepared for the first time. In this case, the RAFT dispersion polymerisation of TFEMA was utilised to prepare hydrophobic sterically-stabilised nanoparticles in *n*-dodecane. The addition of salt to the aqueous phase prior to emulsification was required to ensure the formation of aqueous droplets with a mean diameter of less than 200 nm. Various studies reported in the literature have similarly shown that the addition of salt is essential for preparing surfactant-stabilised nanoemulsions.<sup>19</sup> For the Pickering nanoemulsions reported in this Thesis, Ostwald ripening was inhibited if sufficient added salt was present within the aqueous droplets. In the absence of any added salt, DLS studies indicated that the initial emulsion droplets became unstable within a few hours of their preparation. Such instability may also prevent the formation of droplets of less than 200 nm diameter when employing NaCl concentrations below 0.11 M. To confirm this hypothesis, the effect of varying the salt concentration on the mean droplet diameter of squalane-in-water Pickering nanoemulsions could be examined. Squalane has a significantly lower aqueous solubility than *n*-dodecane so such nanoemulsions should exhibit a much lower rate of Ostwald ripening. Thus increasing the salt concentration should have much less influence on the aqueous droplet diameter when squalane is used for the continuous phase.

The greater understanding gained from the preparation of such w/o Pickering nanoemulsions could be applied to design *non-aqueous* nanoemulsions. Rymaruk *et al.* recently demonstrated that block copolymer nanoparticles can be used to stabilise oil-in-oil (o/o) Pickering macroemulsions.<sup>13</sup> More specifically, poly(3-[tris(trimethylsiloxy)silyl]propyl methacrylate)-poly(benzyl methacrylate) block copolymer nanoparticles were prepared in a

low-viscosity silicone oil *via* RAFT dispersion polymerisation of benzyl methacrylate. These nanoparticles were then homogenised with various immiscible natural oils to generate o/o emulsions. In principle, it should be possible to prepare non-aqueous o/o Pickering nanoemulsions by subjecting such macroemulsions to microfluidisation.

The second half of this Thesis focuses on preparing block copolymer nano-objects with spherical, worm-like or vesicular morphologies by RAFT aqueous emulsion polymerisation of HBMA. Chapter 4 explored the RAFT aqueous emulsion polymerisation of HBMA using a non-ionic PGMA<sub>41</sub> precursor. This system is the third example of a methacrylic monomer that exhibits sufficient aqueous solubility to avoid the problem of kinetically-trapped spheres that is observed for so many RAFT aqueous emulsion polymerisation formulations.<sup>20, 21</sup> Recently, Hatton *et al.* demonstrated that the mean DP of the steric stabiliser block is an important parameter to consider when targeting a specific copolymer morphology.<sup>22, 23</sup> In an initial study, only kinetically-trapped spheres could be prepared when using a PGMA<sub>45</sub> precursor. This is because only kinetically-trapped spherical nanoparticles are accessible owing to inefficient sphere-sphere fusion, which is a prerequisite for the formation of higher-order morphologies.<sup>24</sup> However, using a shorter PGMA<sub>28</sub> precursor enabled access to worms and vesicles. In this Thesis, a pseudo-phase diagram was constructed for a series of PGMA<sub>41</sub>-PHBMA<sub>x</sub> nano-objects at varying concentrations to enable the reproducible preparation of the full range of copolymer morphologies. Thus a significantly longer PGMA<sub>41</sub> precursor can be used to prepare PHBMA-based worms or vesicles compared to the analogous PGMA<sub>28</sub>-PGlyMA<sub>x</sub> formulation reported by Hatton and co-workers.<sup>22, 23</sup> In this context, it would be useful to determine the highest PGMA DP at which higher-order morphologies can still be accessed.

Recent studies have shown that block copolymer vesicles undergo an ‘inward growth’ mechanism during *in situ* SAXS studies of RAFT dispersion polymerisations conducted in either mineral oil<sup>25</sup> or water.<sup>26</sup> More explicitly, the overall vesicle diameter remains essentially unchanged during the final stages of such polymerisations, while the vesicle membrane continues to thicken. This eventually leads to vesicle instability if a sufficiently high core-

forming block DP is targeted.<sup>27</sup> Given that a pure vesicular morphology can be accessed when using relatively high PGMA stabiliser DPs compared to methacrylic monomers with similar aqueous solubility,<sup>20,21</sup> PHBMA should be a good candidate for examining the vesicle growth mechanism during RAFT aqueous emulsion polymerisation. This is because using shorter PGMA blocks may well lead to colloidal instability (incipient flocculation) due to insufficient steric stabilisation.<sup>28</sup>

TEM studies were conducted on aliquots taken at regular intervals during the preparation of PGMA<sub>41</sub>-PHBMA<sub>120</sub> vesicles. Such sampling of the reaction mixture at intermediate monomer conversions indicated that the mechanism by which these vesicles are formed is strikingly similar to that for PGMA<sub>47</sub>-PHPMA<sub>200</sub> vesicles prepared *via* RAFT aqueous dispersion polymerisation.<sup>29</sup> Recently, Brotherton *et al.* utilised *in situ* synchrotron SAXS to monitor the formation of PGMA<sub>29</sub>-PMOEMA<sub>70</sub> vesicles.<sup>20</sup> This technique is statistically much more robust than TEM and also provides structural information for the block copolymer nanoparticles in their native wet state. Moreover, the excellent temporal resolution offered by synchrotron SAXS provided detailed insight into the evolution in copolymer morphology during the MOEMA polymerisation.<sup>20, 25</sup> Similar synchrotron SAXS studies could also be undertaken during the RAFT aqueous emulsion polymerisation of HBMA to complement the TEM studies.

Mable *et al.* demonstrated that relatively hydrophobic core-forming blocks are required to ensure survival of block copolymer nano-objects during high-shear homogenisation.<sup>30</sup> For example, linear PGMA<sub>63</sub>-PHPMA<sub>350</sub> vesicles did not withstand high-shear homogenisation but instead stabilised oil droplets in the form of molecularly-dissolved amphiphilic diblock copolymer chains.<sup>31</sup> However, chain-extending such diblock copolymers with BzMA to form linear PGMA<sub>63</sub>-PHPMA<sub>350</sub>-PBzMA<sub>25</sub> triblock copolymer vesicles was sufficient to prevent vesicle dissociation during emulsification. Similar findings have also been reported for spherical and worm-like copolymer morphologies.<sup>32</sup> In Chapter 4, it was demonstrated that linear PGMA<sub>41</sub>-PHBMA<sub>110</sub> vesicles could survive homogenisation conditions without requiring a more hydrophobic third block. This was attributed to the greater hydrophobic character of PHBMA

compared to PHPMA, which leads to stronger inter-chain attractive forces. It would be interesting to determine the minimum PHBMA DP required for the diblock copolymer nano-objects to survive homogenisation, not least because using either spheres<sup>14</sup> or worms<sup>33</sup> as Pickering emulsifiers is likely to offer advantages over vesicles. For example, spheres would be required to produce the analogous Pickering nanoemulsions (if this is technical feasible),<sup>14</sup> whereas worms provide a comparable specific surface area to that of spheres while adsorbing much more strongly at the oil/water interface.<sup>33</sup>

In Chapter 5, the first thermoresponsive block copolymer to be prepared by RAFT aqueous emulsion polymerisation is reported. Remarkably, a *single* PEG<sub>45</sub>-PHBMA<sub>20</sub> diblock copolymer can form sphere, worms or vesicles simply by varying the solution temperature, despite the relatively hydrophobic nature of the PHBMA core-forming block. Over the past two years, there has been several reports of similar ‘shape-shifting’ thermoresponsive block copolymers that can form sphere, worms or vesicles.<sup>34-36</sup> However, the insoluble structure-directing block of such copolymers is more weakly hydrophobic (e.g. PHPMA or PHBA). In this Thesis, variable temperature <sup>1</sup>H NMR studies indicated significant dehydration of the PEG<sub>45</sub> block on heating. Furthermore, partial hydration of the PHBMA core-forming block is observed above 60 °C. Thus it seems that, for this particular system, subtle changes in the degree of (partial) hydration of both the hydrophilic block and the hydrophobic block are responsible for the morphological transitions that are observed on heating. It is well-known that aqueous solutions of PEG homopolymer can exhibit an LCST-type transition on heating.<sup>37</sup> Moreover, this LCST shifts to lower temperatures for longer PEG chains.<sup>38</sup> On the other hand, increasing the DP of the PEG stabiliser block should increase the degree of steric stabilisation conferred to the PEG-PHBMA nano-objects. Therefore, it would be interesting to examine the effect of varying the PEG stabiliser DP on the thermoresponsive nature of a series of PEG-PHBMA diblock copolymers. Furthermore, the presence of salt is known to reduce the solvent quality for PEG in aqueous solution.<sup>39</sup> In principle, adding salt to the PEG<sub>45</sub>-PHBMA<sub>20</sub> nano-objects should

enable the transition temperatures to be tuned so that they are more suitable for biological applications.<sup>40, 41</sup>

In this Thesis, SAXS has proven to be an invaluable characterisation technique for the analysis of Pickering nanoemulsions and block copolymer nano-objects. In Chapter 2, a two-population model was used to analyse SAXS patterns recorded for Pickering nanoemulsions stabilised by nanoparticles with either charged or neutral end-groups. Although TEM studies provided useful insights with regards to the structure of the droplets, SAXS enabled the nanoemulsions to be quantified in terms of their mean droplet diameter, shell thickness and particle packing efficiency. Similarly, in Chapter 3, SAXS studies confirmed that a loosely-packed monolayer of adsorbed nanoparticles surrounded the aqueous droplets. This was especially useful for such w/o Pickering nanoemulsions, since the particulate nature of the shell was not obviously apparent from electron microscopy studies. In Chapter 4, the importance of characterising block copolymer nano-objects using SAXS was highlighted. More specifically, SAXS readily enabled discrimination between block copolymer spheres and relatively small vesicles. Since the latter did not collapse under ultrahigh vacuum conditions, they could be incorrectly assigned as spheres based on TEM analysis alone. Finally, in Chapter 5, SAXS studies enabled the quantitative analysis of multiple thermally-driven morphological transitions exhibited by a single block copolymer.

## 6.2 References

1. A. Gupta, H. B. Eral, T. A. Hatton and P. S. Doyle, *Soft Matter*, 2016, **12**, 2826-2841.
2. A. Naseema, L. Kovooru, A. K. Behera, K. P. P. Kumar and P. Srivastava, *Adv. Colloid Interface Sci.*, 2021, **287**.
3. T. J. Ashaolu, *Environmental Chemistry Letters*, 2021, **19**, 3381-3395.
4. O. Sonnevile-Aubrun, J. T. Simonnet and F. L'Alloret, *Adv. Colloid Interface Sci.*, 2004, **108-109**, 145-149.
5. D. J. McClements, *Soft Matter*, 2011, **7**, 2297-2316.
6. Z. Du, C. Wang, X. Tai, G. Wang and X. Liu, *ACS Sustain. Chem. Eng.*, 2016, **4**, 983-991.
7. D. J. Kang, H. Bararnia and S. Anand, *ACS Appl. Mater. Interfaces*, 2018, **10**, 21746-21754.
8. Z. Yang, W. Wang, G. Wang and X. Tai, *Colloids Surf., A*, 2020, **585**, 124098.

9. K. H. Persson, I. A. Blute, I. C. Mira and J. Gustafsson, *Colloids Surf., A*, 2014, **459**, 48-57.
10. B. P. Binks, *Langmuir*, 2017, **33**, 6947-6963.
11. B. P. Binks, *Curr. Opin. Colloid Interface Sci.*, 2002, **7**, 21-41.
12. V. J. Cunningham, A. M. Alswieleh, K. L. Thompson, M. Williams, G. J. Leggett, S. P. Armes and O. M. Musa, *Macromolecules*, 2014, **47**, 5613-5623.
13. M. J. Rymaruk, V. J. Cunningham, S. L. Brown, C. N. Williams and S. P. Armes, *J. Colloid Interface Sci.*, 2020, **580**, 354-364.
14. K. L. Thompson, N. Cinotti, E. R. Jones, C. J. Mable, P. W. Fowler and S. P. Armes, *Langmuir*, 2017, **33**, 12616-12623.
15. B. Akpınar, L. A. Fielding, V. J. Cunningham, Y. Ning, O. O. Mykhaylyk, P. W. Fowler and S. P. Armes, *Macromolecules*, 2016, **49**, 5160-5171.
16. J. A. Balmer, O. O. Mykhaylyk, A. Schmid, S. P. Armes, J. P. A. Fairclough and A. J. Ryan, *Langmuir*, 2011, **27**, 8075-8089.
17. Y. De Smet, L. Deriemaeker and R. Finsy, *Langmuir*, 1999, **15**, 6745-6754.
18. J. Weiss, C. Canceliere and D. J. McClements, *Langmuir*, 2000, **16**, 6833-6838.
19. J. Kizling and B. Kronberg, *Colloids Surf.*, 1990, **50**, 131-140.
20. E. E. Brotherton, F. L. Hatton, A. A. Cockram, M. J. Derry, A. Czajka, E. J. Cornel, P. D. Topham, O. O. Mykhaylyk and S. P. Armes, *J. Am. Chem. Soc.*, 2019, **141**, 13664-13675.
21. F. L. Hatton, M. J. Derry and S. P. Armes, *Polym. Chem.*, 2020, **11**, 6343-6355.
22. F. L. Hatton, J. R. Lovett and S. P. Armes, *Polym. Chem.*, 2017, **8**, 4856-4868.
23. F. L. Hatton, A. M. Park, Y. Zhang, G. D. Fuchs, C. K. Ober and S. P. Armes, *Polym. Chem.*, 2019, **10**, 194-200.
24. A. Blanzas, A. J. Ryan and S. P. Armes, *Macromolecules*, 2012, **45**, 5099-5107.
25. M. J. Derry, L. A. Fielding, N. J. Warren, C. J. Mable, A. J. Smith, O. O. Mykhaylyk and S. P. Armes, *Chem. Sci.*, 2016, **7**, 5078-5090.
26. A. Czajka and S. P. Armes, *Chem. Sci.*, 2020, **11**, 11443-11454.
27. N. J. Warren, O. O. Mykhaylyk, A. J. Ryan, M. Williams, T. Doussineau, P. Dugourd, R. Antoine, G. Portale and S. P. Armes, *J. Am. Chem. Soc.*, 2015, **137**, 1929-1937.
28. N. J. W. Penfold, J. R. Whatley and S. P. Armes, *Macromolecules*, 2019, **52**, 1653-1662.
29. A. Blanzas, J. Madsen, G. Battaglia, A. J. Ryan and S. P. Armes, *J. Am. Chem. Soc.*, 2011, **133**, 16581-16587.
30. C. J. Mable, N. J. Warren, K. L. Thompson, O. O. Mykhaylyk and S. P. Armes, *Chem. Sci.*, 2015, **6**, 6179-6188.
31. K. L. Thompson, P. Chambon, R. Verber and S. P. Armes, *J. Am. Chem. Soc.*, 2012, **134**, 12450-12453.
32. C. J. Mable, K. L. Thompson, M. J. Derry, O. O. Mykhaylyk, B. P. Binks and S. P. Armes, *Macromolecules*, 2016, **49**, 7897-7907.
33. K. L. Thompson, C. J. Mable, A. Cockram, N. J. Warren, V. J. Cunningham, E. R. Jones, R. Verber and S. P. Armes, *Soft Matter*, 2014, **10**, 8615-8626.
34. L. P. D. Ratcliffe, M. J. Derry, A. Ianiro, R. Tuinier and S. P. Armes, *Angew. Chem. Int. Ed.*, 2019, **58**, 18964-18970.

35. S. J. Byard, C. T. O'Brien, M. J. Derry, M. Williams, O. O. Mykhaylyk, A. Blanz and S. P. Armes, *Chem. Sci.*, 2020, **11**, 396-402.
36. O. J. Deane, J. Jennings, O. M. Musa, A. Fernyhough and S. P. Armes, *Chem. Mater.*, 2021, in the press.
37. E. E. Dormidontova, *Macromolecules*, 2002, **35**, 987-1001.
38. S. Saeki, N. Kuwahara, M. Nakata and M. Kaneko, *Polymer*, 1976, **17**, 685-689.
39. F. E. Bailey and R. Callard, *J. Appl. Polym. Sci.*, 1959, **1**, 56-62.
40. L. Romero-Azogil, N. J. W. Penfold and S. P. Armes, *Polym. Chem.*, 2020, **11**, 5040-5050.
41. I. Canton, N. J. Warren, A. Chahal, K. Amps, A. Wood, R. Weightman, E. Wang, H. Moore and S. P. Armes, *ACS Cent. Sci.*, 2016, **2**, 65-74.

# Chapter 7:

# Appendix

## 7.1 Structural Models for Small-Angle X-ray Scattering

### Analysis

In general, the intensity of X-rays scattered by a dispersion of nanoparticles [usually represented by the scattering cross section per unit sample volume,  $\frac{d\Sigma}{d\Omega}(q)$ ] can be expressed as:

$$\frac{d\Sigma}{d\Omega}(q) = \sum_{i=1}^n S_i(q) N_i \int_0^{\infty} \dots \int_0^{\infty} F_i(q, r_{1i}, \dots, r_{ki})^2 \Psi_i(r_{1i}, \dots, r_{ki}) dr_{1i} \dots dr_{ki} \quad 7.1$$

where  $n$  is the number of different populations of particles in the dispersion,  $N_i$  is the number density of scattering particles of  $i$ th population,  $F_i(q, r_{1i}, \dots, r_{ki})$  is the form factor that describes the particle morphology of the  $i$ th population using  $k_i$  number of parameters (including contrast and volume parameters of the particles),  $\Psi_i(r_{1i}, \dots, r_{ki})$  is the probability distribution function of parameters describing scattering particle model corresponding to the  $i$ th population, and  $S_i(q)$  is the structure factor arising from interparticle interactions.

Following our prior study of the characterisation of core-shell nanocomposite particles comprising polymer latex cores and particulate silica shells,<sup>1</sup> the SAXS data recorded for o/w and w/o Pickering nanoemulsions were analysed using a two-population model ( $n = 2$ ). Population 1 ( $i = 1$ ) is represented by core-shell spheres (described in 7.1.1), where the cores comprise the oil or water droplets and the adsorbed layer of nanoparticles form the shell. The particulate nature of the shell is described by small homogeneous spheres (described in 7.1.2) or spherical micelles (described in 7.1.3), which corresponds to population 2 ( $i = 2$ ).

#### 7.1.1 Core-Shell Particle Model

The following functions and parameters were used for the core-shell particle ( $i = 1$ ) model:

$$F_1(q, r_{11}) = V_{\text{total}}(\xi_{\text{shell}} - \xi_{\text{sol}})\Phi[q(r_{11} + T_{\text{shell}})] + V_{\text{core}}(\xi_{\text{core}} - \xi_{\text{shell}})\Phi(qr_{11}) \quad 7.2$$

where

$$\Phi(x) = \frac{3[\sin(x) - x\cos(x)]}{(x)^3} \quad 7.3$$

and  $r_{11}$  is the core radius and  $T_{\text{shell}}$  is the shell thickness.  $V_{\text{total}} = \frac{4}{3}\pi(r_{11} + T_{\text{shell}})^3$  and  $V_{\text{core}} = \frac{4}{3}\pi r_{11}^3$  are volumetric parameters for the core-shell particles, while  $\xi_{\text{core}}$ ,  $\xi_{\text{shell}}$  and  $\xi_{\text{sol}}$  are the scattering length densities for the droplet core ( $\xi_{n\text{-dodecane}} = 7.63 \times 10^{10} \text{ cm}^{-2}$  or  $\xi_{\text{H}_2\text{O}} = 9.42 \times 10^{10} \text{ cm}^{-2}$ ), for the particulate shell [volume-averaged scattering length density of spherical micelles  $\bar{\xi}_p = (\xi_s V_s + \xi_c V_c)/(V_s + V_c)$  and for the surrounding medium ( $\xi_{\text{H}_2\text{O}} = 9.42 \times 10^{10} \text{ cm}^{-2}$  or  $\xi_{n\text{-dodecane}} = 7.63 \times 10^{10} \text{ cm}^{-2}$ ), respectively. Here,  $\xi_s$  and  $\xi_c$  are the X-ray scattering length densities of the core and corona blocks, respectively, and  $V_s$  and  $V_c$  are the volumes of the core-forming block and the corona block, respectively. Dispersity of only one parameter (the particle core radius) was considered in the SAXS analysis. It was expressed by a Gaussian distribution:

$$\Psi_1(r_{11}) = \frac{1}{(2\pi\sigma_{R_c}^2)^{\frac{1}{2}}} \exp\left[-\frac{(r_{11} - R_c)^2}{2\sigma_{R_c}^2}\right] \quad 7.4$$

where  $R_c$  is the mean core radius and  $\sigma_{R_c}$  is the standard deviation of the droplet core radius. The number density for the 1<sup>st</sup> population is expressed as:

$$N_1 = \frac{\varphi_{\text{droplet}}}{\int_0^\infty V(r_{11}) \Psi_1(r_{11}) dr_{11}} \quad 7.5$$

where  $\varphi_{\text{droplet}}$  is the relative volume fraction of the core-shell nanoemulsion droplets. In all cases, a dilute dispersion (1% v/v) of nanoemulsions has been used, so the structure factor is set to unity [ $S_1(q)=1$ ].

### 7.1.2 Homogenous Spherical Particle Model

The PGMA<sub>48</sub>-PTFEMA<sub>50</sub> spherical nanoparticles forming the emulsion droplet shell can be represented by a single population (second population) of spherical particles with the following functions and parameters describing the model:

$$F_2(q, r_{12}) = V(r_{12})\Delta\xi f(qr_{12}) \quad 7.6$$

where

$$f(x) = \frac{3[\sin(x) - qr\cos(x)]}{(x)^3} \quad 7.7$$

is the form factor of a spherical particle,  $V(r_{12}) = \pi r_{12}^3/3$  is the volume of the particles and  $\Delta\xi$  is the scattering contrast between the scattering length density of the PGMA<sub>48</sub>-PTFEMA<sub>50</sub> nanoparticles  $\xi_p = [(\xi_s V_s + \xi_c V_c)/(V_s + V_c)]$  and the surrounding medium  $\xi_{sol}$ . Dispersity of the particle size was expressed only by a Gaussian (normal) distribution in the SAXS analysis:

$$\Psi(r_{12}) = \frac{1}{(2\pi\sigma_{R_s}^2)^{\frac{1}{2}}} \exp\left[\frac{-(r_{12} - R_s)^2}{2\sigma_{R_s}^2}\right] \quad 7.8$$

where  $R_s$  is the mean particle radius of PGMA<sub>48</sub>-PTFEMA<sub>50</sub> and  $\sigma_{R_s}$  is the standard deviation of the sphere radius.

In some cases, an effective structure factor expression proposed for interacting spherical particles has been used in Equation 7.1.<sup>2</sup> This is a hard-sphere structure factor based on the Percus-Yevick approximation,  $S_{PY}(q, R_{PY}, f_{PY})$  where  $R_{PY}$  is the interaction radius and  $f_{PY}$  is the hard-sphere effective volume fraction.

### 7.1.3 Spherical Micelle Model

The spherical micelle form factor is given by:<sup>3</sup>

$$F_{s\_mic}(q) = N_s^2 \beta_s^2 A_s^2(q, R_s) + N_s \beta_c^2 F_c(q, R_g) + N_s(N_s - 1) \beta_c^2 A_c^2(q) \\ + 2N_s^2 \beta_s \beta_c A_s(q, R_s) A_c(q) \quad 7.9$$

where  $r_s$  is the radius of the spherical micelle core and  $R_g$  is the radius of gyration of the coronal steric stabiliser block. The  $R_g$  values of the coronal blocks from all data fitting are comparable to the estimated value. For example, the latter can be calculated from the total contour length of the PGMA<sub>41</sub> block,  $L_{\text{PGMA}_{41}} = 41 \times 0.255 \text{ nm} = 10.45 \text{ nm}$  (since the projected contour length per GMA monomer repeat unit is defined by two carbon bonds in an all-trans conformation, or 0.255 nm) and the Kuhn length of 1.53 nm [based on the known literature value for poly(methyl methacrylate)] results in an approximate  $R_g$  of  $(10.45 \times 1.53/6)^{1/2} = 1.63 \text{ nm}$ . The X-ray scattering length contrasts for the core and corona blocks are given by  $\beta_s = V_s(\xi_s - \xi_{\text{sol}})$  and  $\beta_c = V_c(\xi_c - \xi_{\text{sol}})$ , respectively. Here,  $\xi_s$ ,  $\xi_c$  and  $\xi_{\text{sol}}$  are the X-ray scattering length densities of the core block ( $\xi_{\text{PTFEMA}} = 12.76 \times 10^{10} \text{ cm}^{-2}$  or  $\xi_{\text{PHBMA}} = 10.61 \times 10^{10} \text{ cm}^{-2}$ ), corona block ( $\xi_{\text{PGMA}} = 11.94 \times 10^{10} \text{ cm}^{-2}$ ,  $\xi_{\text{PSMA}} = 9.24 \times 10^{10} \text{ cm}^{-2}$  or  $\xi_{\text{PEG}} = 10.85 \times 10^{10} \text{ cm}^{-2}$ ) and solvent ( $\xi_{\text{water}} = 9.42 \times 10^{10} \text{ cm}^{-2}$  or  $\xi_{n\text{-dodecane}} = 7.63 \times 10^{10} \text{ cm}^{-2}$ ), respectively.  $V_s$  and  $V_c$  are the volumes of the core-forming block ( $V_{\text{PTFEMA}}$  or  $V_{\text{PHBMA}}$ ) and the corona block ( $V_{\text{PGMA}}$ ,  $V_{\text{PSMA}}$  or  $V_{\text{PEG}}$ ), respectively. These volumes were calculated using  $V = \frac{M_{n,\text{pol}}}{N_A \rho}$  where the mass density  $\rho$  of the core-forming blocks were taken to be  $\rho_{\text{PHBMA}} = 1.15 \text{ g cm}^{-3}$ ,<sup>3</sup>  $\rho_{\text{TFEMA}} = 1.47 \text{ g cm}^{-3}$ ,<sup>4</sup> and the density of stabiliser blocks was taken to be  $\rho_{\text{PGMA}} = 1.31 \text{ g cm}^{-3}$ ,<sup>5</sup>  $\rho_{\text{PSMA}} = 0.97 \text{ g cm}^{-3}$ ,  $\rho_{\text{PEG}} = 0.97 \text{ g cm}^{-3}$ .<sup>6</sup>  $M_{n,\text{pol}}$  corresponds to the number-average molecular weight of the diblock copolymer chains determined by <sup>1</sup>H NMR spectroscopy.

The sphere form factor amplitude is used for the amplitude of the core self-term:

$$A_s(q, r_1) = \Phi(qr_s) \exp\left(-\frac{q^2 \sigma^2}{2}\right) \quad 7.10$$

where  $\Phi(qr_s) = \frac{3[\sin(qr_s) - qr_s \cos(qr_s)]}{(qr_s)^3}$ . A sigmoidal interface between the two blocks was assumed for the spherical micelle form factor (Equation 7.10). This is described by the exponent term with a width  $\sigma$  accounting for a decaying scattering length density at the micellar interface. This  $\sigma$  value was fixed at 0.25 nm during fitting.

The form factor amplitude of the spherical micelle corona is:

$$A_c(q) = \frac{\int_{r_s}^{r_s+2s} \mu_c(r) \frac{\sin(qr)}{qr} r^2 dr}{\int_{r_s}^{r_s+2s} \mu_c(r) r^2 dr} \exp\left(-\frac{q^2 \sigma^2}{2}\right) \quad 7.11$$

The aggregation number,  $N_s$ , of the spherical micelle is given by:

$$N_s(r_1) = (1 - x_{sol}) \frac{\frac{4}{3} \pi r_1^3}{V_s} \quad 7.12$$

where  $x_{sol}$  is the volume fraction of solvent within the micelle core. A dispersity for one parameter ( $r_s$ ) is assumed for the micelle model, which is described by a Gaussian distribution.

Thus, the dispersity function can be represented as:

$$\Psi(r_s) = \frac{1}{\sqrt{2\pi\sigma_{R_s}^2}} \exp\left(-\frac{(r_s - R_s)^2}{2\sigma_{R_s}^2}\right) \quad 7.14$$

where  $R_s$  is the mean spherical micelle core radius and  $\sigma_{R_s}$  is its standard deviation. The number density per unit volume for the micelle model is expressed as:

$$N = \frac{\varphi}{\int_0^\infty V(r_s) \Psi(r_s) dr_s} \quad 7.15$$

where  $\varphi$  is the total volume fraction of copolymer in the spherical micelles and  $V(r_s)$  is the total volume of copolymer in a spherical micelle  $V(r_s) = (V_s + V_c)N_s(r_s)$ . For a single population model or the two-population model  $r_s$  was assigned to  $r_{11}$  or  $r_{12}$ , respectively (Equation 7.1).

An effective structure factor expression proposed for interacting spherical micelles<sup>8</sup> around the droplets has been used in Equation 7.1:

$$S_s(q) = 1 + \frac{A_{s_{mic}}^{av}(q)^2 [S_{PY}(q, R_{PY}, f_{PY}) - 1]}{F_{s_{mic}}(q)} \quad 7.16$$

Herein the form factor of the average radial scattering length density distribution of micelles is used as  $A_{s_{mic}}^{av}(q) = N_s[\beta_s A_s(q, R_s) + \beta_c A_c(q)]$  and  $S_{PY}(q, R_{PY}, f_{PY})$  is a hard-sphere interaction structure factor based on the Percus-Yevick approximation,<sup>9</sup> where  $R_{PY}$  is the interaction radius and  $f_{PY}$  is the hard-sphere effective volume fraction.

### 7.1.4 Worm-like Micelle Model

The worm-like micelle form factor is given by:<sup>3</sup>

$$\begin{aligned}
 F_{\text{Wmic}}(q, r_w) = & N_w^2(r_w)\beta_s^2 F_w(q, r_w) + N_w(r_w)\beta_c^2 F_c(q, R_g) \\
 & + N_w(r_w)[N_w(r_w) - 1]\beta_c^2 S_{cc}(q) \\
 & + 2N_w^2(r_w)\beta_s\beta_c S_{sc}(q, r_w)
 \end{aligned}
 \tag{7.16}$$

where all the parameters are the same as in the spherical micelles model unless stated otherwise.

The self-correlation term for the worm core with cross-sectional radius  $r_w$  is:

$$F_w(q, r_w) = F_{\text{worm}}(q, L_w, b_w) A_{\text{csworm}}^2(q, r_w) \tag{7.17}$$

where

$$A_{\text{csworm}}^2(q, r_w) = \left[ 2 \frac{J_1(qr_w)}{qr_w} \right]^2 \tag{7.18}$$

and  $J_1$  is the first-order Bessel function of the first kind, and a form factor  $F_{\text{worm}}(q, L_w, b_w)$  for self-avoiding semi-flexible chains represents the worm-like micelles, where  $b_w$  is the Kuhn length and  $L_w$  is the mean contour length. A complete expression for the chain form factor can be found elsewhere.<sup>10</sup>

The mean aggregation number of the worm-like micelle,  $N_w(r_w)$ , is given by:

$$N_w(r_w) = (1 - x_{\text{sol}}) \frac{\pi r_w^2 L_w}{V_s} \tag{7.19}$$

where  $x_{\text{sol}}$  is the volume fraction of solvent within the worm-like micelle core. The possible presence of semi-spherical caps at the two ends of each worm is neglected in this form factor.

A dispersity of one parameter ( $r_w$ ) is assumed for the micelle model, which is described by a Gaussian distribution. Thus, the polydispersity function can be represented as:

$$\Psi(r_w) = \frac{1}{\sqrt{2\pi\sigma_{R_w}^2}} \exp\left(-\frac{(r_w - R_w)^2}{2\sigma_{R_w}^2}\right) \tag{7.20}$$

where  $R_w$  is the volume-average cross-sectional radius and  $\sigma_{R_w}$  is its standard deviation. The number density per unit volume for the micelle model is expressed as:

$$N = \frac{\varphi}{\int_0^\infty V(r_w)\Psi(r_w)dr_w} \quad 7.21$$

where  $\varphi$  is the total volume fraction of copolymer in the worm-like micelles and  $V(r_w)$  is the total volume of copolymer in a worm-like micelle [ $V(r_w) = (V_s + V_c)N_w(r_w)$ ].

### 7.1.5 Vesicle Model

The vesicle form factor is expressed as:<sup>11</sup>

$$\begin{aligned} F_{\text{ves}}(q, r_v, T_v) = & N_v^2(r_v, T_v)\beta_s^2 A_m^2(q, r_v, T_v) + N_v(r_v, T_v)\beta_c^2 F_c(q, R_g) \\ & + N_v(r_v, T_v)[N_v(r_v, T_v) - 1]\beta_c^2 A_{vc}^2(q) \\ & + 2N_v^2(r_v, T_v)\beta_s\beta_c A_m(q, r_v, T_v)A_{vc}(q) \end{aligned} \quad 7.22$$

where all the parameters are the same as in the spherical micelle model unless stated otherwise.

The amplitude of the membrane self-term is:

$$A_m(q, r_v, T_v) = \frac{V_{\text{out}}\Phi(qR_{\text{out}}) - V_{\text{in}}\Phi(qR_{\text{in}})}{V_{\text{out}} - V_{\text{in}}} \exp\left(-\frac{q^2\sigma_{\text{in}}^2}{2}\right) \quad 7.23$$

where  $R_{\text{in}} = r_v - \frac{1}{2}T_v$  is the inner radius of the membrane and  $R_{\text{out}} = r_v + \frac{1}{2}T_v$  is the outer radius of the membrane ( $r_v$  is the radius from the centre of the vesicle to the centre of the membrane and  $T_v$  is the membrane thickness), and  $V_{\text{in}} = \frac{4}{3}\pi R_{\text{in}}^3$  and  $V_{\text{out}} = \frac{4}{3}\pi R_{\text{out}}^3$ . It should be noted that Equation 7.23 differs from the original work in which they were first described.<sup>8</sup> The exponent term in Equation 7.23 represents a sigmoidal interface between the blocks, with a width  $\sigma_{\text{in}}$  accounting for a decaying scattering length density at the membrane surface. The value of  $\sigma_{\text{in}}$  was fixed at 0.25 nm during fitting. The mean vesicle aggregation number,  $N_v(r_v, T_v)$ , is given by

$$N_v(r_v, T_v) = (1 - x_{\text{sol}}) \frac{V_{\text{out}} - V_{\text{in}}}{V_s} \quad 7.24$$

where  $x_{\text{sol}}$  is the volume fraction of solvent within the vesicle membrane. Assuming that there is no penetration of the hydrophilic coronal blocks into the hydrophobic membrane, the amplitude of the vesicle corona self-term is expressed as:

$$A_{vc}(q) = \Psi(qR_g) \frac{1}{2} \left[ \frac{\sin[q(R_{out} + R_g)]}{q(R_{out} + R_g)} + \frac{\sin[q(R_{in} - R_g)]}{q(R_{in} - R_g)} \right] \quad 7.25$$

where the term outside the square brackets is the factor amplitude of the corona block polymer chain such that:

$$\Psi(qR_g) = \frac{1 - \exp(-qR_g)}{(qR_g)^2} \quad 7.26$$

For the vesicle model, it was assumed that two parameters are disperse: the radius from the centre of the vesicle to the centre of the membrane and the membrane thickness ( $r_v$  and  $T_v$ , respectively). Each parameter is considered to have a Gaussian distribution of values, hence the dispersity function can be expressed in each case as:

$$\Psi(r_v, T_v) = \frac{1}{\sqrt{2\pi\sigma_{R_s}^2}} \exp\left(-\frac{(r_v - R_m)^2}{2\sigma_{R_m}^2}\right) \frac{1}{\sqrt{2\pi\sigma_{T_m}^2}} \exp\left(-\frac{(T_v - T_m)^2}{2\sigma_{T_m}^2}\right) \quad 7.27$$

where  $R_m$  is the mean radius from the centre of the vesicle to the centre of the membrane and  $T_m$  is the mean membrane thickness.  $\sigma_{R_m}$  and  $\sigma_{T_m}$  are the standard deviations for  $R_m$  and  $T_m$ , respectively. The number density per unit volume for the vesicle model is expressed as:

$$N = \frac{\varphi}{\int_0^\infty \int_0^\infty V(r_v, T_v) \Psi(r_v, T_v) dr_v dT_v} \quad 7.28$$

where  $\varphi$  is the total *volume fraction* of copolymer in the vesicles and  $V(r_v, T_v)$  is the total *volume* of copolymer in a vesicle [ $V(r_v, T_v) = (V_s + V_c)N_v(r_v, T_v)$ ].

Programming tools within the Irena SAS Igor Pro macros<sup>12</sup> were used to implement the scattering models

## 7.2 UV GPC Calibration Plots

UV chromatograms recorded for known concentrations of the original aqueous PGMA<sub>48</sub>-PTFEMA<sub>50</sub> nanoparticle dispersions to construct a linear calibration plot.

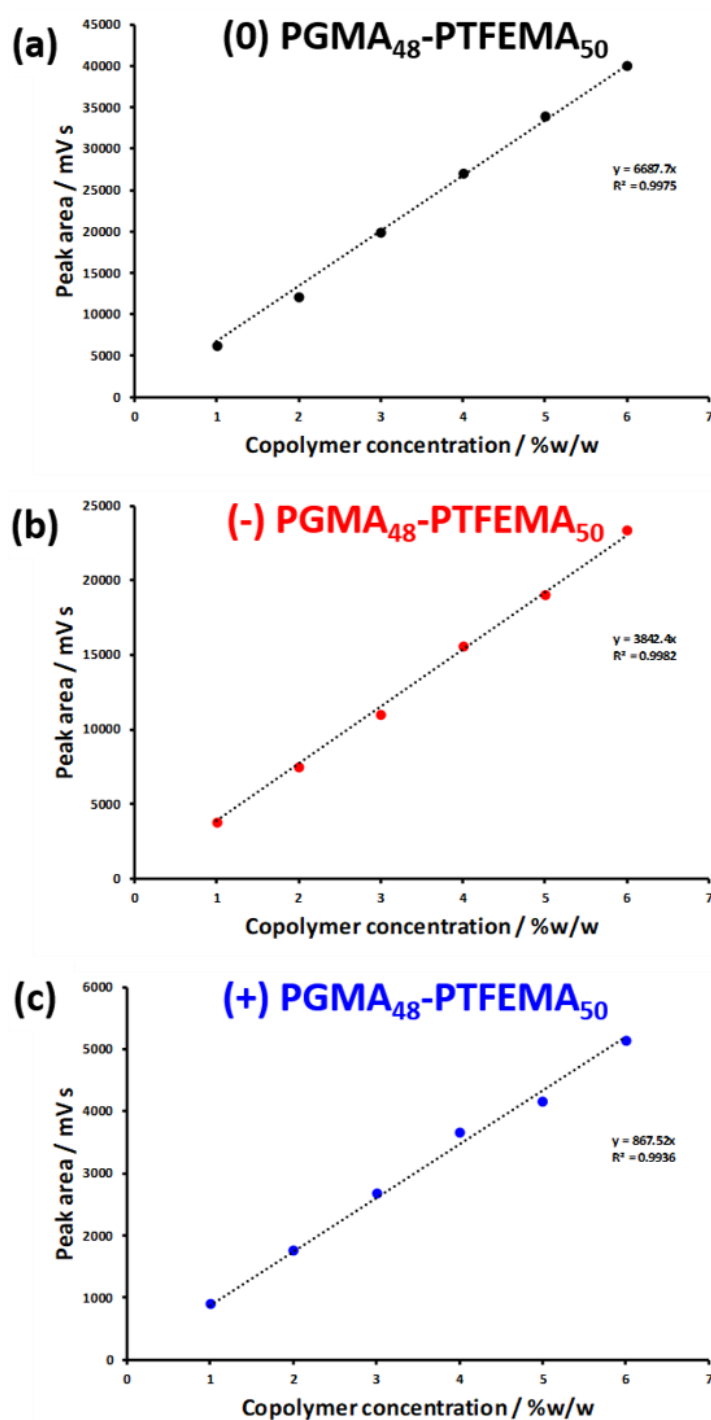


**Figure 7.1.** UV GPC calibration plot constructed for (a) (0) PGMA<sub>48</sub>-PTFEMA<sub>48</sub>, (b) (-) PGMA<sub>48</sub>-PTFEMA<sub>48</sub>, and (c) (+) PGMA<sub>48</sub>-PTFEMA<sub>48</sub> recorded at a fixed UV wavelength of 305 nm, which corresponds to the absorption maximum assigned to the dithiobenzoate or trithiocarbonate RAFT end-groups.

### 7.3 References

1. J. A. Balmer, O. O. Mykhaylyk, A. Schmid, S. P. Armes, J. P. A. Fairclough and A. J. Ryan, *Langmuir*, 2011, **27**, 8075-8089.
2. J. K. Percus and G. J. Yevick, *Physical Review*, 1958, **110**, 1-13.
3. J. Pedersen, *J. Appl. Crystallogr.*, 2000, **33**, 637-640.
4. A. A. Cockram, T. J. Neal, M. J. Derry, O. O. Mykhaylyk, N. S. J. Williams, M. W. Murray, S. N. Emmett and S. P. Armes, *Macromolecules*, 2017, **50**, 796-802.
5. B. Akpinar, L. A. Fielding, V. J. Cunningham, Y. Ning, O. O. Mykhaylyk, P. W. Fowler and S. P. Armes, *Macromolecules*, 2016, **49**, 5160-5171.
6. C. J. Mable, N. J. Warren, K. L. Thompson, O. O. Mykhaylyk and S. P. Armes, *Chem. Sci.*, 2015, **6**, 6179-6188.
7. M. J. Derry, L. A. Fielding, N. J. Warren, C. J. Mable, A. J. Smith, O. O. Mykhaylyk and S. P. Armes, *Chem. Sci.*, 2016, **7**, 5078-5090.
8. J. S. Pedersen, *J. Chem. Phys.*, 2001, **114**, 2839-2846.
9. D. J. Kinning and E. L. Thomas, *Macromolecules*, 1984, **17**, 1712-1718.
10. J. S. Pedersen and P. Schurtenberger, *Macromolecules*, 1996, **29**, 7602-7612.
11. J. Bang, S. Jain, Z. Li, T. P. Lodge, J. S. Pedersen, E. Kesselman and Y. Talmon, *Macromolecules*, 2006, **39**, 1199-1208.
12. J. Ilavsky and P. R. Jemian, *J. Appl. Crystallogr.*, 2009, **42**, 347-353.